Reactive Transport Modelling of High Pressure Gas Flow in Coal

Lee James Hosking

Geoenvironmental Research Centre

Cardiff School of Engineering

Cardiff University

*Thesis submitted in candidature for the degree of Doctor of Philosophy
at Cardiff University*

May 2014

Declaration

This work has not been submitted in substance for any other degree or award at this or any other university or place of learning, nor is being submitted concurrently in candidature for any degree or other award.

Signed……………………………………………………….   *Date* 30th May 2014

Statement 1

This thesis is being submitted in partial fulfilment of the requirements for the degree of PhD.

Signed……………………………………………………….   *Date* 30th May 2014

Statement 2

This thesis is the result of my own independent work/investigation, except where otherwise stated. Other sources are acknowledged by explicit references. The views expressed are my own.

Signed……………………………………………………….   *Date* 30th May 2014

Statement 2

I hereby give consent for my thesis, if accepted, to be available for photocopying and for inter-library loan, and for the title and summary to be made available to outside organisations.

Signed……………………………………………………….   *Date* 30th May 2014

Acknowledgements

There are sincere thanks owed to a good many people; I only hope I can do some justice in the acknowledgements offered here.

I would like to express my gratitude to my supervisors, Professor Hywel Thomas and Dr Majid Sedighi, for providing technical guidance, inspiration and research wisdom alongside support and understanding throughout the various stages of my PhD. I have been able to count myself as one very fortunate student. My thanks also go to Dr Phillip Vardon for his earlier contributions in these regards.

Beyond the good friendship shared, I thank my fellow coal-centric PhD colleague Mojgan for the high quality experimental data which has been of such value in my work. Her time spent in guiding me towards an understanding of the laboratory testing has been much appreciated.

The work undertaken would not have been possible without the financial support of the Seren Project, funded by the Welsh European Funding Office (WEFO). Hence, I gratefully acknowledge all involved in bringing this project to fruition, especially those at the Geoenvironmental Research Centre (GRC), Cardiff University.

Thanks also to all of the past and present members of the GRC, especially my co-conspirators in many smile bringing antics and conversations, Jamie and Ben. It has been good fun to be around such a variety of characters; Shakil, Claire, Ram, Dan, Irfan, Alejandro, Renato, Siva, Sanjana and Vasilis among many others. Moreover, they are all thanked for their encouragement and continued friendship.

For the day to day support offered and for helping me to disperse and create madness in equal measures, I give hearty thanks to Joe. Likewise, I am very thankful for the happy times brought throughout this journey by the likes of Oli, Rado, Martin and Sara.

I reserve a very special mention for Nats. Indeed, it has been an honour to have shared so much with someone so special, and her enthusiasm for my work throughout my time at university has always managed to both surprise and encourage me.

But above all else, I have been able to complete this work based on the love, strength and happiness given to me by my parents and sister. Most especially, I thank my parents for their continual support and for being all-round inspirational people.

Summary

This thesis describes a study of reactive transport processes in fractured rock in response to high pressure gas injection and displacement. This is achieved through the development and application of a theoretical and numerical modelling platform.

A dual porosity, dual permeability framework has been formulated based on a mechanistic approach, which considers the coupled hydraulic, gas/chemical and deformation behaviour of fractured rock. The fracture network and porous rock matrix were treated as overlapping continua with distinct transport and storage properties. Flow in each continuum was considered by advection, diffusion and dispersion mechanisms, and a sink/source term was included for the kinetically controlled sorption of multicomponent gas. A mass exchange term was introduced to couple the continua and allow pressure and concentration differences to develop. The transport properties of non-ideal gas mixtures at high pressure were characterised by appropriate constitutive relationships.

The developed model has been incorporated in an existing coupled thermal, hydraulic, chemical and mechanical framework. A numerical solution was obtained using the finite element method for spatial discretisation and the finite difference method for temporal discretisation. Verification of the approach proposed has been addressed via a series of benchmark tests. The results obtained provide confidence in the accuracy of the numerical implementation of the dual porosity governing equations, including a time splitting approach used to couple the transport module with the mass exchange and geochemical reaction modules.

Key theoretical features have been included to enhance the model capabilities and enable application of the model to study species dependent coal-gas behaviour, especially in relation to carbon dioxide sequestration in coal and enhanced coal bed methane displacement. The development of constitutive relationships describing the feedback of dual porosity physico- and chemo-mechanical deformation on gas transport in coal was considered in detail. Furthermore, a combination of two first-order rate models was used to include the specific gas sorption behaviour in coal.

A detailed validation of the model using high resolution experimental data on gas interactions, transport and displacement in coal has been included. The theoretical models developed for coal-gas interactions were first evaluated, providing a platform to facilitate numerical simulations of gas injection and displacement experiments, performed on intact samples of anthracite coal from the South Wales coalfield. Under the conditions considered and for two injection scenarios, namely, nitrogen and subcritical carbon dioxide injection, it was demonstrated that the model is capable of simulating the salient physical and chemical phenomena involved in gas transport and methane displacement in coal.

More advanced simulations have been performed to study the behaviour for a larger sample size and different gas injection pressures and compositions. The injection of supercritical carbon dioxide and two carbon dioxide-rich gas mixtures at high pressure was considered. It is claimed that a substantive insight has been gained into the coupled behaviour of the material at the laboratory scale. Overall, the analysis carried out in this research indicated that species dependent chemo-mechanical deformation was the dominant factor in smaller core samples. Fracture-matrix exchange and preferential methane desorption by carbon dioxide only became more apparent in larger samples. An appreciation of the effects of sample size on the behaviour observed is therefore important when interpreting experimental data, and implies that due care must be taken in interpreting laboratory scale results towards larger scale applications.

In this work, the capabilities of the new model have been showcased with regards to the study of coal-gas systems. Importantly, the developments presented are more generally relevant and thus enable the study of a broad new range of applications involving multiphase, multicomponent gas/chemical transport in fractured rock.

Nomenclature

Note: the subscript parameter α is used to denote the pore region and becomes F in the fracture continuum and M in the matrix continuum.

a_F	Matrix block width
a_{F0}	Initial matrix block width
a_M	Sub-matrix block dimension
a_{M0}	Initial sub-matrix block dimension
$a_{m\alpha}$	Coefficient for intermolecular interactions
$a_{m\alpha}^i$	Coefficient for intermolecular interactions of component i
$\mathbf{A}$	Defined in equation (4.30)
b_F	Fracture aperture
b_{F0}	Initial fracture aperture
$b_{k\alpha}^i$	Klinkenberg factor of gas component i
b_L^i	Reciprocal of the Langmuir pressure of component i
b_{Ls}^i	Reciprocal of the Langmuir pressure (swelling) of component i
b_M	Matrix pore size
b_{M0}	Initial matrix pore size
$b_{m\alpha}$	Effective molecular volume per mole
$b_{m\alpha}^i$	Effective molecular volume per mole of component i
$\mathbf{B}$	Defined in equation (4.30)
c_d	Dissolved chemical concentration
c_{dA}	Average dissolved chemical concentration
$c_{d\alpha}^i$	Dissolved chemical concentration of component i
c_f	Fracture compressibility
c_{f0}	Initial fracture compressibility
$c_{g\alpha}$	Gas concentration
c_g^i	Gas concentration of component i in a single porosity medium
$c_{g\alpha}^i$	Gas concentration of component i
$\hat{c}_{g\alpha}^i$	Approximate gas concentration of component i
$\mathbf{c}_{\mathbf{g}\alpha s}^j$	Nodal value of gas concentration of component i
$c_{g\alpha}^T$	Total gas concentration
c_{g0}^i	Initial gas concentration of component i in a single porosity medium

C_e	Defined in Table 5.5
C_i	Initial gas concentration
C_s	Defined in Table 5.5
C_s^i	Defined in Table 5.5
C_0	Fixed gas concentration
$C_{c_d c_d, \alpha}$	Defined in equations (3.125) and (3.133)
$C_{c_d c_g, \alpha}$	Defined in equations (3.124) and (3.132)
$C_{c_d l, \alpha}$	Defined in equations (3.123) and (3.131)
$C_{c_d R_d, \alpha}$	Defined in equations (3.126) and (3.134)
$C_{c_g c_g, \alpha}$	Defined in equations (3.93) and (3.98)
$C_{c_g l, \alpha}$	Defined in equations (3.92) and (3.97)
$C_{c_g s_g, M}$	Defined in equation (3.99)
$C_{l c_g, \alpha}$	Defined in equations (3.34) and (3.39)
$C_{ll, \alpha}$	Defined in equations (3.33) and (3.38)
$\mathbf{C}$	Defined in equation (4.30)
$\mathbf{C_{c_d c_d, \alpha}}$	Defined in equation (4.26)
$\mathbf{C_{c_d c_g, \alpha}}$	Defined in equation (4.25)
$\mathbf{C_{c_d l, \alpha}}$	Defined in equation (4.24)
$\mathbf{C_{c_g c_g, \alpha}}$	Defined in equation (4.15)
$\mathbf{C_{c_g l, \alpha}}$	Defined in equation (4.14)
$\mathbf{C_{l c_g, \alpha}}$	Defined in equation (4.20)
$\mathbf{C_{ll, \alpha}}$	Defined in equation (4.19)
D	Coefficient of hydrodynamic dispersion in single porosity medium
$D_{de\alpha}^i$	Effective diffusion coefficient of dissolved component i
$D_{d\alpha}^i$	Diffusion coefficient of dissolved component i
D_g^{0i}	Reference diffusion coefficient of gas component i
$D_{ge\alpha}^i$	Effective diffusion coefficient of gas component i
$D_{g\alpha}^i$	Diffusion coefficient of gas component i
D_{KM}^i	Knudsen diffusion coefficient of gas component i
$D_{m\alpha}^i$	Coefficient of mechanical dispersion of component i
D_α	Coefficient of hydrodynamic dispersion
E	Young's modulus
$f_{c_d, \alpha}^i$	Approximate dissolved chemical flux normal to boundary surface
$\mathbf{f_{c_d, \alpha}}$	Defined in equation (4.29)

$K_{c_g c_g, \alpha}$	Defined in equations (3.94) and (3.100)
$K_{ll, \alpha}$	Defined in equations (3.35) and (3.40)
$\mathbf{K_{c_d c_d, \alpha}}$	Defined in equation (4.28)
$\mathbf{K_{c_d l, \alpha}}$	Defined in equation (4.27)
$\mathbf{K_{c_g c_g, \alpha}}$	Defined in equation (4.16)
$\mathbf{K_{ll, \alpha}}$	Defined in equation (4.21)
K_R	Permeability ratio
K_{rg}	Relative gas permeability of a single porosity medium
$K_{rg\alpha}$	Relative gas permeability
$K_{rl\alpha}$	Relative water permeability
K_α	Intrinsic permeability at the continuum scale
K_α^L	Intrinsic permeability at the local scale
$K_{\alpha 0}$	Initial intrinsic permeability
K_0	Initial intrinsic permeability of single porosity medium
l	Matrix block thickness
L	Defined in equation (4.37)
L_x	Length of domain
m_α	Water retention constant
M_g^i	Molecular mass of gas component i
n	Time level indicator
$\underline{n}$	Direction cosine normal to surface
n	Porosity of single porosity medium
n_d	Total number of dissolved chemical components
n_{elem}	Total number of elements in domain
n_g	Total number of gas components
n_L^i	Langmuir capacity of component i
n_{nod}	Total number of nodes in mesh
n_T	Total porosity
n_α	Porosity
n_α^L	Local porosity
n_0	Initial porosity of single porosity medium
$\mathbf{N}$	Shape function matrix
N_s, N_s	Shape functions
P_R	Reduced pressure
$Q_{c_d, \alpha}^{ex}$	Defined in equations (3.130) and (3.138)

$Q_{c_g,\alpha}^{ex}$	Defined in equations (3.96) and (3.102)
Q_g	Total inlet gas flux
$Q_{l,\alpha}^{ex}$	Defined in equations (3.37) and (3.42)
Q_1^i	Sorption capacity factor of gas component i
Q_2^i	Sorption capacity factor of gas component i
R	Universal gas constant
R^{CH_4}	Percentage of methane produced
$R_{d\alpha}^i$	Sink/source term for geochemistry of dissolved component i
$R_{g\alpha}^i$	Sink/source term for geochemistry of gas component i
R_i^{Ad}	Defined in equation (4.40)
R_i^{Ex}	Defined in equation (4.39)
R_l^{Ex}	Defined in equation (4.38)
$R_{\Omega,\alpha}$	Residual error introduced due to approximation
s	Node indicator
s_d	Adsorbed amount of dissolved chemical
$s_{d\infty}$	Equilibrium adsorbed amount of dissolved chemical
s_{gr}^i	Residual adsorption capacity of gas component i
s_{gt}^i	Adsorbed amount of gas component i at time t
$s_{g\alpha}^i$	Adsorbed amount of gas component i
s_{g0}^i	Initial adsorbed amount of gas component i
$s_{g\infty M}^i$	Equilibrium adsorbed amount of gas component i in matrix continuum
s_α	Matric suction
S_g	Degree of gas saturation of a single porosity medium
$S_{g\alpha}$	Degree of gas saturation
$S_{l\alpha}$	Degree of water saturation
t	Time
T	Temperature
T_c	Critical temperature
T_c^i	Critical temperature of component i
T_R	Reduced temperature
$\mathbf{TL}_{abs}$	Matrix of absolute tolerances
$\mathbf{TL}_{rel}$	Matrix of relative tolerances
u_c	Confining pressure
u_g	Pore gas pressure
u_{gAtm}	Atmospheric pressure

u_{gc}	Critical gas pressure
u_{gc}^i	Critical gas pressure of gas component i
u_{gL}	Outlet gas pressure
$u_{g\alpha}$	Pore gas pressure
u_{g0}	Initial pore gas pressure in a single porosity medium
$u_{g\alpha 0}$	Initial pore gas pressure
u_l	Pore water pressure in a single porosity medium
$u_{l\alpha}$	Pore water pressure
$\hat{u}_{l\alpha}$	Approximate value of pore water pressure
$\mathbf{u}_{l\alpha s}$	Nodal value of pore water pressure
$\mathbf{v}_{gs\alpha}$	Gas seepage velocity
$\mathbf{v}_{g\alpha}$	Bulk gas velocity
$\mathbf{v}_l$	Water velocity
$v_{lx\alpha}$	Water velocity in x spatial dimension
$v_{ly\alpha}$	Water velocity in y spatial dimension
$\mathbf{v}_{l\alpha}$	Velocity of liquid water
$|v_\alpha|$	Absolute average advective velocity
V_B	Bulk volume
V_c^i	Critical volume of component i
$V_{m\alpha}^{Id}$	Molar volume (ideal gas)
$V_{m\alpha}^{Re}$	Molar volume (real gas)
V_T	Total volume
V_α^T	Total volume (pore region α)
w_f	Volumetric weighting factor defined in equation (3.8)
x	Distance in the direction of flow
$X_{g\alpha}^i$	Mole fraction of gas component i
z	Elevation from the reference level
Z	Compressibility factor in a single porosity medium
Z_α	Compressibility factor
α_f	Fracture compressibility change rate
$\alpha_{L\alpha}$	Coefficient of longitudinal dispersion
$\alpha_{T\alpha}$	Coefficient of transverse dispersion
α_α	Water retention constant
β	Geometrical factor for inter-porosity mass exchange
δb_{Fp}	Increment in fracture aperture by pore compression

δb_{Fm}	Increment in fracture aperture by matrix compression
δb_{Fs}	Increment in fracture aperture by sorption strain
δb_{Mp}	Increment in pore size by pore compression
δb_{Mm}	Increment in pore size by matrix compression
δb_{Ms}	Increment in pore size by sorption strain
δ_{ij}	Kronecker delta
δ_{iM}	Constrictivity factor
δV_{α}	Incremental volume
ε_L^i	Langmuir strain for component i
ε_s^i	Sorption strain due to component i
ε_{s0}^i	Initial sorption strain due to component i
Γ^e	Element boundary surface
Γ_d	Sink/source term for dissolved chemical
Γ_d^i	Sink/source term for dissolved chemical component i
Γ_g^i	Sink/source term for gas component i
Γ_l	Water sink/source
$\theta_{g\alpha}$	Volumetric gas content
$\theta_{l\alpha}$	Volumetric water content
$\theta_{lr\alpha}$	Residual volumetric water content
$\theta_{ls\alpha}$	Saturated volumetric water content
Θ	Integration constant, defined in equation (4.31)
κ_α^{ij}	Gas interaction parameter for molecules of the components i and j
λ	Defined in equation (3.2)
λ_D	Dispersivity in the direction of flow
μ_g	Absolute gas viscosity in a single porosity medium
$\mu_{g\alpha}$	Absolute gas viscosity
$\mu_{g\alpha}^D$	Factor for dense gas viscosity
$\mu_{g\alpha}^0$	Reference gas viscosity
$\mu_{l\alpha}$	Absolute water viscosity
ν	Poisson's ratio
ρ_g^A	Arithmetic mean of fracture and matrix gas densities
ρ_g^0	Reference gas density
$\rho_{g\alpha}$	Gas density
ρ_l	Water density
ρ_s	Solid density

$\rho_{s\alpha}$	Solid density (continuum)
σ_{dAdv}	Mass exchange coefficient for dissolved chemical advection
σ_{dDif}^i	Mass exchange coefficient for diffusion of dissolved component i
σ_{gAdv}	Mass exchange coefficient for gas advection
σ_{gDif}^i	Mass exchange coefficient for diffusion of gas component i
σ_i	Collision diameter of component i
σ_l	Mass exchange coefficient for water
τ_g	Gas tortuosity factor of a single porosity medium
$\tau_{g\alpha}$	Gas tortuosity factor
$\tau_{l\alpha}$	Liquid tortuosity factor
τ_r^i	Sorption rate of gas component i
ϕ	Vector of primary variables
ϕ_l	Defined in equation (4.32)
ω_i	Acentricity factor
ω_{dp}	Mass exchange rate
ω_α	Defined in equation (4.1)
$\widehat{\omega}_\alpha$	Defined in equation (4.1)
Ω^e	Element area/volume
Ω_i	Collision integral of component i
Ω_l	Empirical coefficient
∇	Gradient operator

Contents

1

Introduction

1.1   Introduction

Climate change is recognised as one of the great threats facing the global environment and society (UNEP, 2013). Moreover, a large body of evidence highlights anthropogenic activities as the overriding cause of the observed global warming (IPCC, 2013). The principal mechanism has been the increased atmospheric concentration of carbon dioxide from fossil fuel emissions and land use changes. Considering the high demand for energy and the importance of energy security, both developed and developing countries will be unwilling to move away from the reliability offered by fossil fuels in the foreseeable future, especially considering the energy infrastructure already in place (e.g. DECC, 2011). Therefore, combined with the growing energy demand in the emerging economies, fossil fuels are predicted to comprise 75% of the global energy mix in 2035 (IEA, 2011). This has led to the development of strategies for climate change mitigation and adaptation that account for the continued exploitation of fossil fuels (IPCC, 2007; UNEP, 2013).

Natural gas is regarded as the cleanest burning fossil fuel and unconventional gas, which includes shale gas and coalbed methane, is estimated to comprise half of the remaining

natural gas resource (IEA, 2011). In this context, a growing energy output from unconventional gas has positive implications for carbon dioxide emissions and energy security. However, the International Energy Agency (IEA) (2011) predicts that the increased exploitation of unconventional gas must be accompanied by carbon capture and sequestration (CCS) if a significant advance towards emissions targets is to be achieved.

The application of CCS is intended to capture and avoid the emission of carbon dioxide into the atmosphere in three stages: (i) carbon dioxide capture (including separation and compression) at point sources, e.g. power plants, (ii) transportation, and (iii) sequestration by injecting into a suitable deep rock formation (Global CCS Institute, 2012). This work deals with the last of these stages only. There is a natural analogue for CCS, since carbon dioxide storage in geological formations has occurred under natural phenomena for millions of years (IPCC, 2005). Of greatest interest for carbon dioxide sequestration are deep saline aquifers, oil and gas reservoirs and unminable coal beds. These are illustrated in Figure 1.1, where it can be seen that carbon dioxide injection may also be used to enhance the displacement and production of oil and gas.

Naturally occurring fractures are commonly an important feature in candidate rock formations for carbon dioxide sequestration and unconventional oil and gas exploration (e.g. van Golf-Racht, 1982; Ertekin, 1989; Speight, 2012). These fractures effectively divide the rock mass into two distinct porosities, i.e. the fracture network and the discontinuous rock matrix blocks (Bear, 1993). Therefore, an understanding of the physical and chemical processes involved in multiphase flow in fractured rock is essential for the engineering and management of the geoenergy applications discussed. Of particular interest is the different transport and displacement properties/behaviour in the fracture and matrix pore regions, which may be strongly dependent on the inter-porosity and solid-water-chemical interactions. These aspects of the behaviour and the transport and displacement process in general are investigated in this work.

The complexity of the coupled phenomena in fractured rock underpins the challenge faced in the development of numerical models. Nonetheless, the simulation capability offered by the models developed provides an invaluable platform for the assessment and prediction of geoenergy solutions. It is well accepted that numerical models can be applied to

demonstrate technical understanding through theoretical developments and validation with experimental data. This in turn enables simulations to be performed to examine various scenarios at a fraction of the cost of direct testing. Computer modelling is also non-destructive and data can be produced with a high degree of flexibility in relatively short time periods. However, numerical models must only be used in relevant circumstances where the underlying processes are well-understood. It is otherwise likely that important processes may be omitted from the simulations and thus incorrect results obtained.
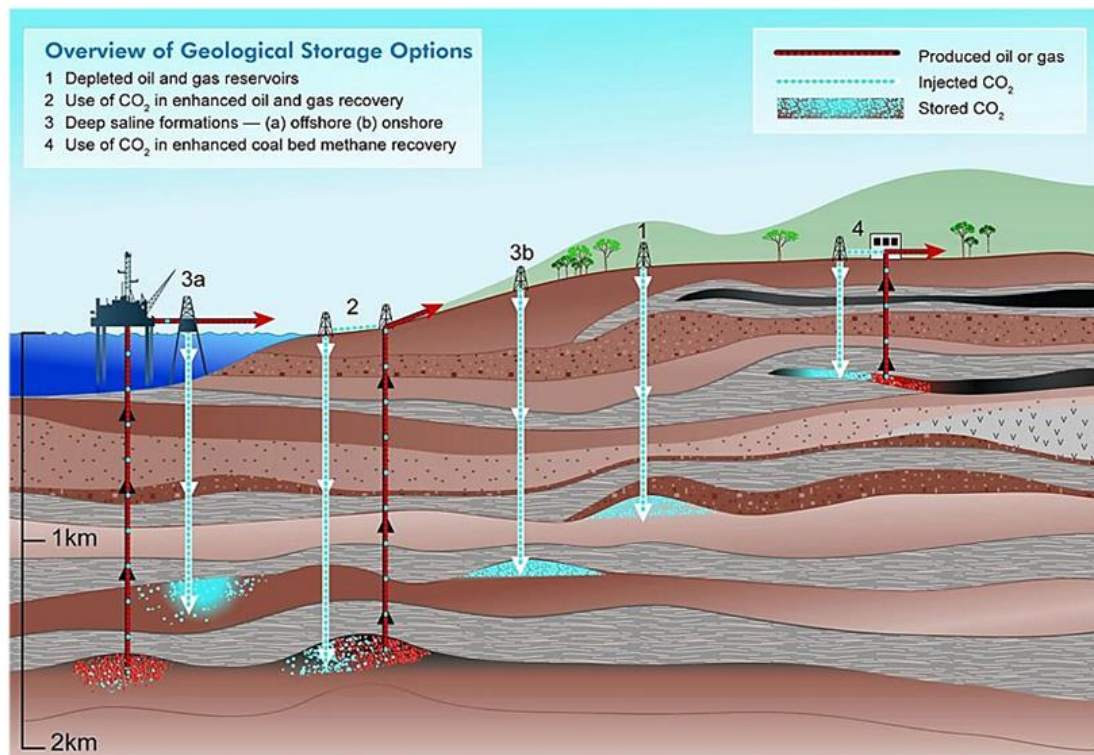
Figure 1.1 Schematic of the suggested geological storage options for carbon dioxide (CO_2) storage. Oil and gas production is also indicated where appropriate (IPCC, 2005).

There are several established modelling techniques which can be adopted to idealise the highly heterogeneous pore structure in fractured rocks, thereby making the related problems more amenable to numerical treatment. One of these is the dual porosity technique, which considers a highly conductive fracture continuum with a low storage capacity and a poorly (or non-) conductive matrix continuum with a high storage capacity (Bear et al., 1993). An inter-porosity exchange term is used to control the flow interactions between the continua (Xu and Pruess, 2001).

Key aspects of the physical and chemical behaviour of fractured rock depend on the properties of the system being considered and the conditions related to the engineering case. In this respect, the theoretical foundations of the dual porosity model have been developed and extended in the study of a wide range of applications, including groundwater flow, contaminant transport, oil and gas exploration, carbon dioxide sequestration and nuclear waste containment (Gerke and van Genuchten, 1993; Di Donato and Blunt, 2004).

A major component of this research is the development of a dual porosity, multiphase, multicomponent gas/chemical reactive transport model, including the behaviour of gas mixtures at high pressure. Whilst a large part of the developed theoretical and computational platform is intended to be generally relevant for the applications listed above, the specific emphasis of the work is on advancing the understanding of high pressure gas transport and displacement processes in coal. In particular, the laboratory scale applications considered are related to carbon dioxide sequestration in coal and enhanced coal bed methane recovery.

With regards to the stated applications, coal is physically and chemically heterogeneous, making it difficult to quantify the material parameters required to develop a numerical simulation. Further, certain aspects of coal behaviour also require the implementation of bespoke analytical tools and theoretical features in numerical models (Clarkson and Bustin, 2010). A good example is the reversible coal swelling response to gas adsorption, which can have a considerable feedback effect on the permeability. Moreover, moisture is known to be an important controlling factor on gas adsorption (Busch and Gensterblum, 2011). It is apparent that certain aspects of the hydraulic, gas/chemical and mechanical behaviour in coal are highly coupled and require careful consideration in the development of a numerical model.

Recent advances in the experimental and computational research have enhanced the understanding of the coupled behaviour. Nonetheless, theoretical developments and numerical modelling research are required in the study of high pressure gas transport and displacement in coal. For example, further work is needed on the inter-porosity flow interactions, multicomponent gas diffusion, adsorption and absorption phenomena, the

chemo-mechanical coupling, and multiphase flow, including high pressure gas dissolution and the subsequent geochemical behaviour. The chemo-mechanical response of the rock is of particular interest due to the swelling behaviour and changes in the macromolecular structure and engineering properties of coal caused by interactions with carbon dioxide (e.g. Larsen, 2004; Masoudian et al., 2013). An enhanced understanding in the aforementioned areas will allow numerical models to be developed with a greater level of theoretical rigour. This is important to ensure the reliability of numerical simulations in predicting the behaviour of a coal-gas-water system under a range of conditions.

Subsequent to the above research considerations, the current field status of carbon dioxide sequestration is addressed in the next section. This is followed in section 1.3 by the principal objectives of the present study and in section 1.4 by an overview of the research background. The scope and limitations of the research are provided in section 1.5, with an overview of the thesis given in section 1.6.

1.2   Status of Field Scale Applications of Carbon Dioxide Sequestration

A number of carbon dioxide sequestration projects have been completed or are currently underway or planned. Table 1.1 provides an overview of selected projects covering the sequestration options mentioned above. It can be seen that a large portion of the current and planned carbon dioxide injection is in saline aquifers, followed by oil and gas fields and lastly coal beds. Based on an analysis given in IPCC (2005), this reflects the maturity and estimated total capacity of each sequestration application. For example, the injection into saline formations and oil and gas fields is already viewed as economically viable under certain conditions (e.g. emissions tax schemes) and has a maturing market, whereas the injection into coal is at the demonstration stage.

As mentioned in the previous section, the application of the developed numerical model considered in this work relates to carbon dioxide sequestration in coal and enhanced coal bed methane recovery. It can be seen in Table 1.1 that a total of 336,000 tonnes of carbon dioxide were injected into a coal bed at the Allison Unit in the San Juan Basin (USA). This represents the largest demonstration of carbon dioxide injection in coal to date, and was achieved via 4 injection wells over an injection period of 6 years starting in 1995 (Reeves

et al., 2003). There were also 16 production wells for the enhanced recovery of coal bed methane. Reeves et al. (2003) gave the following major conclusions:

i. Three volumes of carbon dioxide were injected per volume of methane produced.

ii. Enhanced methane production may provide a considerable offset to the costs associated with CCS.

iii. Carbon dioxide injection reduced the coal permeability, with a consequent loss of injectivity.

Table 1.1 Selected CCS projects, ranging from small pilots to large-scale commercial applications (updated and expanded from IPCC, 2005).

Project name	Country	Injection start [year]	Approx. total / planned injection [tCO_2]	Storage reservoir type
Gorgon	Australia	2015	> 100,000,000	Saline aquifer
Snøhvit	Norway	2008	30,000,000	Saline aquifer
Weyburn	Canada	2000	20,000,000	Oil reservoir (EOR)
Sleipner	Norway	1996	20,000,000	Saline aquifer
In Salah	Algeria	2004	17,000,000	Gas reservoir
K12B	Netherlands	2004	8,000,000	Gas reservoir (EGR)
San Juan Basin (Allison)	USA	1995	336,000	Coal (CO_2-ECBM)
Frio	USA	2004	1,450	Saline aquifer
Appalachian Basin	USA	2009	910	Coal (CO_2-ECBM)
Yubari	Japan	2004	800	Coal (CO_2-ECBM)
RECOPOL	Poland	2004	692	Coal (CO_2-ECBM)
Fenn Big Valley	Canada	1998	200	Coal (CO_2-ECBM)
Qinshui Basin	China	2003	190	Coal (CO_2-ECBM)

Note: EOR = enhanced oil recovery, EGR = enhanced gas recovery, CO_2-ECBM = carbon dioxide-enhanced coalbed methane recovery.

The first two conclusions are clearly positive from a carbon sequestration perspective, whereas the final conclusion is problematic. Similar conclusions have generally been drawn in other demonstration projects, including the RECOPOL project in Poland (van Bergen et al., 2006) and the Yubari project in Japan (Fujioka et al., 2010). In the RECOPOL project, an acceptable injection rate was eventually maintained after a hydraulic fracturing treatment. The loss of injectivity in the Yubari project was only partially recovered by the cyclic injection of nitrogen and carbon dioxide.

Overall, it can be seen that these projects have had some positive implications for the

application. However, they have also drawn attention to the need for continued experimental and computational research and development, both at the laboratory and demonstration scale. In other words, the application remains some distance away from widespread commercial development.

1.3   Study Objectives

Under the development of the multiphase, multicomponent gas/chemical reactive transport model presented in this work, there is a focus on the processes and behaviour which control high pressure gas transport and displacement in fractured rock. Specifically, applications of the model which have been considered are intended to provide a detailed analysis of gas interactions with coal under carbon dioxide injection and methane displacement. The main objectives of this study are to:

  i.   Develop a theoretical framework for the reactive transport of high pressure gas mixtures in fractured rock under coupled hydraulic, gas/chemical and deformation behaviour, based on a dual porosity approach.

  ii. Advance a coupled thermo-hydro-chemo-mechanical (THCM) model to include high pressure gas and dual porosity simulation capabilities.

  iii. Develop and implement appropriate constitutive relationships for dual porosity coal deformation caused by physical and chemical coal-gas interactions, enabling the application of the model to study gas transport in coal.

  iv. Apply and validate the developed model to examine the processes and behaviour which control gas transport and displacement in coal, with support from high resolution experimental results.

  v.   Investigate gas transport and displacement in coal at laboratory scale under a series of conditions of practical importance for carbon dioxide sequestration and methane production.

1.4   Research Background

This work has been undertaken at the Geoenvironmental Research Centre at Cardiff

University, where considerable research, including the development of the numerical computer code COMPASS (**CO**de for **M**odelling **PA**rtially **S**aturated **S**oils), has been performed prior to the study. This section provides the context to this work, and is not intended to replace more detailed reviews of the literature in chapter 2, nor the theoretical formulation in chapter 3.

A theoretical model of coupled transient heat and moisture (TH) transfer in unsaturated soil was developed by Thomas (1985). The principle of conservation of mass was employed for moisture flow and conservation of energy was employed for heat transfer. In this model, moisture vapour transport was assumed to be diffusive following Philip and de Vries (1957) and de Vries (1958). Latent heat transfer was introduced following Luikov (1966). The non-linearity of material parameters was included in the works by Thomas (1987), Thomas (1988a) and Thomas (1988b). Revised time-stepping schemes were investigated under the mentioned coupled TH model by Thomas and Rees (1988) and Thomas and Rees (1990).

Following an experimental investigation into the behaviour of unsaturated sand surrounding a heating rod, Ewen and Thomas (1987) and Ewen and Thomas (1989) amended the vapour transfer diffusivities of the numerical model to simulate coupled heat and moisture transfer processes in unsaturated soil. A numerical simulation in terms of moisture content and temperature was carried out by Ewen and Thomas (1989), including vapour transport via a diffusive mechanism.

Thomas and King (1991) presented a theoretical heat and moisture formulation cast in terms of capillary potential and temperature and found a good agreement with the Ewen and Thomas (1987) experiments. Thomas and Sansom (1995) extended this formulation to include elevated pore air pressures and validation was achieved via comparison with experimental works on sand and clay. This formulation was presented in three-dimensional form, including work on pre- and post-processing, visualisation and parallel computation by Sloper (1997) and Thomas et al. (1998).

Mechanical behaviour and deformation was introduced examining seasonal ground movements by Thomas and Rees (1990; 1993), with an isothermal coupled moisture-mechanical numerical model presented by Thomas et al. (1992) utilising the non-linear

elastic state-surface approach proposed by Lloret and Alonso (1985). This model was applied to seasonal ground movements in the work presented by Thomas and Zhou (1995). An elasto-plastic coupled thermal, hydraulic and mechanical (THM) model was presented by Thomas and He (1994) and Thomas and He (1995) using the elasto-plastic model of Alonso et al. (1990).

Ramesh (1996) applied the THM model to simulate temperature, moisture and void ratio distributions of montmorillonite subjected to heating/hydration. The work also involved the investigation of the isothermal volume change behaviour of compacted kaolinite in suction controlled tests. Thomas and Cleall (1999) extended the THM model to include highly expansive behaviour. Using the developed model, numerical simulations of large scale experiments were presented by Mitchell (2002), Thomas et al. (2003), Melhuish (2004) and Cleall et al. (2006), including an investigation into the microstructure behaviour of bentonite when re-saturating.

Chemical processes were first introduced as non-reactive chemical transport for a single species in the liquid phase (Thomas and Cleall, 1997). Hashm (1999) developed the model for two-dimensional coupled moisture and multicomponent reactive chemical transport by linking the non-reactive transport code with the geochemical model, MINTEQA2 (Allison et al., 1991). The model was applied to simulate a series of leaching cell experiments to study the migration/sorption behaviour of some of the heavy metals. Seetharam (2003) developed the multicomponent reactive transport module of the coupled THCM model. The geochemical reactions were calculated by the geochemical model, MINTEQA2, using a time splitting scheme to solve the transport and reaction equations. The coupled THCM model was used to simulate the reactive transport of chemicals in compacted bentonite under heating and hydration (Seetharam et al., 2006; Cleall et al., 2007).

A number of theoretical and computational developments have recently been made in the model. These have focused mainly on the behaviour of compacted bentonite as the buffer in a geological nuclear waste repository, in addition to the modelling of the large scale THM behaviour of the repository. Singh (2007) presented an experimental and numerical investigation on the heat and moisture transfer in compacted bentonite and kaolinite, with special attention to the vapour transfer in compacted clays. Modifications to the existing

vapour theory were suggested and implemented in the existing THM formulation. Siddiqua (2008) presented an investigation into the effects of elevated temperatures (343 to 473 K) on the THM processes in the model. A pore gas transfer equation and thermo-osmotic effect was developed to account for elevated temperatures.

Vardon (2009) extended the COMPASS model to accommodate three-dimensional THM behaviour in a geological repository, including the development of a high performance computing algorithm using both multi-threaded and message-passing programming paradigms. These developments allowed simulations to be completed in significantly less time. The model was utilised for simulating the THM behaviour of a large-scale experiment, carried out at an underground research laboratory in Sweden.

Thomas et al. (2011) presented the inclusion of biological aspects to the coupled THCM model. The early developments in this area include some biological impacts on coupled transport behaviour in unsaturated porous media. The THCMB model incorporates the biodegradation kinetics of organic substrates.

To include both equilibrium and kinetically controlled chemical reactions, Sedighi (2011) linked the transport module in the COMPASS code with an advanced geochemical model, PHREEQC, version 2.0. The extended THCM model was applied to simulate the transport and fate of multicomponent chemicals in the liquid phase in clays. Subsequently, the combined effects of electrochemical and thermal diffusion potentials on the reactive transport were investigated by Thomas et al. (2012). Masum (2012) developed the geochemical model for multicomponent gas transport, including an extension of the coupling with PHREEQC for gas reactivity. The multicomponent gas formulation was developed under the assumption of an ideal gas.

From the above, it is intended to enhance the capabilities of the THCM model for study in a broad new range of areas involving reactive transport in fractured rock, including the applications to coal-gas interactions considered in this work.

1.5   Scope and Limitations

The scope of the work undertaken in this thesis and in particular the anticipated limitations

are listed below:

i. Numerical approximation is used to find a solution to the system of coupled differential equations. The finite element method is used to provide a spatial solution and the finite difference method is used to provide a temporal solution.

ii. A dual porosity technique is employed to model fractured rock. It is assumed that the fracture and matrix pore regions are distinct, homogenous, isotropic continua, which overlap across the domain and have separate material parameters.

iii. Mass exchange, i.e. the flow interactions between the fracture and matrix continua, is described by including coupling terms in the governing equations.

iv. Geochemical reactions between the pore fluid and solid phase are assumed to only occur in the matrix continuum. This is because the matrix blocks contain the majority of the internal surface area in most fractured rocks, for example coal (Clarkson and Bustin, 2010).

v. Water transfer and multicomponent chemical transport in the liquid phase are included in the theoretical formulation, although gas dissolution is not considered. The applications of the developed model in this work consider a fully dry system.

vi. Constitutive relationships for coal deformation by physical and chemical mechanisms are developed for linear-elastic behaviour, i.e. all strains are fully recoverable.

vii. Isothermal conditions are assumed in the applications.

1.6   Overview of the Thesis

A brief description of each chapter in this thesis is provided below.

Chapter 2 presents a selective review of the current literature most relevant to the remainder of the thesis. A review of the state of the art techniques for modelling transport in fractured rock masses is included. Beyond this, the review focuses on the current understanding of the physical and chemical aspects of high pressure gas transport in coal, which is informed by the recent experimental and computational research efforts.

The theoretical formulation for the coupled hydraulic, chemical and deformation behaviour of fractured rock is described in chapter 3. This chapter deals with the development of the

governing equations for water transfer and multicomponent chemical transport in the liquid and gas phases in a dual porosity medium. Specific attention is given to high pressure gas behaviour and coal-gas interactions. Chapter 4 summarises the numerical formulation for solving the governing equations, including the time splitting approach used to couple the transport terms with the geochemical reaction and mass exchange terms.

A series of verification tests are presented in chapter 5 to ensure that the solution algorithm of the model is correct. Numerical simulation results are compared with the benchmarks provided by analytical solutions or alternative numerical solutions. The tests performed are selective and largely specific to the present work, since it is noted that the numerical model has previously been verified for a number of test cases involving coupled moisture flow, heat transfer and gas/chemical transport.

Chapter 6 presents the application of the developed theoretical and numerical models in laboratory scale tests, including comparisons with high resolution experimental data. This allows an in-depth examination of the validity of the underlying theory describing the material behaviour and processes involved in the major coal-gas interactions and high pressure gas transport and displacement in coal.

The simulations presented in chapter 7 are extensions to those in chapter 6, covering the injection of supercritical phase carbon dioxide, and selected carbon dioxide-rich gas mixtures. A larger domain is used to evaluate the effects of sample size on the observed gas transport and displacement behaviour at the laboratory scale. This is of practical importance, since key aspects of the physical and chemical behaviour occur over different time scales. In other words, the sample size may have a considerable influence on the observed behaviour.

Concluding remarks and suggestions for further research are provided in chapter 8.

1.7 References

Allison, J.D., Brown, D.S. and Novo-Gradac, K.J. (1991). *MINTEQA2 user manual version 3.0*. Environmental Research Laboratory, US EPA.

Alonso, E.E., Gens, A. and Josa, A. (1990). A constitutive model for partially saturated soils. *Géotechnique*, **40**(3), 405-430.

Bear, J. (1993). Modeling flow and contaminant transport in fractured rocks. In: Bear, J. et al. eds. *Flow and contaminant transport in fractured rock*, Academic Press, Inc., pp 1-38.

Busch, A. and Gensterblum, Y. (2011). CBM and CO_2-ECBM related sorption processes in coal: a review. *International Journal of Coal Geology*, **87**, 49-71.

Clarkson, C.R. and Bustin, R.M. (2010). Coalbed methane: current evaluation methods, future technical challenges. *In Proceedings of the SPE Unconventional Gas Conference*, 23-25 February, Pittsburgh, Pennsylvania.

Cleall, P.J., Melhuish, T.A. and Thomas, H.R. (2006). Modelling the three-dimensional behaviour of a prototype nuclear waste repository. *Engineering Geology*, **85**(2), 212-220.

Cleall, P.J., Seetharam, S.C. and Thomas, H.R. (2007). On the inclusion of some aspects of chemical behaviour of an unsaturated soil in thermo-hydro-chemical-mechanical models, II: application and transport of soluble salts in compacted bentonite. *Journal of Engineering Mechanics*, ASCE, **133**, 348-356.

de Vries, D.A. (1958). Simultaneous transfer of heat and moisture in porous media. *Transaction American Geophysical Union*, **39**(5), 909-916.

DECC (2011). *National policy statement for fossil fuel electricity generating infrastructure (EN-2)*. Her Majesty's Stationery Office, London.

Di Donato, G. and Blunt, M.J. (2004). Streamline-based dual-porosity simulation of reactive transport and flow in fractured reservoirs. *Water Resources Research*, **40**, W04203.

Ertekin, T. (1989). Dual-mechanism gas flow dynamics in single- and dual-porosity systems. In Tek, M.R. ed. *Underground storage of natural gas: theory and practice*, Kluwer Academic Publishers, Dordrecht, The Netherlands.

Ewen, J. and Thomas, H.R. (1987). The thermal probe – a new method and its use on an unsaturated sand. *Géotechnique*, **37**, 91-105.

Ewen, J. and Thomas, H.R. (1989). Heating unsaturated medium sand. *Géotechnique*, **39**(3), 455-470.

Fujioka, M., Yamaguchi, S. and Nako, M. (2010). CO_2-ECBM field tests in the Ishikari Coal Basin of Japan. *International Journal of Coal Geology*, **82**, 287-298.

Gerke, H.H. and van Genuchten, M.T. (1993a). A dual-porosity model for simulating the preferential movement of water and solutes in structured porous media. *Water Resources Research*. **29**(2), 305-319.

Global CCS Institute (2012). *The global status of CCS: 2012*. Global CCS Institute, Canberra, Australia.

Hashm, A.A. (1999). *A study of the transport of a selection of heavy metals in unsaturated soils*. Ph.D. Thesis, University of Wales, Cardiff.

IEA (2011). *World energy outlook 2011: executive summary*. International Energy Agency, Paris, France.

IPCC (2005). IPCC special report on carbon capture and storage. *Prepared by Working Group III of the Intergovernmental Panel on Climate Change* [Metz, B. et al. eds.], Cambridge University Press, Cambridge, UK and New York, USA.

IPCC (2007). *Climate change 2007: synthesis report*. Intergovernmental Panel on Climate Change.

IPCC (2013). Summary for policy makers. In: Stocker et al. eds. *Climate change 2013: the physical science basis. Contribution of Working Group I to the Fifth Assessment Report of the Intergovernmental Panel on Climate Change*, Cambridge University Press, Cambridge, UK and New York, USA.

Larsen, J.W. (2004). The effects of dissolved CO_2 on coal structure and properties. *International Journal of Coal Geology*, **57**, 63-70.

Lloret, A. and Alonso, E.E. (1985). State surfaces for partially saturated soils. *In Proceedings of the 11th International Conference of Soil Mechanics and Foundation Engineering*, San Francisco, **2**, 557-562.

Luikov, A.V. (1966). *Heat and Mass Transfer in Capillary Porous Bodies*, Pergamon Press, Oxford.

Masoudian, M.S., Airey, D.W. and El-Zein, A. (2013). A chemo-poro-mechanical model for sequestration of carbon dioxide in coalbeds. *Géotechnique*, **63**(3), 235-243.

Masum, S.A. (2012). *Modelling of reactive gas transport in unsaturated soil – a coupled thermo-hydro-chemical-mechanical approach*. Ph.D. Thesis, Cardiff University, Cardiff.

Melhuish, T.A. (2004). *An investigation of the three-dimensional thermo/hydro/mechanical behaviour of large scale in-situ experiments*. Ph.D. Thesis, Cardiff University, Cardiff, UK.

Mitchell, H.P. (2002). *An investigation into the thermo/hydro/mechanical interactions involved in high level nuclear waste disposal*. Ph.D. Thesis, University of Wales, Cardiff, UK.

Philip, J.R., and de Vries, D.A. (1957). Moisture movement in porous materials under temperature gradients. *Transaction American Geophysical Union*, **38**(2), 222-232.

Ramesh, A.D. (1996). *Modelling the thermo/hydraulic/mechanical behaviour of unsaturated soil using an elasto-plastic constitutive relationship*. Ph.D. thesis. University of Wales Cardiff, UK.

Reeves, S.R., Taillefert, A., Pekot, L. and Clarkson, C. (2003). *The Allison Unit CO_2-ECBM pilot: a reservoir modeling study*. Topical Report, DOE Contract No. DEFC26-00NT40924.

Sedighi, M. (2011). *An investigation of hydro-geochemical processes in coupled thermal,*

hydraulic, chemical and mechanical behaviour of unsaturated soils. Ph.D. Thesis, Cardiff University, Cardiff.

Seetharam, S.C. (2003). *An investigation of the thermo/hydro/chemical/mechanical behaviour of unsaturated soils*. Ph.D. Thesis, Cardiff University, Wales, UK.

Seetharam, S.C., Cleall, P.J. and Thomas, H.R. (2006). Modelling some aspects of ion migration in a compacted bentonitic clay. *Engineering Geology*, **85**, 221-228.

Siddiqua, S. (2008). *An investigation of the influence of elevated temperatures on the thermal-hydraulic-mechanical response of unsaturated soils*. Ph.D. Thesis, Cardiff University, Wales, UK.

Singh, R.M. (2007). *An experimental and numerical investigation of heat and mass movement in unsaturated clays*. Ph.D. Thesis, Cardiff University, Wales, UK.

Sloper, N.J. (1997). *The development of a new three dimensional numerical model for fully coupled heat, moisture and air flow in unsaturated soil incorporating scientific visualisation and parallel computing techniques*. Ph.D. Thesis, University of Wales, Cardiff.

Speight, J.G. (2012). *The chemistry and technology of coal*. 3rd edition. CRC Press, Boca Raton, Florida.

Thomas, H.R. (1985). Modelling two-dimensional heat and moisture transfer in unsaturated soils, including gravity effects. *International Journal of Analytical Methods in Geomechanics*, **9**, 573-588.

Thomas, H.R. (1987). Non-linear analysis of heat and moisture transfer in partly saturated soil. *Journal of Engineering Mechanics, American Society of Civil Engineering*, **113**, 1163- 1180.

Thomas, H.R. (1988a). A non-linear analysis of two-dimensional heat and moisture transfer in partly saturated soil. *International Journal of Analytical Methods in Geomechanics*. **2**, 31- 44.

Thomas H.R. (1988b). The influence of non-linear thermal parameters on moisture content distributions in unsaturated soil. *International Journal of Analytical Methods in Engineering*, **26**, 263-279.

Thomas, H.R. and Rees, S.W. (1988). The use of Lee's algorithm in the analysis of some ground heat and mass transfer problems. *In Proceedings of the 6th International Conference on Numerical Methods in Geomechanics*, Innsbruck, Austria.

Thomas, H.R. and Rees, S.W. (1990). An examination of the performance of a 3-level time stepping algorithm – coupled heat and mass transfer computing. *In Proceedings of the 1st International Conference, Advances in Computer Methods in Heat Transfer*, Southampton, U.K.

Thomas, H.R. and King, S.D. (1991). Coupled temperature/capillary potential variations in unsaturated soil. *Journal of Engineering Mechanics, American Society of Civil Engineers*, **117**, 2475-2491.

Thomas, H.R., Zhou, Z. and He, Y. (1992). Analysis of consolidation of unsaturated soils. *In Proceedings of the 2nd Czechoslovak Conference on Numerical Methods in Geomechanics*,

Prague, Dolezalova, M., eds., vol.1, 242-247.

Thomas, H.R. and Rees, S.W. (1993). The numerical simulation of seasonal soil drying in an unsaturated clay soil. *International Journal of Numerical and Analytical Methods in Geomechanics*, **17**(1), 119-132.

Thomas, H.R. and He, Y. (1994). An elasto-plastic analysis of the thermo/hydraulic/mechanical behaviour of unsaturated soil. *In Proceedings of the 8th International Conference on Computer Methods and Advances in Geomechanics*, Morgantown, Siriwardane, H.J. and Zaman, M.M. eds., Balkema, Rotterdam, 1171-1176.

Thomas, H.R. and He, Y. (1995). Analysis of coupled heat, moisture and air transfer in a deformable unsaturated soil. *Géotechnique*, **45**(4), 677-689.

Thomas, H.R. and Sansom, M.R. (1995). Fully coupled analysis of heat, moisture and air transfer in unsaturated soil. *Journal of Engineering Mechanics, American Society of Civil Engineers*, **121**(3), 392-405.

Thomas, H.R. and Zhou, Z. (1995). A comparison of field measured and numerically simulated seasonal ground movement in unsaturated clay. *International Journal for Numerical and Analytical Methods in Geomechanics*, **19**, 249-265.

Thomas, H.R. and Cleall, P.J. (1997). Chemico-osmotic effects on the behaviour of unsaturated expansive clays. *Geoenvironmental Engineering, Contaminated Ground; Fate of Pollutants and Remediation*, Yong, R.N. and Thomas, H.R., eds., Thomas Telford, London, 272-277.

Thomas, H.R., Rees, S.W. and Sloper, N.J. (1998). Three-dimensional heat, moisture and air transfer in unsaturated soils. *International Journal of Numerical and Analytical Methods in Geomechanics*, **22**(2), 75-95.

Thomas, H.R. and Cleall, P.J. (1999). Inclusion of expansive clay behaviour in coupled thermo hydraulic mechanical models. *Engineering Geology*, **54**, 93-108.

Thomas, H.R., Cleall, P.J., Chandler, N., Dixon, D. and Mitchell, H.P. (2003). Water infiltration into a large-scale in-situ experiment in an underground research laboratory. *Géotechnique*, **53**(2), 207-224.

Thomas H.R., Seetharam, S.C. and Vardon, P.J. (2011). On the inclusion of some biological impacts and influences in coupled transport phenomena in unsaturated soil. *Geotechnical and Geological Engineering*, **29**, 181-191.

Thomas, H.R., Sedighi, M. and Vardon, P.J. (2012). Diffusive reactive transport of multicomponent chemicals under coupled thermal, hydraulic, chemical and mechanical conditions. *Geotechnical and Geological Engineering*, **30**(4), 841-857.

UNEP (2013). *Annual report 2013*. United Nations Environment Programme.

van Bergen, F., Pagnier, H. and Krzystolik, P. (2006). Field experiment of enhanced coalbed methane-CO2 in the upper Silesian basin of Poland. *Environmental Geosciences*, **13**(3), 201-224.

van Golf-Racht, T.D. (1982). *Fundamentals of fractured reservoir engineering*. Elsevier, Amsterdam, The Netherlands.

Vardon, P.J. (2009). *A three-dimensional numerical investigation of the thermo-hydro- mechanical behaviour of a large-scale prototype repository*. Ph.D. Thesis, Cardiff University, Wales, UK.

Xu, T. and Pruess, K. (2002). Modeling multiphase non-isothermal fluid flow and reactive geochemical transport in variably saturated fractured rocks: 1. Methodology. *American Journal of Science*, **301**, 16-33.

2

Literature Review

2.1 Introduction

Interest in the properties and behaviour of low permeability fractured rock formations has increased in recent decades. The main driver has been the heightened need to explore the unconventional oil and gas contained in these formations, as well as their potential to sequester carbon dioxide. The fundamental basis of this work is relevant to the general case of the coupled physical, chemical and mechanical behaviour of fractured rock during high pressure gas transport. Beyond this, the focal point is specific to the particular geoenergy application of carbon dioxide sequestration in coal with methane production. A state of the art review is therefore provided on the coupled behaviour of coal during high pressure gas transport, including the main findings from both experimental and numerical investigations.

An overview of the main physical, chemical and mechanical aspects of gas transport in coal is provided in section 2.2. This includes a description of the relevant properties of coal, including its complex pore structure and chemical and mechanical properties. The discussion is intended to introduce the fundamental aspects of the behaviour and processes

relevant to this work, before they are covered in more detail in the remaining sections of the chapter.

The major properties of gas species and their mixtures can vary significantly with pressure, temperature and composition. Applications such as carbon dioxide sequestration and methane production can result in large spatial and temporal variations in gas pressure and composition. Hence, section 2.3 provides a review of the various models that are available to describe the evolution in the major properties of multicomponent gas under variable conditions.

Fractured rock may be characterised by two distinct porosity systems, namely, a discontinuous porous matrix defined by a fracture network (Bear, 1993). A number of techniques have been developed to model the transport behaviour in fractured rocks, and these are reviewed in section 2.4. This includes a review on the approaches that have been developed to handle the flow interactions between the fracture network and matrix blocks.

Rather than being stored as free gas in the tight pore spaces, the majority of the gas stored in coal is bound to the coal surface in the adsorbed phase (Seidle, 2011). The developments relevant to the modelling of the adsorption/desorption behaviour are discussed in section 2.5. Gas adsorption/desorption can have a significant effect on the transport properties as a result of coal swelling/shrinking. Likewise, the transport of high pressure gas can alter the pore structure via physical mechanisms. As a result, a review of the deformation behaviour related to the various physical and chemical coal-gas interactions is included in section 2.5. The effect of water on the coal-gas interactions is also reviewed.

Section 2.6 reviews the experimental studies on high pressure reactive gas transport and displacement in coal. In particular, the studies which have conducted laboratory scale simulations alongside the experimental work are reviewed. The state of the art on computational studies related to gas transport and displacement in coal is dealt with in section 2.7.

Finally, section 2.8 gives a summary of the literature review, including the main findings.

2.2   Physical and Chemical Aspects of Gas Transport in Coal

This section provides a review of the major properties and processes in relation to gas transport in coal. Section 2.2.1 deals with the major transport properties of coal and the physical, chemical and mechanical processes are reviewed in section 2.2.2. Whilst coal is the focal point of the reviewed literature, a large portion of the discussion is more generally applicable to fractured rock.

2.2.1   Transport Properties

In a representative element of a fractured rock, the total pore volume is divided between the fracture network and the porous rock matrix. Coal is a fractured rock with a clearly defined and uniformly spaced network of natural fractures, or cleats (King et al, 1986; White et al., 2005; Speight, 2012). The cleats run perpendicular to the bedding plane and can be categorised as the more continuous face cleats or the less continuous butt cleats. As illustrated in Figure 2.1, these types of cleat are orthogonal and butt cleats end at the intersections with face cleats.
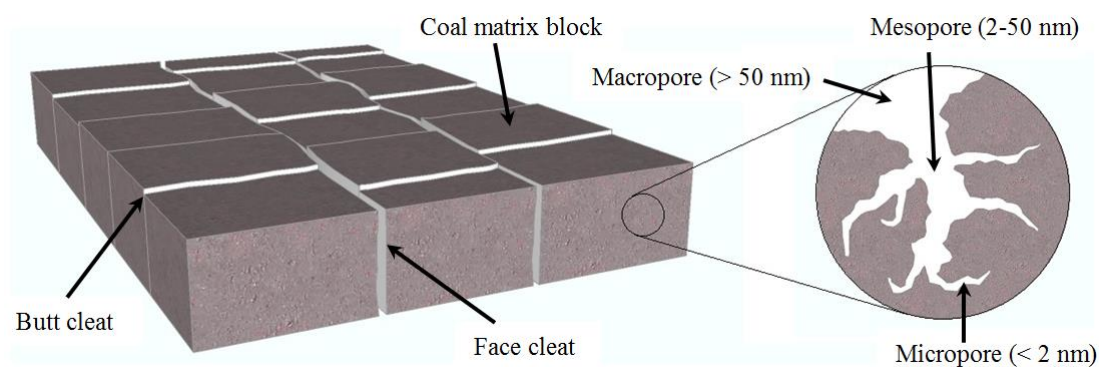
Figure 2.1 Schematic of the natural fractures in coal, i.e. the cleats, and the pore space in the matrix blocks. Pore sizes follow the International Union of Pure and Applied Chemistry (IUPAC) classification (Rouquerol et al., 1994).

Coal is a physically and chemically heterogeneous rock formed mainly of organic material (Haenel, 1992). The coal rank is a measure of the thermal maturity of the organic material in coal and higher rank coals have higher carbon contents (Seidle, 2011). According to Clarkson and Bustin (1999), the porosity in lower rank coals (carbon content < 75%) is

predominantly macroporous, as shown in Figure 2.1. As the rank increases, the role of mesopores and micropores increases. In high rank coals (carbon content > 84%), the porosity is predominantly microporous.

In general, the fracture network in a naturally fractured rock contains a much smaller proportion of the total pore volume than the matrix blocks (Nelson, 2001). Nonetheless, the fracture network typically has a higher permeability and so provides the major conduits for the flow of pore fluids (Sudicky and Frind, 1982; Min et al., 2004; Jaeger et al., 2007).

Spitzer (1981) conducted a series of tests on coal varying in rank from lignite to semi-anthracite. A range of tests, including mercury porosimetry tests, were performed to study the pore volume characteristics and it was found that the porosity varied from 0.013 to 0.43. Similarly, Anderson et al. (1956) and Gan et al. (1972) reported ranges of 0.025 to 0.18 and 0.041 to 0.23 in their respective studies. As observed in these studies, the porosity of coal tends to reduce as the rank increases (Berkowitz, 1979). Owing to the small volume of the fracture network, the greater challenge has been to reliably estimate the contribution of the fractures to the porosity. In this regard, coals from the San Juan and Warrior basins, USA, have been studied the most. Gash (1991) conducted tracer tests and mobile water tests and reported fracture porosities in the range of 0.002 to 0.006.

As mentioned above, the interconnected fracture network provides the main flow conduits in a fractured rock. The fracture permeability in coal typically varies from 1.0×10^{-16} to 1.0×10^{-12} m^2 and is 8 to 9 orders of magnitude higher than the matrix permeability (Seidle, 2011). The presence of more continuous face cleats and less continuous butt cleats, as shown in Figure 2.1, indicates that the horizontal coal permeability is anisotropic to some extent. In fact, permeability ratios of up to 17:1 have been reported for flow in the direction of the face cleats compared to flow in the direction of the butt cleats (Koenig and Stubbs, 1986).

Wang et al. (2007) employed a triaxial stress coal permeameter to measure the permeability of a series of eight 40 mm cubic samples cut from an 80 mm sample. The samples were analysed via surface characterisation, mercury porosimetry and helium pycnometry. The objective was to correlate the measured permeabilities with the major characteristics of the fracture network, particularly the fracture density, orientation,

connectivity, continuity, aperture and tortuosity. Whilst some of the experimental observations were a little inconsistent, the results generally reflected the manner in which coal permeability varies with these characteristics. In other words, the sample with the highest permeability had a dense, well connected and continuous fracture network, whereas the sample with the lowest permeability had a more sparse, poorly connected and discontinuous fracture network. In addition, the highest permeability was 12.5 times larger the lowest permeability, indicating significant heterogeneity at the small scale considered.

Since the fracture aperture in fractured rock is small, the permeability may be sensitive to changes in the stress condition that result in fracture deformation. This was shown in the experimental work of Somerton et al. (1975), who found that coal exhibited varying levels of permeability hysteresis as a result of cyclic loading. Losses in permeability of up to one order of magnitude were observed following a series of triaxial and hydrostatic load cycles in the range of 0.7 to 13.8 MPa.

Depending on the magnitude of the stress, the fracture deformation can result from elastic structural deformation, i.e. normal or shear-induced fracture dilations and compressions (Min et al., 2004), or fracture propagation via structural disintegration. In reactive media, the stress condition can also evolve due to geochemical processes, for example the sorption induced swelling/shrinking of the coal matrix blocks (Seidle, 2011). Fracture propagation is beyond the scope of the present work and has a largely distinct body of literature. By reducing the problem to that of a linear elastic material, a number of models have been developed to describe the evolution in coal permeability under varying stress (e.g. Palmer and Mansoori, 1998; Shi and Durucan, 2004; Robertson and Christiansen, 2006; Connell et al, 2010; Liu et al., 2012).

2.2.2   Physical and Chemical Processes

A schematic of the key processes related to the physical, chemical and mechanical behaviour of coal in applications involving high pressure gas transport and storage is provided in Figure 2.2. The three phase system is divided between the fracture network in the outer ring and the matrix blocks in the inner circle. Gas is introduced to the system via injection, for example carbon dioxide (CO_2) sequestration, and removed by abstraction, for

example methane (CH_4) production. Only water production is included in the schematic, i.e. the effects of hydraulic fracturing are not included. The indicated processes are highly coupled and have a varying impact on the system evolution over a range of time scales. The discussion provided in this section is intended to introduce the fundamentals of these processes, and they are reviewed in greater detail in the subsequent sections of this chapter as required.
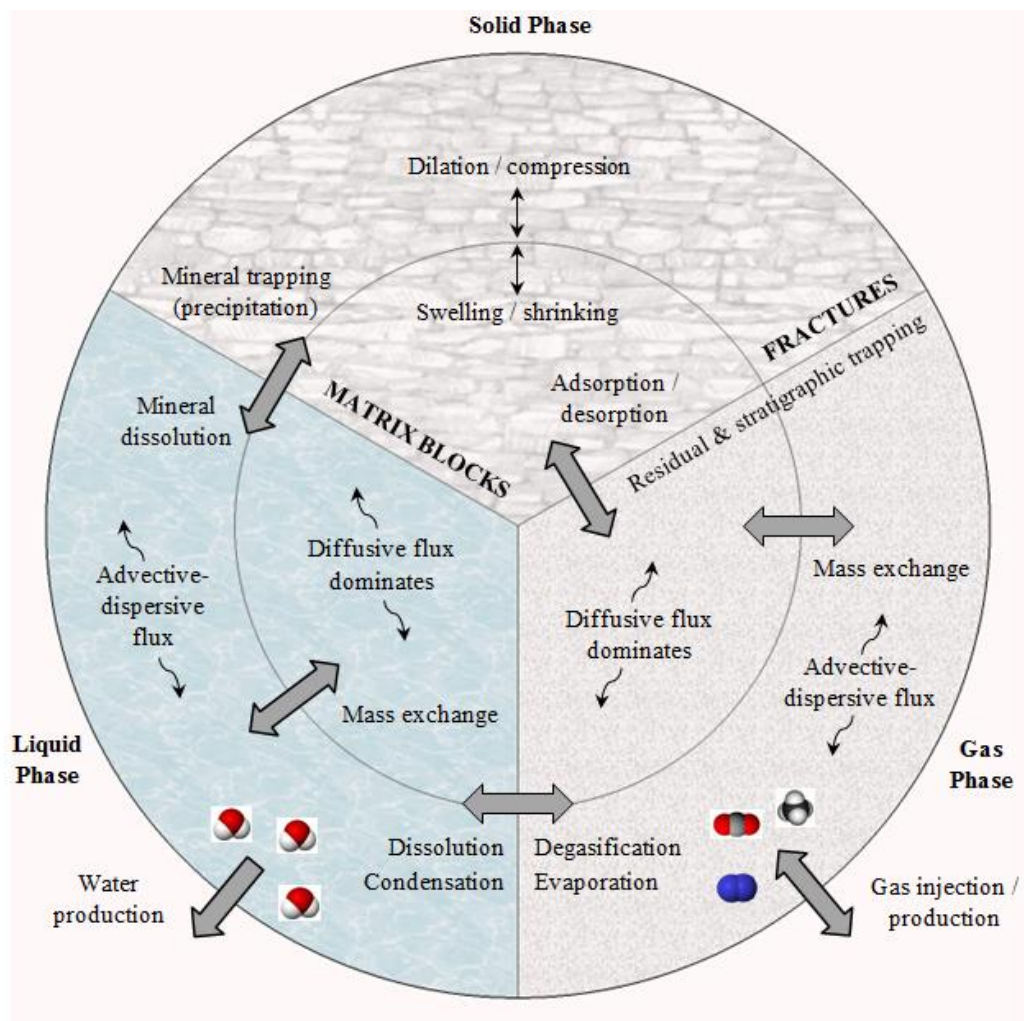
Figure 2.2 Schematic of the major coupled physical, chemical and mechanical processes related to the solid, liquid and gas phases in applications involving high pressure gas transport and storage in coal. Gas storage mechanisms were adopted from Bachu et al. (2007).

A number of authors have reported on the non-isothermal processes involved, although these are not included in Figure 2.2 since the focus of this study is on other aspects of the coupled behaviour. Nonetheless, a brief review of some of the thermal processes discussed

in the literature is provided below.

Simulation results presented by Han et al. (2011) show that the evolution in the CO_2 temperature with depth in an injection well tends towards the formation temperature at a rate depending on the surface temperature, injection rate, well diameter and geothermal gradient. In addition, post-injection temperature fluctuations of up to several Kelvin were attributed to adiabatic (Joule-Thomson) cooling of the injected gas, exothermic gas dissolution and water vapourisation. Differences between the gas temperature and the initial system temperature were shown to influence the evolution in coal permeability in a simulation study presented by Qu et al. (2012). This was attributed to the impact of variable temperatures on the thermal expansion and sorption induced swelling of the coal matrix blocks. These studies indicate that although non-isothermal conditions are not considered further in this work, it should be recognised that variations in the temperature can influence some of the processes illustrated in Figure 2.2.

In relation to gas transport and storage in coal, the hydraulic, gas/chemical and mechanical processes shown may be categorised as:

i.   Transport processes, including mass exchange between the fracture network and the matrix blocks.
ii. Gas storage/trapping and release processes.
iii. Coal deformation processes.

As mentioned in the previous section, it is a general characteristic of fractured rock that the fracture network is the path of least hydraulic resistance. Compared to the advective-dispersive flow regime which prevails in the fracture network, the role of advection in the matrix blocks is often much smaller due to the low intrinsic permeability of the intact rock (Sudicky and Frind, 1982). The advection dominated flow in the fracture network is usually described by Darcy's law (Pashin, 2008). Transport in the matrix blocks is mainly due to various mechanisms of diffusion. In particular, molecular diffusion, Knudsen diffusion, configurational diffusion and surface diffusion occur in microporous media, for example coal (Cui et al., 2004; Freeman et al., 2011). These diffusion mechanisms have been described by Chen et al. (1994) and in chapter 3 of this work. The diffusion process is commonly reduced to a problem of molecular diffusion only and described using Fick's

law (e.g. Masoudian et al., 2013).

Arguably the most important coupling in the modelling of transport in fractured rock is that of the flows in the fracture network and matrix blocks, denoted by the mass exchange processes in Figure 2.2. These local-scale flow interactions are influenced by microscopic processes in the region of the fracture-matrix interface and may be transient and nonlinear, making it difficult to define practical theoretical descriptions for modelling purposes (Gerke and van Genuchten, 1993b).

A number of physical and geochemical processes are responsible for gas storage in fractured rock formations. The time scales involved in gas storage via these mechanisms and the associated storage security are illustrated in Figure 2.3. There are two types of physical storage, namely, stratigraphic trapping and residual trapping (Bachu et al., 2007). Stratigraphic trapping refers to gas stored in structural traps, for example beneath low permeability cap rock, and residual trapping is the storage of gas in the pore space at the minimum (residual) gas content. In terms of geochemical trapping, gas may be dissolved in the groundwater, i.e. solubility trapping, and subsequently react with the rock matrix to form precipitates, i.e. mineral trapping, or react directly with the rock matrix via adsorption (Bachu et al., 2007). Finally, hydrodynamic trapping refers to the geological time scale involved in the upward migration of the injected gas, ensuring that the gas is stored via the mechanisms discussed above before reaching the surface. Adsorption is the dominant storage process of gas in coal, although the role of solubility trapping and mineral trapping increases in the longer term (Golding et al., 2011).

As described in section 2.2.1, coal permeability is stress dependent. If only linear elastic behaviour is considered, the main cause is the dilation and compression of the fractures as a result of various physical and chemical processes. In fact, two major processes are often cited, namely, the physical deformation due to changes in the effective stress and the chemical deformation due to the sorption induced swelling/shrinking of the coal matrix blocks (e.g. Palmer and Mansoori, 1998; Shi and Durucan, 2004; Robertson and Christiansen, 2006; Connell et al, 2010; Liu et al., 2012).

The presence of moisture in coal can have a significant effect on the processes discussed in this section. In particular, moisture is known to influence the gas adsorption capacity (e.g.

Kroos et al., 2002; Day et al., 2008), the gas adsorption rate (e.g. Gruszkiewicz er al., 2009; Pan et al., 2010), the phase relative permeabilities (e.g. Shen et al., 2011; Durucan et al., 2012) and the gas transport and displacement behaviour (e.g. Mazumder and Wolf, 2008; Han et al., 2010). A review of the current understanding of these influences is therefore included in the remaining sections of this chapter where appropriate.
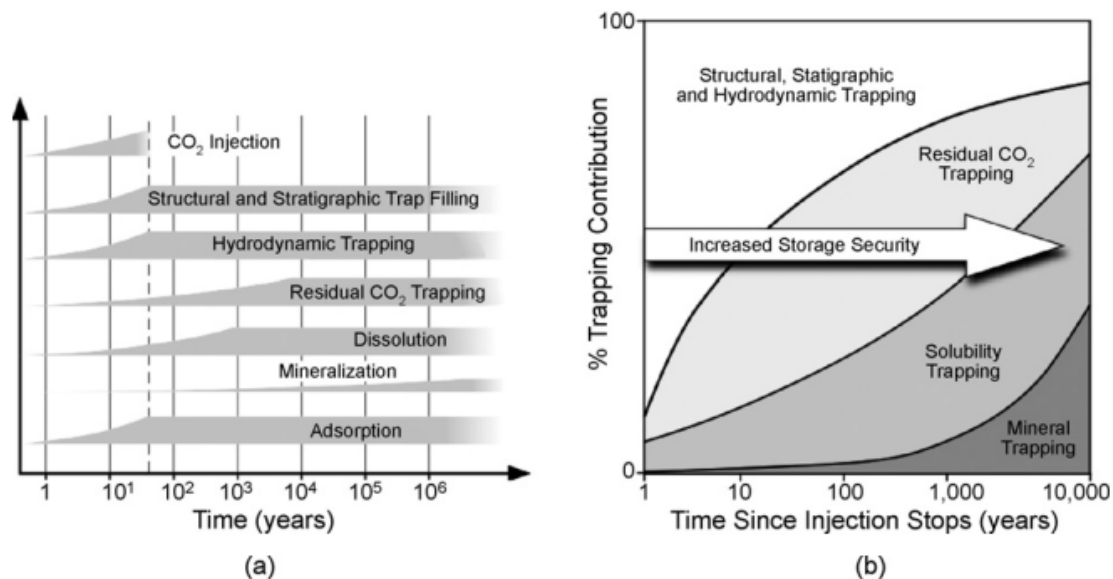
Figure 2.3 Gas storage processes in geological formations: (a) time scales and (b) storage security (adapted by Bachu et al. (2007) from IPCC (2005)).

2.3   Gas Properties at High Pressure

In relation to the main theoretical and applied aspects of this work, the literature review in this section focuses on the properties most relevant to high pressure multicomponent gas transport, namely, the compressibility, viscosity and diffusivity. This is particularly important in applications such as CO_2 sequestration, where the CO_2 may be injected in the supercritical phase with properties very different to the gas phase.

Equations of State (EoS) are relationships between the pressure, temperature and volume of a fluid, i.e. the compressibility. The simplest EoS is the ideal gas law, which assumes that the gas is comprised of infinitesimally small molecules with no intermolecular interactions (Rock, 1983). Although gas approaches this conceptual model as the pressure tends towards zero, the ideal gas law often fails to accurately describe the compressibility

behaviour over a wider range of conditions. This is especially true in the region of the critical point (Poling et al., 2001).

Deviations from ideal gas behaviour are expressed using the compressibility factor, which may be calculated using one of a number of alternative EoS proposed in the literature (e.g. Redlich and Kwong, 1949; Soave, 1972; Peng and Robinson, 1976). In combination with appropriate mixing rules, for example those presented by Kwak and Mansoori (1986), these EoS are widely applied to predict the compressibility behaviour of multicomponent gas (Wei and Sadus, 2000).

Figure 2.4 presents experimental data illustrating the evolution in the compressibility factor for a number of gases across the same range of reduced pressures, P_R, and temperatures, T_R, given by:

$$P_R = \frac{u_g}{u_{gc}} \tag{2.1}$$

$$T_R = \frac{T}{T_c} \tag{2.2}$$

where u_g and T are the gas pressure and temperature, respectively, and u_{gc} and T_c are the critical pressure and temperature, which are defined separately for each gas.

It can be seen that the real gas behaviour approaches the ideal gas law, i.e. a compressibility factor of one, at low P_R and high T_R. A number of works provide the molecular level explanation for the deviations from this behaviour shown under the majority of conditions (e.g. Dickerson et al., 1979; Chang, 2000). Compressibility factors less than one are attributed to the intermolecular attractive forces, which reduce the volume occupied by the real gas compared to an ideal gas at a certain pressure and temperature. Although not shown in the data in Figure 2.4, compressibility factors greater than one are attributed to the intermolecular repulsive forces and the finite volume of the molecules, which oppose reductions in the real gas volume compared to an ideal gas at high pressure.

A detailed review of the gas viscosity models in the literature is provided by Poling et al. (2001). They covered a number of models for the estimation of the viscosity of single component and multicomponent gas at low and high pressures, including real gas

behaviour. Since the present work is concerned with applications involving multicomponent gas at high pressure, for example CO_2 sequestration and CH_4 production, only these models are mentioned here.
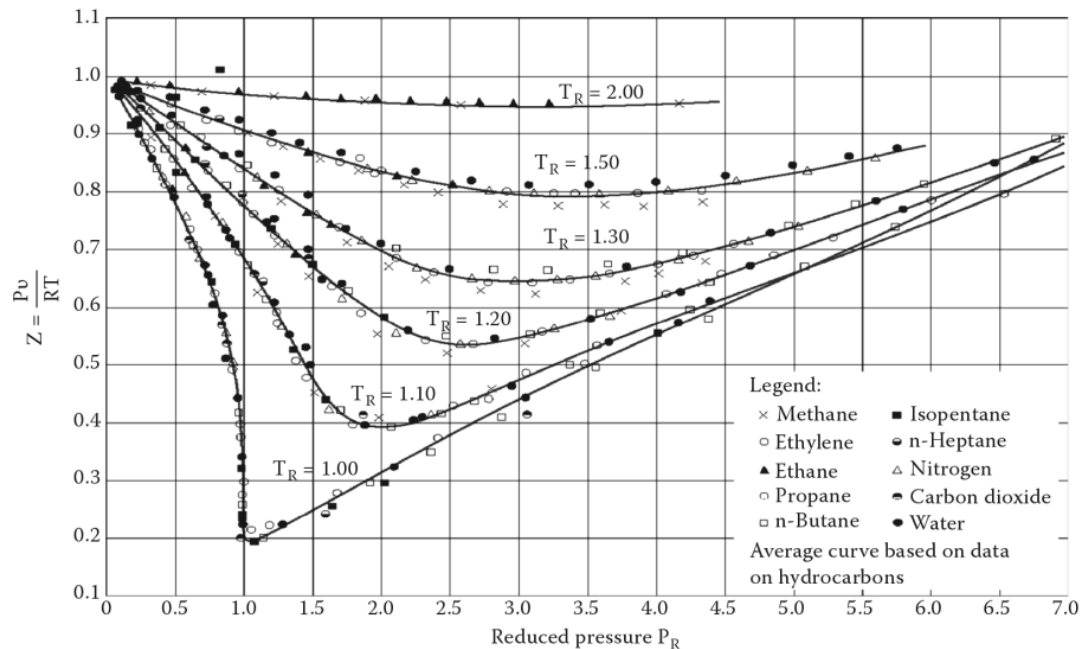
Figure 2.4 Experimental data for the compressibility factor, *Z*, of a number of gases at a range of reduced pressures and temperatures. Reproduced by Annamalai et al. (2011) from Su (1946).

The high pressure gas viscosity models are generally extensions to those developed for single component gas at low pressure. In terms of predicting the viscosity of a single component gas at high pressure, Poling et al. recommend the models of Lucas (1980; 1981) and Chung et al. (1984; 1988). This recommendation was based on comparisons of several models with experimental data. The Lucas and Chung et al. models can be applied for multicomponent gas by defining the gas parameters as functions of composition. Although Poling et al. state that the multicomponent form is slightly less accurate than the single component form, Chung et al. (1988) reported absolute deviations of no more than 9% for non-polar gas mixtures at high pressure.

Similar to the viscosity, the gas diffusivity depends on the pressure and temperature. At low pressure, the diffusion coefficient is inversely proportional to the gas pressure or density (Marrero and Mason, 1972; Poling et al., 2001). However, more complex

behaviour is encountered at high pressure, particularly in the region of the critical point. Cussler (1997) and Poling et al. (2001) cite a lack of reliable experimental data to explain the small number of estimation methods which have been developed. Takahashi (1974) proposed a relationship between the diffusion coefficient at some elevated pressure and a reference diffusion coefficient at low pressure, including a function of the reduced pressure and temperature. Poling et al. report that this method provides a satisfactory agreement with the limited experimental data available. A fundamentally similar empirical method was suggested in Reid et al. (1977), in which the evolution in the diffusion coefficient depends on the ratio of the gas densities at the reference (low) and elevated gas pressures.

2.4　Modelling Fractured Rock

A number of approaches have been developed in the study of transport in fractured rock. In broad terms, the most commonly applied models are equivalent continuum models, dual porosity models and discrete fracture network (DFN) models (Therrien and Sudicky, 1996). The most appropriate type of model in a given scenario may depend on the problem scale/conditions, the available input data, the type of output data required and the available computational resources (Bear, 1993; Samardzioska and Popov, 2005). This section deals with the review of the developed models, including the best practices in their application.

DFN models can be seen as the most rigorous interpretation of a fractured rock mass, since an attempt is made to explicitly model the flow in each significant fracture. The first studies were mainly concerned with investigating the conditions under which a fracture network behaves as a porous medium (e.g. Long et al., 1982; Endo et al., 1984), or better understanding the effect of fracture geometry on the flow behaviour (e.g. Schwartz et al., 1983; Anderson and Dverstorp, 1987). Much of the subsequent research has focused on calibration using field data (e.g. Cacas et al., 1990a; Cacas et al., 1990b) and efficiently upscaling the approach for reservoir simulators (e.g. Derschowitz et al., 2000; Karimi-Fard et al., 2004). In the latter case, this has involved the development of hybrid models that simulate near-field regions as a DFN and far-field regions as an equivalent continuum (Jing and Hudson, 2002).

Despite the advancements described above, the application of DFN models has been

limited by a number of issues, particularly:

i. It remains difficult to obtain the statistical information required to define a DFN model at a suitably practical scale (Singhal and Gupta, 2010).

ii. They remain computationally expensive when applied to complex naturally fractured reservoirs (Samardzioska and Popov, 2005).

iii. The complexity of natural fracture networks makes it difficult to establish whether the essential transport behaviour has been captured, even in cases when the assigned geometric properties appear to be representative (National Research Council, 1996).

For these reasons, the conceptually simpler equivalent continuum and dual porosity models are commonly applied in the study of practical problems. Equivalent continuum models describe the fractured rock as a single homogeneous medium. A homogenisation process is performed to obtain a single set of properties which represent the fracture network and matrix blocks. This has benefits in terms of reducing the data requirements, theoretical complexity and computational cost compared to DFN models (Wu et al., 2004; Samardzioska and Popov, 2005). As a result, the viability of an equivalent continuum model depends mainly on whether the homogenisation process can accurately capture the bulk properties.

This is usually possible provided the fracture network is dense and highly interconnected (i.e. flow in matrix blocks is not important), or there is sufficient mass exchange between the fracture network and matrix blocks to maintain a local equilibrium (Berkowitz, 2002). However, the model becomes less accurate in systems which contain pore regions with markedly different transport and storage behaviour (Bear, 1993). It is then more appropriate to adopt a dual porosity model, whereby the fracture network and matrix blocks are modelled as distinct, overlapping continua coupled by a non-equilibrium mass exchange term, as originally proposed by Barenblatt et al. (1960) and Warren and Root (1963).

A general characteristic of dual porosity models is that the fracture porosity provides the majority of the flow capacity and the matrix porosity provides the majority of the storage capacity. As illustrated in Figure 2.5a, a conventional dual porosity model assumes that the

matrix porosity contains immobile fluids and chemicals so that there is only a single permeability, i.e. the fracture permeability. In this manner, the matrix porosity acts purely as a sink/source to the mobile fluids and chemicals in the fractures. When applied in the study of gas flow and adsorption/desorption in coal, these models may be termed unipore diffusion models (e.g. King et al., 1986; Ozdemir, 2009). This refers to the single-step diffusion process used to describe the kinetics of gas adsorption/desorption in the matrix. These models assume that there is negligible free gas in the matrix porosity, i.e. the gas is exclusively stored in the adsorbed phase.
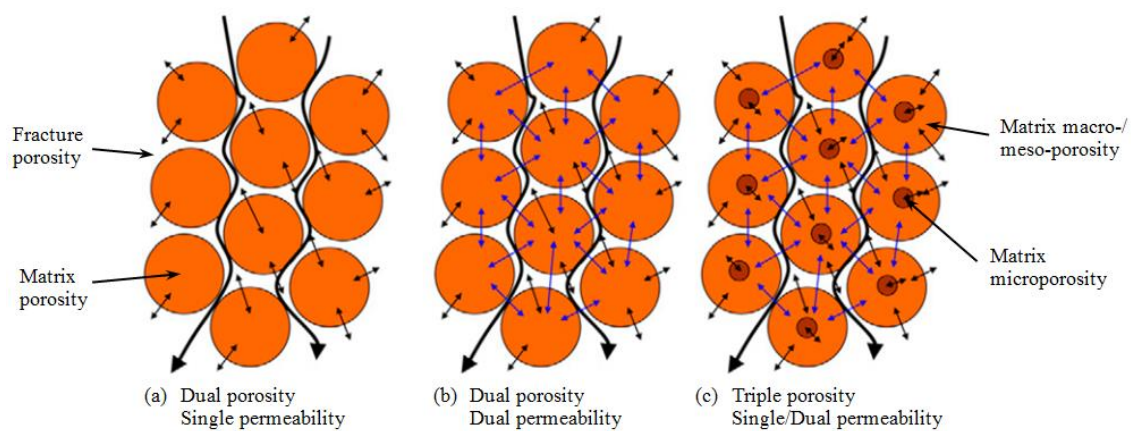
Figure 2.5 Conceptual illustrations of the types of dual/triple porosity models identified in the literature (adapted from Šimůnek and van Genuchten, 2008). Large circles represent the matrix porosity, which in (c) is divided between two pore sizes.

Considering the flow in the matrix porosity results in the dual porosity, dual permeability model shown in Figure 2.5b. These models account for the free gas stored in the matrix porosity. Adsorption/desorption may be included in the governing equations for flow in the matrix porosity by adopting either an equilibrium approach (e.g. Wu et al., 2011) or a kinetics approach (e.g. Thararoop et al., 2012). Finally, the triple porosity model introduced in Figure 2.5c may be appropriate in some cases. For example, the gas adsorption/desorption kinetics in some coals may be best described by a two-step diffusion process in the macro/mesopores and micropores in the so-called bidisperse diffusion models (e.g. Clarkson and Bustin, 1999; Shi and Durucan, 2005).

As mentioned in section 2.2.2, the mass exchange term which governs the inter-porosity flow is an important feature in dual porosity models. This is particularly true in relation to

its role in controlling the bulk mobility of the pore fluids and chemicals in fractured rock models. Two distinct approaches may be identified in the literature, namely, the quasi-steady state mass exchange approach and the transient mass exchange approach. The former approach was adopted in the original works of Barenblatt et al. (1960) and Warren and Root (1963), and assumes that a quasi-steady state pressure distribution prevails in the matrix blocks at all times. In other words, the flow in/out of the matrix blocks is assumed to be steady state in direct proportion to the difference between the fracture pressure or concentration and the volumetric average of the matrix pressure or concentration. A coefficient of mass exchange is included and is usually a function of the fluid mobility and the shape factor, which describes the geometry of the matrix blocks.

Quasi-steady state mass exchange models have been widely applied in the study of transport in dual porosity systems, for example water and solute transport in structured porous media (e.g. Gerke and van Genuchten, 1993a; 1993b; Ma and Shao, 2008) and gas transport in coal (e.g. Wu et al., 2011; Chen et al., 2012a; Talebian et al., 2013). Despite this, the quasi-steady state formulation provides only an approximation of what is initially a transient evolution in the matrix pressure or concentration in response to a change in the fracture conditions. A number of studies have focused on including the transiency by developing time-dependent shape factors, and these have been reviewed by Lemonnier and Bouribaux (2010) and Hassanzadeh et al. (2009). The rate at which the proposed shape factors tend towards the quasi-steady state values depends on the flow problem being considered.

Despite the body of literature devoted to the subject, Hassanzadeh and Pooladi-Darvish (2006) report that the theory surrounding the mass exchange term, particularly the shape factor, remains controversial. They highlighted a lack of substantial improvements in the field and inconsistencies in the developed shape factors. In addition, the transient shape factors have usually been derived for relatively simple boundary conditions at the fracture-matrix interface, for example fixed fracture pressures. In reality, the mass exchange process is more complex due to the dynamics involved.

Samardzioska and Popov (2005) performed a simulation study on flow in two different fractured rock domains using the three principal types of models reviewed in this section,

namely, the equivalent continuum model, the dual porosity model and the DFN model. The homogenised properties for the equivalent continuum model were estimated via a simple volumetric method using equations presented by Bear (1993). In the dual porosity model, the properties in the overlapping fracture and matrix continua were assigned based on an analysis of the total aperture sizes in a cross section perpendicular to the flow. This is analogous to factoring the properties using a volumetric weighting factor, which considers the volume of the fracture network relative to the bulk volume. Overall, the authors reported a good agreement between the results obtained using the different models. The main concern expressed was the uncertainty involved in defining a volumetric weighting factor in rocks which contain a significant number of hydraulically inactive fractures.

2.5   Physical and Chemical Aspects of Coal-Gas Interactions

An introduction to the major physical, chemical and mechanical aspects of gas flow in coal was provided in section 2.2.2. Based on the discussion provided, gas adsorption/desorption and coal deformation are important aspects of coal-gas interactions and can have a considerable impact on the gas transport and storage behaviour. In fact, gas adsorption/desorption is a major mechanism of coal deformation due to the associated swelling/shrinking of the matrix blocks. Therefore, this section provides a combined review of the current understanding of these physical and chemical interactions during gas transport in coal, including the insights from the related experimental, theoretical and modelling work.

2.5.1   Gas Adsorption

White et al. (2005) provided a detailed description of gas adsorption phenomena in coal. Although adsorption is a surface phenomenon, they reported that coals are also capable of absorption, whereby the gas penetrates into the molecular lattice of the coal solids. Absorption may result in a relaxation of the strained, highly cross-linked macromolecular structure of coal, which in turn has a feedback effect on the overall sorption behaviour. The coal swelling due to the adsorption and absorption of certain gases is widely documented (Karacan, 2007), and is discussed in more detail in the following section.

Gas adsorption onto the coal surface can occur due to physical and chemical mechanisms, termed physi-sorption and chemi-sorption, respectively (White et al., 2005). Physi-sorption generally occurs due to van der Waals and electrostatic interactions between the adsorbate molecules and the adsorbent surface. Since chemi-sorption requires a surface chemical bond to be formed, White et al. (2005) reported that it results in a monolayer surface coverage. By comparison, physi-sorption may result in a monolayer or multilayer surface coverage, depending on the gas pressure.

The pore structure of coal has a significant impact on the adsorption/desorption characteristics. For example, the coal matrix blocks contain in excess of 95% of the total internal surface area, and hence almost all of the potential adsorption sites (Shi and Durucan, 2005). As shown in Figure 2.1 and discussed in section 2.2, the coal matrix contains macro-, meso- and micro-pores with a distribution depending on the coal rank. Cui et al. (2004) performed a combined experimental and theoretical analysis of how the pore structure may influence the transport and adsorption of N_2, CH_4 and CO_2 in coal. The outcomes of their work provide an explanation for the key differences in the adsorption behaviour of the gases, namely, the greater CO_2 adsorption capacity, the preference of coal to adsorb CO_2 ahead of N_2 and CH_4, and the faster CO_2 adsorption kinetics. They gave the following conclusions:

i. Adsorption of the smaller CO_2 molecules may occur in ultra-micropores, which are inaccessible to the slightly larger N_2 and CH_4 molecules.

ii. Preferential adsorption of CO_2 occurs as a result of its greater adsorption energy for the majority of pore sizes.

iii. Coal matrix blocks may have an interconnected pore network highly constricted by ultra-micropores, which permit CO_2 diffusion but act as a molecular sieve for N_2 and CH_4. The selective transport would limit the arrival of N_2 and CH_4 at adsorption sites compared to CO_2, thereby influencing the adsorption kinetics.

The final point above was supported by comparisons between the experimental and theoretical N_2, CH_4 and CO_2 macropore diffusivities. It was found that the N_2 and CH_4 diffusivities showed a reasonable agreement with the theoretically predicted trends for free

gas diffusion. This was not the case for CO_2. The experimentally derived diffusivity was up to one order of magnitude greater than those of N_2 and CH_4, whereas the theoretical prediction was for the CO_2 diffusivity to be the smallest. The authors suggested that this difference was due to the above mentioned influence of the ultra-micropores.

Milewska-Duda et al. (2000) conducted a modelling study treating adsorption and absorption as two interacting sub-processes. They concluded that the greater sorption (adsorption plus absorption) capacity of CO_2 in coal may be due to the amount of CO_2 absorption being greater than that of CH_4. As mentioned earlier, coal is known to swell in response to the adsorption and absorption of certain gases, for example CH_4 and CO_2. The findings of Milewska-Duda et al. are therefore consistent with the greater coal swelling caused by CO_2 sorption compared to CH_4 sorption, which has been widely observed in laboratory work (e.g. Ottiger et al., 2008; Durucan et al., 2009). Owing to the difficulties in distinguishing adsorption and absorption in experimental studies (Larsen, 2004), they are often not handled separately in the literature. In fact, a considerable section of the literature refers only to gas adsorption in coal.

Whilst the scope of this work considers applications under isothermal conditions, it is nonetheless important to state that the adsorption capacity of coal is understood to have an inverse relationship with the temperature (e.g. Levy et al., 1997; Azmi et al., 2006). An adsorption isotherm can be used to model the equilibrium adsorbed amount as a function of pressure at a fixed temperature. The IUPAC classification (Sing et al., 1985) includes six typical isotherm shapes and the adsorption of CO_2 and CH_4 is often modelled by a Type I isotherm (White et al., 2005). This isotherm is appropriate for microporous solids, where the capacity is limited by the accessible micropore volume and not the total internal surface area (Sing et al., 1982). White et al. (2005) provided a discussion of the theoretical and empirical equations developed to model a Type I isotherm. In an experimental study conducted by Arri et al. (1992), the extended Langmuir equation was found to provide an acceptable description of the adsorption of binary mixtures of N_2, CH_4 and CO_2 in coal.

Following the review provided in section 2.4, the gas adsorption process can be incorporated into a gas transport model in a number of different ways, depending on the modelling approach adopted. In cases where the coal is modelled as an equivalent

continuum, the reaction kinetics are commonly neglected and the adsorbed amount is not modelled explicitly (e.g. Zhang et al., 2008; Chen et al., 2010; Qu et al., 2012). This typically involves a direct implementation of an equilibrium isotherm in the storage term, which is analogous to a retardation factor. In other words, the adsorption is considered to delay the advance of the gas. However, gas adsorption in coal is well known to be a kinetic reaction, based on the findings from a number of experimental studies (Clarkson and Bustin, 1999; Busch et al., 2004; Gruszkiewicz et al, 2009; Li et al., 2010).

The adsorption kinetics can be included via a non-equilibrium sink/source term in the governing gas transport equations, where the adsorbed amount is usually given as a time-dependent function of the adsorption rate and the gas pressure or concentration. In coal, the adsorption rate is principally determined by the rate of diffusion in the matrix blocks (Busch and Gensterblum, 2011). It follows that the adsorption kinetics are often modelled as a diffusion problem. A good example of this is the unipore diffusion modelling approach (e.g. King et al., 1986; Ozdemir, 2009), where the kinetics are controlled by the rate of diffusion in a spherical micropore matrix. It is assumed that the micropores do not contain free gas and that the adsorbed concentration at the micropore surface instantly reaches equilibrium with the gas pressure or concentration in the fracture porosity. Due to symmetry, a zero-flux boundary condition is prescribed at the centre of the micropore. Under the imposed boundary conditions, gas exchange into or out of the matrix occurs via surface diffusion in response to the changes in the fracture pressure or concentration.

Although the unipore diffusion model is suitable for high rank coals where the matrix is predominantly microporous, the adsorption rate in low rank coals containing a significant volume of macro- and meso-pores may be better described using a two-stage diffusion model (Busch and Gensterblum, 2011). The main reason for this is that the free gas content in the matrix cannot be neglected as in the unipore diffusion model. To deal with the free gas content in the macro- and meso-pores, a number of studies have employed the bidisperse diffusion model (e.g. Clarkson and Bustin, 1999; Shi and Durucan, 2005; Wei et al., 2007a). The matrix is then modelled as a spherical macropore containing a collection of spherical micropores. In this assemblage, the adsorption kinetics are controlled by the rate of free gas diffusion in the macropore and the rate of surface diffusion in the micropores.

Rather than modelling the kinetics in terms of the diffusion stages described above, it is common to simply apply a sorption rate to control the rate of exchange between the free and adsorbed phases. For example, Pini et al. (2011) adopted a first-order rate model to describe the adsorption/desorption of multicomponent gas in coal. Likewise, it is possible to adopt a second-order rate model, or use a combination of two first-order rates (e.g. Busch et al., 2004; Connell et al., 2011). Whilst these rates may be linked to the diffusivities in different regions of the matrix porosity (e.g. Connell et al., 2011), a sorption rate model does not necessitate any assumptions regarding the coal pore structure (Busch et al., 2004). In this manner, the sorption rates can more generally be linked to distinct stages in the adsorption process.

Clarkson and Bustin (1999) and Busch et al. (2004) examined the performance of the unipore/first-order and bidisperse/two first-order approaches via comparisons with the results of adsorption kinetics experiments. In the former study, it was found that the unipore diffusion model generally failed to provide a good agreement with the experimental results. The only exception was for a sample of bright coal (i.e. high vitrinite content, generally higher rank coal) containing a large micropore porosity. By comparison, the bidisperse diffusion model provided a closer agreement with the experimental data for the range of results presented. This was attributed to the greater macro- and meso-pore volume in the dull or banded coal samples (i.e. low vitrinite content, generally lower rank coal), which meant that the kinetics were better described by a two-stage diffusion process occurring in the macro/mesopores and micropores. Similarly, Busch et al. reported that a combination of two first-order rates achieved an improved agreement with the results of their adsorption kinetics experiments compared to the use of a single first-order rate model.

2.5.2   Deformation/Permeability Variations

Coal permeability is highly sensitive to changes in the fracture aperture. As described in section 2.2.1, this is because the fractures provide the main flow conduits. The fracture aperture in coal is widely recognised to be influenced by two principal mechanisms of deformation during gas flow, namely, the fracture compression/dilation due to changes in the effective stress and the sorption induced swelling/shrinking of the matrix blocks (Connell et al., 2010; Li et al., 2013). The complexities related to fracture formation and

propagation are not considered here, i.e. the review is concerned with the elastic (recoverable) strains due to the deformation mechanisms discussed.

As mentioned in section 2.5.1, the coal matrix swells in response to gas adsorption and absorption. A swelling mechanism due to interactions between the sorbed molecules and the macromolecular structure of coal was used by Skawiński (1999) to explain the changes in the permeability of a coal core for the flow of N_2, CH_4 and CO_2. They observed that the displacement of CO_2 by N_2 injection resulted in a recovery of the permeability loss caused by the exposure to CO_2. This indicates N_2 had a lower preference to interact with the coal and that the sorption induced swelling is recoverable. In other words, the coal swells/shrinks in response to varying levels of adsorbed and absorbed gas and displays a strong species dependent behaviour. The reversibility of the swelling/shrinking process has also been observed in other experimental studies (e.g. Rodrigues and Lemos de Sousa, 2002; Battistutta et al., 2010).

Chikatamarla et al. (2009) performed experiments to determine the sorption strain behaviour of coal on exposure to a number of gases, most notably N_2, CH_4 and CO_2. It was found that the sorption strain varied as $CO_2 > CH_4 > N_2$ and was in general linearly proportional to the amount of adsorbed gas, although the gradient of this linear relationship varied between the gases. For example, CO_2 caused a greater swelling per unit volume of adsorbed gas than N_2 and CH_4. This "differential swelling" effect was originally reported by Pekot and Reeves (2002), who showed that CO_2 adsorption may in fact result in a nonlinear swelling response. A nonlinear correlation has also been reported for N_2, CH_4 and CO_2 in the experimental study of Kelemen and Kwiatek (2009).

An attempt at a theoretically rigorous description of the coal swelling phenomenon was made by Pan and Connell (2007). Their approach was based on the work of Myers (2002) on the thermodynamics of adsorption in incompressible microporous adsorbents. Considering that coal must be treated as a compressible adsorbent, Pan and Connell extended Myers' theory to include Scherer's strain model (Scherer, 1987). This allowed an energy balance approach to be applied, where the changes in surface energy due to adsorption were matched by an equivalent elastic energy change in the adsorbent.

Despite the reports of a differential swelling effect and the theoretical developments of Pan

and Connell (2007), the sorption strain is most commonly modelled using a Langmuir-type equation. In fact, this simple approach has been supported by comparisons with experimental data (e.g. Harpalani and Chen, 1995; Levine, 1996).

An additional complexity in the coupling between the gas sorption and deformation behaviour is a possible change in the mechanical properties of the coal. In a series of experiments, Masoudian et al. (2013; 2014) performed triaxial tests on samples of Australian coal and found that the adsorption of CO_2 reduced the Young's modulus by up to 19% and reduced the ultimate strength by 20%. Similar to Skawiński (1999), the authors cite the interactions between the CO_2 and the macromolecular structure of coal as a potential explanation. They suggest that CO_2, as a well-known plasticiser, may have caused a partial breakdown of the cross-linked macromolecules, thereby reducing the resistance to deformation.

Changes in the effective stress resulting in fracture compression/dilation principally occur as a result of changes in the confining pressure and pore pressure (Pan and Connell, 2007; Connell et al., 2010). An elastic mechanical compression/expansion of the matrix blocks may also cause an additional, albeit smaller, change in the fracture aperture (Robertson and Christiansen, 2006). The effective stress dependence of coal permeability has been observed in a number of experimental studies (e.g. Somerton et al., 1975; Durucan and Edwards, 1986; Meng and Li, 2013). It was found that the coal permeability generally decays exponentially with increasing effective stress, for example in the results of Meng and Li (2013) in Figure 2.6. In addition, it can be seen that the permeability failed to recover in the unloading (relief) stage for each of the samples shown. This reflects the stress-history dependent nature of the coal permeability, which was also observed in the other studies cited above. Meng and Li observed that the permeability was more sensitive to stress in water saturated samples.

Although Somerton et al. (1975) reported that the coal permeability to CH_4 was lower than to N_2, the above mentioned studies dealt mainly with the permeability response of coal at different levels of hydrostatic and triaxial confinement. A number of experimental studies have focused more on the measurement of coal permeability using different gases.

As an example, Pini et al. (2009) adopted the transient step method to measure the coal

permeability to helium (He), N_2 and CO_2. This method involves interpreting the rate of system equilibration in response to an increment in the upstream gas pressure. For the injection of the non-sorbing He, it was found that the reduction in effective stress by high pressure gas injection increased the permeability. By comparison, the injection of the sorbing N_2 and CO_2 caused the coal to swell, thereby reducing the permeability compared to that measured for He. As expected, the swelling effect was greater in the case of CO_2. These observations can be seen in Figure 2.7. A number of other studies in which the permeability of coal has been examined are reviewed by Pan and Connell (2012).
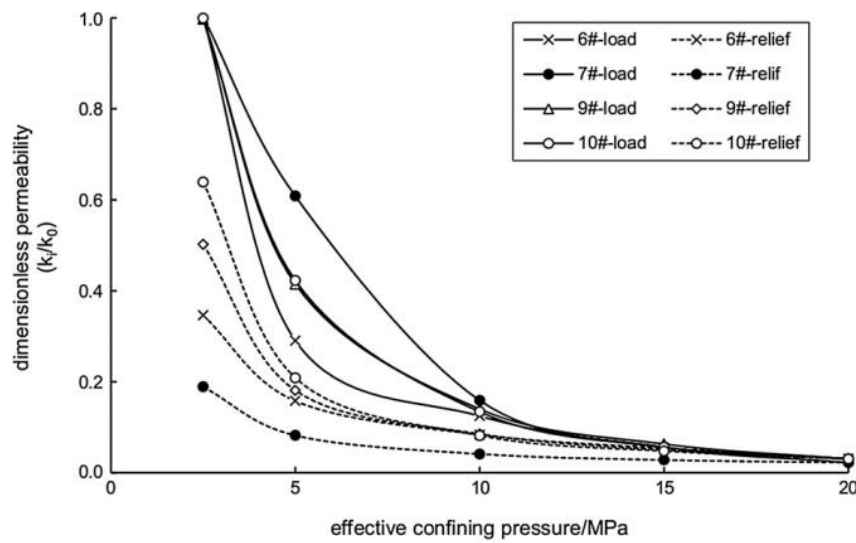
Figure 2.6 Coal permeability evolution for different samples subjected to a single load cycle (Meng and Li, 2013).

The feedback effect of the deformation mechanisms discussed above on coal porosity and permeability is most commonly predicted using analytical models (e.g. Palmer and Mansoori, 1998; Shi and Durucan, 2004; Robertson and Christiansen, 2006; Connell et al, 2010; Liu et al., 2012), although explicit geomechanical models have also been developed (e.g. Gu and Chalaturnyk, 2010). Analytical models express coal deformation in terms of the evolution in the porosity or permeability with respect to a reference (initial) state. Reiss (1980) developed expressions for the porosity and permeability based on different geometrical models of coal, namely, the slab, matchstick and cubic models. These expressions were manipulated to yield:

$$\frac{K}{K_0} = \left(\frac{n}{n_0}\right)^3 \tag{2.3}$$

where K_0 and n_0 are the reference permeability and porosity, respectively, and K and n are the permeability and porosity under a different set of conditions.
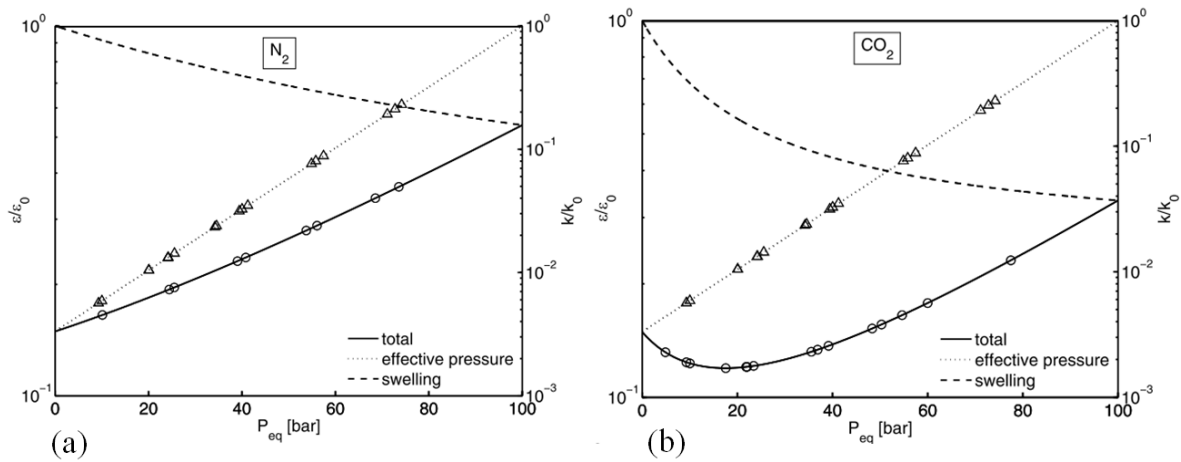
Figure 2.7 Variation of coal porosity (left axis) and permeability (right axis) ratios with equilibrated pressure reported by Pini et al. (2009). Triangles denote He measurements (i.e. no sorption swelling) and circles denote (a) N_2 and (b) CO_2 measurements.

Equation (2.3) is widely adopted in the development of analytical models to relate the changes in the porosity and permeability of coal (e.g. Palmer and Mansoori, 1998; Connell et al, 2010; Liu et al., 2012). A review of some of the most commonly applied analytical models has been provided by Pan and Connell (2012).

Compared to the use of a coupled geomechanical model, Liu et al. (2012) reported the following advantages of analytical models:

   i.   The provision of a closed form solution allows the model to be readily adopted.

  ii.   Each term usually has a clear physical interpretation, which makes the model easier to understand.

 iii.   Reduced computational requirements compared to a coupled geomechanical model.

In addition to the advantages discussed above, a number of assumptions are commonly employed to obtain a concise and practical analytical model, particularly in relation to:

i. Geomechanical conditions, e.g. constant volume, uniaxial strain, constant overburden stress.

ii. Geometry, e.g. slab, matchstick or cubic matrix block models.

iii. Material properties/behaviour, e.g. linear elastic and isotropic material, isothermal conditions, neglect of porosity and permeability in the matrix blocks.

iv. Gas adsorption, e.g. equilibrium approach, swelling/shrinking treated analogously to thermal expansion/contraction.

The developed models have generally been intended for use in predicting and interpreting the permeability response of coal both at the field and laboratory scales (Pan and Connell, 2012). Some models have also been applied in simulator codes for gas transport and displacement in coal (e.g. Connell et al., 2011; Pini et al., 2011; Zhou et al., 2013). In such applications, the neglect of the matrix porosity may have implications. For example, changes in the matrix porosity caused by swelling/shrinking may have a considerable feedback on the rate of gas diffusion. The extension of analytical models to a dual porosity form may therefore be required under certain conditions.

A comprehensive review of the studies related to the comparison and validation of analytical permeability models was included in Pan and Connell (2012). In general, it may be concluded that these models are capable of describing the major trends in coal permeability under a range of conditions. The main challenge is therefore in the choice of the material properties and model parameters, particularly when the available data is limited. History matching is therefore a fairly common practice, although the potential non-uniqueness of the set of history-matched parameters should be recognised (Shi et al., 2008).

2.5.3   Effect of Moisture

Moisture in coal has been shown to influence the gas adsorption capacity and kinetics in a several experimental studies. For example, Kroos et al. (2002) performed CH_4 and CO_2 adsorption experiments on dry and moisture-equilibrated Pennsylvanian coals. It was found that the CH_4 adsorption capacity in moist coal was 20 to 25% lower than in dry coal, depending on the moisture content. Substantial differences were also observed for CO_2

adsorption. Similarly, Day et al. (2008) reported a reduction in the CH_4 and CO_2 adsorption capacities for moisture contents ranging from 0 to 8%. A clear feature of the experimental results was a limiting moisture content above which the adsorption capacity remained stable. This limiting moisture content varied depending on the coal rank and gas species. Day et al. attributed the changes in the adsorption capacity to the preferential adsorption of water molecules at polar sites on the coal surface. At the limiting moisture content, all of the polar sites are occupied and gas adsorption occurs at the hydrophobic sites.

The adsorption kinetics in coal are also affected by the presence of moisture. Grusziewicz et al. (2009) presented a series of experimental results showing the reduction in the adsorption rate as the moisture content was increased, although in contrast to the above mentioned studies they reported only a moderate changes (10 to 20%) in the adsorption capacity. By comparing experiments on different particle size fractions, they suggested that the reduced adsorption rates were caused by the effect of moisture on the diffusion rate and not any changes in the adsorption process at the coal surface. In other words, the moisture may have restricted access to the adsorption sites. Pan et al. (2010) also observed reduced slower adsorption rates as the moisture content was increased. They applied a bidisperse diffusion approach to model the experimental results and concluded that moisture may affect the diffusion differently depending on the pore size, i.e. macro- or micro-pores.

Chen et al. (2012b) presented a numerical model incorporating the above mentioned effects, including the feedback into the sorption induced coal swelling. They developed approximate relationships to describe the effect of moisture on the gas adsorption, gas diffusion and sorption strain in coal. These relationships were validated against selected sets of experimental data from the literature. For example, the single component Langmuir isotherm was extended to describe gas adsorption in moist coal and compared with results from the experimental study by Pan et al. (2010), described above. A selected set of these comparisons is provided in Figure 2.8.

A Langmuir-type sorption strain model was extended to reflect the reduced gas adsorption capacity in moist coal, including an additional term to account for the moisture sorption strain. The relationship was included in the numerical model via an extension of the

analytical permeability model proposed by Shi and Durucan (2004). Finally, the effective gas diffusion coefficient in moist coal was expressed as a function of the moisture content and a decline coefficient.
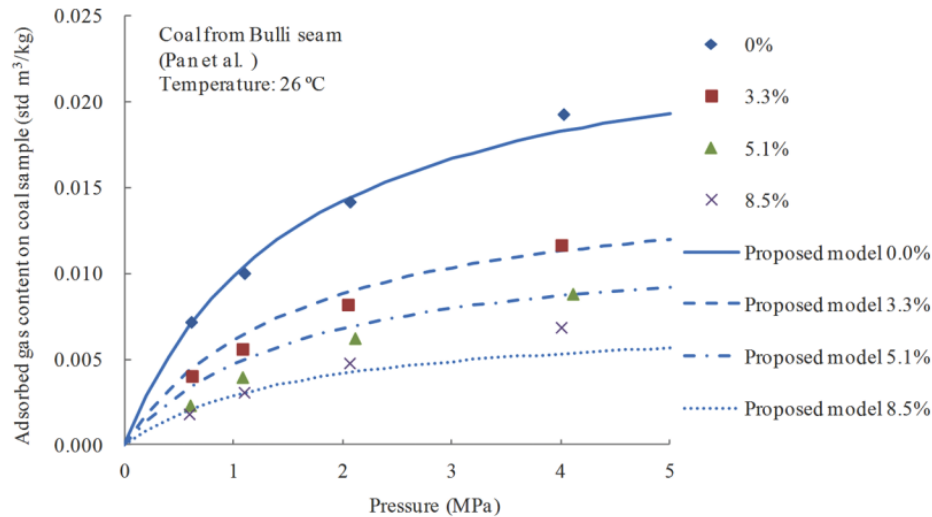
Figure 2.8 Comparisons between the Chen et al. (2012b) model for equilibrium gas adsorption in moist coal and the experimental data of Pan et al. (2010) (adapted from Chen et al.).

2.6   Experimental Studies on Gas Transport and Displacement in Coal

A number of experimental studies have been completed on gas transport and displacement in coal. Most of this work has been carried out with the aim of examining how the major physical and chemical coal-gas interactions (ref. section 2.5) influence the gas transport behaviour, particularly in relation to CO_2 sequestration and CH_4 production applications. In some cases, the reported experimental work is presented alongside laboratory scale numerical simulations (e.g. Jessen et al., 2008; Shi et al., 2008; Connell et al., 2011; Zhou et al., 2013), which are included for validation purposes and to provide additional insights into the observed behaviour. This section deals with a review of the experimental conditions and results, whereas the simulation aspects of these studies are dealt with in the subsequent section.

Experiments were performed by Tsotsis et al (2004) to characterise a bituminous coal (Jamestown seam, Illinois) and study the displacement of CH_4 in a core sample by CO_2 injection. The sample had a length of 170 mm and a diameter of 51 mm. Prior to CO_2

injection, the core was degassed by vacuuming and then loaded with CH_4 in several stages until an equilibrium pressure of 2.86 MPa was achieved. The composition of the produced gas was continuously measured to analyse the system behaviour for the injection of CO_2 at a constant rate of 0.145 standard $m^3\,day^{-1}$, whilst the downstream pressure was regulated at 2.86 to 2.89 MPa. At the end of the experiment, the CH_4 recovery had reached 44.4% and 1.95 CO_2 molecules had been sequestered for each molecule of CH_4 produced. This ratio is in good agreement with the measured adsorption isotherms, indicating the importance of gas adsorption on the observed sequestration and production behaviour.

Jessen et al. (2008) considered the injection of pure and binary gas into a reconstituted coal sample initially saturated with CH_4. The sample was 250 mm in length and 42.5 mm in diameter and formed of crushed coal (Powder River Basin, Wyoming) with a mean particle size of 0.25 mm. Pure N_2, pure CO_2 and a series of binary mixtures were injected at 4.14 MPa and the composition of the produced gas was measured at 5 second intervals. For the pure gas injection, N_2 breakthrough occurred earlier but was considerably more dispersed compared to CO_2. These observations may be attributed to the species dependent coal-gas interactions, most notably the preferential desorption of CH_4 by the injected CO_2 and the swelling response of coal to CO_2 adsorption. For the binary gas injection, N_2 was found to flush the free CH_4 in the pore volumes, whereas the CO_2 displaced the adsorbed CH_4. These findings are qualitatively valuable, but the use of a reconstituted sample limits the quantitative relevance of the results obtained.

The results from a combined experimental and numerical simulation study on supercritical CO_2 injection and CH_4 displacement have been presented by Shi et al. (2008). They tested a dry core sample of Silesian coal with a length of 200 mm and a diameter of 70 mm. Under a confining pressure of 2.5 MPa, the 45 day test consisted of three main stages, namely, CH_4 loading (stage 1), CO_2 injection into a closed system (stage 2) and CO_2 injection with gas production (stage 3). The CO_2 was injected at a relatively low rate to ensure a good level of interaction with the coal matrix. Supercritical CO_2 injection was reached during stage 2, and maintained during stage 3. Gas was produced at a system pressure of around 9 MPa by manually bleeding the backpressure valve, and the composition of the produced gas was measured regularly. The breakthrough of CO_2 occurred after 4 days of production, with the CO_2 fraction reaching 90% after a further 6

days. Interestingly, the measurement of sample length using a linear variable displacement transformer (LVDT) indicated that considerable coal swelling did not occur until the supercritical CO_2 pressure had been reached in the system.

Experiments for N_2 and flue gas (90% N_2, 10% CO_2) injection and CH_4 displacement were performed by Connell et al. (2011). The core sample tested had a length of 114 mm and a diameter of 60 mm and was taken from the Bowen Basin (Australia). A series of experiments was conducted at confining pressures of 4 MPa and 12 MPa, with corresponding injection pressures of 2 MPa and 10 MPa. Aside from an appreciable increase in the gas production rate at the higher pressure, the breakthrough trends were similar in each experiment. In particular, this indicates that the CO_2 had a marginal influence on the system behaviour. Prior to the gas injection and displacement experiments, a characterisation programme was completed, whereby the adsorption isotherms, swelling behaviour and geomechanical properties, including the pore compressibility, were determined. This information was fed into the accompanying simulation study, which is reviewed in the next section.

Zhou et al. (2013) studied the gas injection and displacement behaviour of coal collected from the South Qinshui Basin (China). A core measuring 76.8 mm in length and 37.8 mm in diameter was saturated with CH_4 under a confining pressure of 9.7 MPa with a back pressure of 3.6 MPa. Gas displacement experiments were performed for the injection of pure N_2 and pure CO_2 via a Ruska gas cylinder at a constant water rate of 1.152×10^{-4} m^3 day^{-1}. Similar to observations by Jessen et al. (2008), the breakthrough of N_2 (130 minutes) occurred earlier than that of CO_2 (620 minutes). However, in contrast to Jessen et al., the breakthrough profile for N_2 was less dispersed than for CO_2. Considering the significant differences in the sample size and sample type (i.e. reconstituted and intact cores), it is difficult to recommend a conclusive explanation for this difference between the two sets of results. The coal-gas interactions may have had a marked effect on the system behaviour as a result of the different residence times and pore structures in the samples tested.

Experimental facilities were developed by Hadi Mosleh (2014) with separate analysing units for adsorption/desorption and transport testing on coal samples. Two gas

displacement experiments were performed in a core sample of South Wales coal measuring 120 mm in length and 70 mm in diameter. Before the start of each experiment, the sample was saturated with CH_4 at 5 MPa. For an injection pressure of 5 MPa, the first experiment involved the injection of pure N_2 and the second the injection of pure CO_2. A fixed atmospheric pressure was maintained downstream of the sample. The evolution of the produced gas composition was presented for the two experiments. These results were supported by a detailed characterisation of the coal including the adsorption/desorption behaviour (equilibrium and kinetics) and permeability evolutions for N_2, CH_4 and CO_2. It was found that N_2 breakthrough occurred at 2 minutes, compared to 15 minutes for CO_2. In addition, there was a considerable difference in the longer term breakthrough profiles. The high resolution of experimental data and the detailed coal characteristics provided by Hadi Mosleh (2014) were used in the numerical simulations presented in chapter 6 of this work. An in-depth discussion of the observed gas breakthrough behaviour is then provided.

A series of experiments were performed by Mazumder and Wolf (2008) on five coal cores (two from Beringen, Belgium; two from Silesia, Poland; one from Tupton, UK), ranging from 178 to 334 mm in length and from 70 to 75 mm in diameter. Prior to CO_2 injection, all samples were degassed under a vacuum and then loaded with CH_4 in stages until the desired equilibrium pressure was achieved. It was found that the retention of the injected CO_2 was improved at lower injection rates, i.e. for greater residence times. This may have been due to the greater role of CO_2 diffusion into the matrix blocks and the subsequent adsorption. Whilst four of the experiments were performed on dry samples, the remaining sample (Silesian coal) was performed on moisture equilibrated coal. The effect of moisture was evident from the markedly lower CH_4 displacement efficiency in this experiment.

The effect of moisture on gas transport and displacement in coal has been the subject of several experimental studies. As an example, Shen et al. (2011) and Durucan et al. (2012) examined the nature of two phase flow in coal by characterising the phase relative permeabilities in different rank coals. Shen et al. found that two phase flow was limited to a relatively narrow band of saturations in some samples and that coal may exhibit a high residual moisture content. Considerable variations among the results in the study of Durucan et al. were attributed to sample heterogeneity. It was found that the samples with a narrow two phase flow region contained large dominant fractures.

A review of selected experimental works has been provided in this section. The focus has been on laboratory scale studies relevant to CO_2 sequestration in coal and CH_4 production. A review of the related field scale pilot studies (e.g. van Bergen et al., 2006; Fujioka et al., 2010) has not been provided, since these were discussed in the previous chapter. The experimental studies have provided an enhanced understanding of the gas transport and displacement behaviour in coal under a range of conditions, particularly in relation to the role of species dependent coal-gas interactions. Furthermore, these studies provide a significant resource in the development of numerical models, for example in the provision of detailed coal characteristics and data for validation.

2.7   Computational Studies on Gas Transport and Displacement in Coal

In conjunction with experimental work, analytical and numerical models are useful tools in terms of enhancing the current understanding the complex couplings involved in gas transport and displacement in coal. In a practical sense, the feedback of this understanding can assist in developing more effective techniques for predicting the system behaviour, for example the fate of CO_2 sequestered in the subsurface (Seto et al., 2009). A selective review of the analytical and numerical modelling studies on gas transport and displacement in coal is presented below. This includes a discussion on the numerical simulation components of some of the experimental work described in the previous section.

Under appropriate assumptions and for relatively simple problems, analytical solutions have been developed to describe the transport and displacement of multiple adsorbing gas components in coal, for example those given by Zhu et al. (2003) and Seto et al. (2009). These models share several assumptions, namely, one-dimensional flow, homogeneous and fixed coal properties, isothermal conditions, negligible gravitational effects and equilibrium adsorption/desorption. Whilst the earlier model of Zhu et al. (2003) assumed an immobile water phase and ternary gas, the solution provided by Seto et al. (2009) accounts for two-phase flow and three or four gas components. In both models, multicomponent adsorption/desorption has been described using an extended Langmuir isotherm.

The predictive capabilities of the models with regards to gas transport and preferential gas

displacement behaviour were demonstrated. Nonetheless, the required assumptions limit the wider applicability of the models. As can be seen from sections 2.5.2 and 2.6, this is particularly true in relation to the assumption of a constant porosity and permeability. The requirement for more complex physical and chemical couplings typically makes the numerical treatment of these problems simpler/necessary. As a result, the remainder of this section provides a review of selected numerical simulation studies, including an overview of the available commercial simulator codes.

To assist with the interpretation of the experimental results described in the previous section, Jessen et al. (2008) employed a one-dimensional numerical model. The local equilibrium approach was used to model gas adsorption, whereby the adsorbed gas in the secondary porosity remains at equilibrium with the free gas in the primary porosity. The permeability was prescribed based on experimental measurements and assumed to remain constant.

For the injection of pure N_2 and pure CO_2, a good agreement was found between the evolutions in the experimental and simulated produced gas compositions. This was not achieved in the binary gas injection simulations, although there was a reasonable qualitative agreement in the overall trends. Despite some of the positive results, the testing of a reconstituted sample somewhat limits the value of the results obtained, as mentioned in the previous section. In addition, the use of the numerical model in a detailed analysis of the experimental results may have been precluded by the relative simplicity of the underlying formulation and the idealised simulation conditions.

Shi et al. (2008) implemented a dual porosity, single permeability gas transport formulation in the METSIM2 computer code. A first-order model based on the assumption of quasi-steady state matrix diffusion was used to describe the sorption kinetics. The staged experimental procedure described in the previous section enabled the authors to undertake the calibration of the model in a sequential manner. The sorption rates and permeability were thereby determined via history matching. In fact, the simulation was found to have a low sensitivity to changes in the permeability. This was attributed to the secondary importance of the Darcy flow in the fractures compared to matrix diffusion at the low CO_2 injection rates considered. With the exception of a discrepancy which developed after CO_2

breakthrough, the simulated produced gas composition generally followed the experimental results. It was found that introducing the back pressure variation observed in the experiment offered a marginal improvement in the agreement.

A modified version of the commercial simulator code SIMED II was employed by Connell et al. (2011) for dual porosity simulations of their gas transport and displacement tests (ref. section 2.6). The main objective of the simulations was to evaluate the suitability of the reactive gas transport formulation, particularly the combination of two first-order rate equations which were used to describe gas diffusion into the matrix blocks (i.e. the sorption rate). The permeability model developed in Connell et al. (2010) was implemented in SIMED II, and the gas injection and production rates measured in the experiments were used as controlling parameters in the respective boundary conditions. There was a close agreement between the evolution of the produced gas predicted in the simulations and observed in the experiments. In the history matching process, it was found that the combination of two first-order rate models provided an improved description of the sorption rate compared to a single rate model. The authors attributed this to the presence of two distinct regions in the microporosity, each with an associated rate of adsorption/desorption.

Similar to the above studies, Zhou et al. (2013) utilised a numerical model in order to provide a greater insight into their experimental results (ref. section 2.6). They performed one-dimensional simulations using a dual porosity model in the GEM compositional simulator code in conjunction with the Palmer and Mansoori (1998) permeability model. Small differences between the simulated gas breakthrough and that observed in the experiments were attributed to the simplified representation of the coal structure in the simulations. In other words, the heterogeneity of the sample resulted in a more complex gas displacement efficiency compared to the idealised displacement predicted in the numerical simulation.

The above mentioned studies have involved complementary experimental and simulation components. Other simulation studies have instead used experimental results provided in the literature. As an example, Shi and Durucan (2003) applied a bidisperse diffusion (i.e. triple porosity) model to simulate an experiment performed by Wolf et al. (1999), who

injected CO_2 into a Belgian coal core sample for CH_4 displacement. It was found that a variable micropore diffusivity provided an improved agreement with the experimental results for the produced gas composition. A linear relationship was suggested, whereby the micropore diffusivity declined as the total adsorbate concentration increased. Wei et al. (2007a) also applied a bidisperse diffusion model to simulate the Wolf et al. experiment. They implemented a Maxwell-Stefan diffusion formulation to model the interactions between the gas species in a multicomponent mixture. Similar to Shi and Durucan, a variable micropore diffusivity was defined and a close agreement with the experimental results was reported.

Larger scale simulations on gas transport and displacement are frequently presented in the literature. For example, Pini et al. (2011) conducted a series of numerical simulations on gas injection and CH_4 displacement under conditions representative of a 100 m long coal bed at a depth of 500 m in the Sulcis Coal Province (Sardinia). In an attempt to replicate the conditions after the primary production stage, the initial pressure of CH_4 in the system was set to less than the hydrostatic pressure at a uniform 1.5 MPa. An injection pressure of 4.5 MPa was chosen for the injection of pure N_2, pure CO_2 and certain binary mixtures in separate simulations. A one-dimensional, dual porosity, single permeability modelling approach was used, whereby an adsorption rate was specified for the exchange of gas in/out of the adsorbed phase in the matrix porosity.

It was found that the injection of N_2 gave a faster CH_4 production in the early stages of the simulation period, whereas for CO_2 injection the early production was delayed by the permeability loss resulting from the sorption induced coal swelling. Given the relatively low preference of N_2 to displace adsorbed CH_4, the faster early production can be attributed to the flushing of the free CH_4 stored in the fracture porosity. In the longer term, the stronger displacement behaviour of CO_2 resulted in a faster overall CH_4 production.

As described in section 2.5.3, Chen et al. (2012b) developed a numerical model including constitutive relationships to describe the effect of moisture on the gas adsorption, gas diffusion and sorption strain in coal. Following the validation of these relationships against selected experimental results in the literature, they applied the numerical model in the simulation of gas production under various fixed moisture contents. The simulated system

was a 200 m by 200 m coal seam of 1 m thickness with a 150 m long horizontal drainage well along the centreline. An initial gas pressure of 5 MPa was prescribed.

It was found that the effect of moisture on the above mentioned processes can have a marked impact on the gas storage and transport behaviour. This is clearly illustrated in Figure 2.9, where it can be seen that the highest gas production rate was achieved in the dry system. Increasing the moisture content up to 7% was found to significantly reduce the gas production rate, particularly in the first 40 days of the simulation. Based on these findings, Chen et al. (2012b) suggested that the effect of moisture on gas transport and displacement warrants additional research.
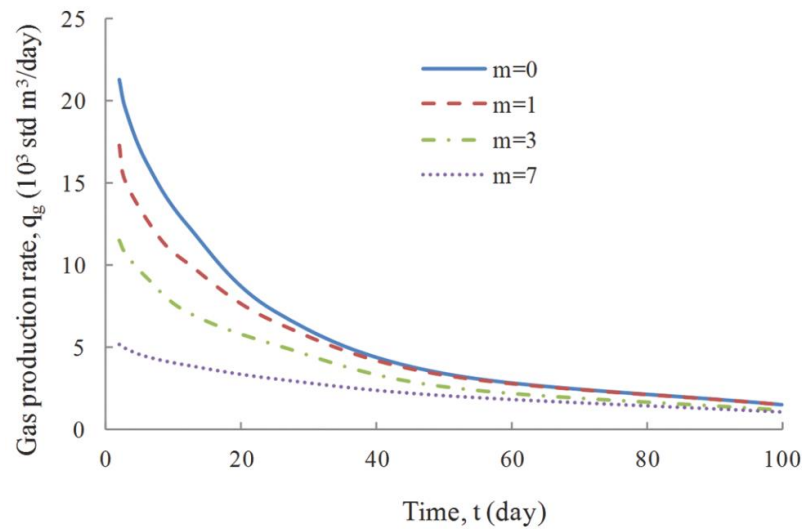
Figure 2.9 Evolution of the gas production rate at various fixed moisture contents, obtained in numerical simulations conducted by Chen et al. (2012b).

The experimental work of Masoudian et al. (2013; 2014) on the changes in the mechanical properties of coal caused by CO_2 adsorption were described in section 2.5.2. Based on the experimental results obtained in the earlier study, Masoudian et al. formed a linear relationship to describe the reduction in Young's modulus as the amount of adsorbed gas increases. By implementing this relationship in a dual porosity numerical model, they were able to investigate the mechanical response of a 100 m radius coal bed to CO_2 injection. It was found that the softening of coal by CO_2 adsorption altered the permeability response of the coal bed. Specifically, the changes in the effective stress due to swelling were reduced

by including a variable Young's modulus, so that a higher permeability was maintained. Masoudian et al. conclude that the softening effect may be an important consideration in the accurate assessment of the performance of CO_2 sequestration in coal.

The computational modelling of gas transport and displacement in coal described above has provided insights into the experimental observations and enabled the study of particular processes and behaviour under a wide range of conditions and scales. Positive results have generally been achieved in the simulation of gas transport and displacement experiments. History matching of parameters is often needed for certain physical and chemical properties, especially as the level of complexity is increased in dual and triple porosity models. This makes it more likely that an agreement with experimental results may be reached with a non-unique set of parameters. Conversely, attempts to minimise the number of parameters required in a model may result in an oversimplified representation of the coal structure. The level of uncertainty may be reduced by detailed laboratory characterisation, employing a clear methodology in the definition of certain parameters and making use of the available literature.

The review provided in this section is supplemented below by a summary of the capabilities of some of the available compositional simulators.

2.7.1 Commercial Simulators

A number of numerical simulators have been developed and tested for the modelling of gas transport and displacement in coal. Wei et al. (2007b) categorised the available simulators as:

i. Conventional black-oil and compositional models. Two phase flow is considered in the fracture network and an equilibrium approach is adopted for gas adsorption/desorption in the matrix. In other words, the interactions between the gas and solid are instantaneous and matrix diffusion is not considered.

ii. Specialised models: these have been developed specifically in the study of CH_4 production from coal beds, and in many cases have been extended for the study of CO_2 sequestration. Two phase flow is considered and various dual and triple porosity formulations and constitutive relationships for coal behaviour may be

employed.

Selected numerical simulators are reviewed here, namely:

   i. Conventional black-oil and compositional models.

      a. GCOMP, BP-Amoco, Houston, USA.

      b. GEM, Computer Modelling Group (CMG) Ltd., Calgary, Canada.

  ii. Specialised models:

      a. COMET 2, Advanced Resources International (ARI), USA.

      b. COMET 3, ARI, USA.

      c. ECLIPSE, Schlumberger (GeoQuest), UK.

      d. SIMED II, Netherlands Institute of Applied Geoscience (TNO), The Netherlands and Industrial Research Organization (CSIRO), Australia.

Law et al. (2002) provided an in-depth review and comparison study of the above mentioned simulators, and a summary of the features discussed is provided in Table 2.1.

Table 2.1 Features of a selection of numerical simulator codes for CO_2 sequestration and CH_4 production in coal (Law et al., 2002).

CBM Simulators	GEM	ECLIPSE	COMET	SIMED II	GCOMP
Mutliple Gas Components (3 or more: CH_4, CO_2 & N_2)	√	✗	√	√	√
Dual Porosity Approach	√	√	√	√	✗
Mixed Gas Diffusion (Different Diffusion Rates)	√	√	√	√	✗
Mixed Gas Adsorption (Extended Langmuir Model)	√	✗	√	√	√
Stress Dependent Permeability and Porosity	√	√	√	√	√
Coal Shrinkage/Swelling	√	✗	√	√	√

It should be noted that the capability to handle more than two gas components is a perquisite in the simulation of flue gas injection (i.e. N_2 and CO_2) (Law et al., 2002). The use of a single porosity model requires the assumption of equilibrium between the free and adsorbed gas, which may limit the applicability since the adsorption/desorption kinetics in coal are well documented. Furthermore, mixed gas adsorption/desorption is required,

except in the simulation of conventional CH_4 production. Whilst the effective stress dependent permeability is important, the availability of constitutive relationships incorporating the strong coal swelling/shrinking response to gas adsorption/desorption is important.

2.8 Conclusions

Key aspects of the physical and chemical behaviour of coal under high pressure mixed gas transport have been reviewed in this chapter. Developments related to the computational techniques which may be employed to model fractured rock, particular coal, were included. The current understanding on the major coal-gas interactions for gas adsorption/desorption and deformation was compiled. Finally, the state of the art on the developed computational models for gas transport and displacement in coal was addressed, with a particular emphasis on the models which have been developed and applied alongside experimental work.

Coal is characterised by at least two distinct porosity regions in the fracture network and matrix blocks, which can have markedly different controls on the bulk behaviour. As an example, it is widely acknowledged that the fracture porosity makes a small contribution to the total porosity, but a major contribution to the total permeability. Although coal is physically and chemically heterogeneous, certain features exhibit a greater uniformity, such as the fracture spacing. This has been an important feature in the development of practical numerical modelling techniques.

There are several techniques which may be employed to model fractured rock, which have been developed and applied under a wide range of conditions with varying levels of theoretical rigour. The high theoretical rigour of discrete fracture network (DFN) models may generally be compromised in most practical cases by the challenge of developing an explicit, representative description of fracture flow with an acceptable computational cost. By comparison, the equivalent continuum approach is applicable provided the flow between the fractures and matrix blocks is sufficiently rapid to maintain a local equilibrium. Since many fractured rocks do not satisfy this condition, dual (or triple) porosity models have instead been widely applied and have proven to be highly versatile.

Carbon dioxide sequestration in geological formations can be expected to involve the injection of CO_2 at conditions near the phase change between the gas and supercritical phases. Relationships are available in the literature to accurately characterise the evolution in the gas properties at high pressure, including gas mixtures, and these should be implemented in computational studies on transport behaviour.

A number of hydraulic, gas/chemical and mechanical processes may influence the system behaviour in coal. It is widely regarded that the gas adsorption/desorption and deformation under high pressure gas transport have the greatest influence. For example, the strong species dependent coal swelling response to the adsorption of certain gas can have a considerable feedback on the permeability. The influence of moisture on these interactions has been reported to be quite high, even at residual moisture contents.

The available experimental results have enhanced the understanding of the gas transport and displacement behaviour in coal under a range of conditions, particularly in relation to the role of species dependent coal-gas interactions. These studies have also provided detailed characteristics and data for the validation and wider application of the developed computational models. In turn, the computational modelling of gas transport and displacement in coal has provided insights into the experimental observations and enabled the study of particular processes and behaviour under a wide range of conditions and scales. The applied models have generally treated the coal as a dual porosity system, although there has been a varying level of rigour in the underlying theoretical formulations. In addition, new features of the developed models are being reported and the results generally indicate that the literature remains some way off a comprehensive description of gas transport and displacement in coal.

2.9 References

Anderson, R.B., Hall, W.K., Lecky, J.A. and Stein, K.C. (1956). Sorption studies on American coals. *The Journal of Physical Chemistry*, **60**(11), 1548-1558.

Andersson, J. and Dverstorp, B. (1987). Conditional simulations of fluid flow in three-dimensional networks of discrete fractures. *Water Resources Research*, **23**(10), 1876-1886.

Annamalai, K., Puri, I.K. and Jog, M.A. (2011). *Advanced thermodynamics engineering*. 2nd edition. CRC Press, Boca Raton, Florida.

Arri, L.E., Yee, D., Morgan, W.D. and Jeansonne, M.W. (1992). Modeling coalbed methane production with binary gas sorption. *In Proceedings of the SPE Rocky Mountain Regional Meeting*, 18-21 May, Casper, Wyoming.

Azmi, A.S., Yusup, S. and Muhamad, S. (2006). The influence of temperature on adsorption capacity of Malaysian coal. *Chemical Engineering and Processing*, **45**, 392-396.

Bachu, S., Bonijoly, D., Bradshaw, J., Burruss, R., Holloway, S., Christensen, N.P. and Mathiassen, O.M. (2007). CO_2 storage capacity estimation: methodology and gaps. *International Journal of Greehouse Gas Conrol*, **1**, 430.443.

Barenblatt, G.I., Zheltov, I.P. and Kochina, I.N. (1960). Basic concepts in the theory of seepage of homogenous liquids in fissured rocks (strata). *Journal of Applied Mathematics and Mechanics*, **24**(5), 1286-1303.

Battistutta, E., van Hemert, P., Lutynski, M., Bruining, H. and Wolf, K-H. (2010). Swelling and sorption experiments on methane, nitrogen and carbon dioxide on dry Selar Cornish coal. *International Journal of Coal Geology*, **84**, 39-48.

Bear, J. (1993). Modeling flow and contaminant transport in fractured rocks. In: Bear, J. et al. eds. *Flow and contaminant transport in fractured rock*, Academic Press, Inc., pp 1-38.

Berkowitz, N. (1979). An introduction to coal technology. Academic Press, San Diego, California.

Berkowitz, B. (2002). Characterizing flow and transport in fractured geological media: a review. *Advances in Water Resources*, **25**, 861-884.

Busch, A., Gensterblum, Y., Kroos, B.M. and Littke, R. (2004). Methane and carbon dioxide adsorption–diffusion experiments on coal: upscaling and modeling. *International Journal of Coal Geology*, **60**, 151-168.

Busch, A. and Gensterblum, Y. (2011). CBM and CO_2-ECBM related sorption processes in coal: a review. *International Journal of Coal Geology*, **87**, 49-71.

Cacas, M.C., Ledoux, E., de Marsily, G., Tillie, B., Barbreau, A., Durand, E., Feuga, B. and Peaudecerf, P. (1990a). Modeling fracture flow with a stochastic discrete fracture network: calibration and validation: 1. The flow model. *Water Resources Research*, **26**(3), 479-489.

Cacas, M.C., Ledoux, E., de Marsily, G., Barbreau, A., Calmels, P., Gaillard, B. and Margritta, R. (1990b). Modeling fracture flow with a stochastic discrete fracture network: calibration and

validation: 2. The transport model. *Water Resources Research*, **26**(3), 491-500.

Chang, R. (2000). *Physical chemistry for the chemical and biological sciences*. 3rd edition. University Science Books, Sausalito, California.

Chen, N.Y., Degnan, T.F., Smith, C.M. (1994). *Molecular transport and reaction in zeolites*. John Wiley & Sons, New York.

Chen, Z., Liu, J., Elsworth, D., Connell, L.D. and Pan, Z. (2010). Impact of CO_2 injection and differential deformation on CO_2 injectivity under in-situ stress conditions. *International Journal of Coal Geology*, **81**, 97-108.

Chen, D., Pan, Z., Liu, J. and Connell, L. (2012a). Characteristic of anisotropic coal permeability and its impact on optimal design of multi-lateral well for coalbed methane production. *Journal of Petroleum Science and Engineering*, **88-89**, 13-28.

Chen, D., Pan, Z., Liu, J. and Connell, L. (2012b). Modeling and simulation of moisture effect on gas storage and transport in coal seams. *Energy and Fuels*, **26**, 1695-1706.

Chikatamarla, L., Bustin, R.M. and Cui, X. (2009). CO_2 sequestration into coalbeds: Insights from laboratory experiments and numerical modeling. In: Grobe et al., eds. *Carbon dioxide sequestration in geological media: State of the Science*, AAPG Studies in Geology 59, Tulsa, Oklahoma.

Chung, T-H., Lee, L.L. and Starling, K.E. (1984). Applications of kinetic gas theories and multiparameter correlation for prediction of dilute gas viscosity and thermal conductivity. *Industrial & Engineering Chemistry Fundamentals*, **23**(1), 8-13.

Chung, T-H., Ajlan, M., Lee, L.L. and Starling, K.E. (1988). Generalized multiparameter correlation for nonpolar and polar fluid transport properties. *Industrial and Engineering Chemistry Research*, **27**, 671-679.

Clarkson, C.R. and Bustin, R.M. (1999). The effect of pore structure and gas pressure upon the transport properties of coal: a laboratory and modeling study. 2. Adsorption rate modelling. *Fuel*, **78**, 1333-1344.

Connell, L.D., Lu, M. and Pan, Z. (2010). An analytical coal permeability model for tri-axial strain and stress conditions. *International Journal of Coal Geology*, **84**, 103-114.

Connell, L.D., Sander, R., Pan, Z., Camilleri, M. and Heryanto, D. (2011). History matching of enhanced coal bed methane laboratory core flood tests. *International Journal of Coal Geology*, **87**, 128-138.

Cui, X., Bustin, R.M. and Dipple, G. (2004). Selective transport of CO_2, CH_4 and N_2 in coals: insights from modeling of experimental gas adsorption data. *Fuel*, **83**, 293-303.

Cussler, E.L. (1997). *Diffusion: mass transfer in fluid systems*. 2nd Edition. Cambridge University Press, Cambridge.

Day, S., Sakurovs, R. and Weir, S. (2008). Supercritical gas sorption on moist coals. *International Journal of Coal Geology*, **74**, 203-214.

Dershowitz, B., LaPointe, P., Eiben, T. and Wei, L. (2000). Integration of discrete feature network methods with conventional simulator approaches. *SPE Reservoir Evaluation & Engineering*, **3**(2), 165-170.

Dickerson, R.E., Gray, H.B. and Haight, G.P. (1979). *Chemical principles*. 3rd edition. Benjamin/Cummings Publishing Company Inc., Menlo Park, California.

Durucan, S. and Edwards, J.S. (1986). The effects of stress and fracturing on permeability of coal. *Mining Science and Technology*, **3**, 205-216.

Durucan, S. Ahsan, M. and Shi, J-Q. (2009). Matrix shrinkage and swelling characteristics of European coals. *Energy Procedia*, **1**, 3055-3062.

Durucan, S., Ahsan, M., Syed, A., Shi, J-Q. and Korre, A. (2012). Two phase relative permeability of gas and water in coal for enhanced coalbed methane recovery and CO_2 storage. *Energy Procedia*, **37**, 6730-6737.

Endo, H.K., Long, J.C.S., Wilson, C.R. and Witherspoon, P.A. (1984). A model for investigating mechanical transport in fracture networks. *Water Resources Research*, **20**(10), 1390-1400.

Freeman, C.M., Moridis, G.J. and Blasingame, T.A. (2011). A numerical study of microscale flow behaviour in tight gas and shale gas reservoir systems. *Transport in Porous Media*, **90**, 253-268.

Fujioka, M., Yamaguchi, S. and Nako, M. (2010). CO_2-ECBM field tests in the Ishikari Coal Basin of Japan. *International Journal of Coal Geology*, **82**, 287-298.

Gan, H., Nandi, S.P. and Walker Jr, P.L. (1972). Nature of the porosity in American coals. *Fuel*, **51**(4), 272-277.

Gash, B.W. (1991). Measurement of rock properties in coal for coalbed methane production. *In Proceedings of the 1991 SPE Annual Technical Conference and Exhibition*, 6-9 October, Dallas, Texas.

Gerke, H.H. and van Genuchten, M.T. (1993a). A dual-porosity model for simulating the preferential movement of water and solutes in structured porous media. *Water Resources Research*. **29**(2), 305-319.

Gerke, H.H. and van Genuchten, M.T. (1993b). Evaluation of a first-order water transfer term for variably saturated dual-porosity flow models. *Water Resources Reseach*, **29**(4), 1225-1238.

Golding, S.D., Uysal, S.T., Boreham, C.J., Kirste, D., Baublys, K.A. and Esterle, J.S. (2011). Adsorption and mineral trapping dominate CO_2 storage in coal seams. *Energy Procedia*, **4**, 3131-3138.

Gruszkiewicz, M.S., Naney, M.T., Blencoe, J.G., Cole, D.R., Pashin, J.C. and Carroll, R.E. (2009). Adsorption kinetics of CO_2, CH_4, and their equimolar mixture on coal from the Black Warrior Basin, West-Central Alabama. *International Journal of Coal Geology*, **77**, 23-33.

Gu, F. and Chalaturnyk, R. (2010). Permeability and porosity models considering anisotropy and discontinuity of coalbeds and application in coupled simulation. *Journal of Petroleum Science and Engineering*, **74**, 113-131.

Hadi Mosleh, M. (2014). *An experimental investigation of flow and reaction processes during gas storage and displacement in coal*. Ph.D. Thesis, Cardiff University, Wales, UK.

Han, F., Busch, A., van Wageningen, N., Yang, J., Liu, Z. and Krooss, B.M. (2010). Experimental study of gas and water transport processes in the inter-cleat (matrix) system of coal: anthracite from Qinshui Basin, China. *International Journal of Coal Geology*, **81**, 128-138.

Han, W.S., Kim, K-Y.,Lu, M., McPherson, B.J., Lu, C. and Lee, S-Y. (2011). Injectivity changes and associated temperature disequilibrium: numerical study. *Energy Procedia*, **4**, 4552-4558.

Haenel, M.W. (1992). Recent progress in coal structure research. *Fuel*, **71**(11), 1211-1223.

Harpalani, S. and Chen, G. (1995). Estimation of changes in fracture porosity of coal with gas emission. *Fuel*, **74**(10), 1491-1498.

Hassanzadeh, H. and Pooladi-Darvish, M. (2006). Effects of fracture boundary conditions on matrix-fracture transfer shape factor. *Transport in Porous Media*, **64**, 51-71.

Hassanzadeh, H., Pooladi-Darvish, M. and Atabay, S. (2009). Shape factor in the drawdown solution for well testing of dual-porosity systems. *Advances in Water Resources*, **32**, 1652-1663.

IPCC (2005). IPCC special report on carbon capture and storage. *Prepared by Working Group III of the Intergovernmental Panel on Climate Change* [Metz, B. et al. eds.], Cambridge University Press, Cambridge, UK and New York, USA.

Jaeger, J.C., Cook, N.G.W. and Zimmerman, R. (2007). *Fundamentals of rock mechanics*. 4th edition. John Wiley & Sons, New York.

Jessen, K., Tang, G-Q. and Kovscek, A.R. (2008). Laboratory and simulation investigation of enhanced coalbed methane recovery by gas injection. *Transport in Porous Media*, **73**, 141-159.

Jing, L. and Hudson, J. A. (2002). Numerical methods in rock mechanics. *International Journal of Rock Mechanics and Mining Sciences*, **39**(4), 409-427.

Karacan, C.Ö. (2007). Swelling-induced volumetric strains internal to a stressed coal associated with CO_2 adsorption. *International Journal of Coal Geology*, **72**, 209-220.

Karimi-Fard, M., Durlofsky, L.J. and Aziz, K. (2004). An efficient discrete-fracture model applicable for general-purpose reservoir simulators. *Society of Petroleum Engineers Journal*, **9**(2), 227-236.

Kelemen, S.R. and Kwiatek, L.M. (2009). Physical properties of selected block Argonne Premium bituminous coal related to CO_2, CH_4, and N_2 adsorption. *International Journal of Coal Geology*, **77**, 2-9.

King, G.R., Ertekin, T. and Schwerer, F.C. (1986). Numerical simulation of the transient behaviour of coal-seam degasification wells. *Society of Petroleum Engineers Formation Evaluation*, **1**(2), 165-183.

Koenig, R.A. and Stubbs, P.B. (1986). Interference testing of a coalbed methane reservoir. *In Proceedings of the 1986 SPE Unconventional Gas Technology Symposium*, 18-21 May,

Louisville, Kentucky.

Krooss, B.M., van Bergen, F., Gensterblum, Y., Siemons, N., Pagnier, H.J.M. and David, P. (2002). High-pressure methane and carbon dioxide adsorption on dry and moisture-equilibrated Pennsylvanian coals. *International Journal of Coal Geology*, **51**, 69-92.

Kwak, T.Y. and Mansoori, G.A. (1986). Van der Waals mixing rules for cubic equations of state. Applications for supercritical fluid extraction modelling. *Chemical Engineering Science*, **41**(5), 1303-1309.

Larsen, J.W. (2004). The effects of dissolved CO_2 on coal structure and properties. *International Journal of Coal Geology*, **57**, 63-70.

Law, D.H-S., van der Meer, L.G.H. and Gunter, W.D. (2002). Numerical simulator comparison study for enhanced coalbed methane recovery processes, part I: pure carbon dioxide injection. *In Proceedings of the 2002 SPE Gas Technology Symposium*, 30 April-2 May, Calgary, Canada.

Lemmonier, P. and Bourbiaux, B. (2010). Simulation of naturally fractured reservoirs. State of the art. Part 2 – matrix-fracture transfers and typical features of numerical studies. *Oil and Gas Science and Technology*, **65**, 263-286.

Levine, J.R. (1996). Model study of the influence of matrix shrinkage on absolute permeability of coal bed reservoirs. In: Gayer, R. and Harris, I., eds. *Coalbed Methane and Coal Geology*, Geological Society Special Publication No. 109, London, 197-212.

Levy, J.H., Day, S.J. and Killingley, J.S. (1997). Methane capacities of Bowen Basin coals related to coal properties. *Fuel*, **76**, 813-819.

Li, D., Liu, Q., Weniger, P., Gensterblum, Y., Busch, A. and Kroos, B.M. (2010). High-pressure sorption isotherms and sorption kinetics of CH_4 and CO_2 on coals. *Fuel*, **89**, 569-580.

Li, J., Liu, D., Yao, Y., Cai, Y. and Chen, Y. (2013). Evaluation and modeling of gas permeability changes in anthracite coals. *Fuel*, **111**, 606-612.

Liu, S., Harpalani, S. and Pillalamarry, M. (2012). Laboratory measurement and modeling of coal permeability with continued methane production: part 2 – modeling results. *Fuel*, **94**, 117-124.

Long, J. C. S., Remer, J.S., Wilson, C.R. and Witherspoon, P.A. (1982). Porous media equivalents for networks of discontinuous fractures. *Water Resources Research*, **18**(3), 645-658.

Lucas, K. (1980). *Phase equilibria and fluid properties in the chemical industry*. Dechema, Frankfurt.

Lucas, K. (1981). Pressure dependence of the viscosity of liquids – a simple estimate. *Chemie Ingenieur Technik*, **53**(12), 959-960.

Ma, D. and Shao, M. (2008). Simulating infiltration into stony soils with a dual-porosity model. *European Journal of Soil Science*, **59**(5), 950-959.

Marrero, T.R. and Mason, E.A. (1972). Gaseous diffusion coefficients. *Journal of Physical and Chemical Reference Data*, **1**(1), 3-118.

Masoudian, M.S., Airey, D.W. and El-Zein, A. (2013). A chemo-poro-mechanical model for sequestration of carbon dioxide in coalbeds. *Géotechnique*, **63**(3), 235-243.

Masoudian, M.S., Airey, D.W. and El-Zein, A. (2014). Experimental investigations on the effect of CO_2 on mechanics of coal. *International Journal of Coal Geology*, **128-129**, 12-23.

Mazumder, S. and Wolf, K.H. (2008). Differential swelling and permeability change of coal in response to CO_2 injection for ECBM. *International Journal of Coal Geology*, **74**, 123-138.

Meng, Z. and Li, G. (2013). Experimental research on the permeability of high-rank coal under a varying stress and its influencing factors. *Engineering Geology*, **162**, 108-117.

Milewska-Duda, J., Duda, J., Nodzeñski, A. and Lakatos, J. (2000). Absorption and adsorption of methane and carbon dioxide in hard coal and active carbon. *Langmuir*, **16**, 5458-5466.

Min, K-B., Rutqvist, J., Tsang, C-F. and Jing, L. (2004). Stress-dependent permeability of fractured rock masses: a numerical study. *International Journal of Rock Mechanics and Mining Sciences*, **41**, 1191-1210.

National Research Council (1996). *Rock fractures and fluid flow: contemporary understanding and applications*. National Academies Press, Washington, D.C., 551.

Nelson, R.A. (2001). *Geologic analysis of naturally fractured reservoirs*. 2nd edition. Gulf Publishing Company, Houston.

Ottiger, S., Pini, R., Storti, G., and Mazzotti, M. (2008). Competitive adsorption equilibria of CO_2 and CH_4 on a dry coal. *Adsorption*, **14**, 539-556.

Ozdemir, E. (2009). Modeling of coal bed methane (CBM) production and CO_2 sequestration in coal seams. *International Journal of Coal Geology*,

Palmer, I. and Mansoori, J. (1998). How permeability depends on stress and pore pressure in coalbeds: A new model. *Society of Petroleum Engineers Reservoir Evaluation and Engineering*, **1**(6), 539-544.

Pan, Z. and Connell, L.D. (2007). A theoretical model for gas adsorption-induced coal swelling. *International Journal of Coal Geology*, **69**, 243-252.

Pan, Z., Connell, L.D., Camilleri, M. and Connelly, L. (2010). Effects of matrix moisture on gas diffusion and flow in coal. *Fuel*, **89**, 3207-3217.

Pan, Z. and Connell, L.D. (2012). Modelling permeability for coal reservoirs: a review of analytical models and testing data. *International Journal of Coal Geology*, **92**, 1-44.

Pashin, J.C. (2008). Coal as a petroleum source rock and reservoir rock. In Suárez-Ruiz, I. et al. eds. *Applied coal petrology: the role of petrology in coal utilization*, Academic Press, Amsterdam, The Netherlands, pp 227-262.

Pekot, L.J. and Reeves, S.R. (2002). *Modeling coal matrix shrinkage and differential swelling with CO_2 injection for enhanced coalbed methane recovery and carbon sequestration applications*. US DOE Topical Report, Contract No. DE-FC26-00NT40924.

Peng, D-Y. and Robinson, D.B. (1976). A new two-constant equation of state. *Industrial and Engineering Chemistry Fundamentals*, **15**(1), 59-64.

Pini, R., Ottiger, S., Burlini, L., Storti, G. and Mazzotti, M. (2009). Role of adsorption and swelling on the dynamics of gas injection in coal. *Journal of Geophysical Research*, **114**, B04203.

Pini, R., Storti, G. and Mazzotti, M. (2011). A model for enhanced coalbed methane recovery aimed at carbon dioxide storage. *Adsorption*, **17**(5), 889-900.

Poling, B.E., Prausnitz, J.M. and O'Connell, J.P. (2001). *The properties of gases and liquids*. 5th edition. McGraw-Hill, New York.

Qu, H., Liu, J., Chen, Z., Wang, J., Pan, Z., Connell, L. and Elsworth, D. (2012). Complex evolution of coal permeability during CO_2 injection under variable temperatures. *International Journal of Greenhouse Gas Control*, **9**, 281-293.

Redlich, O. and Kwong, J.N.S. (1949). On the thermodynamics of solutions. V: An equation of state. Fugacities of gaseous solutions. *Chemical Reviews*, **44**(1), 233-244.

Reid, R.C., Prausnitz, J.M. and Sherwood, T.K. (1977). *The properties of gases and liquids*. 3rd Edition. McGraw-Hill, New York.

Reiss, L.H. (1980). *The reservoir engineering aspects of fractured formations*, Gulf Publishing Company, Houston, Texas.

Robertson, E.P. and Christiansen, R.L. (2006). A permeability model for coal and other fractured, sorptive-elastic media. *Society of Petroleum Engineers Journal*, **13**(3), 314-324.

Rock, P.A. (1983). *Chemical thermodynamics*. University Science Books, Sausalito, California.

Rodrigues, C.F. and Lemos de Sousa, L. (2002). The measurement of coal porosity with different gases. *International Journal of Coal Geology*, **48**, 245-251.

Rouquerol, J., Avnir, D., Fairbridge, C.W., Everett, D.H., Haynes, J.H., Pernicone, N., Ramsay, J.D.F., Sing, K.S.W. and Unger, K.K. (1994). Recommendations for the characterization of porous solids. *Pure and Applied Chemistry*, **66**(8), 1739-1758.

Samardzioska, T. and Popov, V. (2005). Numerical comparison of the equivalent continuum, non-homogeneous and dual porosity models for flow and transport in fractured porous media. *Advances in Water Resources*, **28**, 235-255.

Scherer, G.W. (1986). Dilation of porous glass. *Journal of the American Ceramic Society*, **69**(6), 473–480.

Schwartz, F. W., Smith, L. and Crowe, A.S. (1983). A stochastic analysis of macroscopic dispersion in fractured media. *Water Resources Research*, **19**(5), 1253-1265.

Seidle, J. (2011). *Fundamentals of coalbed methane reservoir engineering*. PennWell Corporation, Tulsa, Oklahoma.

Seto, C.J., Jessen, K. and Orr Jr, F.M. (2009). A multicomponent, two-phase-flow model for CO_2 storage and enhanced coalbed-methane recovery. *Society of Petroleum Engineers Journal*,

14(1), 30-40.

Shen, J., Qin, Y., Wang, G.X., Fu, X., Wei, C. and Lei, B. (2011). Relative permeabilities of gas and water for different rank coals. *International Journal of Coal Geology*, **86**, 266-275.

Shi, J-Q. and Durucan, S. (2004). Drawdown induced changes in permeability of coalbeds: A new interpretation of the reservoir response to primary recovery. *Transport in Porous Media*, **56**(1), 1-16.

Shi, J-Q. and Durucan, S. (2005). Gas storage and flow in coalbed reservoirs: implementation of a bidisperse pore model for gas diffusion in coal matrix. *SPE Reservoir Evaluation & Engineering*, **8**(2), 169-175.

Shi, J-Q., Mazumder, S., Wolf, K-H. and Durucan, S. (2008). Competitive methane desorption by supercritical CO_2 injection in coal. *Transport in Porous Media*, **75**, 35-54.

Šimůnek, J. and van Genuchten, M.T. (2008). Modeling nonequilibrium flow and transport processes using HYDRUS. *Vadose Zone Journal*, **7**(2), 782-797.

Sing, K.S.W., Everett, D.H., Haul, R., Moscou, L., Pierotti, R.A., Rouquérol, J. and Siemieniewska, T. (1982). Reporting physisorption data for gas/solid systems. *Pure & Applied Chemistry*, **54**(11), 2201-2218.

Singhal, B.B.S. and Gupta, R.P. (2010). *Applied hydrogeology of fractured rocks*. 2nd edition. Kluwer Academic Publishers, Dordrecht, The Netherlands.

Soave, G. (1972). Equilibrium constants from a modified Redlich–Kwong equation of state. *Chemical Engineering Science*, **27**, 1197–1203.

Somerton, W.H., Söylemezoğlu, I.M. and Dudley, R.C. (1975). Effect of stress on permeability of coal. *International Journal of Rock Mechanics and Mining Sciences & Geomechanics Abstracts*, **12**, 129-145.

Speight, J.G. (2012). *The chemistry and technology of coal*. 3rd edition. CRC Press, Boca Raton, Florida.

Spitzer, Z. (1981). Mercury porosimetry and its application to the analysis of coal pore structure. *Powder Technology*, **29**(1), 177-186.

Skawiński, R. Considerations referring to coal swelling accompanying the sorption of gases and water. *Archives of Mining Sciences*, **44**, 425-434.

Su, G.J. (1949). Modified law of corresponding states for real gases. *Industrial and Engineering Chemistry*, **38**(8), 803-806.

Sudicky, E.A. and Frind, E.O. (1982). Contaminant transport in fractured porous media: analytical solutions for a system of parallel fractures. *Water Resources Research*, **18**(6), 1634-1642.

Takahashi, S. (1974). Preparation of a generalized chart for the diffusion coefficients of gases at high pressures. *Japanese Journal of Chemical Engineering*, **7**(6), 417-420.

Talebian, M., Al-Khoury, R. and Sluys, L.J. (2012). A computational model for coupled

multiphysics processes of CO2 sequestration in fractured porous media. *Advances in Water Resources*, **59**, 238-255.

Thararoop, P., Karpyn, Z.T., Ertekin, T. (2012). Development of a multi-mechanistic, dual-porosity, dual-permeability, numerical flow model for coalbed methane reservoirs. *Journal of Natural Gas Science and Engineering*, **8**, 121-131.

Therrien, R. and Sudicky, E.A. (1996). Three-dimensional analysis of variably-saturated flow and solute transport in discretely-fractured porous media. *Journal of Contaminant Hydrology*, **23**, 1-44.

Tsotsis, T.T., Patel, H., Najafi, B.F., Racherla, D., Knackstedt, M.A. and Sahimi, M. (2004). Overview of laboratory and modeling studies of carbon dioxide sequestration in coal beds. *Industrial & Engineering Chemistry Research*, **43**, 2887-2901.

van Bergen, F., Pagnier, H. and Krzystolik, P. (2006). Field experiment of enhanced coalbed methane-CO2 in the upper Silesian basin of Poland. *Environmental Geosciences*, **13**(3), 201-224.

Wang, F.Y., Zhu, Z.H., Massarotto, P. and Rudolph, V. (2007). Mass transfer in coal seams for CO_2 sequestration. *American Institute of Chemical Engineers Journal*, **53**(4), 1028-1049.

Warren, J.E. and Root, P.J. (1963). The behaviour of naturally fractured reservoirs. *Society of Petroleum Engineers Journal*, **3**(3), 245-255.

Wei, Y.S. and Sadus, R.J. (2000). Equations of state for the calculation of fluid-phase equilibria. *American Institute of Chemical Engineers Journal*, **46**(1), 169-196.

Wei, X.R., Wang, G.X., Massarotto, P., Golding, S.D. and Rudolph, V. (2007a). Numerical simulation of multicomponent gas diffusion and flow in coals for CO_2 enhanced coalbed methane recovery. *Chemical Engineering Science*, **62**, 4193-4203.

Wei, X.R., Wang, G.X., Massarotto, P., Golding, S.D. and Rudolph, V. (2007b). A review on recent advances in the numerical simulation for coalbed-methane-recovery process. *Society of Petroleum Engineers Journal*, **10**(6), 657-666.

White, C.M., Smith, D.H., Jones, K.L., Goodman, A.L., Jikich, S.A., LaCount, R.B., DuBose, S.B., Ozdemir, E., Morsi, B,I. and Schroeder, K.T. (2005). Sequestration of carbon dioxide in coal with enhanced coalbed methane recovery – a review. *Energy and Fuels*, **19**(3), 659-724.

Wolf, K.H., Hijman, R., Barzandji, O. and Bruining, J. (1999). Laboratory experiments and simulations on the environmentally friendly improvement of CBM-production by carbon dioxide injection. *In Proceedings of the 1999 Coalbed Methane Symposium*, 3-7 May, Tuscaloosa, Alabama, 279-290.

Wu, Y.S., Liu, H.H. and Bodvarsson, G.S. (2004). A triple-continuum approach for modeling flow and transport processes in fractured rock. *Journal of Contaminant Hydrology*, **73**, 145-179.

Wu, Y., Liu, J., Chen, Z., Elsworth, D. and Pone, D. (2011). A dual poroelastic model for CO_2-enhanced coalbed methane recovery. *International Journal of Coal Geology*, **86**, 177-189.

Zhang, H., Liu, J. and Elsworth, D. (2008). How sorption-induced matrix deformation affects gas flow in coal seams: a new FE model. *International Journal of Rock Mechanics & Mining Sciences*, **45**, 1226-1236.

Zhou, F., Hussain, F. and Cinar, Y. (2013). Injecting pure N_2 and CO_2 to coal for enhanced coalbed methane: experimental observations and numerical simulation. *International Journal of Coal Geology*, **116-117**, 53-62.

Zhu, J., Jessen, K., Kovscek, A.R. and Orr Jr, F.M. (2003). Analytical theory of coalbed methane recovery by gas injection. *Society of Petroleum Engineers Journal*, **8**(4), 371-379.

3

Theoretical Formulation

3.1   Introduction

A theoretical formulation for the coupled hydraulic, chemical and deformation behaviour of fractured rock is described in this chapter. Chemical behaviour has been divided between the dissolved chemicals in the water phase and gas chemicals, which form a phase in their own right, i.e. the gas phase. The fractured rock is considered to have a dual porosity, dual permeability structure consisting of a fracture network and porous rock matrix. Each pore scale is treated as a continuum over the domain having properties that represent those of the discrete pore regions. The formulations for the fracture and matrix continua are handled separately where appropriate, and interact with each other under the influence of a mass exchange process. The governing equations for the flow of the liquid and gas phases/components have been derived using a mass balance approach.

The governing equations for coupled thermal, hydraulic and aqueous chemical behaviour have been covered in detail elsewhere (e.g. Thomas and He, 1998; Cleall, 1998; Seetharam, 2003; Sedighi, 2011; Thomas et al., 2012). In addition, the governing equations for the reactive transport of multicomponent gas in a single porosity geo-material have

been presented by Masum (2012), under the assumption of an ideal gas at relatively low pressures. Sink/source terms were linked to an external geochemical model to include the effects of geochemical reactions between gas components and other components/phases.

The formulation presented in this chapter considers the behaviour of non-ideal gas mixtures at high pressure in fractured rock. This is of relevance to applications such as the geological sequestration of carbon dioxide and enhanced coal bed methane recovery.

General aspects of the theoretical formulation are presented in section 3.2, including an introduction to the approach adopted to define the fracture and matrix continua in this work, in addition to the basic assumptions and the primary variables of the formulation. The governing equations describing liquid water transfer in the fracture network and matrix blocks are presented in section 3.3, based on the principle of mass conservation.

In section 3.4, the governing equation for multicomponent reactive gas transport in a dual porosity, dual permeability porous medium is derived. This is followed in section 3.5 by the corresponding derivation of the governing equation for multicomponent dissolved chemical transport. A non-equilibrium approach adopted to deal with reactions between gas and solid phases (i.e. adsorption/desorption) is presented. The general flux of a chemical component includes advective, dispersive and diffusive flux components.

A deformation model is presented in section 3.6 that describes the changes in the porosity and permeability in a fractured rock due to high pressure reactive gas flow. The effects of various physical and chemical mechanisms of deformation are considered. Although the model has been developed for particular applications related to gas flow in coal, the underlying concept is generally applicable to other types of fractured rock.

Finally, a summary of the theoretical formulation is presented in section 3.7.

3.2   Theoretical Formulation – General Aspects

Fractured rocks are highly heterogeneous geo-materials, consisting of a natural fracture network that divides the rock into a large number of interconnected porous matrix blocks. Following the discussion in chapter 2, practical limitations in computational resources

mean that these features can usually only be explicitly modelled at a small scale in sparsely fractured rocks (Pruess and Narasimhan, 1985; Painter, 2005). To overcome this, the dual porosity, dual permeability formulation developed in this work is based on the following key assumptions:

i. The distinct fracture and matrix pore regions present in a fractured rock are treated as homogenous continua, which overlap across the domain and have separate material properties.

ii. Mass exchange, i.e. the flow interactions between the fracture and matrix pore regions, is described by including coupling terms in the governing transport equations for the fracture and matrix continua.

Each continuum is considered to be a three-phase system, consisting of a solid skeleton, pore water and pore gas. Appropriate material properties are assigned in each continuum that produce the overall behaviour equivalent to that observed in the respective pore regions in a fractured rock. Nonetheless, it is important to recognise the main limitations in relation to the development and application of dual porosity, dual permeability models, namely:

i. The complex geometry of the fracture network may be poorly translated to the continuum scale (Arnold et al., 2000). This may limit the formulation to rock with a well-connected, uniformly spaced and continuous fracture network, such as that present in most coals (King et al., 1986).

ii. It can be difficult to obtain reliable estimates of the material properties in each continuum, since characterisation tests often do not (or cannot) make a distinction between the pore regions (Schwartz et al., 2000).

iii. The accuracy of dual continua models may be highly sensitive to the definition of the mass exchange terms (Samardzioska and Popov, 2005). As far as possible, these coupling terms should therefore be developed in terms of measureable parameters, for example fracture spacing, and clearly defined processes, for example advection and diffusion.

Based on the first two limitations given above, it is important to clearly define how the

material properties in each continuum are defined in this formulation. The matrix continuum is assigned the properties of the un-fractured rock, as indicated in Figure 3.1. However, the properties of the rock in the local region of a fracture can be much more complex, and fractures are not necessarily clear flow conduits. Open fractures can be partially or completely blocked by infilling minerals such as carbonates, quartz and clays (Ward, 2002). In addition, the presence of a fracture may have altered the properties of the porous rock matrix surrounding the discontinuity. The extent of this altered zone is likely to be larger in softer rocks, such as coal, compared to harder rocks, such as granite. In this work, an attempt has been made to assign averaged properties to the fracture continuum that account for the presence of open fractures, mineral infillings and the altered rock matrix.

Each flow variable in the formulation has distinct fracture and matrix values at any analysis point in the domain. The dissolved and gas chemical concentrations are expressed as a vector of any number of chemical species in the system, with each species being treated as a primary variable in this formulation. The governing equations for water flow and chemical transport are therefore expressed in terms of six primary variables, as follows:

   i. Pore water pressure in the fractures (u_{lF}).

  ii. Pore water pressure in the matrix (u_{lM}).

 iii. Gas chemical concentrations in the fractures, e.g. for the ith component (c_{gF}^{i}), where i can be *1* to n_g components.

 iv. Gas chemical concentrations in the matrix (c_{gM}^{i}).

  v. Dissolved chemical concentrations (c_{dF}^{i}) in the fractures, where i can be *1* to n_d components.

 vi. Dissolved chemical concentrations in the matrix (c_{dM}^{i}).

The behaviour of the primary variables is included within a coupled hydro-gas-chemical formulation, and the principle of mass conservation is applied to govern the transport processes. Pore water flow is considered to be driven by gradients of total water potential and chemical transport is considered to be driven by the combined mechanisms of

advection, dispersion and diffusion. All of the governing equations are developed in a three-dimensional form.
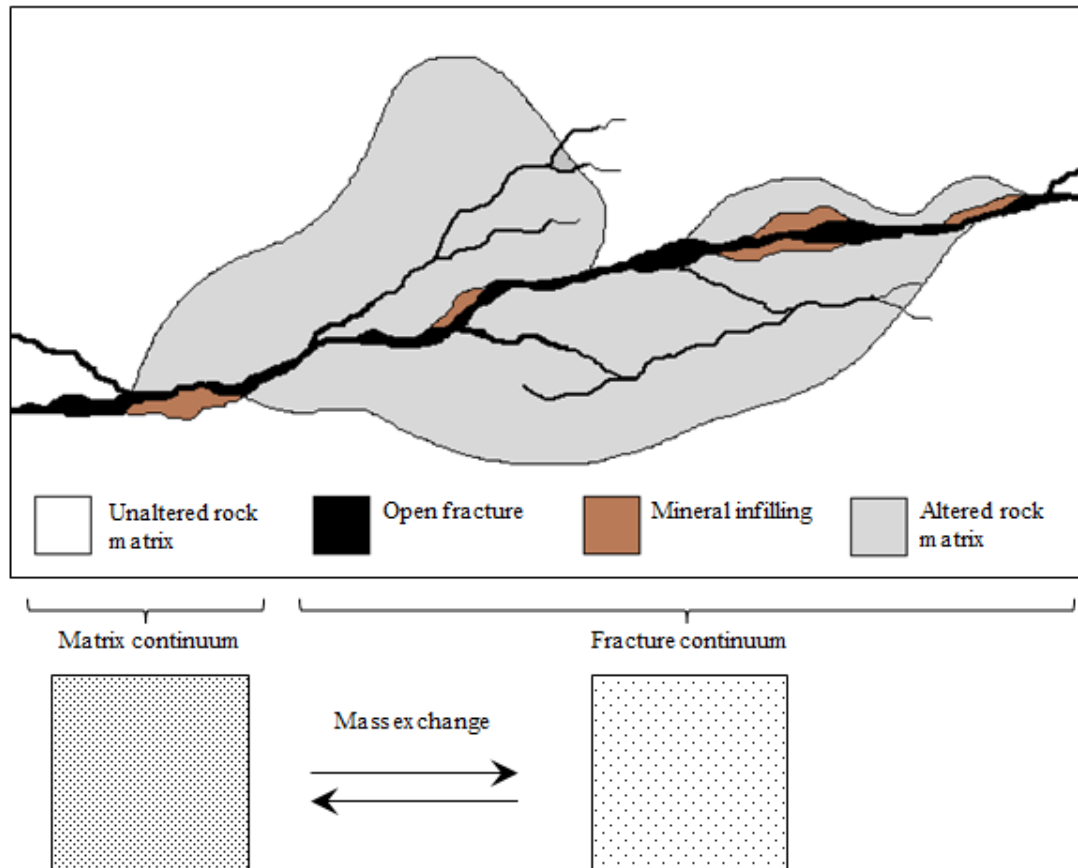
Figure 3.1 Schematic of a segment of a fractured rock, including open fractures, mineral infilling and a zone of altered rock matrix. Also depicted is how each of these features is considered in the dual continuum formulation presented in this work (concept has been adopted from Dershowitz et al, 2003).

Where possible, the formulations for pore water pressure, pore gas and dissolved chemicals are presented in a generalised form applicable to both the fracture and matrix primary variables. If a particular mechanism or process is only applicable in either the fracture or matrix continua, it is presented separately as appropriate. For example, in reactive geo-materials such as coal it may be assumed that the reactions between the pore fluid and solid phase take place only in the porous matrix blocks, which may contain in excess of 95% of the total internal surface area and therefore almost all of the potential adsorption sites (Shi and Durucan, 2005; Clarkson and Bustin, 2010). As a result, solid-gas chemical

interactions in the fractures can usually be neglected.

It is possible to view the formulation as a modular system, with various aspects that can be switched on or off. For example, the primary flow variables in the matrix can be switched off to reduce the formulation to that of a single porosity medium. In such a case, the reactions that previously applied only to the matrix continuum can be switched on in the new single porosity continuum. For consistency, all governing equations in this chapter are presented in the dual porosity form.

The formulation is developed for conditions in which high pressure reactive gas flow occurs in the absence of significant heat sources/sinks, i.e. close to isothermal conditions. Examples include carbon dioxide sequestration and enhanced coal bed methane recovery, for which gas injection typically occurs at significant depth and the formation temperature is assumed to remain stable. A number of studies have considered the non-isothermal processes involved in high pressure gas injection. Temperature fluctuations up to several Kelvin have been attributed to adiabatic (Joule-Thomson) cooling of injected gas, exothermic gas dissolution and heat sinks due to thermal expansion of the solid skeleton (Han et al., 2011; Zhu et al., 2011). In this work these thermal effects are not considered and the formulation is developed under the assumption of isothermal conditions.

3.3   Water Transfer

The principle of conservation of mass dictates that the temporal derivative of the water content is equal to the spatial gradient of the total liquid flux. By including a sink/source term allowing for mass exchange between the fracture and matrix continua this can be expressed mathematically as (Bear, 1993):

$$\frac{\partial(\theta_{l\alpha}\rho_l \delta V_\alpha)}{\partial t} = -\delta V_\alpha \nabla \cdot [\rho_l \mathbf{v}_{l\alpha}] - \delta V_\alpha \lambda \Gamma_l \qquad (3.1)$$

where $\theta_{l\alpha}$ is the volumetric water content in each continuum α, which becomes F to denote the fracture network and M to denote the matrix blocks, ρ_l is the density of water, δV_α is the incremental volume, t is the time, ∇ is the gradient operator, $\mathbf{v}_{l\alpha}$ is the velocity

of water and Γ_l is the sink/source term for mass exchange of water between the fracture and matrix continua. To comply with the principle of mass conservation, a loss of pore water in one continuum due to mass exchange must be balanced by an equal gain in pore water in the other continuum. The parameter λ is therefore defined as:

$$\begin{aligned}
\lambda = 1 \quad &if \quad \alpha = F \\
\lambda = -1 \quad &if \quad \alpha = M
\end{aligned} \tag{3.2}$$

In this work, the mechanical/deformation behaviour of each continuum is not expressed explicitly. Instead, the effect of deformation is included using relationships for porosity and permeability evolution. These relationships describe the changes in porosity and permeability due to a number of physical and chemical interactions between the pore gas and solid. Based on this simplification, the incremental volume, δV_α, can be removed from the temporal derivative in the left hand side of equation (3.1). Dividing both sides of equation (3.1) by δV_α then produces:

$$\frac{\partial(\theta_{l\alpha}\rho_l)}{\partial t} = -\nabla \cdot [\rho_l \mathbf{v}_{l\alpha}] - \lambda \Gamma_l \tag{3.3}$$

The volumetric water content of the fracture network and matrix blocks can be expressed in terms of the degree of saturation and the porosity in each continuum, given as:

$$\theta_{l\alpha} = n_\alpha S_{l\alpha} \tag{3.4}$$

where n_α is the porosity and $S_{l\alpha}$ is the degree of saturation.

Substitution of equation (3.4) into the left hand side of equation (3.3) yields:

$$\frac{\partial(n_\alpha S_{l\alpha}\rho_l)}{\partial t} = -\nabla \cdot [\rho_l \mathbf{v}_{l\alpha}] - \lambda \Gamma_l \tag{3.5}$$

In equation (3.5), the fracture porosity, n_F, is defined as the fraction of the total porosity associated with the fracture network. Likewise, the matrix porosity, n_M, is defined as the fraction of the total porosity associated with the matrix blocks. The total porosity, n_T, is then given by:

$$n_T = n_F + n_M \tag{3.6}$$

The fracture porosity, n_F, is obtained by weighting the local porosity of the fractured zone according to the proportion of the total volume it occupies. This can be expressed mathematically as:

$$n_F = w_f n_F^L \tag{3.7}$$

where n_F^L is the local fracture porosity given by the volume of the pores in the fractured zone divided by the total volume of the fractured zone, i.e. V_F^P / V_F^T. This value is 1.0 in a clear fracture, but may be less due to mineral infillings and any altered zone of rock surrounding the fracture, as illustrated in Figure 3.1. The parameter w_f is the volumetric weighting factor of the fractured rock, defined as (Gerke and van Genuchten, 1993a):

$$w_f = \frac{V_F^T}{V_T} \tag{3.8}$$

where V_F^T is the total volume of the fractured zone and V_T is the total volume of the rock.

Substituting equation (3.7) into equation (3.6) and rearranging gives n_M in terms of n_T, w_f and n_F^L, as:

$$n_M = n_T - w_f n_F^L \tag{3.9}$$

Therefore, provided appropriate values of n_T, w_f and n_F^L are available, the nature of the porosity in the fractured rock can be defined. Although measuring the total porosity n_T of a fractured rock via core analysis does not present a major challenge, it is more difficult to distinguish the fracture porosity from the matrix porosity (van Golf-Racht, 1982). Nonetheless, some field and laboratory techniques are available to estimate the fracture porosity, i.e. $w_f n_F^L$ (Singhal and Gupta, 2010).

The mechanisms that govern the water flux are discussed in the following section.

3.3.1 Mechanism of Water Transfer

In this study, the total water potential is considered as the sum of the potentials due to pressure and gravitational heads, which will be referred to as the hydraulic head. Darcy's law (Darcy, 1856), which provides a definition of the rate of flow of water due to a hydraulic head, has been applied to describe the water flux in each continuum (Bear, 1979):

$$\mathbf{v}_{l\alpha} = -k_{l\alpha}\left[\nabla\left(\frac{u_{l\alpha}}{\rho_l g}\right) + \nabla z\right] \tag{3.10}$$

where g is the gravitational acceleration, z is the elevation and $k_{l\alpha}$ is the unsaturated hydraulic conductivity, which is given by (Bear and Verruijt, 1987):

$$k_{l\alpha} = \frac{K_\alpha K_{rl\alpha}\rho_l g}{\mu_{l\alpha}} \tag{3.11}$$

where K_α is the intrinsic permeability, $K_{rl\alpha}$ is the relative permeability to water and $\mu_{l\alpha}$ is the absolute water viscosity.

The volumetric weighting factor, w_f, defined in equation (3.8) is used to convert the intrinsic permeabilities of the fracture network and matrix blocks from the local scale to the continuum scale, as (Gerke and van Genuchten, 1993a):

$$K_F = w_f K_F^L \tag{3.12}$$

$$K_M = \left(1 - w_f\right)K_M^L \tag{3.13}$$

where K_F^L and K_M^L are the intrinsic permeabilities in the fracture and matrix pore regions at the local scale.

Inspection of equation (3.11) shows that the unsaturated hydraulic conductivity is influenced by a number of factors. These include the intrinsic permeability K_α, which depends on the porous media structure and fabric, the relative water permeability $K_{rl\alpha}$, which depends on the degree of saturation, and the absolute viscosity $\mu_{l\alpha}$, which depends on the pore fluid properties. Turbulence is also known to influence the unsaturated hydraulic conductivity. However, it is not included in this work because the formulation is

applied in relation to flow in coal, which is usually considered to be a laminar process (Harpalani and Chen, 1997).

The relative permeability of an unsaturated porous medium to water can be evaluated from the degree of saturation, giving:

$$K_{rl\alpha} = K_{l\alpha}(S_{l\alpha})$$ (3.14)

Variation of the absolute viscosity in equation (3.11) with temperature T is included using the relationship presented by Kaye and Laby (1973), which is valid for $273K < T < 373K$:

$$\mu_{l\alpha}(T) = 661.2(T - 229)^{-1.562} \times 10^{-3} \pm 0.5\% \quad \text{(Pa s)}$$ (3.15)

3.3.2   Mass Exchange Term for Water

The mass conservation equation (3.1) introduced the water flow through an unsaturated dual porosity medium as two distinct equations coupled by a sink/source term, i.e. Γ_l. This coupling term accounts for the exchange of pore water between the fracture network and porous matrix blocks. In this section the mechanisms that control the magnitude and rate of the mass exchange process are discussed and the mass exchange term is derived.

It has been suggested that a quasi-steady state pore water pressure distribution prevails in the matrix blocks. This allows the water exchange rate to be expressed as a linear function of the difference between the average pore water pressures in the fracture and matrix continua (Barenblatt et al., 1960; Warren and Root, 1963), giving:

$$\Gamma_l = \sigma_l(u_{lF} - u_{lM})$$ (3.16)

where σ_l is the first order mass exchange coefficient for water.

The mass exchange coefficient is related to the geometry of the matrix blocks and certain material parameters of the solid skeleton and pore water. The assumption of quasi-steady state flow in the matrix is strictly only valid for relatively large times after the pore water pressure front has reached the centre of the matrix blocks (Gerke and van Genuchten,

1993a; 1993b). At earlier exchange times, quasi-steady state models provide only an approximation of what is initially an unsteady state process (Lemmonier and Bourbiaux, 2010). A number of authors have presented time-dependent mass exchange coefficients to account for differences in the mass exchange process at small and large times (e.g. Dykhuizen, 1990; Chang et al. 1993; Zimmerman et al. 1993), as discussed in chapter 2. Gerke and van Genuchten (1993b) concluded that the quasi-steady state assumption is a practical approach considering the high level of uncertainty generally involved in the modelling of flow processes in dual porosity media. The mass exchange terms derived in this work have therefore been developed under the assumption of quasi-steady state flow in the matrix blocks.

Despite providing the major flow conduits in a dual porosity system, the fractures make a very small contribution to the total volume compared to the porous matrix blocks (Gilman and Kazemi, 1983). It follows that mass exchange between the pore regions is governed by some combination of the hydraulic properties in each region. In this study the first order mass exchange coefficient for water is developed using the arithmetic mean approach (Gerke and van Genuchten, 1993b), given as:

$$\sigma_l = \Omega_l \frac{\beta}{l^2}\left(\frac{k_l^A}{\rho_l g}\right) \tag{3.17}$$

where Ω_l is an empirical coefficient equal to 0.4, β is a factor related to the geometry of the matrix blocks and l is the typical thickness of a matrix block, which is essentially equal to the fracture spacing. The parameter k_l^A is the arithmetic mean of the hydraulic conductivities in the fracture and matrix continua, evaluated as (Gerke and van Genuchten, 1993b):

$$k_l^A = \frac{k_{lF} + k_{lM}}{2} \tag{3.18}$$

A summary of values for β in equation (3.17) is presented by Hassanzadeh et al. (2009). The suggested values are typically in the order of π^2 for one-dimensional mass exchange, $2\pi^2$ for two-dimensional mass exchange and $3\pi^2$ for three-dimensional mass exchange, with variations due to different geometrical configurations of the matrix blocks.

Substitution of equation (3.17) into equation (3.16) produces:

$$\Gamma_l = \Omega_l \frac{\beta}{l^2} \left(\frac{k_l^A}{\rho_l g} \right) (u_{lF} - u_{lM})$$

(3.19)

The similarity between equations (3.19) and the first term on the right hand side of equation (3.10) reflects that the mass exchange process for water may be viewed as a process controlled by advection between the two continua.

3.3.3   Governing Differential Equations for Water Transfer

The mechanism of water transfer through the fracture network and porous matrix blocks was presented in section 3.3.1. This was followed in section 3.3.2 by a definition of the sink/source term for mass exchange of water between the two continua. A time splitting approach, i.e. the sequential non-iterative approach (SNIA), is used for coupling the transport model and mass exchange model (Steefel and MacQuarrie, 1996). In the SNIA adopted, the water transport equations are solved and the resulting pore water pressures for each node are passed to the mass exchange module. The pore water pressures in each continuum are then adjusted to account for mass exchange. This procedure is repeated in each time step after the convergence criterion has been met. More details of the numerical implementation of the SNIA are provided in the following chapter.

In this section, the equations for flow and mass exchange are included in the equation of mass conservation for water transfer, i.e. equation (3.5). The resulting equation is expanded in terms of the primary variables to give the governing equations for water transfer in a dual porosity medium.

The left hand side of equation (3.5) may be rewritten to give:

$$\rho_l n_\alpha \frac{\partial S_{l\alpha}}{\partial t} = -\nabla \cdot [\rho_l \mathbf{v}_{l\alpha}] - \lambda \Gamma_l$$

(3.20)

The rate of change of porosity is not explicitly considered in equation (3.20). Instead, the porosities of the fracture and matrix continua are modified in each time step to account for a number of physical and chemical interactions between the pore gas and solid, using the

relationships detailed in section 3.6.

An important characteristic of fractured rock is that the fracture porosity is relatively free draining, i.e. has a lower water retention, compared to the matrix porosity (Gerke and van Genuchten, 1993b). With regards to the first term in equation (3.20), it is therefore important to define the water retention behaviour appropriately in each continuum. The rate of change of the degree of water saturation is affected by the difference between pore water pressure and pore gas pressure, known as matric suction (Mitchell and Soga, 2005), and changes to the void ratio caused by deformation (Gallipoli et al., 2003). The effect of the latter is less clearly defined and is often neglected in the study of fairly rigid porous media (Mašín, 2010), such as coal. The degree of saturation in each continuum can then be defined as follows:

$$S_{l\alpha} = S_{l\alpha}(s_\alpha) \tag{3.21}$$

where the parameter s_α is the value of matric suction and can be defined mathematically as (Mitchell and Soga, 2005):

$$s_\alpha = u_{g\alpha} - u_{l\alpha} \tag{3.22}$$

where $u_{g\alpha}$ is the pore gas pressure.

Application of the real gas law allows the pore gas pressure to be expressed in terms of the sum of the partial pressures of the individual gas components, giving:

$$u_{g\alpha} = Z_\alpha RT \sum_{j=1}^{n_g} c_{g\alpha}^j \tag{3.23}$$

where R is the universal gas constant. The compressibility factor, Z_α, will be addressed in section 3.4.1.

Substitution of equation (3.23) into equation (3.22) yields:

$$s_\alpha = Z_\alpha RT \sum_{j=1}^{n_g} c_{g\alpha}^j - u_{l\alpha} \tag{3.24}$$

Based on equation (3.24), the dependence of the degree of saturation on suction can be expressed in terms of the primary variables as:

$$\frac{\partial S_{l\alpha}}{\partial t} = RT \frac{\partial S_{l\alpha}}{\partial s_\alpha} \sum_{j=1}^{n_g} \frac{\partial Z_\alpha c_{g\alpha}^j}{\partial t} - \frac{\partial S_{l\alpha}}{\partial s_\alpha} \frac{\partial u_{l\alpha}}{\partial t} \tag{3.25}$$

Expanding the first term on the right hand side of equation (3.25) gives:

$$RT \frac{\partial S_{l\alpha}}{\partial s_\alpha} \sum_{j=1}^{n_g} \frac{\partial Z_\alpha c_{g\alpha}^j}{\partial t} = RT \frac{\partial S_{l\alpha}}{\partial s_\alpha} \sum_{j=1}^{n_g} \left(Z_\alpha \frac{\partial c_{g\alpha}^j}{\partial t} + c_{g\alpha}^j \frac{\partial Z_\alpha}{\partial t} \right) \tag{3.26}$$

In this work, the value of Z_α is updated in each time step using the equation of state (EoS) proposed by Peng and Robinson (1976), details of which are provided in section 3.4.1. The temporal derivative of the compressibility factor, i.e. $\partial Z_\alpha / \partial t$, has not been considered. Equation (3.26) therefore reduces to:

$$RT \frac{\partial S_{l\alpha}}{\partial s_\alpha} \sum_{j=1}^{n_g} \frac{\partial Z_\alpha c_{g\alpha}^j}{\partial t} = \sum_{j=1}^{n_g} \left(Z_\alpha RT \frac{\partial S_{l\alpha}}{\partial s_\alpha} \right) \frac{\partial c_{g\alpha}^j}{\partial t} \tag{3.27}$$

Substitution of equation (3.27) into equation (3.25) gives:

$$\frac{\partial S_{l\alpha}}{\partial t} = \sum_{j=1}^{n_g} \left(Z_\alpha RT \frac{\partial S_{l\alpha}}{\partial s_\alpha} \right) \frac{\partial c_{g\alpha}^j}{\partial t} - \frac{\partial S_{l\alpha}}{\partial s_\alpha} \frac{\partial u_{l\alpha}}{\partial t} \tag{3.28}$$

The partial derivative of the degree of saturation with respect to suction in equation (3.28) is analogous to the specific water capacity. This term is defined using the gradient of the curve produced by the van Genuchten (1980) relationship for water retention, given as:

$$S_{l\alpha} = \frac{1}{n_\alpha} \left[\theta_{lr\alpha} + \frac{\theta_{ls\alpha} - \theta_{lr\alpha}}{(1 + |\alpha_\alpha s_\alpha|^{m_\alpha})^{1-1/m_\alpha}} \right] \tag{3.29}$$

where $\theta_{lr\alpha}$ and $\theta_{ls\alpha}$ are the residual and saturated volumetric water contents, respectively, and α_α and m_α are constants based on the water retention characteristics in each continuum.

The main constraint of using equation (3.29) in this dual porosity formulation is the lack of

experimental data that can be used to establish the various material constants. This is especially true for coal. Despite this, important features of dual porosity water retention behaviour presented by Gerke and van Genuchten (1993a) may be used to define appropriate water retention curves in each continuum.

Having defined the relationship between the degree of saturation and suction in both continua, substitution of equation (3.28) into the first term on the left hand side of equation (3.20) produces:

$$\left(-\rho_l n_\alpha \frac{\partial S_{l\alpha}}{\partial s_\alpha}\right)\frac{\partial u_{l\alpha}}{\partial t} + \sum_{j=1}^{n_g}\left(\rho_l n_\alpha Z_\alpha RT \frac{\partial S_{l\alpha}}{\partial s_\alpha}\right)\frac{\partial c_{g\alpha}^j}{\partial t} = -\nabla \cdot [\rho_l \mathbf{v}_{l\alpha}] - \lambda \Gamma_l \qquad (3.30)$$

Substituting $\mathbf{v_{l\alpha}}$ from equation (3.10), λ from equation (3.2) and Γ_l from equation (3.19) into the right hand side of equation (3.30) gives the governing equations for water transfer in a dual porosity medium. The governing equations can be represented in a simplified form as:

$$C_{ll,F}\frac{\partial u_{lF}}{\partial t} + \sum_{j=1}^{n_g} C_{lc_g,F}\frac{\partial c_{gF}^j}{\partial t} = \nabla \cdot \left[K_{ll,F}\nabla u_{lF}\right] + J_{l,F} + Q_{l,F}^{ex} \qquad (3.31)$$

$$C_{ll,M}\frac{\partial u_{lM}}{\partial t} + \sum_{j=1}^{n_g} C_{lc_g,M}\frac{\partial c_{gM}^j}{\partial t} = \nabla \cdot \left[K_{ll,M}\nabla u_{lM}\right] + J_{l,M} + Q_{l,M}^{ex} \qquad (3.32)$$

where in equation (3.31):

$$C_{ll,F} = -\rho_l n_F \frac{\partial S_{lF}}{\partial s_F} \qquad (3.33)$$

$$C_{lc_g,F} = \rho_l n_F Z_F RT \frac{\partial S_{lF}}{\partial s_F} \qquad (3.34)$$

$$K_{ll,F} = \frac{k_{lF}}{g} \qquad (3.35)$$

$$J_{l,F} = \rho_l \nabla \cdot (k_{lF}\nabla z) \qquad (3.36)$$

$$Q_{l,F}^{ex} = -\Omega_l \frac{\beta}{l^2}\left(\frac{k_l^A}{\rho_l g}\right)(u_{lF} - u_{lM}) \qquad (3.37)$$

and in equation (3.32):

$$C_{ll,M} = -\rho_l n_M \frac{\partial S_{lM}}{\partial s_M} \qquad (3.38)$$

$$C_{lc_g,M} = \rho_l n_M Z_M RT \frac{\partial S_{lM}}{\partial s_M} \qquad (3.39)$$

$$K_{ll,M} = \frac{k_{lM}}{g} \qquad (3.40)$$

$$J_{l,M} = \rho_l \nabla \cdot (k_{lM} \nabla z) \qquad (3.41)$$

$$Q_{l,M}^{ex} = \Omega_l \frac{\beta}{l^2} \left(\frac{k_l^A}{\rho_l g} \right) (u_{lF} - u_{lM}) \qquad (3.42)$$

3.4   Reactive Transport of Multicomponent Gas

In this formulation pore gas is considered as a mixture of gas species, which collectively form the "gas phase". The reactive transport of multicomponent gas is described in terms of a set of chemical components which are assigned the properties of the chemical species. A chemical component is a mathematical representation that is used to describe the behaviour of each species (Bethke, 1996). The governing equations for multicomponent reactive gas transport have been derived based upon the principle of conservation of mass, which is expressed over a representative incremental volume for each component in the fracture and matrix continua.

The fracture and matrix continua are each regarded as a reactive three phase system, comprised of solid, pore water and pore gas phases. Sink/source terms are presented to calculate the loss/gain of component i due to phase change, chemical reactions and inter-porosity mass exchange. Following the work of Masum (2012) for a single porosity medium, the principle of conservation of mass for the ith gas component in an unsaturated dual porosity medium can be expressed mathematically as:

$$\frac{\partial \left(\theta_{g\alpha} c_{g\alpha}^i \delta V_\alpha \right)}{\partial t} = -\delta V_\alpha \nabla \cdot \mathbf{J}_{\mathbf{g}\alpha}^i - \delta V_\alpha \lambda \Gamma_g^i - \delta V_\alpha R_{g\alpha}^i \qquad (3.43)$$

where $\theta_{g\alpha}$ is the volumetric gas content in continua α, $R_{g\alpha}^i$ represents the sink/source term for geochemical reactions, $\mathbf{J}_{\mathbf{g}\alpha}^i$ is the total flux of gas component i and Γ_g^i is the sink/source

term for mass exchange of gas component i between the fracture and matrix continua.

Gas dissolution in the liquid phase is not considered here as it is assumed that the majority of gas is either free gas or adsorbed gas in the solid phase. The sink/source term $R_{g\alpha}^i$ can therefore be expressed as (Bear and Bachmat, 1990):

$$R_{g\alpha}^i = \rho_s \frac{\partial s_{g\alpha}^i}{\partial t} \tag{3.44}$$

where ρ_s is the density of the solid phase and $s_{g\alpha}^i$ is the adsorbed amount of the ith gas component in the solid phase.

The volumetric gas content of the fracture network and matrix blocks can be expressed in terms of the degree of gas saturation and porosity in each continuum, given as:

$$\theta_{g\alpha} = n_\alpha S_{g\alpha} \tag{3.45}$$

where n_α is the porosity defined in equations (3.7) and (3.9), and $S_{g\alpha}$ is the degree of gas saturation.

As explained in section 3.3, the effect of deformation is included in this formulation using relationships for porosity and permeability changes due to physical and chemical interactions between the pore gas and solid. As a result of this simplification, the incremental volume, δV_α, can be removed from equation (3.43). Substitution of equation (3.44) and equation (3.45) into equation (3.43) and rearranging then produces:

$$\frac{\partial\left(n_\alpha S_{g\alpha} c_{g\alpha}^i\right)}{\partial t} + \rho_s \frac{\partial s_{g\alpha}^i}{\partial t} = -\nabla \cdot \mathbf{J}_{\mathbf{g}\alpha}^i - \lambda \Gamma_g^i \tag{3.46}$$

Before the terms of equation (3.46) are expanded, it is appropriate that the following section characterises the some of the relevant properties of multicomponent gas at high pressure.

3.4.1 Gas Properties at High Pressure

The major properties of gas species and their mixtures are highly dependent on pressure,

temperature and composition (Hagoort, 1988). For example, the phase change of species such as carbon dioxide to supercritical state at high pressure has a significant impact on its behaviour. The key gas properties related to the developed formulation are:

    i. Bulk gas compressibility.
   ii. Bulk gas viscosity.
  iii. Gas diffusion coefficients.

Appropriate relationships to describe the above properties as functions of pressure, temperature and composition have been adopted in this formulation, which are described in this section.

In this work, real gas compressibility behaviour is considered using an equation of state (EoS), which provides a relationship between pressure, volume and temperature (Dake, 1983). Deviations of the behaviour of real gases from ideal gas behaviour are expressed by the compressibility factor Z, which is defined as the ratio of the actual molar volume $V_{m\alpha}^{Re}$ to the ideal gas molar volume $V_{m\alpha}^{Id}$ (Rojey et al., 1994). The EoS proposed by Peng and Robinson (1976) is used because it is widely applied, accurate and yet requires little input data (Wei and Sadus, 2000). The Peng and Robinson EoS expresses the bulk gas pressure as (Peng and Robinson, 1976):

$$u_{g\alpha} = \frac{RT}{V_{m\alpha}^{Id} - b_{m\alpha}} - \frac{a_{m\alpha}}{V_{m\alpha}^{Id\,2} + 2b_{m\alpha}V_{m\alpha}^{Id} - b_{m\alpha}^{\,2}} \qquad (3.47)$$

where $b_{m\alpha}$ is the effective volume of the molecules contained in one mole of bulk gas and $a_{m\alpha}$ is a coefficient accounting for the intermolecular interactions in the mixture.

The parameters $a_{m\alpha}$ and $b_{m\alpha}$ are defined using the van der Waals mixing rules (Kwak and Mansoori, 1986), producing:

$$a_{m\alpha} = \sum_{i=1}^{n_g} \sum_{j=1}^{n_g} X_{g\alpha}^i X_{g\alpha}^j \left(1 - \kappa_\alpha^{ij}\right) \sqrt{a_{m\alpha}^i a_{m\alpha}^j} \qquad (3.48)$$

$$b_{m\alpha} = \sum_{i=1}^{n_g} X_{g\alpha}^i b_{m\alpha}^i \qquad (3.49)$$

where $X_{g\alpha}^i$ is the gas mole fraction of component i, κ_α^{ij} is a binary gas interaction parameter to account for interactions between the molecules of components i and j and $a_{m\alpha}^i$ and $b_{m\alpha}^i$ are the pure component factors for intermolecular interactions and effective volume, respectively. Values of κ_α^{ij} for a wide range of gas species can be found in Wang et al. (2011).

Real gas behaviour may approach the conceptual model of an ideal gas at low pressures and high temperatures. For an ideal gas the factors $a_{m\alpha}$ and $b_{m\alpha}$ are zero and equation (3.47) reduces to the ideal gas law. However, the ideal gas law does not accurately describe the pressure-volume-temperature characteristics of gas under the majority of conditions (Dake, 1983). The factors $a_{m\alpha}$ and $b_{m\alpha}$ are therefore used to form the coefficients of a cubic equation in terms of the compressibility factor Z, which can be solved accordingly. Further details of this procedure can be found in Chen et al. (2006).

Gas mixture viscosity has been included using the semi-empirical model proposed by Chung et al. (1988). This model has been selected because absolute deviations of no more than 9% for non-polar gas mixtures at high pressure were reported, which is suitably accurate for the present formulation. The model is based upon the kinetic theory of gases in combination with empirical density-dependent functions to include the behaviour of dense gas mixtures, giving an expression of the form (Chung et al., 1998):

$$\mu_{g\alpha} = 0.1\left[f\left(\mu_{g\alpha}^0\right) + \mu_{g\alpha}^D\right] \tag{3.50}$$

where $\mu_{g\alpha}$ is the absolute gas viscosity, $f\left(\mu_{g\alpha}^0\right)$ is a function of the gas mixture viscosity at low pressure and $\mu_{g\alpha}^D$ is a further adjustment for dense gases. The parameters in equation (3.50) are fully expanded in Chung et al. (1988).

Experimental data for high pressure gas diffusivity is fairly limited, and as a result only a few approximation methods have been developed (e.g. Takahasi, 1974). In this formulation, a simple empirical model suggested in Reid et al. (1977) is adopted. According to this approach, the gas diffusion coefficients can be presented as:

$$D_{g\alpha}^i = \frac{D_g^{0i}\rho_g^0}{\rho_{g\alpha}} \tag{3.51}$$

where D_g^{0i} is a reference value for the diffusion coefficient obtained experimentally at a certain temperature at a low gas density of ρ_g^0, and $D_{g\alpha}^i$ is the diffusion coefficient at the same temperature but at a higher gas density of $\rho_{g\alpha}$.

3.4.2   Mechanisms of Gas Transport

In general the total flux the ith pore gas component, i.e. $\mathbf{J}_{g\alpha}^i$ in equation (3.46), includes contributions from advective and diffusive transport mechanisms (Bird et al., 1960; Mason et al., 1967), given as:

$$\mathbf{J}_{g\alpha}^i = \mathbf{J}_{gAdv\alpha}^i + \mathbf{J}_{gDif\alpha}^i \tag{3.52}$$

where $\mathbf{J}_{gAdv\alpha}^i$ and $\mathbf{J}_{gDif\alpha}^i$ are the advective and diffusive components of flux, respectively. These components will be discussed separately in the following sections. Dispersion is not considered in equation (3.52) since it is assumed to be negligible in comparison to diffusion. This is reasonable since gas diffusivity is high, with diffusion coefficients being around four orders of magnitude greater than those of solutes (Cussler, 1997).

3.4.2.1   Advection

Advective transport of pore gas is driven by gradients of the bulk gas pressure and is generally expressed using Darcy's law (Webb, 2006). Multicomponent gas advection is a non-segregative transport mechanism because it does not cause separation of the mixture into individual components (Mason et al., 1967). As a result the advective flux of the ith pore gas component is proportional to the mole fraction of that component in the bulk gas phase, giving:

$$\mathbf{J}_{gAdv\alpha}^i = X_{g\alpha}^i \mathbf{J}_{gAdv\alpha} \tag{3.53}$$

where $\mathbf{J}_{gAdv\alpha}$ is the bulk gas advective flux. According to Darcy's law the bulk advective flux is expressed as:

$$\mathbf{J_{gAdv\alpha}} = c_{g\alpha}^T \mathbf{v_{g\alpha}} \tag{3.54}$$

where $\mathbf{v_{g\alpha}}$ is the bulk gas velocity and $c_{g\alpha}^T$ is the total gas concentration, which is equal to the sum of the concentrations of the individual gas components, giving:

$$c_{g\alpha}^T = \sum_{j=1}^{n_g} c_{g\alpha}^j \tag{3.55}$$

Based on equation (3.10), Darcy's law for bulk gas flow in unsaturated porous media can be expressed as:

$$\mathbf{v_{g\alpha}} = -k_{g\alpha} \left[\nabla \left(\frac{u_{g\alpha}}{\rho_{g\alpha} g} \right) + \nabla z \right] \tag{3.56}$$

where $\mathbf{v_{g\alpha}}$ is the bulk gas velocity, z is the elevation and $k_{g\alpha}$ is the unsaturated gas conductivity, which is given by:

$$k_{g\alpha} = \frac{K_\alpha K_{rg\alpha} \rho_{g\alpha} g}{\mu_{g\alpha}} \tag{3.57}$$

where $K_{rg\alpha}$ is the relative permeability to gas.

Substitution of equations (3.23), (3.54) and (3.56) into equation (3.53) yields to final form of the advective flux for the ith gas component, given as:

$$\mathbf{J_{gAdv\alpha}^i} = -\frac{c_{g\alpha}^i k_{g\alpha} Z_\alpha RT}{\rho_{g\alpha} g} \sum_{j=1}^{n_g} \nabla c_{g\alpha}^j - c_{g\alpha}^i k_{g\alpha} \nabla z \tag{3.58}$$

3.4.2.2 Diffusion

The gas diffusive flux in equation (3.52) can involve a combination of the following diffusion processes in porous media (Bird et al., 1960; Cussler, 1997):

   i. Ordinary diffusion
  ii. Knudsen diffusion
 iii. Configurational diffusion
 iv. Pressure diffusion

    v. Forced diffusion

   vi. Thermal diffusion

Pressure diffusion is the movement of heavier molecules to high pressure regions and lighter molecules to low pressure regions (Amali and Rolston, 1993). This process is not considered in this work because the tendency of a gas mixture to separate under a pressure gradient is small enough to be neglected (Bird et al., 1960). The contribution of forced diffusion is only important in ionic systems subject to a local electrical field, and is thus not relevant in this work. Thermal diffusion describes the tendency of a component to diffuse due to thermal gradients. Since the present formulation is developed for isothermal conditions, this process is also not considered. The processes of ordinary, Knudsen and configurational diffusion will be described in the remainder of this section.

Ordinary diffusion describes the tendency of the species contained in a gas mixture to diffuse due to concentration gradients. A generalised form of Fick's law (Fick, 1855) proposed by Onsager (1945) can be used to describe the ordinary diffusion flux in a multicomponent system, which includes self-diffusion ($i = j$) and cross-diffusion ($i \neq j$). The self-diffusion coefficients are typically around an order of magnitude larger than cross-diffusion coefficients (Cussler, 1997). In the present work, only self-diffusion is considered and the ordinary diffusion flux for the ith gas component can be expressed using Fick's law as:

$$\mathrm{J}^{i}_{0\alpha} = -D^{i}_{g\alpha} \nabla c^{i}_{g\alpha} \tag{3.59}$$

where $\mathrm{J}^{i}_{0\alpha}$ is the ordinary diffusion flux and $D^{i}_{g\alpha}$ is the diffusion coefficient defined in equation (3.51).

Equation (3.59) is only valid for free fluid diffusion, and must be modified for applications in porous media. The free diffusion coefficient $D^{i}_{g\alpha}$ is therefore replaced by an effective diffusion coefficient $D^{i}_{ge\alpha}$ that considers the pore structure of the porous medium. Extending equation (3.59) for porous media yields:

$$D^{i}_{ge\alpha} = n_{\alpha} S_{g\alpha} \tau_{g\alpha} D^{i}_{g\alpha} \tag{3.60}$$

where $\tau_{g\alpha}$ is the gas tortuosity factor, which is calculated using the widely adopted Millington and Quirk (1961) model, given as (Scanlon et al., 1999):

$$\tau_{g\alpha} = \frac{\left(n_\alpha S_{g\alpha}\right)^{10/3}}{n_\alpha^2} \tag{3.61}$$

Substitution of equation (3.60) into equation (3.59) yields:

$$J_{0\alpha}^i = -n_\alpha S_{g\alpha} \tau_{g\alpha} D_{g\alpha}^i \nabla c_{g\alpha}^i \tag{3.62}$$

Knudsen diffusion takes place in very tight pores with dimensions that are similar in magnitude or smaller than the molecular mean free path length (Wu et al., 1998), and is therefore ignored in the fracture continuum, giving:

$$J_{KF}^i = 0 \tag{3.63}$$

where J_{KF}^i is the Knudsen diffusion flux in the fracture continuum.

In a Knudsen diffusion regime, the gas molecules only interact with the pore walls and intermolecular interactions can be neglected (Cussler, 1997). According to Mason and Malinauskas (1983), Knudsen diffusion can be described in a similar form to equation (3.62) as:

$$J_{KM}^i = -n_M S_{gM} D_{KM}^i \nabla c_{gM}^i \tag{3.64}$$

where J_{KM}^i is the Knudsen diffusion flux in the matrix continuum D_{KM}^i is the Knudsen diffusion coefficient.

The value of the Knudsen diffusion coefficient can be obtained as a function of certain properties of the pore space and diffusing species (Geankoplis, 1972). In cases where insufficient data is available to properly characterise the pore size distribution, Thorstenson and Pollock (1989) proposed a relationship between the Knudsen diffusion coefficient and Klinkenberg factor $b_{k\alpha}^i$, given as:

$$D_{KM}^i = \frac{K_{gM} b_{kM}^i}{\mu_{gM}^i} \tag{3.65}$$

Heid et al. (1950) and Jones (1972), among others, proposed empirical correlations between $b_{k\alpha}^i$ and $K_{g\alpha}$. These correlations relate to core tests on samples with permeabilities in the range of 1.0×10^{-19} to 1.0×10^{-12} m². In the case of fractured rock such as coal, which is relevant to the applications considered in this work, the matrix permeability may be considerably lower than 1.0×10^{-19} m² (Seidle, 2011). Therefore, the correlations proposed by Heid et al. (1950) and Jones (1972) are regarded as invalid in the scope of this work.

Javadpour et al. (2007) presented a relationship for $b_{k\alpha}^i$ in terms of the gas pressure, molecular mean free path length and mean pore radius. Freeman et al. (2011) expanded this relationship by employing a definition of the mean free path length from the kinetic theory of gases and approximating the mean pore radius using the expression of Karniadakis and Beskok (2001). In combination with equation (3.65), the resulting estimate of the Knudsen diffusion coefficient was given as:

$$D_{KM}^i = \frac{4K_{gM}}{2.81708\sqrt{K_{gM}/n_M}} \sqrt{\frac{\pi RT}{2M_g^i}} \tag{3.66}$$

where M_g^i is the molecular mass of the ith gas component.

The Knudsen diffusion flux is therefore described by equation (3.64) and equation (3.66).

Configurational diffusion can become important in very tight pores with dimensions approaching those of a single molecule (Webb, 2006), and is therefore ignored in the fracture continuum. It is strongly dependent on the size and shape of the gas molecule involved (Xiao and Wei, 1992). There is no widely accepted theoretical approach for configurational diffusion, although it can be included by specifying species dependent constrictivity factors, δ_{iM}, in equation (3.60) (Freeman et al., 2011), producing:

$$D_{geM}^i = n_M S_{gM} \tau_{gM} \delta_{iM} D_{gM}^i \tag{3.67}$$

Based on equation (3.67), the ordinary diffusion flux in the matrix continuum in equation (3.62) can be modified to include the effects of configurational diffusion, giving (Freeman et al., 2011):

$$J^i_{OM} = -n_M S_{gM} \tau_{gM} \delta_{iM} D^i_{gM} \nabla c^i_{gM} \qquad (3.68)$$

The constrictivity factor $(0.0 < \delta_{iM} \leq 1.0)$ accounts for the variable cross section of a pore in the direction of the concentration gradient. This is in contrast to the tortuosity factor, which reflects that the diffusion path is not necessarily parallel to the concentration gradient (van Brakel and Heertjes, 1974). Several empirical models are available for the constrictivity factor, such as those proposed by Beck and Schultz (1970) and Satterfield and Colton (1973).

It is appropriate to include the constrictivity factor in the ordinary diffusion flux following conclusions reached by Cui et al. (2004). They observed inconsistency between experimentally and theoretically derived macropore diffusivities for carbon dioxide, methane and nitrogen in coal. It was postulated that this inconsistency arose due to the macropore network being highly inter-connected by ultra-micropores that permeate the smaller carbon dioxide molecule, but block the slightly larger methane and nitrogen molecules. The role of constrictivity in this formulation is therefore to factor the magnitude of the ordinary diffusion flux in media such as coal.

Based on equation (3.64) and (3.67), the total diffusion flux for the ith gas component in each continuum is given by:

$$J^i_{\mathbf{gDifF}} = -n_F S_{gF} \tau_{gF} D^i_{gF} \nabla c^i_{gF} \qquad (3.69)$$

$$J^i_{\mathbf{gDifM}} = -n_M S_{gM} \left(\tau_{gM} \delta_{iM} D^i_{gM} + D^i_{KM} \right) \nabla c^i_{gM} \qquad (3.70)$$

The significance of diffusion in this dual porosity formulation is not limited to distinct transport mechanisms in the fracture and matrix continua. Diffusion also plays an important role in the sink/source term for non-equilibrium mass exchange. This is because mass exchange between the fracture and matrix continua may be treated as an advective-diffusive problem involving ordinary diffusion and configurational diffusion.

The sink/source terms due to mass exchange between the fracture and matrix continua and kinetic adsorption/desorption are the focus in the following sections.

3.4.3   Mass Exchange Term for Gas

Derivation of the mass exchange term for multicomponent pore gas follows that presented for pore water presented in section 3.3.2. The assumption of a quasi-steady state pore gas pressure distribution in the matrix blocks therefore applies, and the mass exchange process becomes a function of the averaged fracture and matrix pressures/concentrations. Unlike in the exchange of water, which was analogous to a purely advective process, the mass exchange term for pore gas presented here includes components due to both advection and diffusion. The resulting mass exchange term for the ith pore gas component is expressed as:

$$\Gamma_g^i = \sigma_{gAdv}\left(u_{gF} - u_{gM}\right) + \sigma_{gDif}^i\left(c_{gF}^i - c_{gM}^i\right) \tag{3.71}$$

where σ_{gAdv} is the first order mass exchange coefficient for gas advection and σ_{gDif}^i is the first order mass exchange coefficient for diffusion of the ith gas component.

An expression similar to equation (3.17) is used to obtain the mass exchange coefficient for gas advection, giving:

$$\sigma_{gAdv} = \frac{\beta}{l^2}\left(\frac{k_g^A}{\rho_g^A g}\right) \tag{3.72}$$

where the parameters k_g^A and ρ_g^A are the arithmetic means of the gas conductivities and gas densities in the fracture and matrix continua, respectively, evaluated as:

$$k_g^A = \frac{k_{gF} + k_{gM}}{2} \tag{3.73}$$

$$\rho_g^A = \frac{\rho_{gF} + \rho_{gM}}{2} \tag{3.74}$$

It is assumed that the diffusive flux of multicomponent pore gas exchange is an ordinary diffusion process. The mass exchange coefficient for gas diffusion is then given by:

$$\sigma_{gDif}^i = \frac{\beta D_{geM}^i}{l^2} \tag{3.75}$$

where D_{geM}^i is the effective diffusion coefficient defined in equation (3.67).

Substitution of equations (3.72) and (3.75) into equation (3.71) and replacing the pore gas pressures using equation (3.23) yields:

$$\Gamma_g^i = \frac{\beta}{l^2}\left(\frac{k_g^A}{\rho_g^A g}\right)\sum_{j=1}^{n_g}\left(Z_F RT c_{gF}^j - Z_M RT c_{gM}^j\right) + \frac{\beta D_{geM}^i}{l^2}\left(c_{gF}^i - c_{gM}^i\right) \tag{3.76}$$

3.4.4   Sink/Source Term for Adsorption/Desorption

An evaluation of the sink/source term for the adsorption/desorption, or retention, process in reactive media is presented in this section. These reactions are inherently dependent on the available surface area of the sorbent (solid phase) over which interactions with the sorbate (gas) can occur. In dual porosity media, the majority of this interface exists in the porous matrix blocks. For example, micropores in the matrix blocks of coal can account for in excess of 95% of the total internal surface area (Shi and Durucan, 2005; Clarkson and Bustin, 2010). It is therefore appropriate to only consider sorption in the matrix continuum, which for the ith gas component gives:

$$s_{gF}^i = 0 \tag{3.77}$$

Sorption in geo-materials can occur due to physical and chemical mechanisms, termed physi-sorption and chemi-sorption, respectively. Physi-sorption is characterised by the lack of chemical bonding between the sorbent and sorbate, and is usually described in terms of van der Waals interactions (Zangwill, 1988). Chemi-sorption involves the formation of a surface chemical bond between the sorbent and sorbate. Since this formulation does not attempt to distinguish between these mechanisms, the sorption process is consistently referred to as a reaction.

Gas retention behaviour at the coal surface can be treated as an equilibrium or kinetic reaction. Equilibrium sorption is usually included using a retardation factor in the storage

term of the mass balance equation. Formulations of this type do not explicitly consider the loss/gain of free gas due to adsorption/desorption. Instead, the effect of sorption is considered to retard the advance of the component considered (Bear and Verruijt, 1987). The present work considers sorption as a kinetic reaction, which is formulated in a similar manner to that presented in sections 3.3.2 and 3.4.3 for mass exchange between the fracture and matrix continua. This yields a first-order kinetics equation for the ith gas component of the form (King et al., 1986):

$$\frac{ds_{gM}^i}{dt} = \tau_r^i \big(s_{g\infty M}^i - s_{gM}^i\big) \tag{3.78}$$

where τ_r^i is the sorption rate and $s_{g\infty M}^i$ is the adsorbed amount at equilibrium with the free gas pressure in the matrix continua.

The reaction described in equation (3.78) is driven by the difference between the equilibrium and actual adsorbed amounts, and takes place at a rate controlled by the sorption rate. Values for the sorption rate are usually chosen based on a literature review (e.g. Pini et al. 2011), or by history matching the results of adsorption/desorption kinetics experiments (e.g. Busch et al., 2004).

Applying the method of separation of variables to equation (3.78) gives:

$$\int_{s_{gM}^i\big|_n}^{s_{gM}^i\big|_{n+1}} \frac{1}{s_{g\infty M}^i - s_{gM}^i} ds_{gM}^i = \int_{t|_n}^{t|_{n+1}} \tau_r^i dt \tag{3.79}$$

where n denotes the time step.

Performing the integral in equation (3.79) over a time step Δt and assessing the equilibrium adsorbed amount at the midinterval produces:

$$ln\left(\frac{s_{g\infty M}^i\big|_{n+1/2} - s_{gM}^i\big|_n}{s_{g\infty M}^i\big|_{n+1/2} - s_{gM}^i\big|_{n+1}}\right) = \tau_r^i \Delta t \tag{3.80}$$

The time stepping scheme used to define the terms in equation (3.80) is discussed in

greater detail in the next chapter. Rearrangement of equation (3.80) gives:

$$s_{gM}^i\big|_{n+1} = s_{g\infty M}^i\big|_{n+1/2}\left(1 - e^{-\tau_r^i \Delta t}\right) + s_{gM}^i\big|_n e^{-\tau_r^i \Delta t} \tag{3.81}$$

A wide range of theoretical and empirical isotherm models are available to describe the absolute amount of gas adsorbed in a reactive solid for a given gas pressure under isothermal conditions. White et al. (2005) discuss the development and validity of these models. In this formulation the extended Langmuir isotherm is used and the equilibrium adsorbed amount of the ith gas component is given by the following expression (Ruthven, 1984; Yang, 1987):

$$s_{g\infty M}^i = \frac{n_L^i b_L^i Z_M R T c_{gM}^i}{1 + Z_M R T \sum_{j=1}^{n_g} b_L^j c_{gM}^j} \tag{3.82}$$

where n_L^i is the Langmuir capacity and b_L^i is the reciprocal of the Langmuir pressure.

Equations (3.81) and (3.82) together define the kinetic adsorption/desorption reaction included in the multicomponent pore gas transport formulation.

3.4.5 Governing Equations for Gas Transport

The transport mechanisms of multicomponent pore gas in a dual porosity medium were described in section 3.4.2 in terms of advective and diffusive fluxes. In sections 3.4.3 and 3.4.4 the sink/source terms in the mass balance equation (3.46) were developed. A sequential non-iterative approach (SNIA) is used to couple the transport model with the mass exchange and reactions modules (e.g. Steefel and MacQuarrie, 1996). Details of the numerical implementation of the SNIA are provided in the following chapter. In the SNIA the gas transport equations are solved and the resulting concentrations for each node are first passed to the mass exchange module and then to the reactions module.

The governing equations for multicomponent pore gas transport are now assembled using the components of the equation given in the previous sections. The final equations are presented in terms of the primary variables.

Expanding the first term on the left hand side of equation (3.46) produces:

$$\frac{\partial\left(n_\alpha S_{g\alpha} c_{g\alpha}^i\right)}{\partial t} = n_\alpha S_{g\alpha} \frac{\partial c_{g\alpha}^i}{\partial t} + n_\alpha c_{g\alpha}^i \frac{\partial S_{g\alpha}}{\partial t} \tag{3.83}$$

The rate of change of porosity is not explicitly considered in equation (3.83). Instead, the porosity of the fracture and matrix continua is modified in each time step to account for a number of physical and chemical interactions between the pore gas and solid, using the relationships detailed in section 3.6.

It is useful to express the second term on the right hand side of equation (3.83) in terms of the temporal derivative of the degree of water saturation, as:

$$n_\alpha c_{g\alpha}^i \frac{\partial S_{g\alpha}}{\partial t} = -n_\alpha c_{g\alpha}^i \frac{\partial S_{l\alpha}}{\partial t} \tag{3.84}$$

Substitution of equation (3.28) into equation (3.84) then yields:

$$-n_\alpha c_{g\alpha}^i \frac{\partial S_{l\alpha}}{\partial t} = \left(n_\alpha c_{g\alpha}^i \frac{\partial S_{l\alpha}}{\partial s_\alpha}\right)\frac{\partial u_{l\alpha}}{\partial t} + \sum_{j=1}^{n_g}\left(-n_\alpha c_{g\alpha}^i Z_\alpha RT \frac{\partial S_{l\alpha}}{\partial s_\alpha}\right)\frac{\partial c_{g\alpha}^j}{\partial t} \tag{3.85}$$

Equation (3.85) can then be substituted into the right hand side of equation (3.83), yielding:

$$\frac{\partial\left(n_\alpha S_{g\alpha} c_{g\alpha}^i\right)}{\partial t} = \left(n_\alpha c_{g\alpha}^i \frac{\partial S_{l\alpha}}{\partial s_\alpha}\right)\frac{\partial u_{l\alpha}}{\partial t} \\ + \sum_{j=1}^{n_g}\left(\delta_{ij} n_\alpha S_{g\alpha} - n_\alpha c_{g\alpha}^i Z_\alpha RT \frac{\partial S_{l\alpha}}{\partial s_\alpha}\right)\frac{\partial c_{g\alpha}^j}{\partial t} \tag{3.86}$$

where δ_{ij} is the Kronecker delta, which is equal to 1 if $i = j$ and otherwise equal to 0.

Substituting equation (3.86) into the mass balance equation (3.46) gives:

$$\left(n_\alpha c_{g\alpha}^i \frac{\partial S_{l\alpha}}{\partial s_\alpha}\right)\frac{\partial u_{l\alpha}}{\partial t} + \sum_{j=1}^{n_g}\left(\delta_{ij} n_\alpha S_{g\alpha} - n_\alpha c_{g\alpha}^i Z_\alpha RT \frac{\partial S_{l\alpha}}{\partial s_\alpha}\right)\frac{\partial c_{g\alpha}^j}{\partial t} \\ + \rho_s \frac{\partial s_{g\alpha}^i}{\partial t} = -\nabla \cdot \mathbf{J_{g\alpha}^i} - \lambda \Gamma_g^i \tag{3.87}$$

Substituting equations (3.58), (3.69) and (3.70) into equation (3.52), and grouping similar terms, produces:

$$\mathbf{J}_{\mathbf{g}F}^{i} = -\sum_{j=1}^{n_g} \left[\frac{c_{gF}^i k_{gF} Z_F RT}{\rho_{gF} g} + \delta_{ij} n_F S_{gF} \tau_{gF} D_{gF}^i \right] \nabla c_{gF}^j - c_{gF}^i k_{gF} \nabla z \tag{3.88}$$

$$\mathbf{J}_{\mathbf{g}M}^{i} = -\sum_{j=1}^{n_g} \left[\frac{c_{gM}^i k_{gM} Z_M RT}{\rho_{gM} g} + \delta_{ij} n_M S_{gM} \left(\tau_{gM} \delta_{iM} D_{gM}^i + D_{KM}^i \right) \right] \nabla c_{gM}^j$$
$$- c_{gM}^i k_{gM} \nabla z \tag{3.89}$$

Substituting the total pore gas fluxes from equations (3.88) and (3.89), λ from equation (3.2) and Γ_g^i from equation (3.76) into the right hand side of equation (3.87), whilst taking account of equation (3.77), gives the governing equations for multicomponent pore gas transport in a dual porosity medium. The governing equations can be represented in a simplified form as:

$$C_{c_g l,F} \frac{\partial u_{lF}}{\partial t} + \sum_{j=1}^{n_g} C_{c_g c_g,F} \frac{\partial c_{gF}^j}{\partial t} = \nabla \cdot \left[\sum_{j=1}^{n_g} K_{c_g c_g,F} \nabla c_{gF}^j \right] + J_{c_g,F} + Q_{c_g,F}^{ex} \tag{3.90}$$

$$C_{c_g l,M} \frac{\partial u_{lM}}{\partial t} + \sum_{j=1}^{n_g} C_{c_g c_g,M} \frac{\partial c_{gM}^j}{\partial t} + C_{c_g s_g,M} \frac{\partial s_{gM}^i}{\partial t}$$
$$= \nabla \cdot \left[\sum_{j=1}^{n_g} K_{c_g c_g,M} \nabla c_{gM}^j \right] + J_{c_g,M} + Q_{c_g,M}^{ex} \tag{3.91}$$

where in equation (3.90):

$$C_{c_g l,F} = n_F c_{gF}^i \frac{\partial S_{lF}}{\partial s_F} \tag{3.92}$$

$$C_{c_g c_g,F} = \delta_{ij} n_F S_{gF} - n_F c_{gF}^i Z_F RT \frac{\partial S_{lF}}{\partial s_F} \tag{3.93}$$

$$K_{c_g c_g,F} = \frac{c_{gF}^i k_{gF} Z_F RT}{\rho_{gF} g} + \delta_{ij} n_F S_{gF} \tau_{gF} D_{gF}^i \tag{3.94}$$

$$J_{c_g,F} = \nabla \cdot \left(c_{gF}^i k_{gF} \nabla z \right) \tag{3.95}$$

$$Q_{c_g,F}^{ex} = -\frac{\beta}{l^2} \left(\frac{k_g^A}{\rho_g^A g} \right) \sum_{j=1}^{n_g} \left(Z_F RT c_{gF}^j - Z_M RT c_{gM}^j \right) - \frac{\beta D_{geM}^i}{l^2} \left(c_{gF}^i - c_{gM}^i \right) \tag{3.96}$$

and in equation (3.91):

$$C_{c_g l,M} = n_M c_{gM}^i \frac{\partial S_{lM}}{\partial s_M} \tag{3.97}$$

$$C_{c_g c_g,M} = \delta_{ij} n_M S_{gM} - n_M c_{gM}^i Z_M RT \frac{\partial S_{lM}}{\partial s_M} \tag{3.98}$$

$$C_{c_g s_g,M} = \rho_s \tag{3.99}$$

$$K_{c_g c_g,M} = \frac{c_{gM}^i k_{gM} Z_M RT}{\rho_{gM} g} + \delta_{ij} n_M S_{gM} \left(\tau_{gM} \delta_{iM} D_{gM}^i + D_{KM}^i \right) \tag{3.100}$$

$$J_{c_g,M} = \nabla \cdot \left(c_{gM}^i k_{gM} \nabla z \right) \tag{3.101}$$

$$Q_{c_g,M}^{ex} = \frac{\beta}{l^2} \left(\frac{k_g^A}{\rho_g^A g} \right) \sum_{j=1}^{n_g} \left(Z_F RT c_{gF}^j - Z_M RT c_{gM}^j \right) + \frac{\beta D_{geM}^i}{l^2} \left(c_{gF}^i - c_{gM}^i \right) \tag{3.102}$$

3.5   Reactive Transport of Multicomponent Chemicals in Liquid Phase

The governing equations for multicomponent dissolved chemical transport have been derived based upon the principle of conservation of mass. The equations are developed based on the terms for mass accumulation, net flux and sinks/sources introduced in the previous section for the reactive transport of multicomponent gas. Sink/source terms are included to calculate the loss/gain of each component in the fracture and matrix equations due to mass exchange between the continua and geochemical reactions. The latter are not discussed in any depth in this formulation, but have been detailed elsewhere (Seetharam, 2003; Sedighi, 2011).

Following the work of Seetharam (2003) and Sedighi (2011) for a single porosity medium, the principle of conservation of mass for the ith dissolved chemical component in an unsaturated dual porosity medium can be expressed mathematically as:

$$\frac{\partial \left(\theta_{l\alpha} c_{d\alpha}^i \delta V_\alpha \right)}{\partial t} + \frac{\partial \left(\theta_{l\alpha} R_{d\alpha}^i \delta V_\alpha \right)}{\partial t} = -\delta V_\alpha \nabla \cdot \mathbf{J}_{\mathbf{d}\alpha}^i - \delta V_\alpha \lambda \Gamma_d^i \tag{3.103}$$

where $R_{d\alpha}^i$ represents the sink/source term for geochemical reactions, $\mathbf{J}_{\mathbf{d}\alpha}^i$ is the total flux of dissolved chemical component i and Γ_d^i is the sink/source term for mass exchange of

dissolved chemical component i between the fracture and matrix continua.

Substituting equation (3.4) into the left hand side of equation (3.103) and removing the incremental volume, δV_α, as in sections 3.3 and 3.4 gives:

$$\frac{\partial\left(n_\alpha S_{l\alpha} c_{d\alpha}^i\right)}{\partial t} + \frac{\partial\left(n_\alpha S_{l\alpha} R_{d\alpha}^i\right)}{\partial t} = -\nabla \cdot \mathbf{J}_{d\alpha}^i - \lambda \Gamma_d^i \tag{3.104}$$

where n_α is the porosity defined in equations (3.7) and (3.9).

The major transport mechanisms for multicomponent dissolved gas are described in the following section.

3.5.1   Mechanisms of Dissolved Chemical Transport

In general the total flux the ith dissolved chemical component $\mathbf{J}_{d\alpha}^i$ in equation (3.104) includes contributions from advective, dispersive and diffusive transport mechanisms (Bear and Verruijt, 1978), given as:

$$\mathbf{J}_{d\alpha}^i = \mathbf{J}_{dAdv\alpha}^i + \mathbf{J}_{dDis\alpha}^i + \mathbf{J}_{dDif\alpha}^i \tag{3.105}$$

where $\mathbf{J}_{dAdv\alpha}^i$, $\mathbf{J}_{dDis\alpha}^i$ and $\mathbf{J}_{dDif\alpha}^i$ are the advective, dispersive and diffusive components of flux, respectively. The combination of the dispersive and diffusive components is referred to as hydrodynamic dispersion. These components will be discussed separately in the following sections.

3.5.1.1   Advection

Dissolved chemicals are translated at the rate of movement of the bulk water phase (Steefel, 2008). The rate of advection is therefore obtained using the average linear velocity of the bulk water, given in equation (3.10). The advective flux for the ith dissolved chemical component can then be expressed as (Bear and Verruijt, 1987, Seetharam, 2003, Sedighi, 2011):

$$\mathbf{J}_{dAdv\alpha}^i = c_{d\alpha}^i \mathbf{v}_{l\alpha} \tag{3.106}$$

Substitution for $\mathbf{v}_{l\alpha}$ from equation (3.10) gives the following final form of the advective flux component:

$$\mathrm{J}^{i}_{\mathbf{dAdv}\alpha} = -c^{i}_{d\alpha}k_{l\alpha}\left[\nabla\left(\frac{u_{l\alpha}}{\rho_{l}g}\right) + \nabla z\right] \tag{3.107}$$

3.5.1.2 Dispersion

Irregular pore geometry causes local deviations from the average pore water velocity, resulting in a mixing process termed mechanical dispersion that is macroscopically similar to diffusive transport (Steefel, 2008). Mechanical dispersion causes longitudinal spreading of the solute in the direction of flow and transverse spreading of the solute perpendicular to the direction of flow (Sedighi, 2011). These processes can be described in terms of averaged and measureable quantities as (Bear and Verruijt, 1987):

$$\mathrm{J}^{i}_{\mathbf{dDis}\alpha} = -n_{\alpha}S_{l\alpha}D^{i}_{m\alpha}\nabla c^{i}_{d\alpha} \tag{3.108}$$

where $D^{i}_{m\alpha}$ is the coefficient of mechanical dispersion and can be expressed as a function of the average velocity (Pickens and Gillham, 1980):

$$D^{i}_{m\alpha} = \frac{\alpha_{T\alpha}|v_{l\alpha}|\delta_{ij}}{n_{\alpha}S_{l\alpha}} + (\alpha_{L\alpha} - \alpha_{T\alpha})\frac{v_{lx}v_{ly}}{n_{\alpha}S_{l\alpha}|v_{l\alpha}|} \tag{3.109}$$

where $\alpha_{T\alpha}$ and $\alpha_{L\alpha}$ are the coefficients of transverse and longitudinal dispersion, respectively, $|v_{\alpha}|$ is the absolute average advective velocity and $v_{lx\alpha}$ and $v_{ly\alpha}$ are the water velocities in the x and y spatial dimensions, respectively.

According to Therrien and Sudicky (1996), mechanical dispersion in the matrix blocks of a fractured rock is small in comparison to diffusion. It is therefore neglected in this formulation, giving:

$$\mathrm{J}^{i}_{\mathbf{dDis}F} = -n_{F}S_{lF}D^{i}_{mF}\nabla c^{i}_{dF} \tag{3.110}$$

$$\mathrm{J}^{i}_{\mathbf{dDis}M} = 0 \tag{3.111}$$

3.5.1.3 Diffusion

The process of molecular diffusion is the spreading of solute molecules in the fluid by virtue of their kinetic motion, even when the fluid is at rest (Crank, 1975). This diffusive flux is strictly proportional to gradients in chemical potential (Denbigh, 1981). In this work, as is usual in most practical applications, it is assumed to be proportional to gradients in concentration. Thermal diffusion has been shown to occur in the presence of temperature gradients (Lasaga, 1988; Sedighi, 2011; Thomas et al., 2012), although it is not considered here since the present formulation is developed under isothermal conditions.

The diffusive flux for multicomponent dissolved chemical transport can be obtained using Fick's law, as:

$$J_{dDif\alpha}^{i} = -n_{\alpha} S_{l\alpha} D_{de\alpha}^{i} \nabla c_{d\alpha}^{i} \qquad (3.112)$$

where $D_{de\alpha}^{i}$ is the effective molecular diffusion coefficient, which can be expressed in the same manner as equation (3.67) for pore gas, giving for the ith dissolved component:

$$D_{de\alpha}^{i} = n_{\alpha} S_{l\alpha} \tau_{l\alpha} \delta_{i\alpha} D_{d\alpha}^{i} \qquad (3.113)$$

where $\tau_{l\alpha}$ is the tortuosity factor and $D_{d\alpha}^{i}$ is the diffusion coefficient in free water.

3.5.2 Mass Exchange Term for Dissolved Chemicals

The sink/source term presented here for mass exchange of solutes between the fracture and matrix continua is conceptually identical to that for multicomponent pore gas detailed in section 3.4.3. Quasi-steady state concentration gradients are therefore assumed to prevail in the matrix at all times, and the exchange process is driven by advective and diffusive fluxes. The main difference is that the driving mechanism for mass exchange of solutes is the difference in the averaged bulk pore water pressure in the fracture and matrix continua. The resulting mass exchange term for the ith dissolved chemical component is expressed as:

$$\Gamma_d^i = \sigma_{dAdv}(u_{lF} - u_{lM}) + \sigma_{dDif}^i(c_{dF}^i - c_{dM}^i) \tag{3.114}$$

where σ_{dAdv} is the first order mass exchange coefficient for solute advection and σ_{dDif}^i is the first order mass exchange coefficient for diffusion of the ith dissolved chemical component.

By making an analogy with equations (3.72) and (3.75), equation (3.114) can be expanded to yield:

$$\Gamma_d^i = \frac{\beta}{l^2}\left(\frac{k_l^A}{\rho_l g}\right)(u_{lF} - u_{lM}) + \frac{\beta D_{deM}^i}{l^2}(c_{dF}^i - c_{dM}^i) \tag{3.115}$$

where the parameter k_l^A was defined in equation (3.18).

3.5.3   Governing Equations for Dissolved Chemical Transport

The transport mechanisms of multicomponent dissolved chemicals in a dual porosity medium were described in section 3.5.1 in terms of advective, dispersive and diffusive fluxes. This was followed in section 3.5.2 by a description of the sink/source term for mass exchange of solute between the fracture and matrix continua. The sink/source term for geochemical reactions in equation (3.104) is not expanded in this work, but is retained in the governing equations for generality.

As in section 3.4 for pore gas, the sequential non-iterative approach (SNIA) is used to couple the transport model with the mass exchange and reactions models (e.g. Steefel and MacQuarrie, 1996; Seetharam, 2008). Details of the numerical implementation of the SNIA are provided in the following chapter. A detailed discussion of the geochemical reactions included in the model is provided by Sedighi (2011).

Expanding the first term on the left hand side of equation (3.104) produces:

$$n_\alpha S_{l\alpha}\frac{\partial c_{d\alpha}^i}{\partial t} + n_\alpha c_{d\alpha}^i\frac{\partial S_{l\alpha}}{\partial t} + n_\alpha S_{l\alpha}\frac{\partial R_{d\alpha}^i}{\partial t} = -\nabla \cdot \mathbf{J}_{d\alpha}^i - \lambda\Gamma_d^i \tag{3.116}$$

The rate of change of porosity is not explicitly considered in equation (3.116). Instead, the

porosity of the fracture and matrix continua is modified in each time step to account for a number of physical and chemical interactions between the pore gas and solid, using the relationships detailed in section 3.6. The second term in equation (3.116) may be expanded through substitution of equation (3.28), as:

$$n_\alpha c_{d\alpha}^i \frac{\partial S_{l\alpha}}{\partial t} = \left(-n_\alpha c_{d\alpha}^i \frac{\partial S_{l\alpha}}{\partial s_\alpha}\right)\frac{\partial u_{l\alpha}}{\partial t} + \sum_{j=1}^{n_g}\left(n_\alpha c_{d\alpha}^i Z_\alpha RT \frac{\partial S_{l\alpha}}{\partial s_\alpha}\right)\frac{\partial c_{g\alpha}^j}{\partial t} \tag{3.117}$$

Substituting equation (3.117) into the left hand side of equation (3.116) gives:

$$\left(-n_\alpha c_{d\alpha}^i \frac{\partial S_{l\alpha}}{\partial s_\alpha}\right)\frac{\partial u_{l\alpha}}{\partial t} + \sum_{j=1}^{n_g}\left(n_\alpha c_{d\alpha}^i Z_\alpha RT \frac{\partial S_{l\alpha}}{\partial s_\alpha}\right)\frac{\partial c_{g\alpha}^j}{\partial t} + n_\alpha S_{l\alpha}\frac{\partial c_{d\alpha}^i}{\partial t}$$
$$+ n_\alpha S_{l\alpha}\frac{\partial R_{d\alpha}^i}{\partial t} = -\nabla \cdot \mathbf{J}_{d\alpha}^i - \lambda \Gamma_d^i \tag{3.118}$$

Substituting equations (3.107) and (3.110) to (3.112) into equation (3.105) and grouping similar terms gives the total dissolved chemical flux for the ith component in the fracture and matrix continua as:

$$\mathbf{J}_{dF}^i = -\left[\frac{c_{dF}^i k_{lF}}{\rho_l g}\nabla u_{lF}\right] - \left[n_F S_{lF}\left(D_{mF}^i + D_{deF}^i\right)\nabla c_{dF}^i\right] - \left[c_{dF}^i k_{lF}\nabla z\right] \tag{3.119}$$

$$\mathbf{J}_{dM}^i = -\left[\frac{c_{dM}^i k_{lM}}{\rho_l g}\nabla u_{lM}\right] - \left[n_M S_{lM} D_{deM}^i\nabla c_{dM}^i\right] - \left[c_{dF}^i k_{lF}\nabla z\right] \tag{3.120}$$

Substituting the total dissolved chemical flux from equations (3.119) and (3.120), λ from equation (3.2) and Γ_d^i from equation (3.115) into the right hand side of equation (3.118) gives the governing equations for multicomponent dissolved chemical transport in a dual porosity medium. The governing equations can be represented in a simplified form as:

$$C_{c_d l,F}\frac{\partial u_{lF}}{\partial t} + \sum_{j=1}^{n_g} C_{c_d c_g,F}\frac{\partial c_{gF}^j}{\partial t} + C_{c_d c_d,F}\frac{\partial c_{dF}^j}{\partial t} + C_{c_d R_d,F}\frac{\partial R_{dF}^i}{\partial t}$$
$$= \nabla \cdot \left[K_{c_g l,F}\nabla u_{lF}\right] + \nabla \cdot \left[K_{c_d c_d,F}\nabla c_{dF}^i\right] + Q_{c_d,F}^{ex} \tag{3.121}$$

$$
\begin{aligned}
C_{c_d l,M} \frac{\partial u_{lM}}{\partial t} &+ \sum_{j=1}^{n_g} C_{c_d c_g,M} \frac{\partial c_{gM}^{j}}{\partial t} + C_{c_d c_d,M} \frac{\partial c_{dM}^{j}}{\partial t} + C_{c_d R_d,M} \frac{\partial R_{dM}^{i}}{\partial t} \\
&= \nabla \cdot \left[K_{c_g l,M} \nabla u_{lM} \right] + \nabla \cdot \left[K_{c_d c_d,M} \nabla c_{dM}^{i} \right] + Q_{c_d,M}^{ex}
\end{aligned}
\tag{3.122}
$$

where in equation (3.121):

$$
C_{c_d l,F} = -n_F c_{dF}^{i} \frac{\partial S_{lF}}{\partial s_F}
\tag{3.123}
$$

$$
C_{c_d c_g,F} = n_F c_{dF}^{i} Z_F R T \frac{\partial S_{lF}}{\partial s_F}
\tag{3.124}
$$

$$
C_{c_d c_d,F} = n_F S_{lF}
\tag{3.125}
$$

$$
C_{c_d R_d,F} = n_F S_{lF}
\tag{3.126}
$$

$$
K_{c_d l,F} = \frac{c_{dF}^{i} k_{lF}}{\rho_l g}
\tag{3.127}
$$

$$
K_{c_d c_d,F} = n_F S_{lF} \left(D_{mF}^{i} + D_{deF}^{i} \right)
\tag{3.128}
$$

$$
J_{c_d,F} = \nabla \cdot \left(c_{gF}^{i} k_{gF} \nabla z \right)
\tag{3.129}
$$

$$
Q_{c_d,F}^{ex} = -\frac{\beta}{l^2} \left(\frac{k_l^A}{\rho_l g} \right) (u_{lF} - u_{lM}) - \frac{\beta D_{deM}^{i}}{l^2} \left(c_{dF}^{i} - c_{dM}^{i} \right)
\tag{3.130}
$$

and in equation (3.122):

$$
C_{c_d l,M} = -n_\alpha c_{dM}^{i} \frac{\partial S_{lM}}{\partial s_M}
\tag{3.131}
$$

$$
C_{c_d c_g,M} = n_M c_{dM}^{i} Z_M R T \frac{\partial S_{lM}}{\partial s_M}
\tag{3.132}
$$

$$
C_{c_d c_d,M} = n_M S_{lM}
\tag{3.133}
$$

$$
C_{c_d R_d,M} = n_M S_{lM}
\tag{3.134}
$$

$$
K_{c_d l,M} = \frac{c_{dM}^{i} k_{lM}}{\rho_l g}
\tag{3.135}
$$

$$
K_{c_d c_d,M} = n_M S_{lM} D_{deM}^{i}
\tag{3.136}
$$

$$
J_{c_d,M} = \nabla \cdot \left(c_{gM}^{i} k_{gM} \nabla z \right)
\tag{3.137}
$$

$$Q_{c_d,M}^{ex} = \frac{\beta}{l^2}\left(\frac{k_l^A}{\rho_l g}\right)(u_{lF} - u_{lM}) + \frac{\beta D_{deM}^i}{l^2}\left(c_{dF}^i - c_{dM}^i\right) \tag{3.138}$$

3.6 Effect of Deformation on Permeability and Porosity

The governing equations of the primary flow variables presented in sections 3.3, 3.4 and 3.5 were developed for a dual porosity deformable porous medium. Mechanical behaviour/deformation is not explicitly considered in the formulation. Instead, the feedback of deformation to the flow processes is included using a model that considers the associated evolution in porosity and permeability.

3.6.1 Background of the Deformation Model

The theory described so far in this chapter has been presented in a general form intended to be applicable to reactive flow in a wide range of fractured porous media. Since the focus of this work is mainly on reactive gas flow in coal, the deformation model described in this section is developed for this particular application. Nevertheless, many of the concepts employed are generally applicable to a number of geo-materials that can be described as fractured sorptive elastic media.

Physical and chemical interactions between the gas and solid skeleton can change the equilibrium stress condition in a dual porosity system as gas flows at high pressure. The subsequent deformation can have a feedback to the transport and reaction processes via changes in the porosity and permeability. The major physical and chemical interactions responsible for this behaviour, which are considered in the present work, are explained below:

i. Fracture aperture in coal, and therefore fracture permeability, is known to be sensitive to changes in effective stress (e.g. Somerton et al., 1975), i.e. changes in confining pressure and pore pressure.

ii. Mechanical compression or expansion of the matrix blocks.

iii. Swelling/shrinking stresses may be induced via the adsorption/desorption of gases in the coal matrix, most notably carbon dioxide (Reucroft and Patel, 1986).

A range of analytical models have been developed that relate the physical and chemical mechanisms of coal deformation with changes in porosity and permeability. A review of the main contributions in this area can be found in chapter 2, or in Palmer (2009) and Pan and Connell (2012). A problem with the most commonly used analytical models is that they do not distinguish between the fracture and matrix pore regions (e.g. Palmer and Mansoori, 1998; Shi and Durucan, 2004; Cui and Bustin, 2005), which limits their suitability to the present formulation. In addition, the majority of these models were developed in relation to field conditions with the assumption of uniaxial strain. The focus of this work is on reactive flow in coal at laboratory conditions with hydrostatic confinement, for which the assumption of uniaxial strain loses validity.

The deformation model presented in this section is developed based on the dual porosity, dual permeability framework adopted throughout this work. It is conceptually based on the models of Levine (1996) and Robertson and Christiansen (2006), in which changes in fracture aperture due to separate mechanisms are summed and linked to changes in fracture permeability.

Robertson and Christiansen (2006) formed the fracture network using a collection of uniformly-sized cubic matrix blocks subject to hydrostatic confining pressure, assuming that the matrix blocks have zero porosity and permeability. In order to extend their concept to a dual porosity, dual permeability form, a revision to their geometrical configuration is proposed. The fracture network is defined in the same manner as by Robertson and Christiansen (2006). However, instead of neglecting the matrix pore volume, it is formed by a collection of cubic sub-matrix blocks, as shown in Figure 3.2. The geometry of the system is then defined by the fracture aperture b_F, the matrix block width a_F and the more arbitrary matrix pore size b_M and sub-matrix block dimension a_M.

To ensure that the deformation model retains a functional form, the following general assumptions are made:

   i. Coal is a dual poroelastic medium.

   ii. Fracture and matrix continuum properties are homogeneous and isotropic.

   iii. Absolute permeability depends only on gas flow and reaction. The effect of pore

water is considered via relative phase permeabilities (ref. equations (3.10) and (3.56)).

iv. Strains are infinitesimal.

v. Matrix pores are much stiffer than fractures.

vi. Changes in porosity and permeability are assumed to depend mainly on changes in b_α and not a_α, as assumed by Robertson and Christiansen (2006).
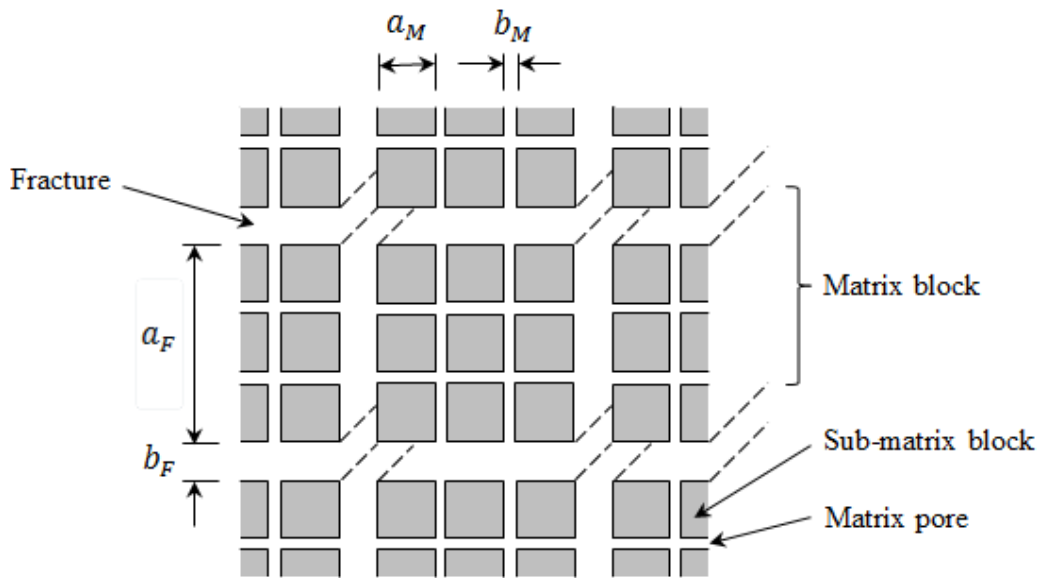
Figure 3.2 Schematic of the conceptual geometry used to develop the dual porosity, dual permeability deformation model.

In this work, changes in porosity and permeability are attributed to:

i. Fracture and matrix pore compressibility.

ii. Matrix block compressibility.

iii. Sorption induced matrix block strain.

As a result of the assumption that matrix pores are much stiffer than fractures (i.e. assumption v.), the pore compressibility is only considered in the fracture continuum. Further to this, assumption vi. implies that only the changes in b_α due to the above deformation mechanisms are considered. The accumulative deformation in each continuum can therefore be described by the following expressions:

$$\delta b_F = b_F - b_{F0} = \delta b_{Fp} + \delta b_{Fm} + \delta b_{Fs} \tag{3.139}$$

$$\delta b_M = b_M - b_{M0} = \delta b_{Mm} + \delta b_{Ms} \tag{3.140}$$

where the subscript 0 denotes the initial condition. The subscripts p, m and s are used to denote changes in b_α due to pore compressibility, matrix block compressibility and sorption induced matrix block strain, respectively.

3.6.2 Fracture Porosity and Permeability

Based on the cubic geometry illustrated in Figure 3.2, the equation for fracture porosity presented by Robertson and Christiansen (2006) can be expressed for a dual porosity geo-material, as:

$$n_F = \frac{3b_F}{a_F} \tag{3.141}$$

Robertson and Christiansen (2006) developed expressions for the increments in fracture aperture δb_F in equation (3.139) for a single component gas. In this work, these expressions are expanded for the dual continua, multicomponent case, giving:

$$\delta b_{Ff} = -b_{F0} c_f \left[(u_c - u_{c0}) - (u_{gF} - u_{gF0}) \right] \tag{3.142}$$

$$\delta b_{Fm} = \frac{a_{F0}(1 - 2\nu)}{E} (u_{gF} - u_{gF0}) \tag{3.143}$$

$$\delta b_{Fs} = -a_{F0} \sum_{j=1}^{n_g} \left(\varepsilon_s^j - \varepsilon_{s0}^j \right) \tag{3.144}$$

where c_f is the fracture compressibility, u_c is the hydrostatic confining pressure, ν is Poisson's ratio, E is Young's modulus and ε_s^j is the sorption induced strain for the jth pore gas component in the matrix continuum.

By assuming that the confining pressure remains constant, equation (3.142) reduces to:

$$\delta b_{Ff} = b_{F0} c_f (u_{gF} - u_{gF0}) \tag{3.145}$$

Substituting equations (3.143) to (3.145) into equation (3.139) and rearranging gives:

$$b_F = b_{F0} + b_{F0}c_f\left(u_{gF} - u_{gF0}\right) + \frac{a_{F0}(1 - 2v)}{E}\left(u_{gF} - u_{gF0}\right)$$
$$- a_{F0}\sum_{j=1}^{n_g}\left(\varepsilon_s^j - \varepsilon_{s0}^j\right)$$

(3.146)

From equation (3.146), with assumption vi. in section 3.6.1, the differential of fracture porosity can be expressed mathematically as:

$$dn_F = \frac{\partial n_F}{\partial b_F}\frac{\partial b_F}{\partial u_{gF}}du_{gF} + \frac{\partial n_F}{\partial b_F}\sum_{j=1}^{n_g}\frac{\partial b_F}{\partial \varepsilon_s^j}d\varepsilon_s^j$$

(3.147)

The partial derivative of the fracture porosity with respect to fracture aperture in equation (3.147) can be evaluated using equation (3.141) to give:

$$dn_F = \frac{3}{a_F}\frac{\partial b_F}{\partial u_{gF}}du_{gF} + \frac{3}{a_F}\sum_{j=1}^{n_g}\frac{\partial b_F}{\partial \varepsilon_s^j}d\varepsilon_s^j$$

(3.148)

Integrating both sides of equation (3.148) from time zero to time t yields:

$$\int_{n_{F0}}^{n_F}dn_F = \frac{3}{a_F}\int_{u_{gF0}}^{u_{gF}}\frac{\partial b_F}{\partial u_{gF}}du_{gF} + \frac{3}{a_F}\sum_{j=1}^{n_g}\int_{\varepsilon_{s0}^j}^{\varepsilon_s^j}\frac{\partial b_F}{\partial \varepsilon_s^j}d\varepsilon_s^j$$

(3.149)

Evaluating the partial derivatives of the fracture aperture with respect to fracture pore gas pressure and sorption induced strain using equation (3.146) yields:

$$\frac{\partial b_F}{\partial u_{gF}} = b_0c_f + \frac{a_{F0}(1 - 2v)}{E}$$

(3.150)

$$\frac{\partial b_F}{\partial \varepsilon_s^j} = -a_{F0}$$

(3.151)

Substituting equation (3.150) and equation (3.151) into equation (3.149) and expanding gives:

$$\int_{n_{F0}}^{n_F}dn_F = \frac{3}{a_F}\int_{u_{gF0}}^{u_{gF}}b_0c_f\,du_{gF} + \frac{3a_{F0}}{a_F}\int_{u_{gF0}}^{u_{gF}}\frac{(1 - 2v)}{E}du_{gF}$$
$$- \frac{3a_{F0}}{a_F}\sum_{j=1}^{n_g}\int_{\varepsilon_{s0}^j}^{\varepsilon_s^j}d\varepsilon_s^j$$

(3.152)

If it is assumed that the change in matrix block width is small relative to its initial value, $a_{F0}/a_F \approx 1$ and equation (3.152) simplifies to:

$$\int_{n_{F0}}^{n_F} dn_F = \frac{3b_0}{a_{F0}} \int_{u_{gF0}}^{u_{gF}} c_f \, du_{gF} + 3 \int_{u_{gF0}}^{u_{gF}} \frac{(1-2\nu)}{E} du_{gF} - 3 \sum_{j=1}^{n_g} \int_{\varepsilon_{s0}^j}^{\varepsilon_s^j} d\varepsilon_s^j \qquad (3.153)$$

Substituting equation (3.141) into the first term on the right hand side of equation (3.153) gives:

$$\int_{n_{F0}}^{n_F} dn_F = n_{F0} \int_{u_{gF0}}^{u_{gF}} c_f \, du_{gF} + 3 \int_{u_{gF0}}^{u_{gF}} \frac{(1-2\nu)}{E} du_{gF} - 3 \sum_{j=1}^{n_g} \int_{\varepsilon_{s0}^j}^{\varepsilon_s^j} d\varepsilon_s^j \qquad (3.154)$$

The integrals can then be evaluated to produce:

$$n_F = n_{F0} + n_{F0} c_f \left(u_{gF} - u_{gF0} \right) \\ + 3 \left[\frac{(1-2\nu)}{E} \left(u_{gF} - u_{gF0} \right) - \sum_{j=1}^{n_g} \left(\varepsilon_s^j - \varepsilon_{s0}^j \right) \right] \qquad (3.155)$$

McKee et al. (1988) concluded that although a constant value of the fracture compressibility c_f can be used to successfully fit experimental data, a stress dependent value may sometimes be required. They proposed the following expression:

$$c_f = -\frac{c_{f0}}{\alpha_f \left(u_{gF} - u_{gF0} \right)} \left(1 - e^{\alpha_f \left(u_{gF} - u_{gF0} \right)} \right) \qquad (3.156)$$

where c_{f0} is the initial fracture compressibility and α_f is the fracture compressibility change rate.

Using this relationship, the fractures become stiffer as the fracture pore pressure is reduced. Substituting equation (3.156) into (3.155) yields:

$$n_F = n_{F0} - \frac{n_{F0} c_{f0}}{\alpha_f} \left(1 - e^{\alpha_f \left(u_{gF} - u_{gF0} \right)} \right) \\ + 3 \left[\frac{(1-2\nu)}{E} \left(u_{gF} - u_{gF0} \right) - \sum_{j=1}^{n_g} \left(\varepsilon_s^j - \varepsilon_{s0}^j \right) \right] \qquad (3.157)$$

The multicomponent sorption strain terms in equation (3.157) are evaluated using a Langmuir strain isotherm model. This approach has been used in all of the most commonly used deformation models, and is supported by comparisons with experimental data (e.g. Harpalani and Chen, 1995; Levine, 1996). In multicomponent form, the Langmuir strain isotherm is given by:

$$\varepsilon_s^j = \frac{\varepsilon_L^j b_L^j Z_M RT c_{gM}^j}{1 + Z_M RT \sum_{k=1}^{n_g} b_L^k c_{gM}^k} \tag{3.158}$$

where ε_L^j and b_L^j are the Langmuir strain and inverse Langmuir pressure constants for the jth component, respectively.

It is noted that equation (3.158) assumes that the amount of adsorbed gas is at equilibrium with the free gas concentration in the matrix. Whilst this assumption is not strictly valid in this work, since a kinetic sorption model has been used, it has been made to preserve the practicality of the deformation model.

It is assumed that the absolute permeability in the fracture continuum can be obtained using the cubic law proposed by Reiss (1980), which is given by:

$$\frac{K_F}{K_{F0}} = \left(\frac{n_F}{n_{F0}}\right)^3 \tag{3.159}$$

Combining equations (3.157) and equation (3.159) gives:

$$K_F = K_{F0}\left\{1 - \frac{c_{f0}}{\alpha_f}\left(1 - e^{\alpha_f(u_{gF} - u_{gF0})}\right) \right.$$
$$\left. + \frac{3}{n_{F0}}\left[\frac{(1-2\nu)}{E}\left(u_{gF} - u_{gF0}\right) - \sum_{j=1}^{n_g}\left(\varepsilon_s^j - \varepsilon_{s0}^j\right)\right]\right\}^3 \tag{3.160}$$

Equation (3.160) can be expressed in terms of the pore gas concentration primary variables using the real gas law given in equation (3.23), giving the following final forms of the fracture porosity and permeability equations:

$$n_F = n_{F0} - \frac{n_{F0}c_{f0}}{\alpha_f}\left[1 - e^{\alpha_f \sum_{j=1}^{ng}\left(Z_F RT c_{gF}^j - Z_{F0} RT c_{gF0}^j\right)}\right]$$
$$+ 3\sum_{j=1}^{ng}\left[\frac{(1-2\nu)}{E}\left(Z_F RT c_{gF}^j - Z_{F0} RT c_{gF0}^j\right) - \left(\varepsilon_s^j - \varepsilon_{s0}^j\right)\right] \tag{3.161}$$

$$K_F = K_{F0}\left\{1 - \frac{c_{f0}}{\alpha_f}\left[1 - e^{\alpha_f \sum_{j=1}^{ng}\left(Z_F RT c_{gF}^j - Z_{F0} RT c_{gF0}^j\right)}\right]\right.$$
$$\left.+ \frac{3}{n_{F0}}\sum_{j=1}^{ng}\left[\frac{(1-2\nu)}{E}\left(Z_F RT c_{gF}^j - Z_{F0} RT c_{gF0}^j\right) - \left(\varepsilon_s^j - \varepsilon_{s0}^j\right)\right]\right\}^3 \tag{3.162}$$

3.6.3   Matrix Porosity and Permeability

A major advantage of the geometry shown in Figure 3.2 is that it allows a procedure similar to that used in the previous section to be used in developing the matrix deformation equations.

Assumption v. in section 3.6.1 stated that the matrix pores are assumed to be much stiffer than the fractures. This allows the pore compressibility deformation mechanism to be neglected in the matrix deformation equations. Matrix block compression causes a gain in fracture porosity and a loss in matrix porosity, whilst sorption induced strains result in a similar variation in porosity in both continua. Through inspection of equations (3.142), (3.143) and (3.144), expressions for changes in b_M can then be obtained, as:

$$\delta b_{Mf} = 0 \tag{3.163}$$

$$\delta b_{Mm} = -\frac{a_{M0}(1-2\nu)}{E}\left(u_{gF} - u_{gF0}\right) \tag{3.164}$$

$$\delta b_{Ms} = -a_{M0}\sum_{j=1}^{ng}\left(\varepsilon_s^j - \varepsilon_{s0}^j\right) \tag{3.165}$$

Via substitution of the above increments into equation (3.140), and following the same procedure used in the previous section for the fracture equations, matrix porosity can be obtained as:

$$n_M = n_{M0} - 3\left[\frac{(1-2\nu)}{E}\left(u_{gF} - u_{gF0}\right) + \sum_{j=1}^{ng}\left(\varepsilon_s^j - \varepsilon_{s0}^j\right)\right] \tag{3.166}$$

The absolute permeability in the matrix continuum can be obtained using equations (3.159) and (3.166), as:

$$K_M = K_{M0} \left\{ 1 - \frac{3}{n_{M0}} \left[\frac{(1-2\nu)}{E} \left(u_{gF} - u_{gF0} \right) + \sum_{j=1}^{n_g} \left(\varepsilon_s^j - \varepsilon_{s0}^j \right) \right] \right\}^3 \qquad (3.167)$$

Equation (3.167) can be expressed in terms of the pore gas concentration primary variables using the real gas law given in equation (3.23), giving the following final forms of the matrix porosity and permeability equations:

$$n_M = n_{M0} - 3 \sum_{j=1}^{n_g} \left[\frac{(1-2\nu)}{E} \left(Z_F RT c_{gF}^j - Z_{F0} RT c_{gF0}^j \right) + \left(\varepsilon_s^j - \varepsilon_{s0}^j \right) \right] \qquad (3.168)$$

$$K_M = K_{M0} \left\{ 1 - \frac{3}{n_{M0}} \sum_{j=1}^{n_g} \left[\frac{(1-2\nu)}{E} \left(Z_F RT c_{gF}^j - Z_{F0} RT c_{gF0}^j \right) \right. \right.$$
$$\left. \left. + \left(\varepsilon_s^j - \varepsilon_{s0}^j \right) \right] \right\}^3 \qquad (3.169)$$

Together, equations (3.161), (3.162), (3.168) and (3.169) describe the deformation model that has been developed in this work. The effects of various physical and chemical interactions between the gas and solid phases in a dual porosity medium have been considered. The model provides additional capabilities to the formulation to study high pressure reactive gas transport in fractured rock in applications that involve significant changes in porosity and permeability.

3.7 Summary

This chapter presented the theoretical formulation for the hydraulic, gas/chemical and deformation behaviour of a dual porosity medium, i.e. fractured rock, under isothermal conditions. The governing equations were presented in terms of pore water pressures, gas chemical concentrations and dissolved chemical concentrations. Many of the fundamental aspects of these equations have been covered in detail elsewhere for single porosity media, such as unsaturated soil (Thomas and He, 1998; Seetharam, 2003; Sedighi, 2011; Masum, 2012). The formulations of water transfer, pore gas transport and dissolved chemical

transport have been further developed in this work considering the processes in a dual porosity medium, and high pressure gas effects.

The complex structure of fractured rock was modelled using a dual porosity, dual permeability framework. In this approach, the fracture network and porous matrix blocks were treated as distinct continua that overlap across the domain and interact via a mass exchange process. Each continuum was prescribed properties that produce behaviour equivalent to the discrete features in an actual fractured rock. This has been achieved by factoring the local pore scale properties of the fracture and matrix pore regions using a volumetric weighting factor.

The principle of conservation of mass was used as the basis for the governing equations in each continuum. Advective and ordinary diffusive fluxes were described using Darcy's law and Fick's law, respectively. Knudsen and configurational diffusion were also considered in the total gas flux in the matrix continuum. Sink/source terms were included to model mass exchange between the fracture and matrix continua and geochemical reactions.

A particular emphasis was placed on including theoretical features related to high pressure gas transport and solid-gas interactions. Development was undertaken to describe the properties of multicomponent gas at high pressure in terms of the bulk gas compressibility, bulk gas viscosity and gas diffusion coefficients. The adsorption/desorption process was modelled using a first-order kinetics approach. In addition, a deformation model was developed to describe the changes in the porosity and permeability in a dual porosity system due to various physical and chemical interactions between the gas and solid phases. These features provide additional capabilities to the dual porosity, dual permeability formulation to study high pressure reactive gas transport in geo-materials, such as the processes involved in carbon dioxide sequestration and enhanced coal bed methane recovery.

3.8   References

Amali, S. and Rolston, D.E. (1993). Theoretical investigation of multicomponent volatile organic vapour diffusion: Steady-state fluxes. *Journal of Environmental Quality*, **22**, 825-831.

Arnold, B.W., Zhang, H. and Parsons, A.M. (2000). Effective-porosity and dual-porosity approaches to solute transport in the saturated zone at Yucca Mountain: Implications for repository performance assessment. In Faybishenko, B. et al. eds. *Dynamics of fluids in fractured rock*, AGU, Washington, D.C.

Barenblatt, G.I., Zheltov, I.P. and Kochina, I.N. (1960). Basic concepts in the theory of seepage of homogenous liquids in fissured rocks (strata). *Journal of Applied Mathematics and Mechanics*, **24**(5), 1286-1303.

Bear, J. (1979). *Hydraulics of groundwater*. McGraw Hill, New York.

Bear, J. and Verruijt, A. (1987). *Modeling groundwater flow and pollution*. D. Reidel Publishing Company, Dordrecht, The Netherlands.

Bear, J. and Bachmat, Y. (1990). *Introduction to modeling of transport phenomena in porous media*. Kluwer Academic Publishers, Dordrecht, The Netherlands.

Bear, J. (1993). Modeling flow and contaminant transport in fractured rocks. In: Bear, J. et al. eds. *Flow and contaminant transport in fractured rock*, Academic Press, Inc., pp 1-38.

Beck, R.E. and Schultz, J.S. (1970). Hindered diffusion in macroporous membranes with known pore geometry. *Science*, **170**, 1302-1305.

Bethke, C.M. (1996). *Geochemical reaction modelling: concepts and applications*. Oxford University Press, Oxford.

Bird, R.B., Stewart, W.E. and Lightfoot, E.N. (1960). *Transport phenomena*. John Wiley and Sons, New York.

Busch, A., Gensterblum, Y., Kroos, B.M. and Littke, R. (2004). Methane and carbon dioxide adsorption-diffusion experiments on coal: upscaling and numerical modeling. *International Journal of Coal Geology*, **60**, 151-168.

Chang, M-M. (1993). *Deriving the shape factor of a fractured rock matrix*. U.S. Department of Energy.

Chen, Z., Huan, G. and Ma, Y. (2006). *Computational methods for multiphase flows in porous media*. SIAM, Philadelphia.

Chung, T-H., Ajlan, M., Lee, L.L. and Starling, K.E. (1988). Generalized multiparameter correlation for nonpolar and polar fluid transport properties. *Industrial and Engineering Chemistry Research*, **27**, 671-679.

Clarkson, C.R. and Bustin, R.M. (2010). Coalbed methane: current evaluation methods, future technical challenges. *In Proceedings of the SPE Unconventional Gas Conference*, 23-25

February, Pittsburgh, Pennsylvania.

Cleall, P.J. (1998). *An investigation of the thermo/hydraulic/mechanical nehaviour of unsaturated soils, including expansive clays*. Ph.D. Thesis, Cardiff University, Cardiff.

Cui, X., Bustin, R.M. and Dipple, G. (2004). Selective transport of CO_2, CH_4 and N_2 in coals: insights from modeling of experimental gas adsorption data. *Fuel*, **83**, 293-303.

Cui, X. and Bustin, R.M. (2005). Volumetric strain associated with methane desorption and its impact on coalbed gas production from deep coal seams. *AAPG Bulletin*, **89**(9), 1181-1202.

Cunningham, R.S. and Geankoplis, C.J. (1968). Effects of different structures of porous solids on diffusion of gases in the transition region. *Industrial and Engineering Chemistry Fundamentals*, **7**(4), 535-542.

Cussler, E.L. (1997). *Diffusion: mass transfer in fluid systems*. 2nd Edition. Cambridge University Press, Cambridge.

Crank, J. (1975). *The mathematics of diffusion*. 2nd Edition. Oxford University Press, Oxford.

Dake, L.P. (1978). *Fundamentals of reservoir engineering*. Elsevier, Amsterdam, The Netherlands.

Darcy, H. (1856). *Les Fontaines Publiques de la Ville de Dijon*. Dalmont, Paris.

Denbigh, K.G. (1981). *The principles of chemical equilibrium*. 4th Edition. Cambridge University Press, Cambridge.

Dershowitz, W., Winberg, J., Hermanson, J., Byegard, J., Tullborg, E-L., Anderson, P. and Mazurek, M. (2003). *Äspö Task Force on modeling of groundwater flow and transport of solutes – Task 6C – A semi synthetic model of block scale conductive structures at the Äspö HRL*, International SKB Progress Report IPR-03-13.

Dykhuizen, R.C. (1990). A new coupling term for dual-porosity models. *Water Resources Research*, **26**, 351-356.

Fick, A. (1855). Ueber diffusion. *Poggendorff's Annalen der Physik und Chemie*, **94**, 59-86.

Freeman, C.M., Moridis, G.J. and Blasingame, T.A. (2011). A numerical study of microscale flow behaviour in tight gas and shale gas reservoir systems. *Transport in Porous Media*, **90**, 253-268.

Gallipoli, D., Wheeler, S.J. and Karstunen, M. (2003). Modelling the variation of degree of saturation in a deformable unsaturated soil. *Géotechnique*, **53**(1), 105-112.

Geankoplis, C.J. (1972). *Mass transport phenomena*. Holt, Rinehart and Winston, Inc., New York.

Gerke, H.H. and van Genuchten, M.T. (1993a). A dual-porosity model for simulating the preferential movement of water and solutes in structured porous media. *Water Resources Research*. **29**(2), 305-319.

Gerke, H.H. and van Genuchten, M.T. (1993b). Evaluation of a first-order water transfer term for variably saturated dual-porosity flow models. *Water Resources Reseach*, **29**(4), 1225-1238.

Gilman, J.R. and Kazemi, H. (1983). Improvements in Simulation of Naturally Fractured

Reservoirs. *Society of Petroleum Engineers Journal*, 23(4), 695-707.

Hagoort, J. (1988). *Fundamentals of gas reservoir engineering*. Elsevier, Amsterdam, The Netherlands.

Han, W.S., Kim, K-Y.,Lu, M., McPherson, B.J., Lu, C. and Lee, S-Y. (2011). Injectivity changes and associated temperature disequilibrium: numerical study. *Energy Procedia*, **4**, 4552-4558.

Harpalani, S. and Chen, G. (1995). Estimation of changes in fracture porosity of coal with gas emission. *Fuel*, **74**(10), 1491-1498.

Hassanzadeh, H., Pooladi-Darvish, M. and Atabay, S. (2009). Shape factor in the drawdown solution for well testing of dual-porosity systems. *Advances in Water Resources*, **32**, 1652-1663.

Heid, J.G., McMahon, J.J., Nielsen, R.F. and Yuster, S.T. (1950). Study of the permeability of rocks to homogenous fluids. *API Drilling and Production Practice*, 230-246.

Javadpour, F., Fisher, D. and Unsworth, M. (2007). Nanoscale gas flow in shale sediments. *Journal of Canadian Petroleum Technology*, **46**(10), 55-61.

Jones, S.C. (1972). A rapid accurate unsteady-state Klinkenberg parameter. *Society of Petroleum Engineers Journal*, **12**(5), 383-397.

Karniadakis, G.E. and Beskok, A. (2001). *Microflows: fundamentals and simulation*. Springer, Berlin.

Kaye, G.W.C. and Laby, T.M. (1973). *Tables of physical and chemical constants*. 14th Edition, Longmans, London.

King, G.R., Ertekin, T. and Schwerer, F.C. (1986). Numerical simulation of the transient behaviour of coal-seam degasification wells. *Society of Petroleum Engineers Formation Evaluation*, **1**(2), 165-183.

Kwak, T.Y. and Mansoori, G.A. (1986). Van der Waals mixing rules for cubic equations of state. Applications for supercritical fluid extraction modelling. *Chemical Engineering Science*, **41**(5), 1303-1309.

Lasaga, A.C. (1998). *Kinetic theory in the earth sciences*. Princeton Series in Geochemistry, Princeton University Press.

Lemmonier, P. and Bourbiaux, B. (2010). Simulation of naturally fractured reservoirs. State of the art. Part 2 – matrix-fracture transfers and typical features of numerical studies. *Oil and Gas Science and Technology*, **65**, 263-286.

Levine, J.R. (1996). Model study of the influence of matrix shrinkage on absolute permeability of coal bed reservoirs. In: Gayer, R. and Harris, I., eds. *Coalbed Methane and Coal Geology*, Geological Society Special Publication No. 109, London, 197-212.

Mašín, D. (2010). Predicting the dependency of a degree of saturation on void ratio and suction using effective stress principle for unsaturated soils. *International Journal for Numerical and Analytical Methods in Geomechanics*, **34**, 73-90.

Mason, E.A., Malinauskas, A.P. and Evans, R.B. (1967). Flow and diffusion of gases in porous media. *The Journal of Chemical Physics*, **46**(8), 3199-3217.

Mason, E.A. and Malinauskas, A.P. (1983). *Gas transport in porous media: the Dusty-Gas model*. Chemical Engineering Monograph 17, Elsevier, New York.

Masum, S.A. (2012). *Modelling of reactive gas transport in unsaturated soil – a coupled thermo-hydro-chemical-mechanical approach*. Ph.D. Thesis, Cardiff University, Cardiff.

McKee, C.R. (1988). Stress-dependent permeability and porosity of coal and other geologic formations. *Society of Petroleum Engineers Formation Evaluation*, **3**(1), 81-91.

Millington, R.J. and Quirk, J.M. (1961). Permeability of porous solids. *Transactions of the Faraday Society*, **57**, 1200-1207.

Mitchell, J.K. and Soga, K. (2005). *Fundamentals of soil behaviour*. 3rd Edition. John Wiley and Sons, Hoboken, New Jersey.

Onsager, L. (1945). Theories and problems of liquid diffusion *Annals of the New York Academy of Sciences*, **46**, 241-265.

Painter, S. and Cvetkovic, V. (2005). Upscaling discrete fracture network simulations: An alternative to continuum transport model. *Water Resources Research*, **41**(2), 1-10.

Palmer, I. and Mansoori, J. (1998). How permeability depends on stress and pore pressure in coalbeds: A new model. *Society of Petroleum Engineers Reservoir Evaluation and Engineering*, **1**(6), 539-544.

Palmer, I. (2009). Permeability changes in coal: Analytical modeling. *International Journal of Coal Geology*, **77**, 119-126.

Pan, Z. and Connell, L.D. (2012). Modelling permeability for coal reservoirs: A review of analytical models and testing data. *International Journal of Coal Geology*, **92**, 1-44.

Peng, D-Y. and Robinson, D.B. (1976). A new two-constant equation of state. *Industrial and Engineering Chemistry Fundamentals*, **15**(1), 59-64.

Pickens, J.F. and Gilham, R.W. (1980). Finite element analysis of solute transport under hysteretic unsaturated flow conditions. *Water Resources Research*, **16**(6), 1071-1078.

Pini, R., Storti, G. and Mazzotti, M. (2011). A model for enhanced coalbed methane recovery aimed at carbon dioxide storage. *Adsorption*, **17**(5), 889-900.

Pruess, K. and Narasimhan, T. (1985). A practical approach for modeling fluid and heat flow in fractured porous media. *Society of Petroleum Engineers Journal*, **25**(1), 14-26.

Reid, R.C., Prausnitz, J.M. and Sherwood, T.K. (1977). *The properties of gases and liquids*. 3rd Edition. McGraw-Hill, New York.

Reiss, L.H. (1980). *The reservoir engineering aspects of fractured formations*, Gulf Publishing Company, Houston, Texas.

Reucroft, P.J. and Patel, H. (1986). Gas-induced swelling in coal. *Fuel*, **65**(6), 816-820.

Robertson, E.P. and Christiansen, R.L. (2006). A permeability model for coal and other fractured, sorptive-elastic media. *Society of Petroleum Engineers Journal*, **13**(3), 314-324.

Rojey, A., Jaffret, C., Cornot-Gandolphe, S., Durand, B., Jullian, S. and Valais, M. (1994). *Natural gas: production, processing, transport.* Éditions Technip, Paris, France.

Ruthven, D.M. (1984). *Principles of adsorption and adsorption processes*. Wiley, New York.

Samardzioska, T. and Popov, V. (2005). Numerical comparison of the equivalent continuum, non-homogenous and dual porosity models for flow and transport in fractured porous media. *Advances in Water Resources*, **28**, 235-255.

Satterfield, C.N. and Colton, C.K. (1973). Restricted diffusion in liquids with fine pores. *American Institute of Chemical Engineers Journal*, **19**, 628-635.

Scanlon, B.R., Nicot, J.P. and Massmann, J.M. (1999). Soil gas movement in unsaturated systems. In: Sumner, M.E. ed. *Handbook of soil science*, CRC Press, Boca Raton, Florida.

Schwartz, R.C., Juo, A.S.R. and McInnes, K.J. (2000). Estimating parameters for a dual-porosity model to describe nonequilibrium, reactive transport in a fine-textured soil. *Journal of Hydrology*, **229**, 149-167.

Sedighi, M. (2011). *An investigation of hydro-geochemical processes in coupled thermal, hydraulic, chemical and mechanical behaviour of unsaturated soils*. Ph.D. Thesis, Cardiff University, Cardiff.

Seetharam, S.C. (2003). *An investigation of the thermo/hydro/chemical/mechanical behaviour of unsaturated soils*. Ph.D. Thesis, Cardiff University, Wales, UK.

Seidle, J. (2011). *Fundamentals of coalbed methane reservoir engineering*. PennWell Corporation, Tulsa, Oklahoma, USA.

Shi, J-Q. and Durucan, S. (2004). Drawdown induced changes in permeability of coalbeds: A new interpretation of the reservoir response to primary recovery. *Transport in Porous Media*, **56**(1), 1-16.

Shi, J-Q. and Durucan, S. (2005). Gas storage and flow in coalbed reservoirs: Implementation of a bidisperse pore model for gas diffusion in a coal matrix. *SPE Reservoir Evaluation and Engineering*, **8**(2), 169-175.

Singhal, B.B.S. and Gupta, R.P. (2010). *Applied hydrogeology of fractured rocks*. 2nd edition. Springer, Dordrecht, The Netherlands.

Somerton, W.H., Söylemezoglu, I.M. and Dudley, R.C. (1975). Effect of stress on permeability of coal. *International Journal of Rock Mechanics and Mining Sciences & Geomechanics Abstracts*, **12**, 129-145.

Steefel, C.I. and MacQuarrie, K.T.B. (1996). Approaches to modelling of reactive transport in porous media. In: Lichtner et al., eds. *Reactive transport in porous media, Reviews in*

Mineralogy, 34. Mineralogical Society of America, Washington, D.C.

Steefel, C.I. (2008). *Geochemical kinetics and transport*. In Brantley, S.L., Kubicki, J.D. and White, A.F., eds. *Kinetics of Water-Rock Interaction*, Springer, 545-589.

Takahashi, S. (1974). Preparation of a generalized chart for the diffusion coefficients of gases at high pressures. *Japanese Journal of Chemical Engineering*, **7**(6), 417-420.

Therrien, R. and Sudicky, E.A. (1996). Three-dimensional analysis of variably-saturated flow and solute transport in discretely-fractured porous media. *Journal of Contaminant Hydrology*, **23**(1-2), 1-44.

Thomas, H.R. and He, Y. (1998). Modelling the behaviour of unsaturated soil using an elasto-plastic constitutive relationship. *Géotechnique*, **48**(5), 589-603.

Thomas, H.R., Sedighi, M. and Vardon, P.J. (2012). Diffusive reactive transport of multicomponent chemicals under coupled thermal, hydraulic, chemical and mechanical conditions. *Geotechnical and Geological Engineering*, **30**(4), 841-857.

Thorstenson, D.C. and Pollock, D.W. (1989). Gas transport in unsaturated zones: multicomponent systems and the adequacy of Fick's Laws. *Water Resources Reseach*, **25**¸ 477-507.

van Brakel, J. and Heertjes, P.M. (1974). Analysis of diffusion in macroporous media in terms of a porosity, a tortuosity and a constrictivity factor. *International Journal of Heat and Mass Transfer*, **17**, 1093-1103.

van Golf-Racht, T.D. (1982). *Fundamentals of fractured reservoir engineering*. Elsevier, Amsterdam, The Netherlands.

van Genuchten, M.T. (1980). A closed-form equation for predicting the hydraulic conductivity of unsaturated soils. *Soil Science Society of America Journal*, **44**(5), 892-898.

Wang, J., Ryan, D., Anthony, E.J. and Wigston, A. (2011). *Effects of impurities on geological storage of carbon dioxide*. IEAGHG.

Ward, C.R. (2002). Analysis and significance of mineral matter in coal seams. *International Journal of Coal Geology*, **50**(1), 135-168.

Warren, J.E. and Root, P.J. (1963). The behaviour of naturally fractured reservoirs. *Society of Petroleum Engineers Journal*, **3**(3), 245-255.

Webb, S.W. (2006). Gas transport mechanisms. In: Ho, C.K. and Webb, S.W. eds. *Gas transport in porous media*, Springer, Dordrecht, The Netherlands.

Wei, Y.S. and Sadus, R.J. (2000). Equations of state for the calculation of fluid-phase equilibria. *American Institute of Chemical Engineers Journal*, **46**(1), 169-196.

White, C.M., Smith, D.H., Jones, K.L., Goodman, A.L., Jikich, S.A., LaCount, R.B., DuBose, S.B., Ozdemir, E., Morsi, B,I. and Schroeder, K.T. (2005). Sequestration of carbon dioxide in coal with enhanced coalbed methane recovery – a review. *Energy and Fuels*, **19**(3), 659-724.

Wu, Y-S., Pruess, K. and Persoff, P. (1998). Gas flow in porous media with Klinkenberg effects. *Transport in Porous Media*, **32**, 117-137.

Xiao, J. and Wei, J. (1992). Diffusion mechanism of hydrocarbons in zeolites – I: Theory. *Chemical Engineering Science*, **47**(5), 1123-1141.

Yang, R.T. (1987). *Gas separation by adsorption processes*. Butterworth, London.

Zangwill, A. (1988). *Physics at surfaces*. Cambridge University Press, Cambridge.

Zhu, W.C., Wei, C.H., Liu, J., Qu, H.Y. and Elsworth, D. (2011). A model of coal-gas interaction under variable temperatures. *International Journal of Coal Geology*, **86**, 213-221.

Zimmerman, R.W., Chen, G., Hagdu, T. and Bodvarsson, G.S. (1993). A numerical dual-porosity model with semianalytical treatment of fracture/matrix flow. *Water Resources Research*, **29**(7), 2127-2137.

4

Numerical Formulation

4.1 Introduction

A numerical algorithm has been developed to obtain a solution to the highly coupled governing equations presented in the previous chapter. The developed solution is based on the finite element method (FEM) to spatially discretise the set of equations, and the finite difference method (FDM) for temporal discretisation. A sequential non-iterative approach (SNIA) has been used to couple the flow processes with the sink/source terms for the mass exchange process and geochemical reactions. Details of the SNIA adopted are also provided in this chapter. It is noted that a direct analytical solution to boundary value problems is generally only available in the very simplest of cases (Lewis and Schrefler, 1998), which is why the numerical approach described in this chapter has been adopted.

The numerical formulation for the coupled equations describing the thermal, hydraulic and mechanical behaviour of unsaturated single porosity media have been described in detail by Ramesh (1996), Cleall (1998) and Vardon (2009). Extension of this numerical formulation to dissolved chemical transport was made by Seetharam (2003) and Sedighi (2011). Finally, Masum (2012) presented the numerical formulation for the governing

equations of the transport of multicomponent gas. In the present work, the numerical formulation for coupled hydraulic and gas/chemical behaviour in a dual porosity medium has been developed. Since the focus of this study is on the reactive transport of multicomponent gas, the development of the numerical solution for the transport of gas components in the fracture and matrix continua is covered in detail. The numerical formulations for water transfer and multicomponent dissolved chemical transport are presented in a summarised form.

Section 4.2 describes the spatial discretisation of the governing equations via the Galerkin weighted residual method. The spatially discretised equations are presented in a matrix form along with the details of the temporal discretisation in section 4.3. A fully implicit mid-interval backward-difference time-stepping algorithm is used in this formulation. The use of the SNIA in the coupling of the transport and sink/source terms is explained in section 4.4.

A summary of the numerical formulation is provided in section 4.5.

4.2   Spatial Discretisation

In the present study, the weighted residual method has been employed to spatially discretise the governing equations. The technique yields approximate solutions to sets of nonlinear partial differential equations considering appropriate boundary conditions (Huebner and Thornton, 1982). Specifically, the well-documented Galerkin weighted residual method is used (Zienkiewicz and Taylor, 1989). This method has been shown to be suitable for the type of highly coupled governing equations presented in the previous chapter (e.g. Thomas and He, 1995; Seetharam et al., 2007; Sedighi, 2011; Thomas et al., 2012).

The development of the finite element equations using the Galerkin weighted residual method has been described in detail in the literature (e.g. Huebner and Thornton, 1982; Zienkiewicz and Taylor, 1989). As a result, the spatial discretisation of the governing equations is presented in this chapter in an abbreviated form. Since a similar process has been followed for each of the primary flow variables, only the formulation for

multicomponent pore gas transport is presented in detail. The final form of the discretised equations for water transfer and dissolved chemical transport are provided for completeness.

From the Galerkin weighted residual method, the primary variables (unknowns) and their spatial derivatives are approximated using shape functions. For an element with n_{node} nodes, this gives:

$$\omega_\alpha \approx \widehat{\omega}_\alpha = \sum_{s=1}^{n_{node}} N_s \omega_{s\alpha} \tag{4.1}$$

$$\nabla\widehat{\omega}_\alpha = \sum_{s=1}^{n_{node}} (\nabla N_s)\omega_{s\alpha} \tag{4.2}$$

where ω_α represents any of the primary variables in continua α out of $u_{l\alpha}$, $c_{g\alpha}^i$ and $c_{d\alpha}^i$, N_s is the shape function, the subscript s is the node indicator for the element and the symbol, $\widehat{}$, denotes the approximate value of the primary variable.

4.2.1 Spatial Discretisation for Multicomponent Gas Transport Equations

The governing equations for multicomponent gas transport in a dual porosity medium were presented in a general form for the n_g components in chapter 3. The procedure for spatial discretisation remains the same for each component; therefore this section considers only the ith component. The governing equations for the ith gas component in the fracture and matrix continua can be expressed in a general form as:

$$
\begin{aligned}
&-C_{c_g l,\alpha}\frac{\partial \widehat{u}_{l\alpha}}{\partial t} - \sum_{j=1}^{n_g} C_{c_g c_g,\alpha}\frac{\partial \widehat{c}_{g\alpha}^j}{\partial t} - C_{c_g s_g,\alpha}\frac{\partial s_{g\alpha}^i}{\partial t} \\
&+ \nabla\cdot\left[\sum_{j=1}^{n_g} K_{c_g c_g,\alpha}\nabla\widehat{c}_{g\alpha}^j\right] + J_{c_g,\alpha} + Q_{c_g,\alpha}^{ex} = R_{\Omega,\alpha}
\end{aligned}
\tag{4.3}
$$

where the residual error, $R_{\Omega,\alpha}$, is introduced as a result of the substitution of the approximate values of the primary variables in place of the actual values.

In equation (4.3), the third and sixth terms are the sink/source terms for geochemical reactions and mass exchange between the continua, respectively. Since the SNIA has been

used, the exchange/reaction processes in equation (4.3) are handled only once in each time step, after convergence in the solution of the transport equations has been achieved. A description of the numerical treatment of the exchange/reaction terms using the SNIA is given in section 4.4. The transport equation with these terms removed is given by:

$$
\begin{aligned}
-C_{c_g l,\alpha}\frac{\partial \hat{u}_{l\alpha}}{\partial t} - \sum_{j=1}^{n_g} C_{c_g c_g,\alpha}\frac{\partial \hat{c}_{g\alpha}^j}{\partial t} \\
+ \nabla \cdot \left[\sum_{j=1}^{n_g} K_{c_g c_g,\alpha}\nabla \hat{c}_{g\alpha}^j \right] + J_{c_g,\alpha} = R_{\Omega,\alpha}
\end{aligned}
\tag{4.4}
$$

The residual error, $R_{\Omega,\alpha}$, can be expressed mathematically as:

$$
R_{\Omega,\alpha} = \omega_\alpha - \hat{\omega}_\alpha
\tag{4.5}
$$

Application of the Galerkin weighted residual method is intended to minimise the residual error over the element using the shape functions, i.e. N_r, as weighting coefficients, which yields:

$$
\int_{\Omega^e} N_r R_{\Omega,\alpha} d\Omega^e = 0
\tag{4.6}
$$

where Ω^e is the element area/volume. Substitution of equation (4.4) into equation (4.6) gives:

$$
\int_{\Omega^e} N_r \left[\begin{aligned}
-C_{c_g l,\alpha}\frac{\partial \hat{u}_{l\alpha}}{\partial t} - \sum_{j=1}^{n_g} C_{c_g c_g,\alpha}\frac{\partial \hat{c}_{g\alpha}^j}{\partial t} \\
+ \nabla \cdot \left[\sum_{j=1}^{n_g} K_{c_g c_g,\alpha}\nabla \hat{c}_{g\alpha}^j \right] + J_{c_g,\alpha}
\end{aligned} \right] d\Omega^e = 0
\tag{4.7}
$$

Using the method of integration by parts, the weak form of equation (4.7) can be obtained. The third and fourth terms can be expressed as:

$$
\begin{aligned}
\int_{\Omega^e} N_r \nabla \cdot \left[\sum_{j=1}^{n_g} K_{c_g c_g,\alpha}\nabla \hat{c}_{g\alpha}^j \right] d\Omega^e = \int_{\Omega^e} \nabla \cdot \left[N_r \sum_{j=1}^{n_g} K_{c_g c_g,\alpha}\nabla \hat{c}_{g\alpha}^j \right] d\Omega^e \\
- \int_{\Omega^e} \sum_{j=1}^{n_g} K_{c_g c_g,\alpha} \nabla \hat{c}_{g\alpha}^j \nabla N_r d\Omega^e
\end{aligned}
\tag{4.8}
$$

and:

$$\int_{\Omega^e} N_r J_{c_g,\alpha} d\Omega^e = \int_{\Omega^e} N_r \nabla \cdot \left(c_{g\alpha}^i k_{g\alpha} \nabla z \right) d\Omega^e$$

$$= \int_{\Omega^e} \nabla \cdot \left(N_r c_{g\alpha}^i k_{g\alpha} \nabla z \right) d\Omega^e - \int_{\Omega^e} c_{g\alpha}^i k_{g\alpha} \nabla z \nabla N_r d\Omega^e$$

(4.9)

Substitution of equations (4.8) and (4.9) into the fourth and fifth terms on the right hand side of equation (4.7) yields:

$$\int_{\Omega^e} \begin{bmatrix} \nabla \cdot \left[N_r \sum_{j=1}^{n_g} K_{c_g c_g,\alpha} \nabla \hat{c}_{g\alpha}^j \right] - \sum_{j=1}^{n_g} K_{c_g c_g,\alpha} \nabla \hat{c}_{g\alpha}^j \nabla N_r \\ + \nabla \cdot \left(N_r c_{g\alpha}^i k_{g\alpha} \nabla z \right) - c_{g\alpha}^i k_{g\alpha} \nabla z \nabla N_r \\ + N_r \left[-C_{c_g l,\alpha} \frac{\partial \hat{u}_{l\alpha}}{\partial t} - \sum_{j=1}^{n_g} C_{c_g c_g,\alpha} \frac{\partial \hat{c}_{g\alpha}^j}{\partial t} \right] \end{bmatrix} d\Omega^e = 0 \qquad (4.10)$$

Using the Gauss-Green divergence theorem (e.g. Zienkiewicz and Morgan, 1982), the second order differential terms in equation (4.10) are reduced to first order and surface integrals are introduced for all elements in the domain. These integrals cancel on the shared surfaces of adjacent elements, and so only contributions from the boundary surfaces of the domain are non-zero. This gives:

$$\int_{\Omega^e} \begin{bmatrix} -\sum_{j=1}^{n_g} K_{c_g c_g,\alpha} \nabla \hat{c}_{g\alpha}^j \nabla N_r - c_{g\alpha}^i k_{g\alpha} \nabla z \nabla N_r \\ + N_r \left[-C_{c_g l,\alpha} \frac{\partial \hat{u}_{l\alpha}}{\partial t} - \sum_{j=1}^{n_g} C_{c_g c_g,\alpha} \frac{\partial \hat{c}_{g\alpha}^j}{\partial t} \right] \end{bmatrix} d\Omega^e$$

$$+ \int_{\Gamma^e} N_r \left[\sum_{j=1}^{n_g} K_{c_g c_g,\alpha} \nabla \hat{c}_{g\alpha}^j + c_{g\alpha}^i k_{g\alpha} \nabla z \right] \underline{n} d\Gamma^e = 0$$

(4.11)

where Γ^e is the element boundary surface and $\underline{n}$ is the direction cosine normal to the surface.

Introducing and expanding expressions for the derivatives of the primary variables in equation (4.11), and using vector notation produces the following expression:

$$
\sum_{j=1}^{n_g} \int_{\Omega^e} \left[K_{c_g c_g, \alpha} \nabla \mathbf{N}^T \nabla \mathbf{N} \right] d\Omega^e \, \mathbf{c}_{\mathbf{g}\alpha s}^{\mathrm{j}} + \int_{\Omega^e} \left[C_{c_g l, \alpha} \mathbf{N}^T \mathbf{N} \right] d\Omega^e \frac{\partial \mathbf{u}_{\mathbf{l}\alpha s}}{\partial t}
$$

$$
+ \sum_{j=1}^{n_g} \int_{\Omega^e} \left[C_{c_g c_g, \alpha} \mathbf{N}^T \mathbf{N} \right] d\Omega^e \frac{\partial \mathbf{c}_{\mathbf{g}\alpha s}^{\mathrm{j}}}{\partial t} + \int_{\Omega^e} \left[c_{g\alpha}^i k_{g\alpha} \mathbf{N}^T \nabla z \right] d\Omega^e \tag{4.12}
$$

$$
+ \int_{\Gamma^e} \mathbf{N}^T \left[f_{c_g, \alpha}^i \right] \underline{n} d\Gamma^e = 0
$$

where $f_{c_g, \alpha}^i$ is the approximate pore gas flux normal to the boundary surface, $\mathbf{N}$ is the shape function matrix and the terms $\mathbf{u}_{\mathbf{l}\alpha s}$ and $\mathbf{c}_{\mathbf{g}\alpha s}^{\mathrm{j}}$ are the vectors of the pore water pressure and gas concentrations at nodes, respectively.

Equation (4.12) can be rewritten in a concise matrix form as:

$$
\mathbf{C}_{\mathbf{c_g l}, \alpha} \frac{\partial \mathbf{u}_{\mathbf{l}\alpha s}}{\partial t} + \sum_{j=1}^{n_g} \mathbf{C}_{\mathbf{c_g c_g}, \alpha} \frac{\partial \mathbf{c}_{\mathbf{g}\alpha s}^{\mathrm{j}}}{\partial t} + \sum_{j=1}^{n_g} \mathbf{K}_{\mathbf{c_g c_g}, \alpha} \, \mathbf{c}_{\mathbf{g}\alpha s}^{\mathrm{j}} = \mathbf{f}_{\mathbf{c_g}, \alpha}^{\mathrm{i}} \tag{4.13}
$$

where for a domain with n_{elem} elements:

$$
\mathbf{C}_{\mathbf{c_g l}, \alpha} = \sum_{e=1}^{n_{elem}} \int_{\Omega^e} \left[C_{c_g l, \alpha} \mathbf{N}^T \mathbf{N} \right] d\Omega^e \tag{4.14}
$$

$$
\mathbf{C}_{\mathbf{c_g c_g}, \alpha} = \sum_{e=1}^{n_{elem}} \int_{\Omega^e} \left[C_{c_g c_g, \alpha} \mathbf{N}^T \mathbf{N} \right] d\Omega^e \tag{4.15}
$$

$$
\mathbf{K}_{\mathbf{c_g c_g}, \alpha} = \sum_{e=1}^{n_{elem}} \int_{\Omega^e} \left[K_{c_g c_g, \alpha} \nabla \mathbf{N}^T \nabla \mathbf{N} \right] d\Omega^e \tag{4.16}
$$

$$
\mathbf{f}_{\mathbf{c_g}, \alpha}^{\mathrm{i}} = \sum_{e=1}^{n_{elem}} \int_{\Omega^e} \left[c_{g\alpha}^i k_{g\alpha} \mathbf{N}^T \nabla z \right] d\Omega^e - \sum_{e=1}^{n_{elem}} \int_{\Gamma^e} \mathbf{N}^T \left[f_{c_g, \alpha}^i \right] \underline{n} d\Gamma^e \tag{4.17}
$$

The formulation presented in this section can be repeated for any number of chemical components.

For completeness, the final forms of the spatially discretised equations for pore water transfer and multicomponent dissolved chemical transport are presented in the following sections.

4.2.2   Spatial Discretisation for Pore Water Transfer

Repeating the formulation in section 4.2.1 for the pore water pressure primary variable, $u_{l\alpha}$, in dual porosity media yields:

$$\mathbf{C_{ll,\alpha}} \frac{\partial \mathbf{u_{l\alpha s}}}{\partial t} + \sum_{j=1}^{n_g} \mathbf{C_{lc_g,\alpha}} \frac{\partial \mathbf{c_{g\alpha s}^j}}{\partial t} + \mathbf{K_{ll,\alpha} u_{l\alpha s}} = \mathbf{f_{l,\alpha}} \tag{4.18}$$

where:

$$\mathbf{C_{ll,\alpha}} = \sum_{e=1}^{n_{elem}} \int_{\Omega^e} \left[C_{ll,\alpha} \mathbf{N}^T \mathbf{N} \right] d\Omega^e \tag{4.19}$$

$$\mathbf{C_{lc_g,\alpha}} = \sum_{e=1}^{n_{elem}} \int_{\Omega^e} \left[C_{lc_g,\alpha} \mathbf{N}^T \mathbf{N} \right] d\Omega^e \tag{4.20}$$

$$\mathbf{K_{ll,\alpha}} = \sum_{e=1}^{n_{elem}} \int_{\Omega^e} \left[K_{ll,\alpha} \nabla \mathbf{N}^T \nabla \mathbf{N} \right] d\Omega^e \tag{4.21}$$

$$\mathbf{f_{l,\alpha}} = \sum_{e=1}^{n_{elem}} \int_{\Omega^e} [\rho_l k_{l\alpha} \mathbf{N}^T \nabla z] d\Omega^e - \sum_{e=1}^{n_{elem}} \int_{\Gamma^e} \mathbf{N}^T [f_{l,\alpha}] \underline{n} d\Gamma^e \tag{4.22}$$

where $f_{l,\alpha}$ is the approximate total pore water flux normal to the boundary surface.

4.2.3   Spatial Discretisation for Multicomponent Dissolved Chemical Transport Equations

Repeating the formulation in section 4.2.1 for the dissolved chemical concentration primary variables, $c_{d\alpha}^i$, in dual porosity media yields:

$$\begin{aligned}
&\mathbf{C_{c_d l,\alpha}} \frac{\partial \mathbf{u_{l\alpha s}}}{\partial t} + \sum_{j=1}^{n_g} \mathbf{C_{c_d c_g,\alpha}} \frac{\partial \mathbf{c_{g\alpha s}^j}}{\partial t} + \sum_{j=1}^{n_g} \mathbf{C_{c_d c_d,\alpha}} \frac{\partial \mathbf{c_{d\alpha s}^j}}{\partial t} \\
&+ \mathbf{K_{c_d l,\alpha} u_{l\alpha s}} + \sum_{j=1}^{n_g} \mathbf{K_{c_d c_d,\alpha}} \, \mathbf{c_{d\alpha s}^j} = \mathbf{f_{c_d,\alpha}^i}
\end{aligned} \tag{4.23}$$

where:

$$\mathbf{C_{c_d l,\alpha}} = \sum_{e=1}^{n_{elem}} \int_{\Omega^e} \left[C_{c_d l,\alpha} \mathbf{N}^T \mathbf{N} \right] d\Omega^e \tag{4.24}$$

$$\mathbf{C_{c_d c_g},\alpha} = \sum_{e=1}^{n_{elem}} \int_{\Omega^e} \left[C_{c_d c_g,\alpha} \mathbf{N}^T \mathbf{N} \right] d\Omega^e \tag{4.25}$$

$$\mathbf{C_{c_d c_d},\alpha} = \sum_{e=1}^{n_{elem}} \int_{\Omega^e} \left[C_{c_d c_d,\alpha} \mathbf{N}^T \mathbf{N} \right] d\Omega^e \tag{4.26}$$

$$\mathbf{K_{c_d l},\alpha} = \sum_{e=1}^{n_{elem}} \int_{\Omega^e} \left[K_{c_d l,\alpha} \nabla \mathbf{N}^T \nabla \mathbf{N} \right] d\Omega^e \tag{4.27}$$

$$\mathbf{K_{c_d c_d},\alpha} = \sum_{e=1}^{n_{elem}} \int_{\Omega^e} \left[K_{c_d c_d,\alpha} \nabla \mathbf{N}^T \nabla \mathbf{N} \right] d\Omega^e \tag{4.28}$$

$$\mathbf{f_{c_d},\alpha} = \sum_{e=1}^{n_{elem}} \int_{\Omega^e} \left[c_{d\alpha}^i k_{l\alpha} \mathbf{N}^T \nabla z \right] d\Omega^e - \sum_{e=1}^{n_{elem}} \int_{\Gamma^e} \mathbf{N}^T \left[f_{c_d,\alpha}^i \right] \underline{n} d\Gamma^e \tag{4.29}$$

where $f_{c_d,\alpha}^i$ is the approximate total dissolved chemical flux normal to the boundary surface.

4.3 Temporal Discretisation and Matrix Representation of Governing Equations

To determine the values of the primary variables over time, a numerical algorithm for temporal discretisation has been used. In this work a fully implicit mid-interval backward-difference time-stepping algorithm is employed. This approach has been shown to provide a suitable solution for highly non-linear equations similar to those presented in the present work (Cook, 1981; Thomas et al., 1998).

The sets of spatially discretised equations for pore water transfer, multicomponent pore gas transport and multicomponent solute transport were developed in section 4.2. These equations are presented in a matrix form in Figure 4.1. The null entries in the coefficient matrices reflect that a time splitting technique, i.e. the SNIA, has been used to handle the interactions between the fracture and matrix continua. In this approach, the solutions to the transport equations in the fracture and matrix continua are handled separately until the convergence criterion has been met. The converged transport solution is then passed to the mass exchange module, which calculates the interactions between the continua in the time step. The SNIA is described in greater detail in section 4.4.

$$
\begin{bmatrix}
C_{ll,F} & 0 & C_{lc_d^{1\to nd},F} & 0 & C_{lc_g^{1\to ng},F} & 0 \\
0 & C_{ll,M} & 0 & C_{lc_d^{1\to nd},M} & 0 & C_{lc_g^{1\to ng},M} \\
C_{c_d^{1\to nd}l,F} & 0 & C_{c_d^{1\to nd}c_d^{1\to nd},F} & 0 & C_{c_d^{1\to nd}c_g^{1\to ng},F} & 0 \\
0 & C_{c_d^{1\to nd}l,M} & 0 & C_{c_d^{1\to nd}c_d^{1\to nd},M} & 0 & C_{c_d^{1\to nd}c_g^{1\to ng},M} \\
C_{c_g^{1\to ng}l,F} & 0 & C_{c_g^{1\to ng}c_d^{1\to nd},F} & 0 & C_{c_g^{1\to ng}c_g^{1\to ng},F} & 0 \\
0 & C_{c_g^{1\to ng}l,M} & 0 & C_{c_g^{1\to ng}c_d^{1\to nd},M} & 0 & C_{c_g^{1\to ng}c_g^{1\to ng},M}
\end{bmatrix}
\times
\begin{bmatrix}
\dot{u}_{lFs} \\
\dot{u}_{lMs} \\
\dot{c}_{dFs}^{1\to nd} \\
\dot{c}_{dMs}^{1\to nd} \\
\dot{c}_{gFs}^{1\to ng} \\
\dot{c}_{gMs}^{1\to ng}
\end{bmatrix}
$$

$$
+
\begin{bmatrix}
K_{ll,F} & 0 & K_{lc_d^{1\to nd},F} & 0 & K_{lc_g^{1\to ng},F} & 0 \\
0 & K_{ll,M} & 0 & K_{lc_d^{1\to nd},M} & 0 & K_{lc_g^{1\to ng},M} \\
K_{c_d^{1\to nd}l,F} & 0 & K_{c_d^{1\to nd}c_d^{1\to nd},F} & 0 & K_{c_d^{1\to nd}c_g^{1\to ng},F} & 0 \\
0 & K_{c_d^{1\to nd}l,M} & 0 & K_{c_d^{1\to nd}c_d^{1\to nd},M} & 0 & K_{c_d^{1\to nd}c_g^{1\to ng},M} \\
K_{c_g^{1\to ng}l,F} & 0 & K_{c_g^{1\to ng}c_d^{1\to nd},F} & 0 & K_{c_g^{1\to ng}c_g^{1\to ng},F} & 0 \\
0 & K_{c_g^{1\to ng}l,M} & 0 & K_{c_g^{1\to ng}c_d^{1\to nd},M} & 0 & K_{c_g^{1\to ng}c_g^{1\to ng},M}
\end{bmatrix}
\times
\begin{bmatrix}
u_{lFs} \\
u_{lMs} \\
c_{dFs}^{1\to nd} \\
c_{dMs}^{1\to nd} \\
c_{gFs}^{1\to ng} \\
c_{gMs}^{1\to ng}
\end{bmatrix}
+
\begin{bmatrix}
f_{l,F} \\
f_{l,M} \\
f_{c_d,F}^{1\to nd} \\
f_{c_d,M}^{1\to nd} \\
f_{c_g,F}^{1\to nd} \\
f_{c_g,M}^{1\to nd}
\end{bmatrix}
=
\begin{bmatrix}
0 \\ 0 \\ 0 \\ 0 \\ 0 \\ 0
\end{bmatrix}
$$

Figure 4.1 Matrix representation of the spatially discretised governing equations, with the terms $\dot{\mathbf{u}}_{lFs}$, $\dot{\mathbf{u}}_{lMs}$, $\dot{\mathbf{c}}_{dFs}^{1\to nd}$, $\dot{\mathbf{c}}_{dMs}^{1\to nd}$, $\dot{\mathbf{c}}_{gFs}^{1\to ng}$ and $\dot{\mathbf{c}}_{gMs}^{1\to ng}$ represent the temporal derivatives of the pore water pressure, solute concentrations and pore gas concentrations in the dual porosity system, respectively. For convenience, the multicomponent system is represented by the superscript $\mathbf{1 \to nd}$ and $\mathbf{1 \to ng}$.

Using compact notation, the matrices in Figure 4.1 can then be conveniently expressed as:

$$\mathbf{A}\phi + \mathbf{B}\frac{\partial \phi}{\partial t} + \mathbf{C} = \{0\} \tag{4.30}$$

where $\mathbf{A}$, $\mathbf{B}$ and $\mathbf{C}$ are the matrices of coefficients and ϕ is the vector of primary variables.

Application of the fully-implicit mid-interval backward-difference time-stepping algorithm to equation (4.30) yields (Thomas et al., 1998):

$$\mathbf{A}^{\phi_l}[(1-\Theta)\phi^{\mathrm{n}} + \Theta\phi^{\mathrm{n}+1}] + \mathbf{B}^{\phi_l}\left[\frac{\phi^{\mathrm{n}+1} - \phi^{\mathrm{n}}}{\Delta t}\right] + \mathbf{C}^{\phi_l} = \{0\} \tag{4.31}$$

where Θ is an integration constant equal to 1 for an implicit time integration scheme, 0.5 for a Crank-Nicholson scheme and 0 for an explicit scheme. The superscript parameter ϕ_l denotes the level at which the matrices $\mathbf{A}$, $\mathbf{B}$ and $\mathbf{C}$ are evaluated, and can be expressed in general as:

$$\phi_l = \vartheta(n+1) + (1-\vartheta)(n) \tag{4.32}$$

where ϑ is a constant that defines the interval for which the matrices of coefficients are evaluated. For the fully implicit mid-interval algorithm used in this work the constants Θ and ϑ take the values of 1 and 0.5, respectively.

Substitution of these constants into equation (4.31) produces:

$$\mathbf{A}^{\mathrm{n}+1/2}\phi^{\mathrm{n}+1} + \mathbf{B}^{\mathrm{n}+1/2}\left[\frac{\phi^{\mathrm{n}+1} - \phi^{\mathrm{n}}}{\Delta t}\right] + \mathbf{C}^{\mathrm{n}+1/2} = \{0\} \tag{4.33}$$

Equation (4.33) can be rearranged to give:

$$\phi^{\mathrm{n}+1} = \left[\mathbf{A}^{\mathrm{n}+1/2} + \frac{\mathbf{B}^{\mathrm{n}+1/2}}{\Delta t}\right]^{-1}\left[\frac{\mathbf{B}^{\mathrm{n}+1/2}\phi^{\mathrm{n}}}{\Delta t} - \mathbf{C}^{\mathrm{n}+1/2}\right] \tag{4.34}$$

In order to obtain the solution for $\phi^{\mathrm{n}+1}$ in equation (4.34) the values of the matrices of coefficients is required at the mid-interval. Hence, a direct solution is not available and an iterative solution procedure called a predictor-corrector algorithm is used, which takes the

following form:

i. Evaluation of matrices $\mathbf{A}$, $\mathbf{B}$ and $\mathbf{C}$ at time n. This first estimate is termed the predictor.

ii. An estimate of the matrices $\mathbf{A}$, $\mathbf{B}$ and $\mathbf{C}$ at the mid-interval time $n + 1/2$ is made based on the values of the predictor and the previous time step. This is termed the corrector.

iii. Convergence is evaluated using one of the following conditions:

$$\left| \phi_{iC}^{n+1} - \phi_{(i-1)C}^{n+1} \right| < \mathbf{TL}_{abs} \qquad (4.35)$$

$$\left| \frac{\phi_{iC}^{n+1} - \phi_{(i-1)C}^{n+1}}{\phi_{(i-1)C}^{n+1}} \right| < \mathbf{TL}_{rel} \qquad (4.36)$$

where i is the iteration level, subscript C indicates the use of the corrector value and $\mathbf{TL}_{abs}$ and $\mathbf{TL}_{rel}$ are the matrices of absolute and relative tolerances, respectively.

iv. If the convergence criterion specified in stage iii is not satisfied, the algorithm returns to stage ii where the corrector becomes the new predictor. However, if convergence has been achieved the analysis moves onto the next time step and the procedure is repeated.

A number of factors control the number of iterations required to achieve convergence in the predictor-corrector algorithm. These include the simulation conditions, the variable gradients, the assigned material parameters and the time step size. To improve the efficiency of the solution procedure a variable time step is used. If the number of iterations exceeds a user specified value then the time step size is reduced by a factor. Likewise, if convergence is achieved in less iteration than a specified value the time step size is increased by a factor.

This model has been incorporated in a computer code COMPASS, the **Co**de for **M**odelling **Pa**rtially **S**aturated **S**oils, which has been incrementally developed at the Geoenvironemtnal Reseach Centre (GRC), Cardiff University (e.g. Thomas et al., 1998).

The types of boundary conditions that can be adopted in COMPASS have been discussed

by Thomas and He (1998). Flow problems involving only flow variables, these can be summarised here as:

  i. Dirichlet condition (prescribed value of $\omega_\alpha = \omega_\alpha^*$ on boundary Γ^d)

 ii. Neumann condition (prescribed flux $J_\alpha = J_\alpha^*$ on boundary Γ^n)

iii. Cauchy condition (prescribed convection condition on boundary Γ^c)

4.4   Coupling Between Transport and Exchange/Reaction Terms

As reported earlier in the chapter, the sequential non-iterative approach (SNIA) is used to couple the transport terms with the geochemical reaction and mass exchange terms in the governing flow equations. Time splitting methods such as the SNIA have been successfully used in previous studies to couple COMPASS with geochemical reaction models such as MINTEQA2 and PHREEQC (Seetharam, 2003; Sedighi, 2011; Masum, 2012). The coupling with external models was explained in detail in the cited works and is not covered here. In this study, COMPASS modules have been specifically developed to include non-equilibrium adsorption/desorption reactions and mass exchange between the fracture and matrix continua. The use of the SNIA in coupling these modules with the transport module is now detailed.

Sequential methods have been developed to overcome the large computational cost associated with solving the transport and reaction terms simultaneously, which is referred to as the global implicit method (Kee et al., 1987; Steefel and Lasaga, 1994). The SNIA is a time splitting approach in which the transport stage and exchange/reaction stages are completed sequentially in each time step (Steefel and Macquarrie, 1996). In other words, the transport equations are first solved before being modified in the mass exchange and adsorption/desorption modules. A coupled solution at each time step is obtained once the transport solution has satisfied the convergence criterion and then been modified for the mass exchange and adsorption/desorption. The analysis then moves forward to the next step.

The first stage of the computation in each time step using the SNIA involves only the transport processes. It can be expressed mathematically as (Steefel and MacQuarrie, 1996):

$$\frac{\left(c_{r\alpha}^i\right)^{Transport} - \left(c_{r\alpha}^i\right)^{n}}{\Delta t} = L\left(\mathrm{J}_{c_{r\alpha}^i}\right)^{n} \tag{4.37}$$

where subscript r becomes d for solute concentrations and g for gas concentrations, superscript n denotes the time step and L is the spatial operator applying to the fluxes $\mathrm{J}_{c_{r\alpha}^i}$.

In equation (4.37), the changes in chemical concentrations associated with the transport processes are obtained using the values obtained from the previous time step, n. The new values are then modified to account for the inter-continua mass exchange and adsorption/desorption reactions.

The sink/source term for mass exchange is evaluated first, giving the following expressions for pore water pressure and chemical concentrations:

$$\frac{(u_{l\alpha})^{Exchange} - (u_{l\alpha})^{Transport}}{\Delta t} = R_{u_l}^{Ex} \tag{4.38}$$

$$\frac{\left(c_{r\alpha}^i\right)^{Exchange} - \left(c_{r\alpha}^i\right)^{Transport}}{\Delta t} = R_{i}^{Ex} \tag{4.39}$$

where R_{l}^{Ex} and R_{i}^{Ex} denote the rate of mass exchange between the fracture and matrix continua for pore water and the ith chemical component, respectively.

Together, equations (4.37), (4.38) and (4.39) give the solution for non-reactive multiphase flow through a fractured rock. Adsorption/desorption is included for reactive chemical components in a similar manner, as:

$$\frac{\left(c_{r\alpha}^i\right)^{n+1} - \left(c_{r\alpha}^i\right)^{Exchange}}{\Delta t} = R_{i}^{Ad} \tag{4.40}$$

where R_{i}^{Ad} denotes the rate of the adsorption/desorption reaction for the ith component.

A summary of the SNIA used to couple transport and exchange/reaction processes in this study is provided in Figure 4.2.

4.5   Conclusions

A numerical solution has been developed in this chapter that provides a solution to the highly coupled and non-linear sets of equations given in chapter 3 for reactive flow in fractured rock. Application of the finite element method for the spatial discretisation of the governing equations was described in detail for multicomponent reactive gas transport. The spatially discretised equations for pore water transfer and multicomponent solute transport have been given in summary form. A mid-interval backward-difference scheme was employed to achieve temporal discretisation.

A sequential non-iterative approach (SNIA) has been adopted to couple the transport equations and non-equilibrium sink/source terms for inter-continua mass exchange and geochemical reactions, such as adsorption/desorption. In each time step the transport equations are first solved in each continuum with no exchange/reaction. Once the transport equations have converged, the values of the primary flow variables are modified accordingly in the mass exchange and reaction modules.

The numerical formulation described in this chapter has been incorporated into the COMPASS computer code. The developed solution will be tested and compared against a series of benchmarks in chapter 5 for the purpose of verification.
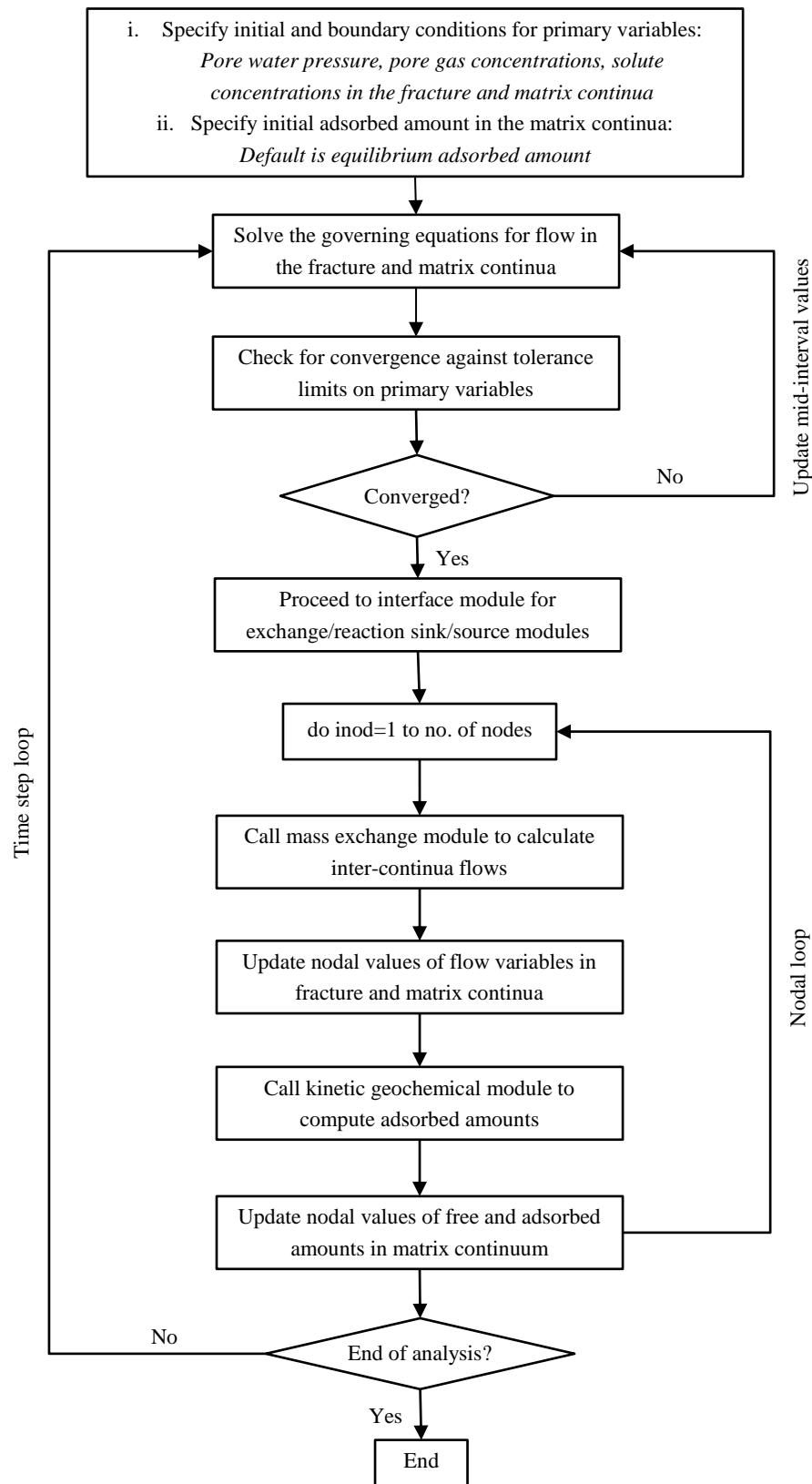
Figure 4.2 Flowchart of the sequential non-iterative approach (SNIA) adopted for coupling the transport and exchange/reaction modules in COMPASS.

4.6   References

Cleall, P.J. (1998). *An investigation of the thermo/hydraulic/mechanical nehaviour of unsaturated soils, including expansive clays*. PhD Thesis, Cardiff University, Cardiff.

Cook, R.D. (1981). *Concepts and applications of finite element analysis*. John Wiley and Sons, New York.

Huebner, K.H. and Thornton, E.A. (1982). *The finite element method for Engineers*. John Wiley and Sons, New York.

Kee, R.J., Petzold, L.R., Smooke, M.D. and Grcar, J.F. (1985). Implicit methods in combustion and chemical kinetics modelling. In: Brackbill and Cohen, eds. *Multiple Time Scales*. Academic Press, New York.

Lewis, R.W. and Schrefler, B.A. (1998). *The finite element method in the static and dynamic deformation and consolidation of porous media*. 2nd Edition. John Wiley and Sons, Chichester, England.

Masum, S.A. (2012). *Modelling of reactive gas transport in unsaturated soil – a coupled thermo-hydro-chemical-mechanical approach*. PhD Thesis, Cardiff University, Cardiff.

Ramesh, A.D. (1996). *Modelling the thero/hydraulic/mechanical behaviour of unsaturated soil using an elasto-plastic constitutive relationship*. PhD Thesis, University of Wales, Cardiff.

Sedighi, M. (2011). *An investigation of hydro-geochemical processes in coupled thermal, hydraulic, chemical and mechanical behaviour of unsaturated soils*. PhD Thesis, Cardiff University, Cardiff.

Seetharam, S.C. (2003). *An investigation of the thermro/hydro/chemical/mechanical behaviour of unsaturated soils*. Ph.D. Thesis, Cardiff University, Wales, UK.

Seetharam, S.C., Thomas, H.R. and Cleall, P.J. (2007). Coupled thermo-hydro-chemical-mechanical model for unsaturated soils – Numerical algorithm. *International Journal of Numerical Methods in Engineering*, **70**, 1480-1511.

Steefel, C.I. and Lasaga, A.C. (1994). A coupled model for transport of multiple chemical species and kinetic precipitation/dissolution reactions with application to reactive flow in single phase hydrothermal systems. *American Journal of Science*, **294**, 529-592.

Steefel, C.I. and MacQuarrie, K.T.B. (1996). Approaches to modelling of reactive transport in porous media. In: Lichtner et al., eds. *Reactive transport in porous media, Reviews in Mineralogy, 34*. Mineralogical Society of America, Washington, DC.

Thomas, H.R. and He, Y. (1995). Analysis of coupled heat, moisture and air transfer in a deformable unsaturated soil. *Géotechnique*, **45**(4), 677-689.

Thomas, H.R., Rees, S.W. and Sloper, N.J. (1998). Three-dimensional heat, moisture and air transfer in unsaturated soils. *International Journal of Numerical and Analytical Methods in Geomechanics*. **22**(2), 75-95.

Thomas, H.R., Sedighi, M. and Vardon, P.J. (2012). Diffusive reactive transport of multicomponent chemicals under coupled thermal, hydraulic, chemical and mechanical conditions. *Geotechnical and Geological Engineering*, **30**(4), 841-857.

Vardon, P.J. (2009). *A three-dimensional numerical investigation of the thermo-hydro-mechanical behaviour of a large-scale prototype repository*. PhD Thesis, Cardiff University, Cardiff.

Zienkiewicz, O.C. and Morgan, K. (1982). *Finite elements and approximation*. John Wiley and Sons, New York.

Zienkiewicz, O.C. and Taylor, R.L. (1989). *The finite element method*. 4th Edition. McGraw Hill, New York.

5

Model Verification

5.1   Introduction

To allow the model developed in chapters 3 and 4 to be employed for predictive purposes, a series of verification tests have been performed to: (i) assess the accuracy of the implementation of the theoretical and numerical formulations in the model, and (ii) achieve a further confidence in the reliability of the solution algorithms applied. Verification tests are performed to ensure that the solution algorithm of the model is correct, whilst validation tests are applied to ensure that the underlying theory accurately reflects the material behaviour and processes involved. In this chapter, the verification benchmarks, simulation conditions and results achieved for a range of tests are presented. The validation of the numerical model is the core objective in chapter 6, where the model is applied at the laboratory scale and the results are compared with a series of experimental data.

The main objective of the verification exercises presented is to evaluate the capabilities of the model related to: (i) reactive flow in fractured rock, particularly multicomponent real gas transport, (ii) inter-porosity mass exchange, and (iii) adsorption/desorption kinetics. Verification of the model for the above components is achieved using analytical solutions

or alternative numerical solutions.

A number of studies have examined the accuracy of the theoretical and numerical implementation in COMPASS for cases involving coupled moisture, air, heat and deformation (e.g. King, 1991; Sansom, 1995). Mitchell (2002) performed further verification tests for coupled thermal, hydraulic and mechanical behaviour following developments made by Thomas and He (1995), Thomas and Sansom (1995), Thomas and He (1998), Thomas et al. (1998) and Cleall (1998). Extensive verification and validation of the multicomponent dissolved chemical module was completed by Seetharam (2003) and Sedighi (2011), and the multicomponent gas module was verified by Masum (2012). The tests presented in this work are concerned with the new developments in the formulation for coupled hydro-gas-chemical behaviour in fractured rock, including high pressure gas transport.

The verification test presented in section 5.2 evaluates the implementation of the non-reactive fracture and matrix gas transport equations for a single chemical/gas component in one dimension. Since this test is concerned with examining the advective and diffusive transport mechanisms, the mass exchange between the continua is not included. This simplification allows comparisons to be made with the results obtained using the analytical solution for advective-diffusive transport presented by Ogata and Banks (1961).

Section 5.3 considers a verification test for the development of a steady state gas concentration profile due to gas injection and abstraction in a single porosity medium. The results are compared with a steady state analytical solution to verify that the predicted gas concentration profile follows that expected for a highly compressible fluid.

Verification tests for multicomponent gas transport at high pressure with adsorption/desorption reaction kinetics are presented in section 5.4. With reference to section 3.4.2, the advective flux of multicomponent gas is modelled as a non-segregative transport phenomenon (Mason et al., 1967). The test considers a single porosity medium and adsorption/desorption is modelled using the reaction kinetics model developed in section 3.4.4. In addition, appropriate models are used to determine the properties of the gas at high pressure, taking into account real gas behaviour. The results from a numerical

modelling study presented by Pini et al. (2011) provide a benchmark for these tests. The simulations involve the displacement of methane by gas injected at high pressure in coal. Two injection scenarios are considered to complete this verification, namely, pure carbon dioxide and pure nitrogen.

In section 5.5, the coupling between the transport module and geochemical reaction module for adsorption/desorption kinetics is examined. The simulations consider a constant pore water flux and solute transport at a range of reaction rates. Results are compared with those obtained by Šimůnek and van Genuchten (2008) using the HYDRUS-1D code.

The results for dual porosity, dual permeability simulations, presented by Šimůnek and van Genuchten (2008), are used in section 5.6 to verify the coupling scheme between the transport and inter-porosity mass exchange components of the model. The simulations involve chemical transport in the fracture and matrix continua under fully saturated conditions with constant pore water fluxes and non-equilibrium mass exchange. The results obtained using COMPASS and HYDRUS-1D are compared for a range of chemical mass exchange rates.

Finally, the major conclusions from the verification tests are provided in section 5.8.

5.2   Gas Advection and Diffusion in One Dimension (Test I)

Pore gas transport occurs due to advective and diffusive flux components, as discussed in section 3.4.2. The verification exercise presented in this section examines the pure diffusive and advective-diffusive transport of an ideal gas component in one dimension in a fractured rock. It has been assumed that flow in the fracture and matrix continua occurs independently (i.e. there is no mass exchange between the fracture and matrix continua). This allows the results obtained from the numerical model to be compared with an analytical solution presented by Ogata and Banks (1961). The main objective of the exercise is to assess the accuracy of the numerical model in predicting the transient distribution of a gas component, subject to the different flow regimes that exist in the fracture network and matrix blocks of a fractured rock.

5.2.1   Analytical Solution

For the case of one dimensional transport of a single ideal gas component in a homogenous isotropic porous medium, the advection-diffusion equation can be expressed as:

$$\frac{\partial c_{g\alpha}}{\partial t} = D_{ge\alpha}\frac{\partial^2 c_{g\alpha}}{\partial x^2} - \mathbf{v_{gs\alpha}}\frac{\partial c_{g\alpha}}{\partial x} \tag{5.1}$$

where x is the distance in the direction of flow and $\mathbf{v_{gs\alpha}}$ is the gas seepage velocity. All other symbols have been defined previously in chapter 3. It is again noted that the subscript α becomes F to denote the fracture network and M to denote the matrix blocks.

Ogata and Banks (1961) presented an analytical solution to equation (5.1) considering the following initial and boundary conditions:

$$c_{g\alpha}(x, 0) = C_i \tag{5.2}$$

$$c_{g\alpha}(0, t) = C_0 \tag{5.3}$$

$$\frac{\partial c_{g\alpha}(\infty, t)}{\partial t} = 0 \tag{5.4}$$

The analytical solution given by Ogata and Banks (1961) is as follows:

$$\begin{aligned}
c_{g\alpha}(x, t) = C_i + \frac{C_0 - C_i}{2}\Bigg[& erfc\left(\frac{x - \mathbf{v_{gs\alpha}}t}{2\sqrt{D_{ge\alpha}t}}\right) \\
& + exp\left(\frac{\mathbf{v_{gs\alpha}}x}{D_{ge\alpha}}\right)erfc\left(\frac{x + \mathbf{v_{gs\alpha}}t}{2\sqrt{D_{ge\alpha}t}}\right)\Bigg]
\end{aligned} \tag{5.5}$$

Equation (5.5) has been used to calculate the gas concentration profiles for comparison with the results obtained using the numerical model.

5.2.2   Pure Diffusion (Test I-a)

By setting the seepage velocities $\mathbf{v_{gs\alpha}}$ in equation (5.5) to zero, the solution reduces to that for pure diffusion. The numerical simulation was performed using a 1 m by 0.1 m two dimensional domain. Flow was constrained to the x direction since the effects of gravity were ignored and there were no imposed gradients in the y direction.

5.2.2.1 Simulation Conditions

The simulation domain described above was discretised into 100 equally sized 4-noded quadrilateral elements. The model was run with initial and maximum time steps of 10 and 360 seconds, respectively, for a simulation period of 4 hours. Figure 5.1 provides a summary of the initial and boundary conditions which were applied to the domain. Initially, the porous medium contained no gas and boundary conditions were prescribed for a constant source (i.e. $x = 0$ m) concentration of 10 mol m^{-3} and a fixed concentration of 0 mol m^{-3} at the far field boundary (i.e. $x = 1$ m). The system remained dry and isothermal at 318 K.

Injection boundary conditions	Initial conditions	Far field boundary conditions
$c_{gF} = c_{gM} = C_i = 10.0\ mol\ m^{-3}$	$c_{gF} = c_{gM} = C_0 = 0.0\ mol\ m^{-3}$	$\dfrac{\partial c_{gF}}{\partial t} = \dfrac{\partial c_{gM}}{\partial t} = 0.0$

Figure 5.1 Schematic of the initial and boundary conditions applied for the pure diffusion simulation (Test I-a) and advection-diffusion simulation (Test I-b).

Table 5.1 details the material parameters that were applied. The values of the porosity were chosen to reflect that the matrix block pore region in a fractured rock occupies a greater fraction of the total pore volume than the fracture network. Carbon dioxide (CO_2) was used as the diffusing component and the free air diffusion coefficient at standard conditions was set to a representative value based on data provided in Cussler (1997). The effective diffusion coefficient in equation (5.5) was calculated using the Millington and Quirk (1961) tortuosity relationship.

5.2.2.2 Results and Discussion

Figure 5.2 presents the CO_2 concentration profiles for pure diffusion in the fracture and matrix continua, which were obtained using the analytical solution and numerical model. A greater diffusive flux is observed in the matrix continuum because its higher porosity implies a less tortuous diffusion path, thereby yielding a higher effective diffusion coefficient.

There is a good agreement between the two sets of results in Figure 5.2, indicating that the

diffusive transport mechanism has been implemented correctly in the transport module for the case of a single gas component.

Table 5.1 Material parameters for the pure diffusion simulation (Test I-a).

Material parameter	Relationship / value
Fracture porosity, n_F (-)	0.10
Matrix porosity, n_M (-)	0.20
Free diffusion coefficient, $D_{g\alpha}$ (m^{2}s^{-1})	1.25×10^{-5}
Tortuosity (Millington and Quirk, 1961), $\tau_{g\alpha}$ (-)	$\left(n_\alpha S_{g\alpha}\right)^{10/3} / n_\alpha{}^2$
Degree of gas saturation, $S_{g\alpha}$ (-)	1.0
Temperature, T (K)	318
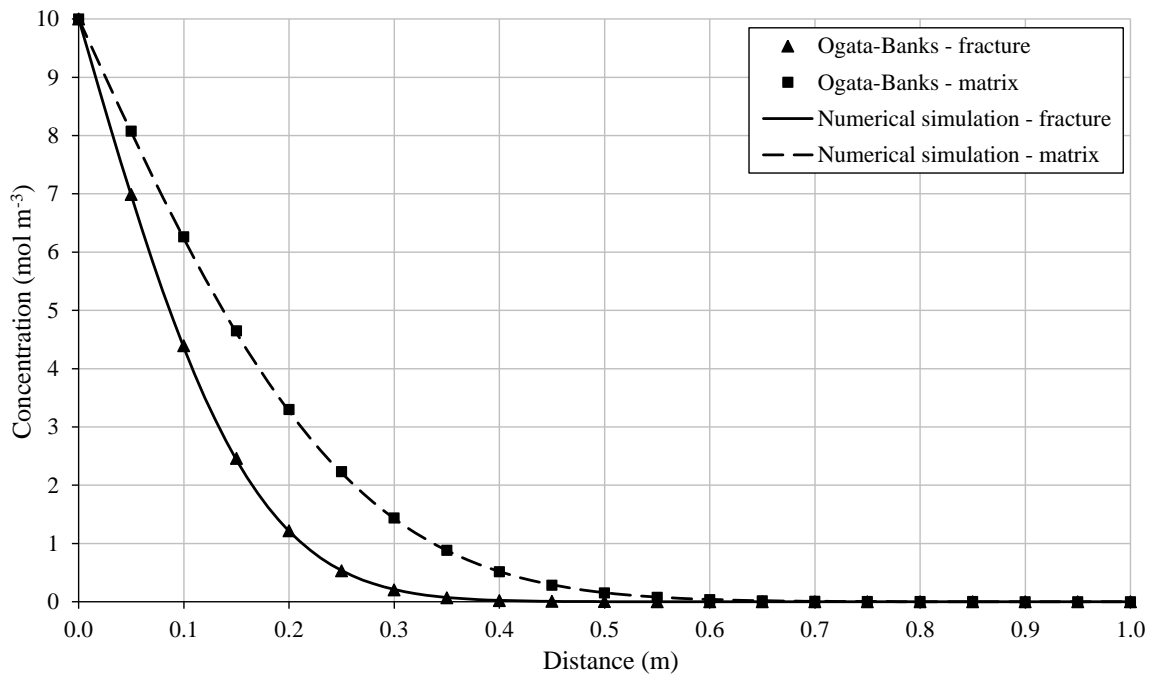
Figure 5.2 Gas concentration profiles in the fracture and matrix continua after 4 hours of simulation for the diffusion only case (Test I-a).

5.2.3   Advection and Diffusion

In the exercise presented in this section, the same simulation conditions as those given in

the previous section for pure diffusion were adopted, except that the advective flux component was activated in each continuum. The additional material parameters required to calculate the advective flux components in the model are given in Table 5.2. The intrinsic permeability in the fracture continuum was set to one order of magnitude larger than in the matrix continuum. This reflects that the fractures provide the major flow conduits in a fractured rock (Gilman and Kazemi, 1983).

Table 5.2 Additional material parameters for the advective-diffusive simulation (Test I-b).

Material parameter	Relationship / value
Fracture intrinsic permeability, K_F (m^2)	1.0×10^{-15}
Matrix intrinsic permeability, K_M (m^2)	1.0×10^{-16}
Gas dynamic viscosity, $\mu_{g\alpha}$ (Pa s)	1.8×10^{-5}

Equation (5.5) describes the combined effect of advection and diffusion if both the seepage velocity, $\mathbf{v_{gs\alpha}}$, and the effective diffusion coefficient, $D_{ge\alpha}$, are defined. Darcy's law was used to calculate $\mathbf{v_{gs\alpha}}$, given by (Delleur, 1999):

$$\mathbf{v_{gs\alpha}} = \frac{\mathbf{v_{g\alpha}}}{n_\alpha} = \frac{K_\alpha}{n_\alpha \mu_{g\alpha}} \frac{RT(C_i - C_0)}{L} \tag{5.6}$$

where $\mathbf{v_{g\alpha}}$ is the Darcy velocity and L is the length of the domain, i.e. 1 m.

It is noted that equation (5.6) assumes a linear gas concentration gradient across the domain due to the imposed boundary conditions. In other words, the concentration gradient is assumed to be the steady state gradient neglecting the gas compressibility. As a result, the values of $\mathbf{v_{gs\alpha}}$ obtained were approximations of the average velocities for the scenario considered. Substituting for the parameters in equation (5.6) using the boundary conditions given in Figure 5.1 and the material parameters given in Table 5.1 and Table 5.2 gave $\mathbf{v_{gsF}} = 1.47 \times 10^{-5}$ ms^{-1} and $\mathbf{v_{gsM}} = 7.34 \times 10^{-7}$ ms^{-1}. These values were used in the analytical solution.

5.2.3.1   Results and Discussion

The concentration profiles for advective-diffusive flow in the fracture and matrix continua have been obtained using the analytical solution and numerical model, as shown in Figure 5.3. There is a good agreement between the two sets of results, which indicates that the advective transport mechanism has also been correctly implemented in the transport module for the case of a single ideal gas component. As expected, the influence of the advective flux was greater in the fracture continuum than in the matrix continuum.
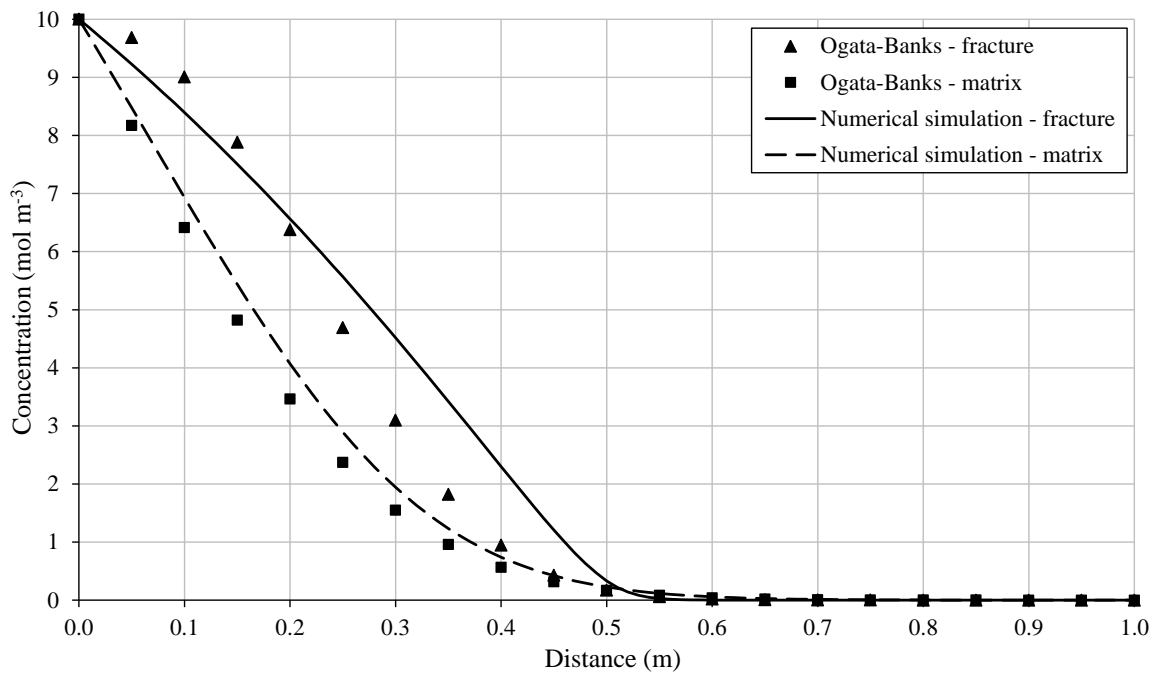
Figure 5.3 Gas concentration profiles in the fracture and matrix continua after 4 hours of simulation for the advection and diffusion case (Test I-b).

The differences between the analytical and numerical concentration profiles in Figure 5.3 can be attributed to the approximate velocities which were used in the analytical solution. As described in the previous section, these velocities were calculated using equation (5.6) assuming a steady state concentration profile and neglecting the gas compressibility. In the numerical simulation, the spatial and temporal discretisation meant that the velocity was calculated across each element in each time step. Furthermore, the gas compressibility was considered. As a result, the advective fluxes predicted by the analytical solution and the numerical model were slightly different, which is reflected in Figure 5.3.

5.3   Steady State Advection-Diffusion of Multicomponent Gas (Test II)

In contrast to the majority of liquids, most notably water, gas is a highly compressible fluid. Its bulk density can therefore vary greatly with pressure, which can have a significant effect on gas transport. This section presents an exercise to test the gas compressibility predicted by the numerical model during steady state advection and diffusion. The simulation considers a system initially saturated with methane (CH_4), which is replaced by CO_2 injection. Wu et al. (1998) presented an analytical solution to the steady-state, one-dimensional mass balance equation for gas transport in a homogenous single porosity system. The solution is used as the benchmark in the exercise, and calculates the steady state concentration profile that develops for the injected CO_2. The transport of multicomponent gas under transient conditions is also discussed for the gas displacement scenario considered.

5.3.1   Analytical Solution

Since the formulation is reduced to a single porosity form in this exercise, the inter-continua mass exchange term is removed. Furthermore, the effects of geochemical reactions and gravity are neglected. Substituting for the total flux from equation (3.88) then allows the mass balance expression in equation (3.46) to be expressed in a simplified form for multicomponent ideal gas, as:

$$\frac{\partial\left(nS_g c_g^i\right)}{\partial t} = \nabla \cdot \sum_{j=1}^{n_g} \left[\left(\frac{c_g^i K K_{rg} RT}{\mu_g} + \delta_{ij} nS_g \tau_g D_g^i \right) \nabla c_g^j \right] \tag{5.7}$$

where n and K are the porosity and intrinsic permeability of the single porosity medium, respectively.

For steady state gas flow in a dry system, the left hand side of equation (5.7) becomes zero and the relative gas permeability, K_{rg}, is equal to one, producing:

$$\nabla \cdot \sum_{j=1}^{n_g} \left[\left(\frac{c_g^i KRT}{\mu_g} + \delta_{ij} nS_g \tau_g D_g^i \right) \nabla c_g^j \right] = 0 \tag{5.8}$$

An analytical solution to a mass balance equation similar to equation (5.8) has been

presented by Wu et al. (1998). The solution is adopted here, only expressed in terms of gas concentrations instead of the bulk gas pressure used in the original solution. The solution is based on a fixed mass flux inlet boundary condition and a fixed pressure outlet boundary condition, which for multicomponent ideal gas in an isothermal system is equivalent to:

$$\sum_{j=1}^{n_g} J_g^j(0,t) = Q_g \tag{5.9}$$

$$RT \sum_{j=1}^{n_g} c_g^j(L_x,t) = u_{gL} \tag{5.10}$$

where J_g^j is the gas flux for the jth component, Q_g is the total gas flux at the inlet boundary, L_x is the length of the domain and u_{gL} is the pressure at the outlet boundary. The analytical solution is then given by (Wu et al., 1998):

$$c_g^T(x) = \frac{1}{RT}\sqrt{u_{gL}^2 + \frac{2Q_g RT \mu_g (L_x - x)}{K}} \tag{5.11}$$

Equation (5.11) has been used to calculate the total gas concentration profile at steady state for comparison with the results obtained using the numerical model.

5.3.2   Simulation Conditions

The numerical simulation was performed for a 10 m by 1 m two dimensional domain, which was spatially discretised into 200 equally sized 4-noded quadrilateral elements. A summary of the initial and boundary conditions which were used is given in Figure 5.4.

The domain was initially saturated with CH_4 at atmospheric pressure. A constant CO_2 flux equal to 5.68×10^{-3} mol m^{-2} s^{-1} was prescribed at the injection boundary. For the abstraction boundary, the total gas concentration was restrained by a prescribed atmospheric pressure condition, i.e. $u_{gL} = 0.1 \times 10^6$ Pa.

Since it has been assumed in this exercise that the multicomponent gas behaves as an ideal gas, the compressibility factor, Z, was set to 1.0. The simulation was performed under isothermal conditions with a constant temperature of 318 K. The relationships and

parameters of the model related to diffusion were the same as those provided in Table 5.1. A summary of the additional material parameters used in this verification exercise is given in Table 5.3.

Injection boundary conditions	Initial conditions	Abstraction boundary conditions
$Q_g^{CO_2} = 5.68 \times 10^{-3} \, mol \, m^{-2}s^{-1}$	$c_g^{CO_2} = 0.0 \, mol \, m^{-3}$ $c_g^{CH_4} = 37.82 \, mol \, m^{-3}$	$RT \sum_{j=1}^{n_g} c_g^j = 0.1 \times 10^6 Pa$ $\sum_{j=1}^{n_g} \frac{\partial c_g^j}{\partial t} = 0.0$

Figure 5.4 Schematic of the initial and boundary conditions used in Test II.

Table 5.3 Material parameters used in Test II.

Material parameter	Relationship / value
Porosity, n (-)	0.10
Permeability, K (m^2)	1.0×10^{-15}
Gas dynamic viscosity, μ_g (Pa s)	1.84×10^{-5}

5.3.3 Results and Discussion

Figure 5.5 shows the concentration of gases in the domain at various times as the injected CO_2 replaces the CH_4 and reaches a steady state condition. The results obtained from the numerical model after 6 hours and 18 hours of the analysis have been included to illustrate the multicomponent gas flow during the gas displacement process. The result of the CO_2 profile at steady state indicates a good correlation between the numerical simulation and analytical solution.

The observed steady state concentration profile for the injection and abstraction of CO_2 is different to that of an incompressible fluid. Since gas is highly compressible, its density varies significantly with concentration, i.e. pressure. This gives rise to the non-linear steady state profiles shown for both the numerical model and the analytical solution in Figure 5.5.
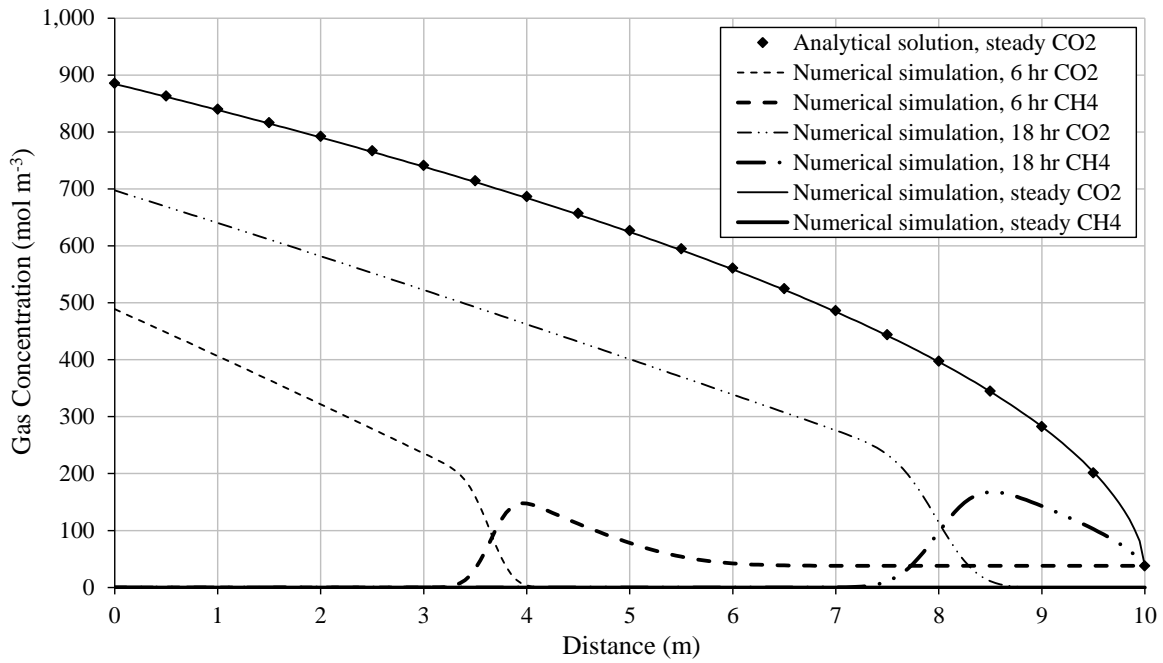
Figure 5.5 Transient and steady state profiles of CO_2 and CH_4 in the domain obtained using the numerical model. A comparison with the steady state results obtained using the analytical solution is also provided (Test II).

During the transient stage, the CO_2 has displaced the CH_4 at the injection front. The transient concentration profiles shown in Figure 5.5 indicate that the advection process does not cause lateral mixing in multicomponent mixtures, which follows the expected trend for laminar flow (Batchelor, 2000). The slight dispersion of the breakthrough front as it advanced across the domain can be attributed to diffusion. It may therefore be concluded that the advective flow mechanism, which has been modelled using Darcy's law, produces the expected behaviour for multicomponent pore gas transport.

5.4   Multicomponent Real Gas Transport with Adsorption/Desorption (Test III)

In this section, a verification exercise is presented which examines multicomponent gas transport, including real gas behaviour and solid-gas geochemical interactions. The main objective is to verify the implementation of multicomponent real gas behaviour and adsorption/desorption reactions in the model. Real gas behaviour has been included using the equation of state (EoS) presented by Peng and Robinson (1976), as described in section

3.4.1. In addition, the gas mixture viscosity has been calculated using a semi-empirical model presented by Chung et al. (1988), which was detailed in section 3.4.1. A summary of the major parameters required by the EoS and viscosity model is provided in Table 5.4. With reference to section 3.4.4, the amount of adsorbed gas has been described using a kinetics approach in which the equilibrium condition is calculated using the extended Langmuir isotherm.

Table 5.4 Selected gas properties required by the equation of state and gas mixture viscosity model (Reid et al., 1977).

Gas parameter	Value		
	CH_4	CO_2	N_2
Critical pressure, u_{gc}^i (Pa)	4.60×10^6	7.38×10^6	3.39×10^6
Critical temperature, T_c^i (K)	190.4	304.1	126.2
Critical volume, V_c^i (m^3 mol^{-1})	9.92×10^{-5}	9.39×10^{-5}	8.98×10^{-5}
Acentricity factor, ω_i (-)	0.011	0.239	0.039
Molecular mass, M_g^i (kg mol^{-1})	0.0160	0.0440	0.0280

The results obtained using the developed model are compared with the results of a numerical modelling study presented by Pini et al. (2011) for two scenarios of high pressure gas flow and reaction. Both scenarios deal with high pressure gas injection and the displacement of CH_4 in coal. The first simulation scenario (Test III-a) is based on CO_2 sequestration in coal, and considers the displacement of CH_4 by pure CO_2 injection. The second scenario (Test III-b) evaluates how the displacement of CH_4 is affected by the composition of the injected gas. Test III-b considers the injection of pure nitrogen (N_2), which has a lower affinity for adsorption in coal compared to both CO_2 and CH_4. In line with the work presented by Pini et al. (2011), the permeability model of Gilman and Beckie (2000) is used to describe the deformation of the coal due to physical and chemical interactions with the gas.

Since this exercise is mainly concerned with the verification of the multicomponent gas transport mechanisms and the sink/source term for gas adsorption/desorption, the system is

treated as a single porosity medium. This allows the focus of the analysis to remain on the relevant aspects of the formulation.

5.4.1 Simulation Conditions

The system considered was a 100 m long domain with a unit height, which was discretised into 500 equally-sized 4-noded quadrilateral elements. A summary of the initial and boundary conditions used in Tests III-a and III-b is provided in Figure 5.6.

Injection boundary conditions	Initial conditions	Abstraction boundary conditions
Test III-a: $c_g^{CO_2} = 1881.85\ mol\ m^{-3}$ Test III-b: $c_g^{N_2} = 1522.50\ mol\ m^{-3}$	Free gas: $c_g^{CO_2} = c_g^{N_2} = 0.0\ mol\ m^{-3}$ $c_g^{CH_4} = 582.44\ mol\ m^{-3}$ Adsorbed gas: $s_{gM}^{CO_2} = s_{gM}^{N_2} = 0.0\ mol\ kg^{-1}$ $s_{gM}^{CH_4} = 0.753\ mol\ kg^{-1}$	$RT \sum_{j=1}^{n_g} c_g^j = 0.1 \times 10^6 Pa$ $\sum_{j=1}^{n_g} \frac{\partial c_g^j}{\partial t} = 0.0$

Figure 5.6 Schematic of the initial and boundary conditions used in Test III-a (CO_2 injection) and Test III-b (N_2 injection).

The coal was considered to be initially saturated with CH_4 at a pressure of 1.5 MPa. In both injection scenarios, the gas was injected at a constant pressure of 4 MPa. Figure 5.6 presents a schematic of the specified gas pressures, which have been expressed in terms of the primary variables of gas concentrations via the Peng and Robinson (1976) EoS described in section 3.4.1 (using the parameters provided in Table 5.4). The abstraction boundary condition was fixed at atmospheric pressure for the multicomponent mixture, i.e. $u_g = 0.1 \times 10^6$ Pa.

A small initial time step of 10 seconds was adopted to handle the initially steep concentration gradients imposed by the boundary conditions. The maximum time step was set to 3,600 seconds. The system remained isothermal at 318 K throughout the simulation period.

The relationships used to describe the bulk gas compressibility, viscosity and diffusivity were described in section 3.4.1. As described previously, the compressibility factor was calculated using the EoS proposed by Peng and Robinson (1976), which was applied to multicomponent gas using the van der Waals mixing rules (Kwak and Mansoori, 1986). The viscosity of the real gas mixture was obtained using the semi-empirical model of Chung et al. (1988). The relationships and parameters related to the diffusion of gases in this problem are the same as those provided in Table 5.1.

As discussed in section 3.6, mechanical behaviour is not explicitly considered in this work. Instead, the feedback of deformation to the flow processes is included by considering the associated evolution in porosity and permeability. As adopted in Pini et al. (2011), the permeability model proposed by Gilman and Beckie (2000) was used in this exercise to implicitly model the deformation behaviour of coal. The model can be expressed as (Gilman and Beckie, 2000):

$$\frac{K}{K_0} = \left(\frac{n}{n_0}\right)^3 = exp\left[-\frac{9(1-2v)C_e}{En_0}(u_c - u_g) - \frac{9(1-2v)C_s E}{En_0}s\right] \qquad (5.12)$$

where v and E are Poisson's ratio and the Young's modulus, respectively, n_0 is the initial porosity, u_c is the overburden pressure and s is the total sorption strain obtained using the Langmuir swelling isotherm. The coefficients C_e and C_s are described in Pini et al. (2011) and defined in Table 5.5, which provides a summary of the physical and chemical parameters used in the simulations.

### 5.4.2   Results and Discussion

Figure 5.7 and Figure 5.8 show the results obtained using the numerical model after 42 days of analysis for Test III-a and Test III-b, respectively. In both tests the results show a close agreement with the benchmarks provided by Pini et al. (2011).

Due to the higher affinity of the coal to adsorb CO_2, the injected CO_2 preferentially displaced the adsorbed CH_4. The accelerated desorption of CH_4 produced the sharp breakthrough front shown in Figure 5.7, which is similar to that observed in Test II in section 5.3 for a system dominated by the advective transport of multicomponent gas.

Table 5.5 Material parameters used for Test III-a and Test III-b (adopted from Pini et al. (2011)).

Material parameter	Relationship / value		
Initial porosity, n_0 (-)	0.0984		
Initial permeability, K_0 (m^2)	9.87×10^{-15}		
Sorption rate, τ_r^i (s^{-1})	1.0×10^{-5}		
Poisson's ratio, v (-)	0.26		
Young's modulus, E (Pa)	1.12×10^9		
Overburden pressure, u_c (Pa)	1.00×10^7		
Coal density, ρ_s (kg m^{-3})	1,356.6		
C_e (-)	4.676		
C_s (-)	$C_s = \sum_{i=1}^{n_g} C_s^i X_g^i$		
	CH$_4$	CO$_2$	N$_2$
C_s^i (-)	1.480	0.623	2.337
Langmuir capacity, n_L^i (mol kg^{-1})	1.56	2.49	1.52
Langmuir constant (sorption), b_L^i (Pa^{-1})	6.26×10^{-7}	1.25×10^{-6}	1.40×10^{-7}
Langmuir strain, ε_L^i (-)	2.33×10^{-2}	4.90×10^{-2}	1.70×10^{-2}
Langmuir constant (swelling), b_{LS}^i (Pa^{-1})	3.47×10^{-7}	3.80×10^{-6}	5.19×10^{-8}

Figure 5.8 shows that the injection of N$_2$ had a considerable impact on the gas displacement process, with the injected gas having advanced much more rapidly and mixed with CH$_4$ along a smoother breakthrough front. This is because: (i) coal has a lower preference for the adsorption of N$_2$ than CH$_4$, and (ii) N$_2$ adsorption did not cause the swelling induced permeability loss associated with CO$_2$ adsorption. As a result, N$_2$ did not displace the adsorbed CH$_4$ in the same manner as CO$_2$. Less N$_2$ was immobilised via adsorption and the system permeability remained higher. This meant that the displacement of the free CH$_4$ occurred more rapidly, causing breakthrough of N$_2$ at the abstraction boundary. The significant spreading of the injection front can be attributed to the fact that the adsorbed CH$_4$ was displaced much more gradually by N$_2$ compared to CO$_2$.
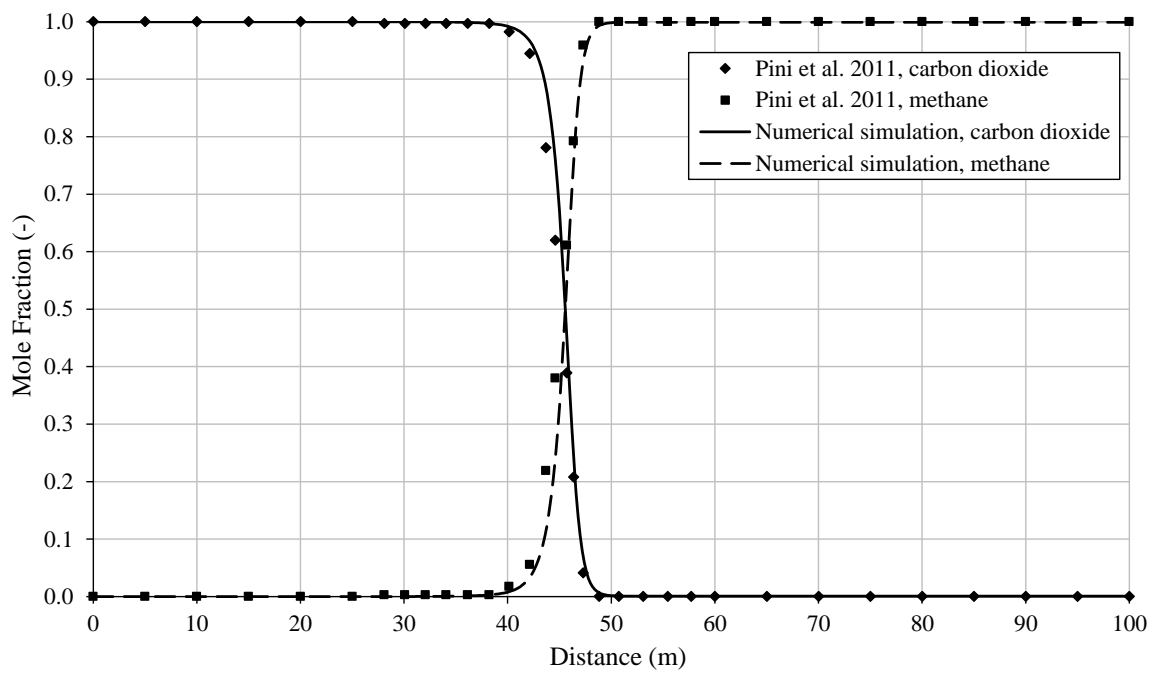
Figure 5.7 Gas composition of CH_4 and CO_2 along the domain after 42 days (Test III-a). Comparison between simulation results and those of Pini et al. (2011).
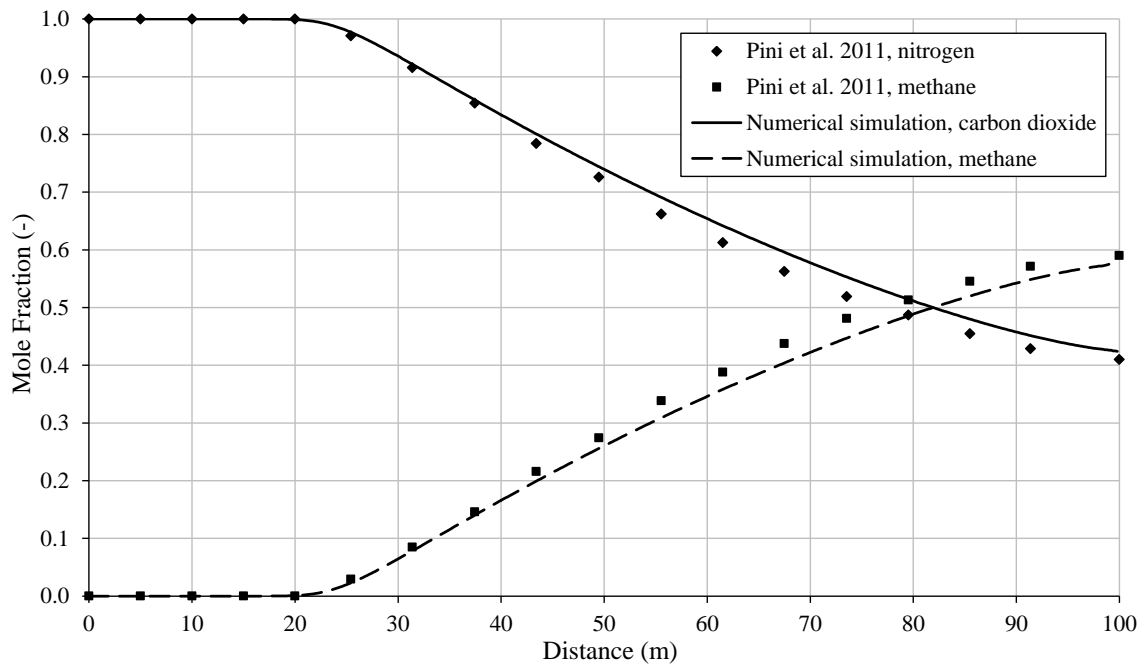
Figure 5.8 Gas composition of CH_4 and N_2 along the domain after 42 days (Test III-a). Comparison between simulation results and those of Pini et al. (2011).

Based on the results achieved and under the conditions of the simulation problems described, it can be concluded that the transport behaviour of multicomponent real gas, including adsorption/desorption kinetics, has been implemented accurately in the numerical model.

5.5   Influence of Sorption Rate on Chemical Transport (Test IV)

The verification exercise presented in section 5.4 described the transient flow of multicomponent gas with sorption kinetics described by a single rate. This made it difficult to examine the behaviour of the adsorption/desorption kinetics module in isolation. The exercise presented in this section considers chemical transport under various sorption rates. This allows the performance of the reaction module to be verified in greater depth.

The results obtained using the numerical model are compared with those obtained by Šimůnek and van Genuchten (2008) considering the chemical transport and reaction kinetics model in the HYDRUS-1D computer code. The simulations involve the one-dimensional transport of a chemical component in the liquid phase at a steady water flow rate in a single porosity medium, including kinetically controlled adsorption.

The governing equation for multicomponent chemical transport in a fractured rock, developed in chapter 3, is reduced under the conditions applied in this exercise to the following form:

$$\theta_l \frac{\partial c_d}{\partial t} + \frac{\partial s_d}{\partial t} = -\frac{\partial \mathbf{v_l} c_d}{\partial x} - \frac{\partial}{\partial x}\left(\theta_l D \frac{\partial c_d}{\partial x}\right) \tag{5.13}$$

where s_d represents the sink/source term for chemical adsorption/desorption, $\mathbf{v_l}$ is the water velocity and D is the coefficient of hydrodynamic dispersion, which is a lumped parameter including the effects of mechanical dispersion and molecular diffusion in the model (Bear and Verruijt, 1987). The second term on the left hand side of equation (5.13) is defined considering the first-order kinetics model (section 3.4.4), producing:

$$\frac{\partial s_d}{\partial t} = \tau_r (s_{d\infty} - s_d) \tag{5.14}$$

where s_d is the actual adsorbed amount and $s_{d\infty}$ is the adsorbed amount at equilibrium. Šimůnek and van Genuchten (2008) used a simple linear relationship to obtain $s_{d\infty}$, giving:

$$s_{d\infty} = \rho_s K_d c_d \tag{5.15}$$

where ρ_s is the adsorbed phase density and K_d is the distribution coefficient.

Based on the chemical transport and reaction kinetics model defined in the above equations, Šimůnek and van Genuchten (2008) presented the results of chemical transport simulations at a number of sorption rates. In order to use these results as benchmarks in the present verification exercise, the injection of a chemical into a saturated porous medium at steady state water flow conditions is simulated. Constant values are prescribed for the volumetric water content, coefficient of hydrodynamic dispersion and pore water velocity in equation (5.13), allowing the influence of the sorption rate on chemical transport to be examined in isolation. The results are presented as chemical breakthrough curves for each of the sorption rates considered, and compared with those presented by Šimůnek and van Genuchten (2008).

5.5.1 Simulation Conditions

A two-dimensional domain with 1.0 m length and 0.1 m width was spatially discretised into 500 equally-sized 4-noded quadrilateral elements, with the analysis point for the chemical breakthrough located at 0.1 m into the system. Figure 5.9 provides a summary of the initial and boundary conditions prescribed in the simulations.

Boundary conditions	Initial conditions	Boundary conditions
$u_l = 10.0 \, Pa$	$u_l = 10.0 \, Pa$	$u_l = 0.0 \, Pa$
$c_d = 1.0 \, mol \, m^{-3}$	$c_d = 0.0 \, mol \, m^{-3}$	$\dfrac{\partial c_d}{\partial t} = 0.0$

Figure 5.9 Schematic of the initial and boundary conditions used for Test IV.

The domain remained fully saturated with water throughout the simulation period and the pore water pressure gradient was fixed by the imposed boundary conditions. An arbitrary

chemical component was introduced to the system using a fixed concentration boundary condition, and a far field concentration of 0.0 mol m^{-3} was prescribed at the opposite boundary. The numerical simulations were performed for a period of 20 days, with initial and maximum time steps of 100 and 3,600 seconds, respectively.

Šimůnek and van Genuchten (2008) prescribed a steady state pore water velocity, $\mathbf{v_l}$, equal to 5.79×10^{-7} ms^{-1}. The influence of molecular diffusion was neglected in the calculation of the coefficient of hydrodynamic dispersion, D. By considering only the effects of mechanical dispersion, Šimůnek and van Genuchten (2008) employed the following expression for D:

$$D = \lambda_D \frac{\mathbf{v_l}}{\theta_l} \tag{5.16}$$

where λ_D is the dispersivity in the direction of flow, which was given as 0.01 m.

A series of simulations were performed for three different sorption rates. The results for the chemical breakthrough at the analysis point are compared with those obtained by Šimůnek and van Genuchten (2008) using HYDRUS-1D. A summary of the physical and chemical parameters used in the simulations is provided in Table 5.6.

Table 5.6 Material parameters used for the simulation of solute transport at different sorption rate constants (Test IV).

Material parameter	Relationship / value		
Porosity, n (-)	0.50		
Degree of water saturation, S_l (-)	1.0		
Adsorbed phase density, ρ_s (kg m^{-3})	1,500		
Distribution coefficient, K_d (m^3 kg^{-1})	0.001		
Pore water velocity, $\mathbf{v_l}$ (m s^{-1})	5.79×10^{-7}		
Hydrodynamic dispersion coefficient, D (m^2 s^{-1})	1.16×10^{-8}		
	Test IV-a	Test IV-b	Test IV-c
Sorption rates, τ_r (s^{-1})	1.16×10^{-6}	5.79×10^{-6}	1.16×10^{-4}

5.5.2   Results and Discussion

The chemical breakthrough curves for each of the sorption rates defined in Table 5.6 have been presented in Figure 5.10. There is a close agreement between the results obtained using the numerical model and those presented by Šimůnek and van Genuchten (2008) using HYDRUS-1D.
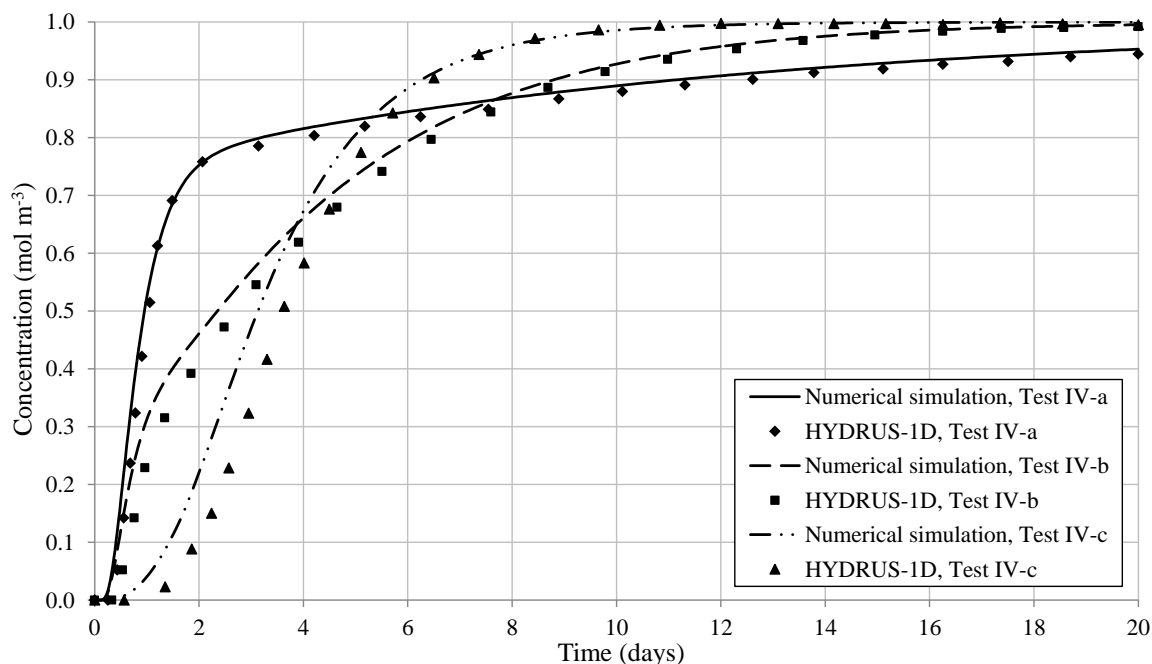
Figure 5.10 Chemical breakthrough at different sorption rates (Tests IVa-c), obtained using the numerical model and by Šimůnek and van Genuchten (2008) using HYDRUS-1D.

Two distinct features of the breakthrough curves can be observed in Figure 5.10, namely, the time taken for the chemical arrival and the time taken to reach equilibrium conditions. For Test IV-a, the sorption rate was set to a relatively low value and as a result, it took a longer time for the adsorbed phase to reach equilibrium with the free gas phase after chemical breakthrough. Increasing the sorption rate, as prescribed in Tests IV-b and IV-c, reduced the time taken to reach equilibrium. In other words, at higher sorption rates the chemical was removed from the mobile phase more rapidly. It follows that a higher sorption rate effectively retarded the initial breakthrough of the chemical, as shown in Figure 5.10.

As the sorption rate was increased, the breakthrough curves tended towards a shape for a

non-reactive advective-dispersive transport scenario. This is the expected trend since the adsorbed phase reached equilibrium rapidly after initial breakthrough. As a result, the non-equilibrium conditions only existed in a relatively narrow region behind the breakthrough front. The non-equilibrium region became larger using smaller values of the sorption rate. This explains why the breakthrough curve in Test IV-a tended towards the steady state concentration of 1.0 mol m^{-3} at a slower rate than in Test IV-b, which likewise tended towards the steady state condition at a slower rate than in Test IV-c.

In combination with the previous section, the exercise described in this section has served to verify the coupling between the transport and reaction kinetics modules in the numerical model. In particular, the exercise has illustrated the capability of the model to simulate the influence of the reaction rate on chemical transport.

5.6   Chemical Transport and Exchange in a Dual Porosity, Dual Permeability Medium (Test V)

The verification exercise presented in section 5.2 for chemical transport in a fractured rock was performed with no interactions between the fracture and matrix continua. It was shown that the advective flux is the dominant transport mechanism in the fracture continuum, whilst the diffusive flux is dominant in the matrix continuum. The main objective of the verification exercise presented in this section is to examine the sink/source term for mass exchange, which controls the flow interactions between the continua. In particular, this involves verifying that the sequential non-iterative approach (SNIA) for coupling the transport and mass exchange modules has been implemented correctly in the numerical model.

As in section 5.5, the results obtained using the numerical model have been compared with those obtained by Šimůnek and van Genuchten (2008) using the HYDRUS-1D computer code. The dual porosity, dual permeability formulation implemented in HYDRUS-1D considers one-dimensional chemical transport in the fracture and matrix continua and is largely based on the work of Gerke and van Genuchten (1993a; 1993b). In contrast to the governing equation of chemical transport developed in chapter 3, the dual porosity, dual permeability simulations presented in Šimůnek and van Genuchten (2008) assumed

equilibrium adsorption/desorption. With simplification, the governing equation for the transport of a chemical component in the fracture and matrix continua becomes:

$$(\theta_{l\alpha} + \rho_{s\alpha}K_{d\alpha})\frac{\partial c_{d\alpha}}{\partial t} = -\frac{\partial \mathbf{v}_{l\alpha}c_{d\alpha}}{\partial x} - \frac{\partial}{\partial x}\left(\theta_{l\alpha}D_\alpha\frac{\partial c_{d\alpha}}{\partial x}\right) - \lambda\Gamma_d \qquad (5.17)$$

where λ has been defined in equation (3.2) and Γ_d is the sink/source term for mass exchange of the solute between the continua.

In equation (5.17), the effect of equilibrium sorption on chemical transport is included using a retardation factor in the mass accumulation term on the left hand side. The linear isotherm given in equation (5.15) is used to describe the amount of adsorbed chemical at equilibrium.

Šimůnek and van Genuchten (2008) presented a set of simulation results for the case of chemical transport in a fractured rock subject to steady state water flow. Since the pore water pressures in the fracture and matrix continua remain equilibrated throughout the analysis, the advective term in the sink/source term for chemical mass exchange, defined in section 3.5.2, is set to zero. The mass exchange term in the exercise is therefore defined in a similar manner to that used by Šimůnek and van Genuchten (2008), giving:

$$\Gamma_d = \omega_{dp}\theta_{lM}\left(c_{dF}^i - c_{dM}^i\right) \qquad (5.18)$$

where ω_{dp} is the mass exchange rate.

Šimůnek and van Genuchten (2008) performed a series of simulations in which different values of ω_{dp} were used to investigate how the mass exchange rate influences chemical transport in a dual porosity, dual permeability system. The results of these simulations are used as the benchmarks for this verification exercise. As in section 5.5, all results are presented in the form of chemical breakthrough curves. The influence of different mass exchange rates is evaluated by comparing the breakthrough curves in the fracture and matrix continua. In addition, the average breakthrough concentration is calculated using the concentrations from each continuum using the following expression:

$$c_{dA} = \frac{c_{dF} + c_{dM}}{2} \tag{5.19}$$

where c_{dA} is the average breakthrough concentration.

5.6.1 Simulation Conditions

This exercise considers a two-dimensional domain of 1.0 m length and 0.1 m width, which was spatially discretised into 500 equally sized 4-noded quadrilateral elements. The analysis point for the chemical breakthrough was located at 0.1 m into the system. Figure 5.11 provides a summary of the initial and boundary conditions used in the simulations. The conditions in the fracture and matrix continua were the same as those applied in the single porosity simulations detailed in section 5.5. A shorter time period of 10 days was considered to reflect the accelerated transport in the dual porosity, dual permeability system compared to the single porosity system considered in Test IV. The maximum time step was set to 1,800 seconds.

Boundary conditions	Initial conditions	Boundary conditions
$u_{lF} = u_{lF} = 10.0 \, Pa$	$u_{lF} = u_{lF} = 10.0 \, Pa$	$u_{lF} = u_{lF} = 0.0 \, Pa$
$c_{dF} = c_{dM} = 1.0 \, mol \, m^{-3}$	$c_{dF} = c_{dM} = 0.0 \, mol \, m^{-3}$	$\dfrac{\partial c_{dF}}{\partial t} = \dfrac{\partial c_{dM}}{\partial t} = 0.0$

Figure 5.11 Schematic of the initial and boundary conditions used for Test V.

It is worth mentioning that the dual porosity, dual permeability concept developed by Gerke and van Genuchten (1993a), as used in HYDRUS-1D, handles the definition of the fracture and matrix continua in a different way to that described in chapter 3 of this work. They defined the material parameters and fluxes in each continuum at the local scale, whereas in this work they are defined at the bulk scale. An in-depth discussion on the background and procedures involved in converting from the local scale to the bulk scale was provided in chapter 3. Importantly, both approaches produce the same overall behaviour and the material parameters in each continuum can easily be converted between the two models using the volumetric weighting factor, w_f, which was defined in chapter 3 as:

$$w_f = \frac{V_F^T}{V_T} \tag{5.20}$$

where V_F^T is the total volume of the fractured zone and V_T is the total volume of the domain.

As an example of this, Šimůnek and van Genuchten (2008) set w_f to be 0.1 and prescribed pore water velocities of 3.47×10^{-6} ms^{-1} and 3.47×10^{-7} ms^{-1} in the fracture and matrix continua, respectively. These values were converted from the local scale to the bulk scale using w_f via the following expressions:

$$\mathbf{v}_{lF} = 3.47 \times 10^{-6} w_f = 3.47 \times 10^{-7} \text{ ms}^{-1} \tag{5.21}$$

$$\mathbf{v}_{lM} = 3.47 \times 10^{-7} (1 - w_f) = 3.12 \times 10^{-7} \text{ ms}^{-1} \tag{5.22}$$

As in Test IV, the effects of molecular diffusion were ignored and the values of hydrodynamic dispersion were calculated using equation (5.16) assuming $\lambda_{D\alpha} = 0.01$ m.

Table 5.7 provides a summary of the physical and chemical parameters used in the numerical simulations. It can be seen in Table 5.7 that the mass exchange rate in Test V-a was set to zero. This effectively reduced the problem to a form similar to that considered in Test I, where the continua behaved as independent flow conduits (i.e. no flow interactions between the continua). The effects of different mass exchange rates were considered in Tests V-b and V-c, with the rate in Test V-c being five times higher than that used in Test V-b. The results for chemical breakthrough at the analysis point are compared with those obtained by Šimůnek and van Genuchten (2008) using HYDRUS-1D.

5.6.2   Results and Discussion

The chemical breakthrough curves obtained from the simulations described in section 5.6.1 have been presented in Figures 5.12, 5.13 and 5.14. In each case there is a close correlation between the results obtained using the numerical model and those presented by Šimůnek and van Genuchten (2008) using HYDRUS-1D.
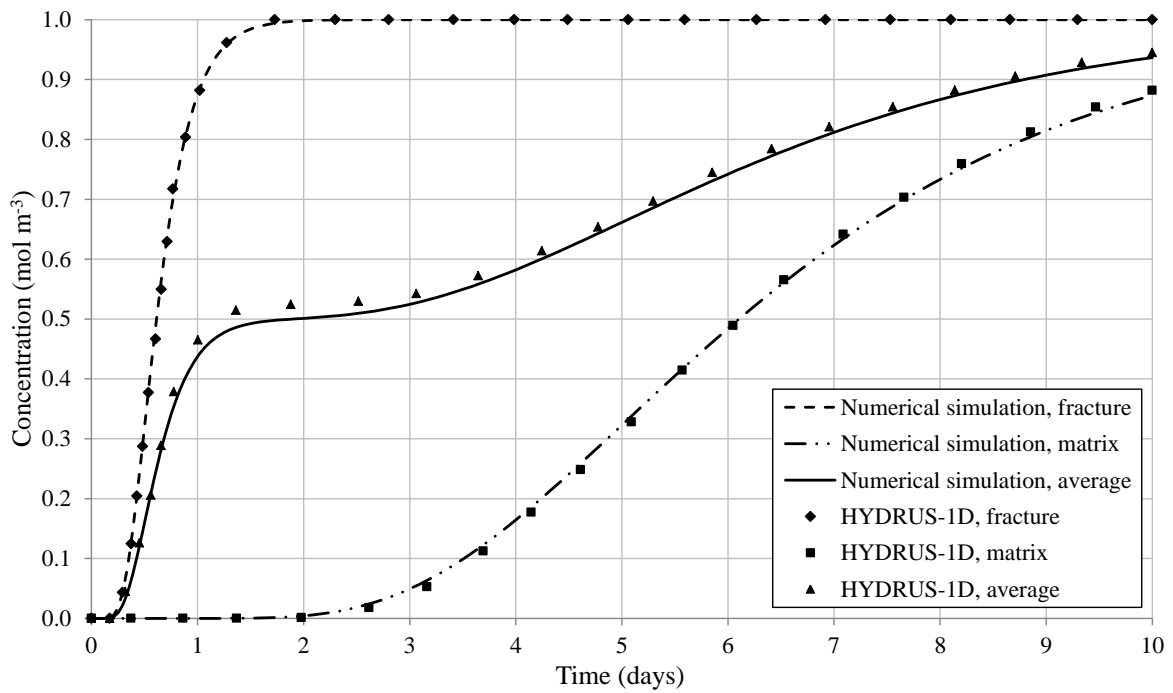
Figure 5.12 shows the chemical breakthrough curves with zero mass exchange between the

fracture and matrix continua. A sharp curve was observed in the fracture continuum, compared to a slightly delayed and more progressive breakthrough in the matrix continuum. This is mainly because the fracture porosity provided a considerably lower chemical storage capacity compared to that in the matrix. In the early stages of the simulation, the average concentration followed the sharp trend observed in the fracture continuum. It then briefly stabilised in the region of 0.5 mol m^{-3} as the fracture flow reached the steady state unit concentration and the matrix flow remained small. A gradual increase in the average concentration was then observed due to solute breakthrough in the matrix continuum.

The breakthrough curves shown in Figure 5.13 and Figure 5.14 present the role of mass exchange on chemical transport in a dual porosity, dual permeability medium. Figure 5.13 shows the results for the intermediate value of the mass exchange rate used in Test V-b. The curves retain some of the characteristics discussed above in relation to Test V-a.

Table 5.7 Material parameters used for Test V.

Material parameter	Relationship / value		
Volumetric weighting factor, w_f (-)	0.10		
Fracture continuum porosity, n_F (-)	0.05		
Matrix continuum porosity, n_M (-)	0.45		
Degree of water saturation, $S_{l\alpha}$ (-)	1.0		
Fracture continuum density, ρ_{sF} (kg m^{-3})	150		
Matrix continuum density, ρ_{sM} (kg m^{-3})	1,350		
Distribution coefficient, $K_{d\alpha}$ (m^3 kg^{-1})	0.001		
	Fracture	Matrix	
Pore water velocity, $\mathbf{v}_{l\alpha}$ (m s^{-1})	3.47×10^{-7}	3.12×10^{-7}	
Hydrodynamic dispersion coefficient, D_α (m^{2}s^{-1})	6.94×10^{-8}	6.94×10^{-9}	
	Test V-a	Test V-b	Test V-c
Solute mass exchange rate constants, ω_{dp} (s^{-1})	0.0	1.16×10^{-6}	5.80×10^{-6}

Figure 5.12 Chemical breakthrough curves with zero mass exchange (Test V-a), obtained using the numerical model and by Šimůnek and van Genuchten (2008) using HYDRUS-1D.
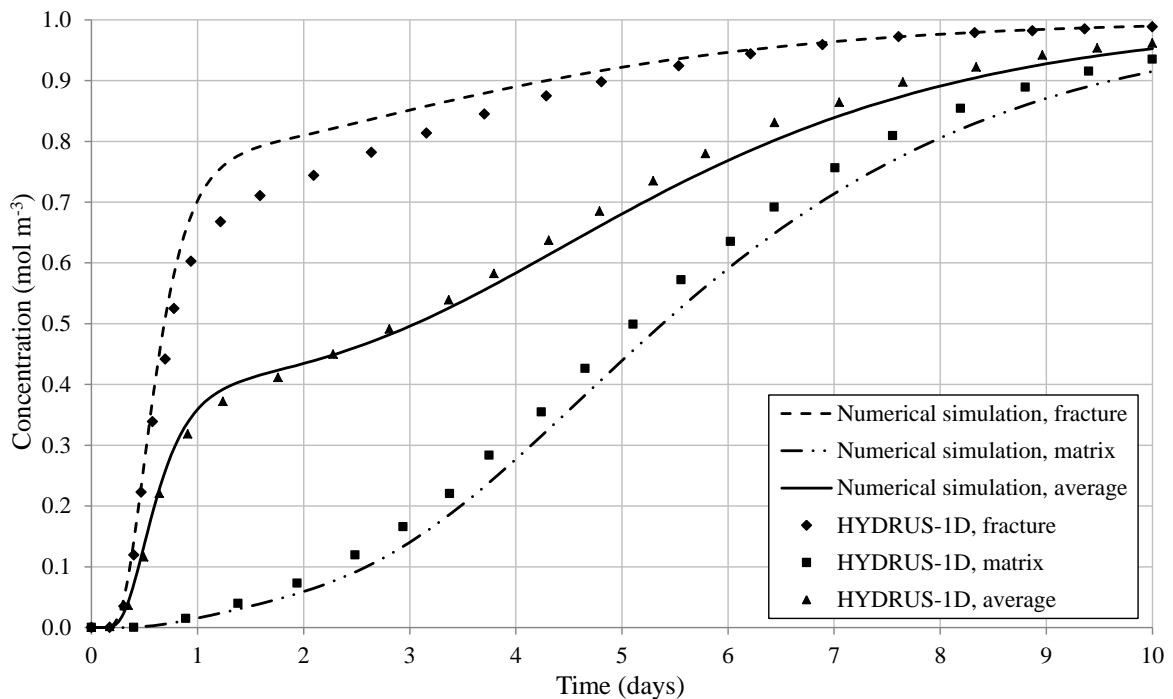
Figure 5.13 Chemical breakthrough curves with a mass exchange rate of 1.16×10^{-6} s^{-1} (Test V-b), obtained using the numerical model and by Šimůnek and van Genuchten (2008) using HYDRUS-1D.
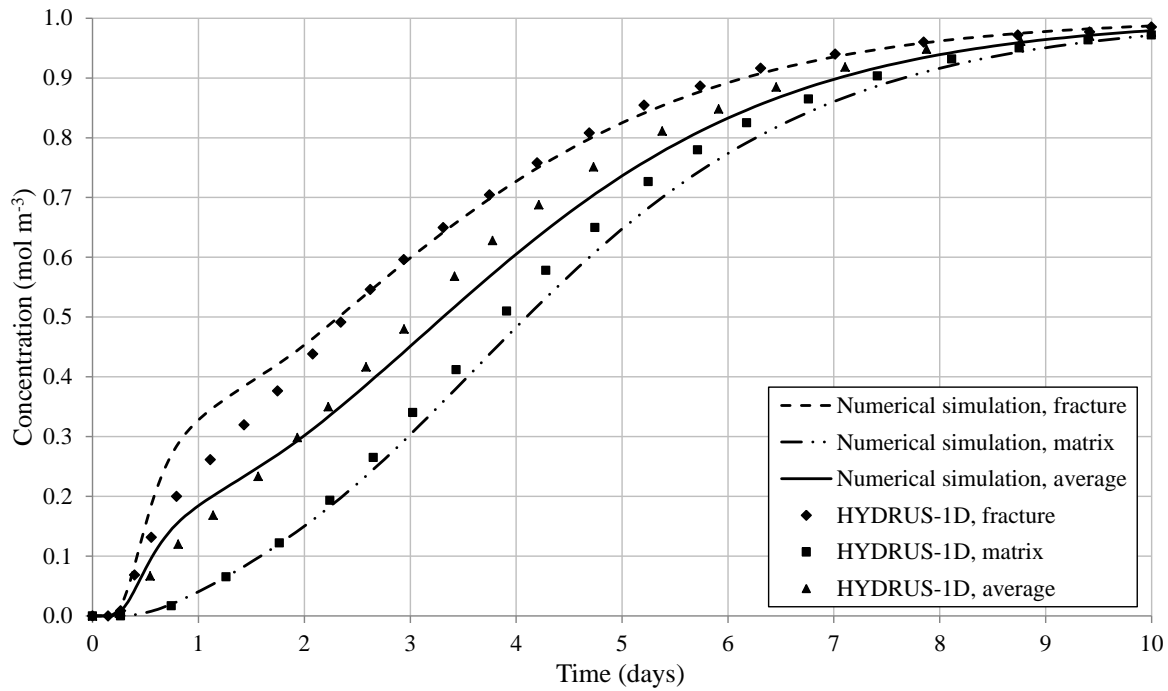
Figure 5.14 Chemical breakthrough curves with a mass exchange rate of 5.80×10^{-6} s^{-1} (Test V-c), obtained using the numerical model and by Šimůnek and van Genuchten (2008) using HYDRUS-1D.

Most notable is the sharp initial increase in the fracture concentration compared to the highly dispersed breakthrough of the chemical in the matrix. However, in contrast to Test V-a, there was a pronounced tailing of the fracture curve after 1 day and chemical breakthrough in the matrix occurred earlier. This follows the expected trend since, across the majority of the domain, the concentration in the fracture was higher than in the matrix, causing the chemical to be exchanged from the fracture continuum into the matrix continuum.

In Test V-c the mass exchange rate was five times higher than in Test V-b. A comparison of the breakthrough curves in Figure 5.13 and Figure 5.14 illustrates how the higher mass exchange rate increased the rate of equilibration of the chemical concentrations in the fracture and matrix continua. This is because the resistance to flow from the fracture continuum into the matrix continuum was effectively reduced. Further increases in the mass exchange rate would have resulted in the rapid equilibration of chemical concentrations in the dual porosity, dual permeability system. The breakthrough curves

would then have tended towards those predicted by a single porosity, single permeability equivalent continuum model.

Having analysed the breakthrough curves in Figures 5.12, 5.13 and 5.14, it can be concluded that the sink/source term for mass exchange between the fracture and matrix continua produces the expected behaviour. Furthermore, the results were found to be in close agreement with the benchmarks provided by Šimůnek and van Genuchten (2008) using HYDRUS-1D. This provides further confidence on the accuracy of the sink/source term for mass exchange implemented in the numerical model.

5.7   Conclusions

This chapter has described a number of verification exercises, which were performed to evaluate the major components of the developed numerical model related to reactive flow in fractured rock. The major focus of these exercises was on verifying that the particular components related to the real gas transport, adsorption/desorption kinetics and inter-porosity mass exchange have been correctly implemented in the model. The main outcomes of each these exercises are summarised below.

Two verification exercises were presented to examine the ability of the numerical model to simulate the different transport regimes that occur in the fracture and matrix pore regions of a fractured rock. Comparisons were made against analytical solutions for pure diffusive and advective-diffusive gas transport, assuming no interactions between the fracture and matrix continua. The simulation results reflected that the advective flux is the dominant transport mechanism in the fracture network, whilst the diffusive flux is dominant in the matrix blocks. The results obtained from the numerical model were found to be in close agreement with the analytical solutions adopted. It can be concluded that the governing equations for advective and diffusive transport in the fracture and matrix continua have been correctly implemented in the model for the flow of a single ideal gas component.

A verification exercise was performed to ensure that the steady state gas concentration profile predicted by the numerical model follows that expected for a highly compressible fluid. The simulation considered a system initially saturated with methane, which was

replaced by carbon dioxide injection. The injected carbon dioxide displaced the methane at a sharp front with little mixing. This indicates that the multicomponent form of Darcy's law used in the model produces the expected transport behaviour under the conditions applied. The predicted steady state concentration profile was in close agreement with the analytical solution considered, which provided a quantitative benchmark for the exercise.

The simulation results for the reactive transport of multicomponent real gas at high pressure were compared with those presented in the literature for an alternative numerical model. In particular, the exercise employed the constitutive relationships describing real gas compressibility and viscosity, in addition to the sink/source term for adsorption/desorption kinetics. The predicted results correlate well with those obtained from the alternative model for two different flow scenarios, in which the strong influence of the adsorption/desorption behaviour of the gases was observed. This served to verify the components in the model related to reactive real gas transport.

A set of simulations was completed to examine the coupling between the transport and geochemical reaction modules in the numerical model in greater detail. In the simulations, the influence of the sorption rate on the chemical breakthrough was evaluated. The simulation results were compared with those obtained from the literature for the HYDRUS-1D simulator code. A close agreement between the two sets of results was observed. As a result, it can be concluded that the time splitting approach adopted to couple the transport and reaction modules has been implemented correctly in the numerical model.

A series of simulations were performed to assess the coupling between the transport and mass exchange modules in the dual porosity, dual permeability model. Similar to the exercise described above, results were presented in the form of chemical breakthrough curves. Appropriate material parameters and steady state fluxes were applied in the fracture and matrix continua and the effect of different mass exchange rates was examined. A close correlation was found between the numerical simulation results and the benchmarks provided by HYDRUS-1D. It can be concluded that the time splitting approach adopted to solve the flow interactions between the fracture and matrix continua has been implemented accurately in the numerical model.

The verification tests presented in this chapter have provided a detailed assessment of the numerical implementation of the theoretical framework for reactive flow in fractured rock. Further confidence in the accuracy of the implementation of the theoretical and numerical formulations has been achieved in the exercises presented. The application and validation of the model at the laboratory scale is presented in the following chapter. This includes an in-depth investigation of the processes and behaviour involved in flow in a dual porosity, dual permeability medium. Specifically, the focus of this work will shift towards high pressure gas flow and interactions in coal, which is relevant in geoenergy applications such as carbon dioxide sequestration in coal and enhanced methane production.

5.8   References

Batchelor, G.K. (2000). *An introduction to fluid dynamics*. Cambridge University Press, Cambridge.

Bear, J. and Verruijt, A. (1987). *Modeling groundwater flow and pollution*. D. Reidel Publishing Company, Dordrecht, The Netherlands.

Chung, T-H., Ajlan, M., Lee, L.L. and Starling, K.E. (1988). Generalized multiparameter correlation for nonpolar and polar fluid transport properties. *Industrial and Engineering Chemistry Research*, **27**, 671-679.

Cleall, P.J. (1998). *An investigation of the thermo/hydraulic/mechanical nehaviour of unsaturated soils, including expansive clays*. PhD Thesis, Cardiff University, Cardiff.

Cussler, E.L. (1997). *Diffusion: mass transfer in fluid systems*. 2nd Edition. Cambridge University Press, Cambridge.

Delleur, J.W. (1999). Elementary groundwater flow and transport processes. In: Delleur, J.W. ed. *The handbook of groundwater engineering*, CRC Press LLC, Boca Raton, Florida.

Gerke, H.H. and van Genuchten, M.T. (1993a). A dual-porosity model for simulating the preferential movement of water and solutes in structured porous media. *Water Resources Research*. **29**(2), 305-319.

Gerke, H.H. and van Genuchten, M.T. (1993b). Evaluation of a first-order water transfer term for variably saturated dual-porosity flow models. *Water Resources Reseach*, **29**(4), 1225-1238.

Gilman, J.R. and Kazemi, H. (1983). Improvements in Simulation of Naturally Fractured Reservoirs. *Society of Petroleum Engineers Journal*, 23(4), 695-707.

Gilman, A. and Beckie, R. (2000). Flow of coalbed methane to a gallery. *Transport in Porous Media*, **41**(1), 1-16.

King, S.D. (1991). *A potential based model of coupled heat and moisture transfer in unsaturated soil*. PhD Thesis, University of Wales, Cardiff, UK.

Kwak, T.Y. and Mansoori, G.A. (1986). Van der Waals mixing rules for cubic equations of state. Applications for supercritical fluid extraction modelling. *Chemical Engineering Science*, **41**(5), 1303-1309.

Mason, E.A., Malinauskas, A.P. and Evans, R.B. (1967). Flow and diffusion of gases in porous media. *The Journal of Chemical Physics*, **46**(8), 3199-3217.

Masum, S.A. (2012). *Modelling of reactive gas transport in unsaturated soil – a coupled thermo-hydro-chemical-mechanical approach*. PhD Thesis, Cardiff University, Cardiff.

Millington, R.J. and Quirk, J.M. (1961). Permeability of porous solids. *Transactions of the Faraday Society*, **57**, 1200-1207.

Mitchell, H.P. (2002). *An investigation into the thermo/hydro/mechanical interactions involved in*

high level nuclear waste disposal. PhD Thesis, University of Wales, Cardiff, UK.

Ogata, A. and Banks, R.B. (1961). A solution of the differential equation of longitudinal dispersion in porous media. *US Geological Survey Professional Papers*, **34**, 411-A, A1-A9.

Peng, D-Y. and Robinson, D.B. (1976). A new two-constant equation of state. *Industrial and Engineering Chemistry Fundamentals*, **15**(1), 59-64.

Pini, R., Storti, G. and Mazzotti, M. (2011). A model for enhanced coalbed methane recovery aimed at carbon dioxide storage. *Adsorption*, **17**(5), 889-900.

Reid, R.C., Prausnitz, J.M. and Sherwood, T.K. (1977). *The properties of gases and liquids*. 3rd Edition. McGraw-Hill, New York.

Sansom, M.R. (1995). *A fully coupled numerical analysis of mass, air, and heat transfer in unsaturated soil*. PhD Thesis, University of Wales, Cardiff, UK.

Sedighi, M. (2011). *An investigation of hydro-geochemical processes in coupled thermal, hydraulic, chemical and mechanical behaviour of unsaturated soils*. PhD Thesis, Cardiff University, Cardiff.

Seetharam, S.C. (2003). *An investigation of the thermro/hydro/chemical/mechanical behaviour of unsaturated soils*. Ph.D. Thesis, Cardiff University, Wales, UK.

Šimůnek, J. and van Genuchten, M.T. (2008). Modeling nonequilibrium flow and transport processes using HYDRUS. *Vadose Zone Journal*, **7**(2), 782-797.

Thomas, H.R. and He, Y. (1995). Analysis of coupled heat, moisture and air transfer in a deformable soil. *Géotechnique*, **45**(4), 677-689.

Thomas, H.R. and Sansom, M.R. (1995). A fully coupled analysis of heat, moisture and air transfer in unsaturated soil. *Journal of Engineering Mechanics*, ASCE, **12**(3), 392-405.

Thomas, H.R. and He, Y. (1998). Modelling the behaviour of unsaturated soil using an elasto-plastic constitutive relationship. *Géotechnique*, **48**(5), 589-603.

Thomas, H.R., He, Y. and Onofrei, C. (1998). An examination of the validation of a model of the hydro/thermo/mechanical behaviour of engineered clay barriers. *International Journal of Numerical and Analytical Methods in Geomechanics*, **22**, 49-71.

Wu, Y-S., Pruess, K. and Persoff, P. (1998). Gas flow in porous media with Klinkenberg effects. *Transport in Porous Media*, **32**, 117-137.

Zhou, F., Hussain, F. and Cinar, Y. (2013). Injecting pure N_2 and CO_2 to coal for enhanced coalbed methane: experimental observations and numerical simulation. *International Journal of Coal Geology*, **116-117**, 53-62.

6

Model Application and Validation

6.1 Introduction

A major component of this work is the application of the formulation described in chapters 3 and 4 in a laboratory scale validation exercise. This includes comparisons with a series of experimental data related to high pressure gas injection in coal cores. The design, construction and commission of experimental facilities, and all subsequent tests adopted in the simulations, have been undertaken by Hadi Mosleh (2014). The simulations presented in this chapter are related to some of the major physical and chemical aspects of gas flow and interactions in coal. The simulations are designed to validate the formulation and numerical model developed for multicomponent reactive gas transport in fractured rock by using the experimental data as a benchmark.

The experimental programme conducted by Hadi Mosleh (2014) focused on investigating the key aspects of coal-gas interactions, including the adsorption/desorption and transport behaviour. To achieve this, the experimental apparatus included two main analysing units; one for testing the equilibrium and kinetics of gas adsorption/desorption in coal samples,

and the other for testing the transport and deformation behaviour in coal cores. A more detailed description of the experimental facilities is provided in appendix A. This includes a summary of the materials and methods employed in the experiments.

A wide range of experimental data was produced from each of the tests described in appendix A. It was therefore necessary to be quite selective of the particular tests that were simulated to meet the main objective of validating the formulation. In this regard, the focal point of the chapter is on the numerical simulation of the experiments for gas injection and displacement in coal. In support of these simulations, it is important to have a good understanding of the adsorption/desorption and deformation behaviour of the coal. This understanding is developed in sections 6.3 and 6.4, where selected sets of the relevant experimental data are compared with the results obtained using the developed theoretical models.

With reference to section 3.4, the gas adsorption kinetics have been described in this work using a first-order rate model. In section 6.3, the main objective is to examine this approach via comparisons between the results of the adopted adsorption kinetics model and experimental data. This includes an analysis of the adsorption equilibrium and kinetics behaviour of the coal samples due to exposure to carbon dioxide, methane and nitrogen at a range of pressures under a controlled temperature.

In section 6.4, the results obtained using the developed deformation model (ref. section 3.6) are compared with experimental permeability data for an intact coal core. An analysis of the various physical and chemical deformation mechanisms considered in the model is included. The experimental permeability data used in section 6.4 was determined at steady state flow conditions for a number of gases at a range of confining pressures and pore pressures.

Section 6.5 presents the numerical simulations of gas injection and displacement in a coal core. Two injection scenarios are considered for a system initially saturated with methane. In the first scenario, the injected gas is pure nitrogen, and in the second scenario pure carbon dioxide is used. Experimental results are presented in the form of the produced gas composition, and are compared with the predictions of the numerical model for the major

purpose of validating the dual porosity, dual permeability formulation as a whole. Information from the analyses presented in sections 6.3 and 6.4 is used to provide the material properties required for these simulations.

Finally, conclusions from the work described above are provided in section 6.5.

6.2 Experimental Results

The experimental results obtained by Hadi Mosleh (2014) for gas injection into a coal core and methane (CH_4) displacement are presented in this section. Figure 6.1 and Figure 6.2 show the evolution in the produced gas composition for the injection of pure nitrogen (N_2), i.e. Test A, and pure carbon dioxide (CO_2), i.e. Test B, respectively.

It is useful to characterise the curves in terms of the time taken for the breakthrough of the injected gas and the longer term behaviour as the system tended towards equilibrium, i.e. pure N_2 or pure CO_2 production. Taken as when the composition of the produced gas
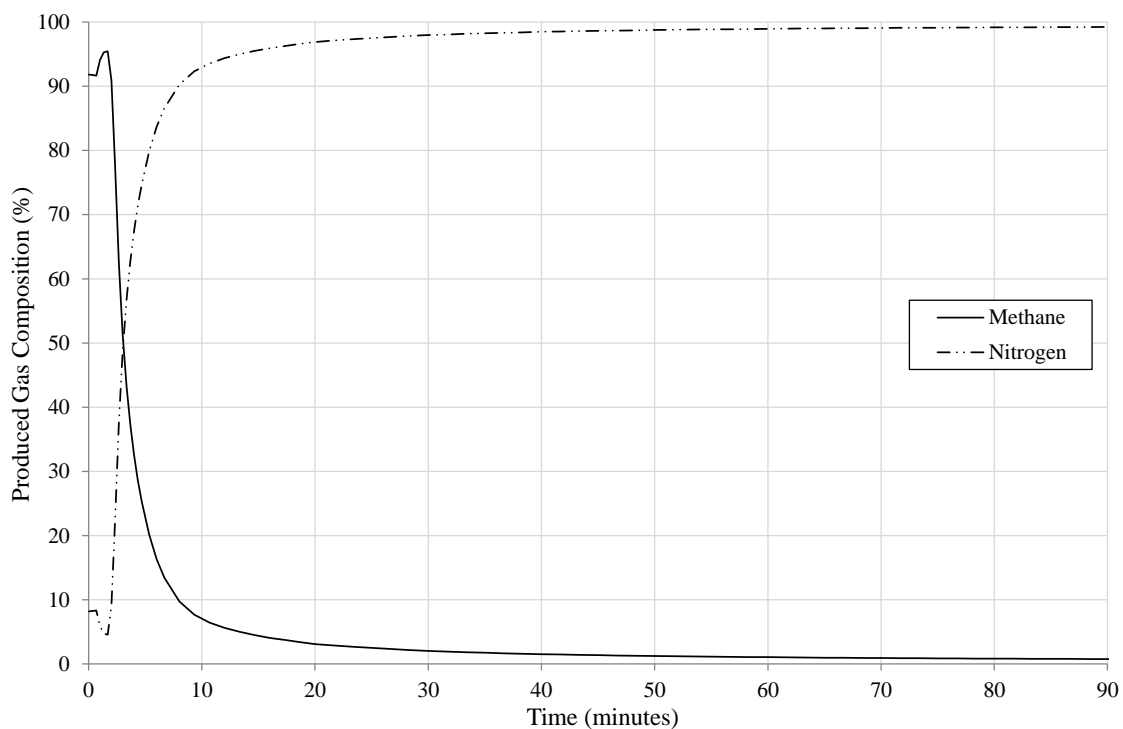
Figure 6.1 Produced gas composition for N_2 injection and CH_4 displacement (Test A) conducted by Hadi Mosleh (2014).
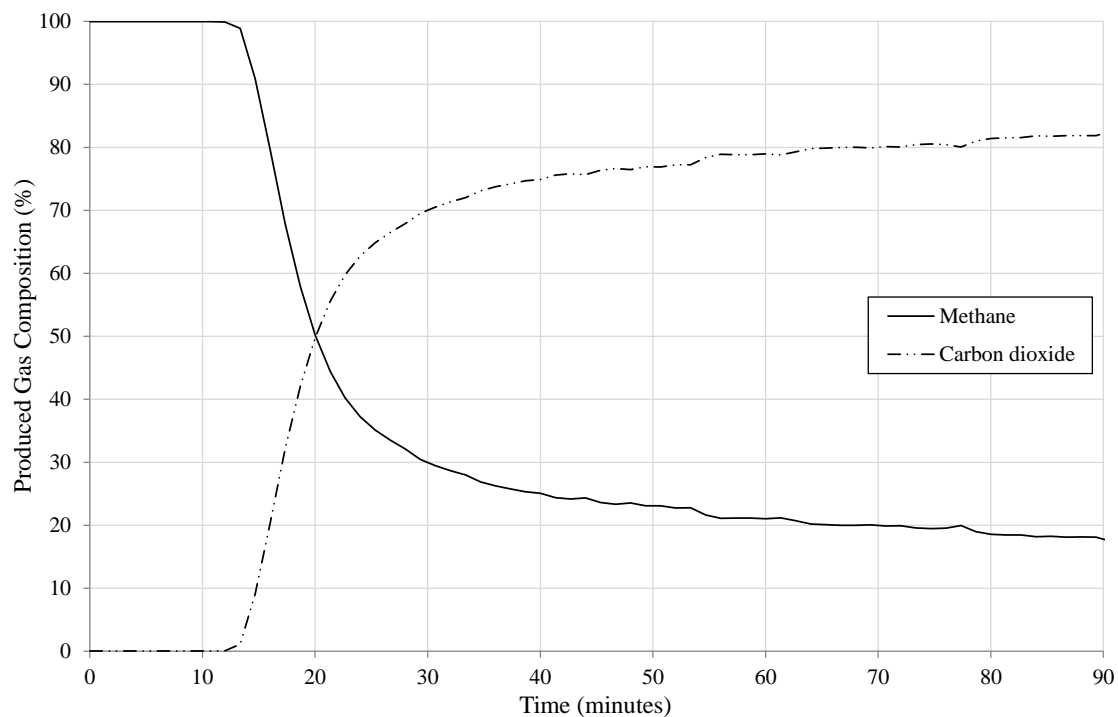
Figure 6.2 Produced gas composition for CO_2 injection and CH_4 displacement (Test B) conducted by Hadi Mosleh (2014).

reached 10% N_2 or CO_2, the breakthrough in Test A occurred at just over 2 minutes, compared to 15 minutes in Test B. The longer term gas production in Test A was close to pure N_2. By comparison, the fraction of CH_4 maintained in the produced gas was significantly larger in Test B. A detailed discussion of the various processes and behaviour that affect the characteristics of the breakthrough curves is developed in the remaining sections of this chapter.

6.3 Gas Adsorption

This section presents the results obtained using the theoretical model developed in section 3.4.4 to describe the adsorption of N_2, CH_4 and CO_2 in powdered coal samples. The material parameters and model conditions have been based on the laboratory tests conducted by Hadi Mosleh (2014), which are described in appendix A. The results of the theoretical model are discussed and compared with the experimental data for validation purposes.

Since the experiments were performed using powdered coal samples with a grain size fraction in the range of 0.5 to 1 mm, it is likely that the fractured structure of the coal was destroyed. Furthermore, once the valve between the reference and sample cells was opened at the start of a pressure step, it has been assumed that each grain was exposed to a uniform pore gas pressure (e.g. Busch et al., 2004). This implies that the time taken to reach equilibrium conditions was governed mainly by the kinetics of the adsorption process and not by bulk gas movement in the void volume between the grains. By neglecting gas transport, the theoretical model for gas adsorption kinetics was applied directly to describe the adsorption kinetics.

6.3.1   Material Parameters and Model Conditions

A summary of the material parameters and constitutive relationships required to model the gas adsorption, including the adsorption properties of the experimental gases, is provided in Table 6.1.

Table 6.1 Material parameters used in the modelling of the adsorption kinetics experiments.

Material parameter	Relationship / value		
Temperature, T (K)	298		
Coal density, ρ_s (kg m^{-3})	1,495.85		
Compressibility factor, Z (-)	Peng-Robinson EoS (see section 3.4.1)		
	N$_2$	CH$_4$	CO$_2$
Langmuir capacity, n_L^i (mol kg^{-1})	0.68	1.09	1.26
Langmuir pressure, P_L^i (Pa)	1.86×10^6	0.90×10^6	0.20×10^6
Langmuir constant, b_L^i (Pa^{-1})	5.38×10^{-7}	1.11×10^{-6}	5.00×10^{-6}
Average adsorption rate, τ_r^i (s^{-1})	6.70×10^{-5}	5.00×10^{-5}	3.60×10^{-4}

The gas compressibility factor was calculated via the Peng and Robinson (1976) equation of state (EoS), detailed in section 3.4.1, using the gas parameters provided in Table 5.4. With reference to the adsorption kinetics model described in section 3.4.4, the absolute amount of gas adsorbed at equilibrium conditions was described using an extended

Langmuir isotherm. The coal density and other adsorption parameters presented in Table 6.1 were calculated and presented in Hadi Mosleh (2014). Figure 6.3 shows the resulting absolute adsorption isotherm curves for each of the experimental gases up to 5 MPa.
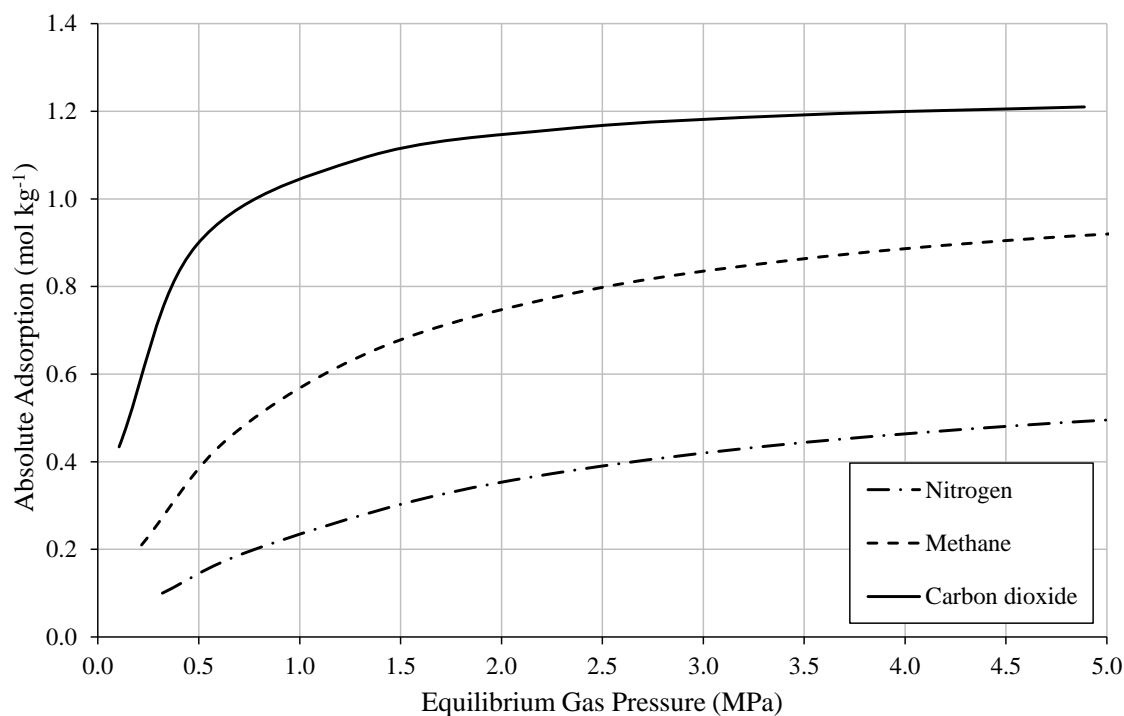
Figure 6.3 Absolute adsorption isotherms for the experimental gases, based on the Langmuir parameters reported in Table 6.1.

As described in appendix A, the adsorption behaviour of the powdered coal was evaluated at a number of pressure steps, corresponding to reference cell pressures of 0.5, 1.0, 2.0, 3.0, 4.2, 5.5 and 7.0 MPa. The first-order adsorption rates given in Table 6.1 are the average values found to provide a good description of the kinetics of each gas at the range of pressures considered (Hadi Mosleh, 2014).

For the purpose of validating the adsorption kinetics module developed in the model, the results presented in this section are limited to a selected pressure step. For each gas, this pressure step has been chosen to best represent the average adsorption kinetics across the range of test data. For each of the chosen pressure steps, it was important to prescribe the initial free gas concentrations based on the experimental measurements after the valve between the reference and sample cells was opened. The initial adsorbed amount at the start of each step was calculated using the Langmuir isotherm model with the equilibrium

free gas concentrations at the end of the previous step.

A summary of the initial conditions used in the model is provided in Table 6.2, where u_{g0} and c_{g0}^i are the initial free gas pressure and corresponding gas concentration, respectively, and s_{g0}^i is the initial adsorbed amount.

Table 6.2 Initial conditions used in the modelling of the kinetic adsorption experiments.

Gas	Step no.	u_{g0} [MPa]	c_{g0}^i [mol m^{-3}]	s_{g0}^i [mol kg^{-1}]
Nitrogen	5	3.423	1,397.65	0.387
Methane	5	3.390	1,506.56	0.828
Carbon dioxide	4	2.353	1,102.80	0.954

6.3.2   Adsorption Kinetics

The results of the modelling of the adsorption kinetics experiments for N_2, CH_4 and CO_2 are presented in Figure 6.4, Figure 6.5 and Figure 6.6, respectively. The bracketed pressures refer to the gas pressure in the reference cell before the valve connecting it to the sample cell was opened at the start of each pressure step. To facilitate the comparisons between the gases, the equilibration curves have been normalised using an approach suggested by Busch et al. (2004). In this approach the curves for each gas species are expressed in terms of the residual (unoccupied) adsorption capacity, s_{gr}^i, which is given by (Busch et al., 2004):

$$s_{gr}^i = \frac{s_{gt}^i - s_{g\infty}^i}{s_{g0}^i - s_{g\infty}^i} \tag{6.1}$$

where s_{g0}^i and $s_{g\infty}^i$ are the initial and equilibrium absolute adsorbed amounts at the start of each pressure step and s_{gt}^i is the absolute adsorbed amount at time t.

Figure 6.4, Figure 6.5 and Figure 6.6 show that the adsorption rate of CO_2 is significantly higher than those of N_2 and CH_4. Compared with the experimental results, the single first-order rate model describes the adsorption kinetics reasonably well. However, in each case
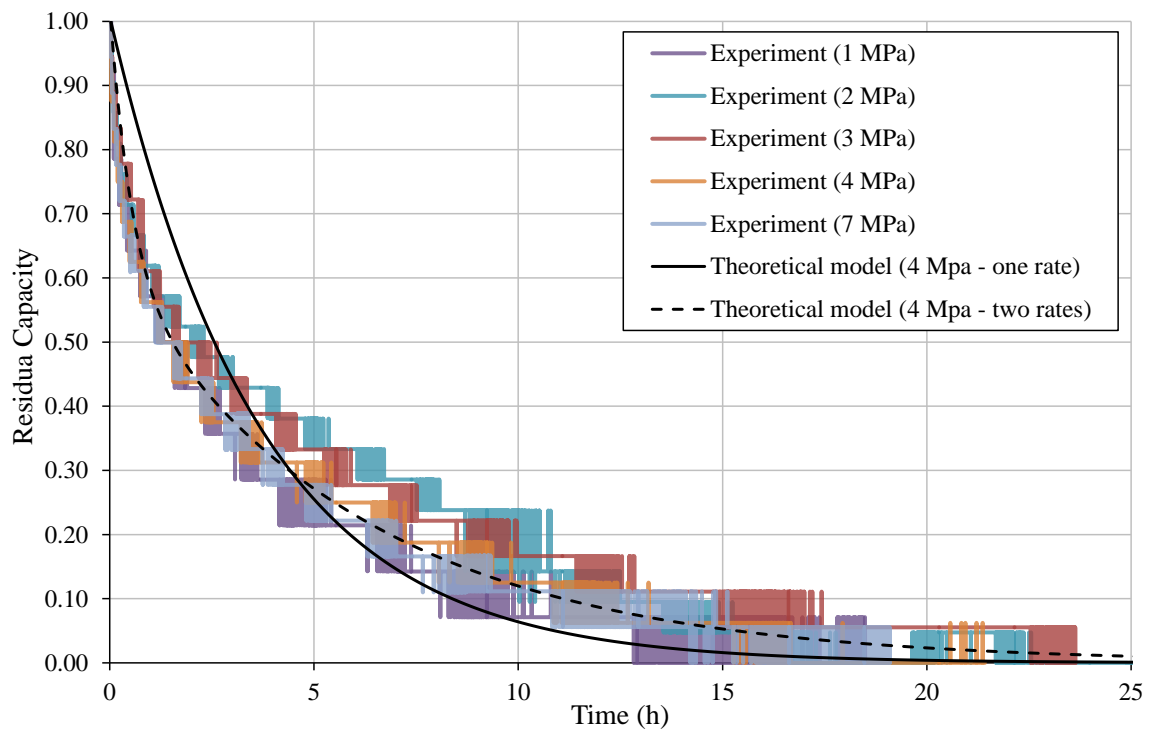
Figure 6.4 Comparison between nitrogen adsorption kinetics observed in the laboratory and the results obtained using a first-order kinetic and two combined first-order kinetic models.
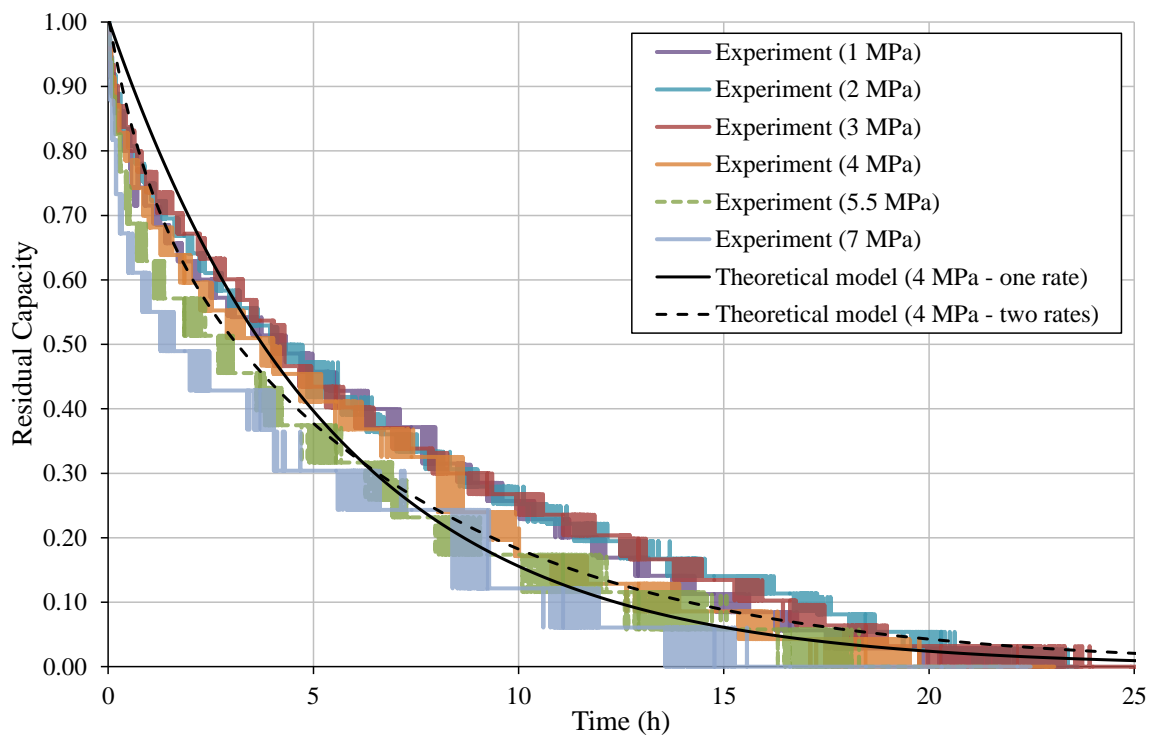
Figure 6.5 Comparison between methane adsorption kinetics observed in the laboratory and the results obtained using a first-order kinetic and two combined first-order kinetic models.
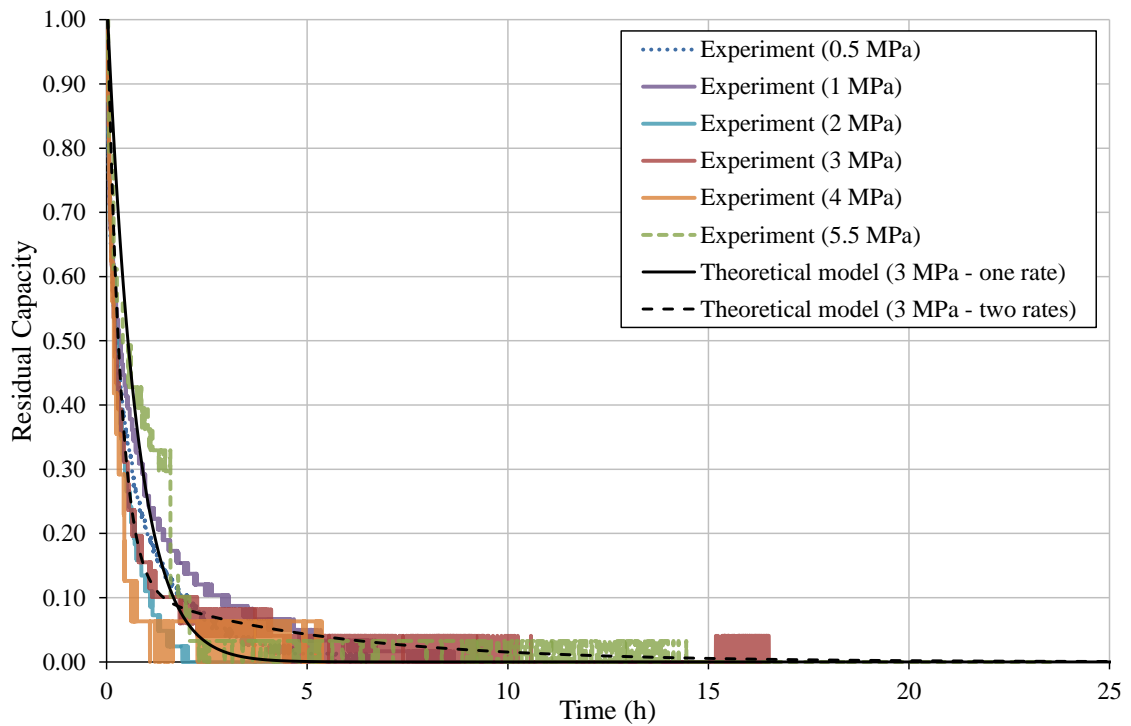
Figure 6.6 Comparison between carbon dioxide adsorption kinetics observed in the laboratory and the results obtained using a first-order kinetic and two combined first-order kinetic models.

the rate of adsorption is slightly underestimated at the early times in the test and slightly overestimated at later times. It was therefore decided to extend the theoretical model so that the adsorption kinetics were described by a combination of two first-order rates. The results obtained using the extended model are indicated by the dashed curves in Figure 6.4, Figure 6.5 and Figure 6.6.

Recalling from section 3.4, the single first-order rate model is given by:

$$s_g^i\big|_{n+1} = s_{g\infty}^i\big|_{n+1/2}\left(1 - e^{-\tau_r^i\Delta t}\right) + s_g^i\big|_n e^{-\tau_r^i\Delta t} \tag{6.2}$$

where the subscript n denotes the time step.

The two combined first-order rate model has been implemented using the approach presented by Busch et al. (2004), so that equation (6.2) can be rewritten as:

$$s_g^i\big|_{n+1} = \left[s_{g\infty1}^i\big|_{n+1/2}\left(1 - e^{-\tau_{r1}^i\Delta t}\right) + s_{g1}^i\big|_n e^{-\tau_{r1}^i\Delta t}\right]$$
$$+ \left[s_{g\infty2}^i\big|_{n+1/2}\left(1 - e^{-\tau_{r2}^i\Delta t}\right) + s_{g2}^i\big|_n e^{-\tau_{r2}^i\Delta t}\right] \qquad (6.3)$$

where the subscripts 1 and 2 denote the terms related to each adsorption rate.

Equation (6.3) is therefore defined in terms of two first-order models with two sets of equilibrium isotherms and rates, denoted by the square brackets. The overall adsorption behaviour is given by the superposition of the two models, and sorption capacity factors are used to partition the bulk adsorption behaviour between these models, with the following constraints:

$$0 \leq Q_1^i \leq 1 \qquad (6.4)$$

$$Q_2^i = 1 - Q_1^i \qquad (6.5)$$

where Q_1^i and Q_2^i are the sorption capacity factors for the ith gas component. Using these factors, the initial adsorbed amount is defined as:

$$s_{g0}^i = s_{g01}^i + s_{g02}^i \qquad (6.6)$$

where:

$$s_{g01}^i = Q_1^i s_{g0}^i \qquad (6.7)$$

$$s_{g02}^i = \left(1 - Q_1^i\right)s_{g0}^i \qquad (6.8)$$

In addition, the equilibrium adsorbed amounts in equation (6.3) are given by modified Langmuir isotherms (Ruthven, 1984; Yang, 1987), as:

$$s_{g\infty1}^i = \frac{Q_1^i n_L^i b_L^i ZRT c_g^i}{1 + ZRT \sum_{j=1}^{n_g} b_L^j c_g^j} \qquad (6.9)$$

$$s_{g\infty2}^i = \frac{Q_2^i n_L^i b_L^i ZRT c_g^i}{1 + ZRT \sum_{j=1}^{n_g} b_L^j c_g^j} \qquad (6.10)$$

where n_L^i is the Langmuir capacity and b_L^i is the reciprocal of the Langmuir pressure.

The two combined first-order rate constants and sorption capacity factors were obtained by fitting the model results and the experimental data. A summary of the parameters used in the adsorption kinetics modelling is given in Table 6.3. The single first-order rates from Table 6.1 are repeated for completeness.

Table 6.3 Summary of the adsorption rate constants obtained from the single first-order and two combined first-order adsorption kinetics models.

Gas	Single first-order rate	Two combined first-order rates			
	τ_r^i [s⁻¹]	τ_{r1}^i [s⁻¹]	τ_{r2}^i [s⁻¹]	Q_1^i	Q_2^i
N_2	6.70×10^{-5}	5.00×10^{-4}	4.10×10^{-5}	0.35	0.65
CH_4	5.00×10^{-5}	3.00×10^{-4}	3.60×10^{-5}	0.20	0.80
CO_2	3.70×10^{-4}	7.00×10^{-4}	5.50×10^{-5}	0.85	0.20

In Figure 6.4, Figure 6.5 and Figure 6.6, it is clear that the adsorption kinetics are more accurately modelled using the two combined first-order rate model presented in equation (6.3) compared to the single first-order rate model in equation (6.2). This is consistent with the findings of Busch et al. (2004). The remainder of this section explores the possible reasons why the combined rate model provides a better fit compared to the single rate model, and why the adsorption behaviour of CO_2 is markedly different to that of N_2 and CH_4.

For each of the gases, the first rate was specified to model the initially rapid adsorption stage in each test, whilst the other was specified to model the more gradual stage that followed. The sorption capacity factors were used to govern the relative contribution of each of these stages to the overall kinetics. For CO_2, the overall behaviour was dominated by the rapid first stage, resulting in a high Q_1^i factor of 0.80. For N_2 and CH_4, the overall kinetics were found to be more dependent on the slower second stage, resulting in lower Q_1^i factors of 0.35 and 0.20, respectively.

Although adsorption is a surface phenomenon, the time taken to reach equilibrium in a pressure step was not only dependent on how quickly the gas molecules physically or

chemically interacted with the coal surface upon contact. Instead, the time taken for the molecules to arrive at the adsorption sites within the coal grains must also be considered. This process is often modelled as a diffusion step, for example in the bidisperse diffusion models that have been used to describe gas adsorption kinetics in coal (e.g. Clarkson and Bustin, 1999; Shi and Durucan, 2003).

Based on the physical description of the adsorption kinetics given above, it is possible to explore some of the likely physical processes that could be responsible for the observed behaviour. The main problem with this is that there is a lack of definitive evidence to support conclusions related to gas diffusion and surface interactions in the complex meso- and micro-pores in coal. This is particularly true in relation to the species dependent nature of these processes observed in this study. Despite this, a number of good attempts have been made to develop explanations of the pore scale processes that govern gas adsorption kinetics in coal (e.g. Milewska-Duda et al., 2000; Cui et al., 2004).

As in this study, a number of authors have found that a combination of two rates improves the prediction of gas adsorption kinetics compared to a single rate (e.g. Clarkson and Bustin, 1999; Busch et al., 2004). The explanation of this behaviour might be related to the contributions of the mesopores and micropores to the overall adsorption capacity. Since the samples were powdered with a grain size fraction of 0.5 to 1 mm, the fracture network and a portion of the macropore (> 50 nm) structure would have been lost. However, it is reasonable to assume that much of the distribution of meso- (between 2 and 50 nm) and micro-pores (< 2 nm) would have been largely unaffected (Cui et al., 2004). As a result, the initially rapid stage of adsorption may be attributed to storage in the more open mesopores, with the subsequent slower stage of adsorption due to storage in the less accessible micro-pores. Such an explanation would go some way to explaining why CO_2 adsorption kinetics are governed by the first stage, whilst N_2 and CH_4 kinetics are governed by the second stage. This is because it has been postulated that N_2 and CH_4 adsorb mainly in micropores, whereas CO_2 adsorbs both in micropores and in multiple layers in meso-pores (Mastalerz et al., 2004).

Cui et al. (2004) conducted a theoretical investigation of gas adsorption kinetics in coal based on the molecular size and adsorption energies of the different species in different

sized pores. They found that CO_2 was able to access pores with a smaller half-width (0.289 nm) compared to N_2 (0.305 nm) and CH_4 (0.310 nm). The authors therefore concluded that the adsorption kinetics of CO_2 in coal may be faster than N_2 and CH_4 if the meso- and micro-pore network is highly constricted by ultra-micropores with a width less than 0.6 nm. In this scenario, the CO_2 molecules would typically reach an adsorption site quicker than the N_2 or CH_4 molecules. It is therefore possible that the powdered coal samples used in the experiments had a heterogeneous, interconnected pore network constricted by ultra-micropores which acted as a molecular sieve. This would go some way towards explaining why the adsorption kinetics of CO_2 shown in Figure 6.6 are so different to those of N_2 and CH_4 shown in Figure 6.4 and Figure 6.5, respectively.

It is likely that a combination of the above processes is responsible for the observed behaviour. Therefore, the CO_2 molecules may have adsorbed in multiple layers in the mesopores, whilst the greater adsorption energy and smaller kinetic diameter permitted their more rapid access to the micropores. In contrast, the N_2 and CH_4 molecules may have been restricted to single layer adsorption in the mesopores, and faced more resistance in entering the micropores due to their lower adsorption energy and larger kinetic diameter.

6.4   Prediction of Permeability Evolution

Coal permeability is known to be sensitive to changes in the effective stress (Somerton et al., 1975). In addition, the adsorption/desorption of gases, most notably CO_2, can cause additional changes in the permeability as the solid skeleton swells/shrinks (Connell, 2009). The main objective in this section is to evaluate the ability of the deformation model developed in section 3.6 to predict the changes in permeability as different gases flow in coal. This is an important stage in the model validation to ensure that appropriate permeability relationships have been adopted in the simulations for gas injection and CH_4 displacement in coal, which are presented in section 6.5.

The performance of the deformation model is examined by comparing the predicted changes in the permeability of coal with experimental data for the flow of N_2, CH_4 and CO_2. Since the coal matrix permeability is typically in the region of 8 to 9 orders of

magnitude less than that in the fracture network (Seidle, 2011), the contribution of the matrix permeability to the total permeability was neglected. The changes in the total permeability were therefore predicted using the fracture permeability equation, which from section 3.6 is given by:

$$
\begin{aligned}
K_F = K_{F0} \Bigg\{ 1 &- \frac{c_{f0}}{\alpha_f} \Bigg[1 - e^{\alpha_f \sum_{j=1}^{n_g} \left(Z_F RT c_{gF}^j - Z_{F0} RT c_{gF0}^j \right)} \Bigg] \\
&+ \frac{3}{n_{F0}} \sum_{j=1}^{n_g} \Bigg[\frac{(1-2v)}{E} \left(Z_F RT c_{gF}^j - Z_{F0} RT c_{gF0}^j \right) - \left(\varepsilon_s^j - \varepsilon_{s0}^j \right) \Bigg] \Bigg\}^3
\end{aligned}
\tag{6.11}
$$

It should be recalled that in equation (6.11), the second term expresses the change in permeability due to fracture compressibility, the third term due to matrix block compressibility and the final term due to sorption induced matrix block strain. In addition to applying and validating this model, an analysis of the importance of each of these mechanisms of deformation is presented in this section.

6.4.1 Input Data for the Permeability Model

As discussed in appendix A, the experimental permeability data were calculated based on the steady state flow of each gas through a coal core at a range of injection and confining pressures. Comparisons between the experimental permeabilities and those predicted by equation (6.11) are made for N_2, CH_4 and CO_2 at confining pressures of 4, 5 and 6 MPa. The permeability of the coal was calculated by Hadi Mosleh (2014) using the flow measurement data at three injection pressures for each confining pressure, as shown in Table 6.4. The downstream pressure in all tests was maintained at atmospheric pressure, i.e. 0.1 MPa.

In order to predict the changes in permeability using equation (6.11), the material parameters and initial conditions first needed to be established. A summary of the input data used in the deformation model for each confining pressure is provided in Table 6.5. Values for the initial fracture compressibilities, c_{f0}, and the fracture compressibility change rate, α_f, were based on the ranges suggested by Robertson and Christiansen (2008). The parameter c_{f0} was a key fitting parameter and the final values reported in Table 6.5

were found to provide an optimal fit for all three gases at each confining pressure. The final values are similar to that used by Liu and Rutqvist (2010), i.e. 4.3×10^{-7} Pa^{-1}, but are greater than the range suggested by Robertson and Christiansen (2008), i.e. 2.45×10^{-8} to 2.61×10^{-7} Pa^{-1}. The Poisson's ratio, v, and Young's modulus, E, of coal were chosen based on a literature survey.

Table 6.4 Summary of the injection pressures used at each confining pressure in the permeability experiments with N_2, CH_4 and CO_2.

Confining Pressure [MPa]	Injection Pressure Steps [MPa]		
	Step 1	Step 2	Step 3
4.0	2.5	3.0	3.5
5.0	3.5	4.0	4.5
6.0	4.5	5.0	5.5

As described in section 3.6, the sorption induced strain terms, ε_s^i and ε_{s0}^i, were calculated using a Langmuir-type strain isotherm, in which the linear strain constants, ε_L^i, were originally based on a literature survey and then modified to fit the experimental permeability data as required. The literature survey involved a review of 17 computational and experimental works and gave $0.0025 \leq \varepsilon_L^{N_2} \leq 0.0057$, $0.0030 \leq \varepsilon_L^{CH_4} \leq 0.0078$ and $0.0046 \leq \varepsilon_L^{CO_2} \leq 0.0163$. The final value for $\varepsilon_L^{N_2}$ was the same as that reported by Robertson and Christiansen (2006) and Zhou et al. (2013), whereas the final values for $\varepsilon_L^{CH_4}$ and $\varepsilon_L^{CO_2}$ were similar to those found by Levine (1996).

Since the permeability experiments were conducted at steady state flow conditions, the free gas in the fracture and matrix pore regions would have been at equilibrium. The matrix free gas concentrations used to calculate the sorption strain terms were therefore set to the same values as the fracture concentrations. In section 6.3, the adsorption parameters provided in Table 6.1 related to the adsorption isotherm since only the adsorption kinetics were being evaluated. For gas desorption, Hadi Mosleh (2014) reported a degree of hysteresis and therefore the Langmuir pressures, P_L^i, used in this section were set to the average of the adsorption and desorption isotherms.

Table 6.5 Input material parameters and initial conditions for the prediction of permeability changes using equation (6.11).

| Material parameter	Relationship / value		
Compressibility change rate, α_f (Pa⁻¹)	4.41×10^{-7}		
Poisson's ratio, υ (-)	0.34		
Young's modulus, E (Pa)	2.71×10^{9}		
Initial fracture porosity, n_{F0} (-)	0.0025		
	N_2	CH_4	CO_2
Langmuir linear strain constant, ε_s^i (-)	0.0025	0.0030	0.0080
Average Langmuir pressure, P_L^i (Pa)	1.730×10^{6}	0.675×10^{6}	0.500×10^{6}
Average Langmuir constant, b_L^i (Pa⁻¹)	5.780×10^{-7}	1.481×10^{-6}	2.000×10^{-6}
4 MPa Confining Pressure			
Initial fracture compressibility, c_{f0} (Pa⁻¹)	6.53×10^{-7}		
	N_2	CH_4	CO_2
Initial gas pressure (step 1), u_{g0} (Pa)	2.13×10^{6}	2.09×10^{6}	2.05×10^{6}
Initial permeability (step 1), K_F (m²)	1.85×10^{-16}	4.43×10^{-17}	4.58×10^{-17}
5 MPa Confining Pressure			
Initial fracture compressibility, c_{f0} (Pa⁻¹)	4.35×10^{-7}		
	N_2	CH_4	CO_2
Initial gas pressure (step 1), u_{g0} (Pa)	2.89×10^{6}	2.87×10^{6}	2.85×10^{6}
Initial permeability (step 1), K_F (m²)	1.62×10^{-16}	4.32×10^{-17}	2.13×10^{-17}
6 MPa Confining Pressure			
Initial fracture compressibility, c_{f0} (Pa⁻¹)	3.05×10^{-7}		
	N_2	CH_4	CO_2
Initial gas pressure (step 1), u_{g0} (Pa)	3.69×10^{6}	3.72×10^{6}	3.78×10^{6}
Initial permeability (step 1), K_F (m²)	1.48×10^{-16}	3.88×10^{-17}	8.57×10^{-18}

The permeabilities calculated by Hadi Mosleh (2014) using the experimental flow measurements represent the average values across the sample in each test. It was therefore important to approximate the average pore gas pressures in the sample corresponding to these permeabilities. Since gas is compressible, the steady state pore gas pressure does not vary linearly down a pressure gradient. As a result, the average gas pressures were found by running simulations for each injection scenario, and then taking an average of the predicted steady state gas pressure over the domain. The resulting pressures and the corresponding permeabilities were then used to plot the experimental permeability data. In Table 6.5, the initial permeabilities, K_{F0}, and gas pressures, u_{gF0}, used in the deformation model relate to the step 2 injection pressures at each confining pressure.

An estimate of the initial porosity, n_{F0}, was more difficult due to a lack of data. As shown in Table 6.5, n_{F0} was set to 0.0025. It is important to recognise the inherent uncertainty involved in estimating n_{F0} without supporting data for the specific coal sample. However, a reasonable effort has been made to identify a value that results in a good fit of the experimental data and is supported by the literature. For example, the fracture porosities for coals from the San Juan basin, USA, are generally accepted to be somewhere in the range of 0.002 to 0.006 (Gash et al., 1992; Harpalani and Chen, 1995). Based on this, it may be concluded that the estimated fracture porosity of 0.0025 is reasonable.

6.4.2   Comparison of Experimental and Predicted Permeability

In this section, the changes in coal permeability observed in the experiments are compared with the predictions of the deformation model. An analysis of the importance of the various deformation mechanisms considered in this work is also presented. Figure 6.7, Figure 6.8 and Figure 6.9 compare the experimental permeability data with the predictions of the deformation model at each confining pressure for N_2, CH_4 and CO_2, respectively. In general, there is a good agreement between the experimental data points and the predicted permeability curves. This is especially true for N_2 and CO_2.

However, the experimental data points covered a relatively narrow range of effective stress. It is also important to appreciate the level of uncertainty in approximating the average gas pressures which have been assigned to the experimental permeability data.
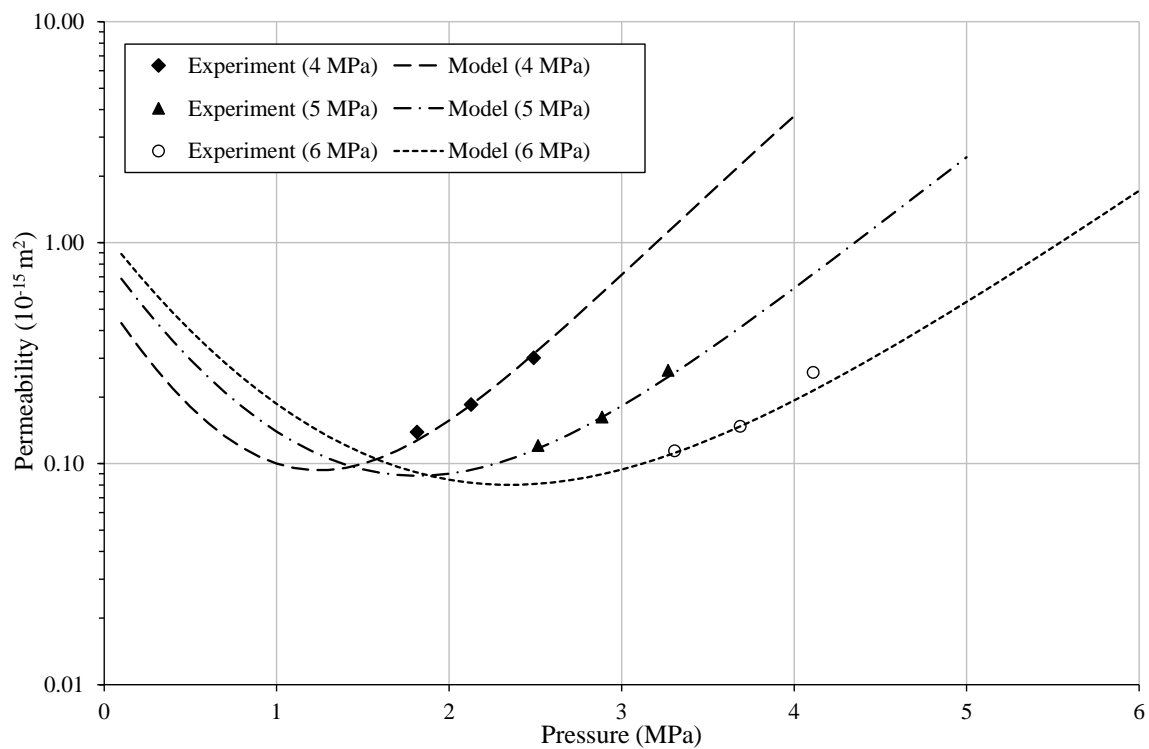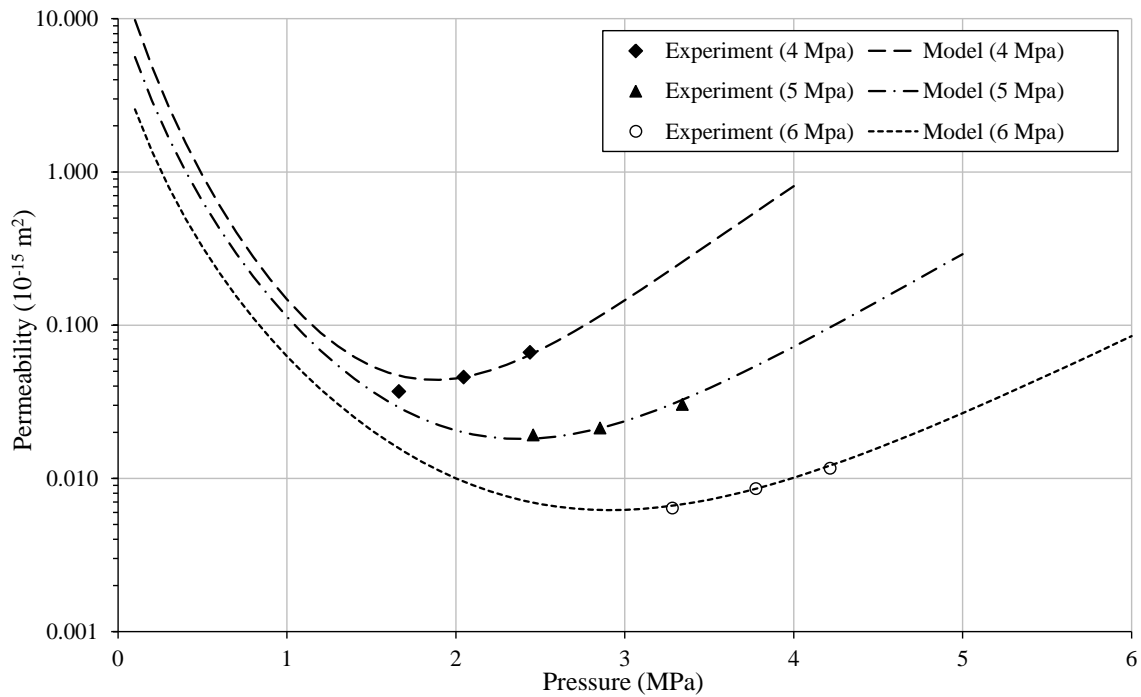
Figure 6.7 Variation of the coal permeability to nitrogen with pressure observed in the experimental work and predicted by equation (6.11) at each confining pressure.
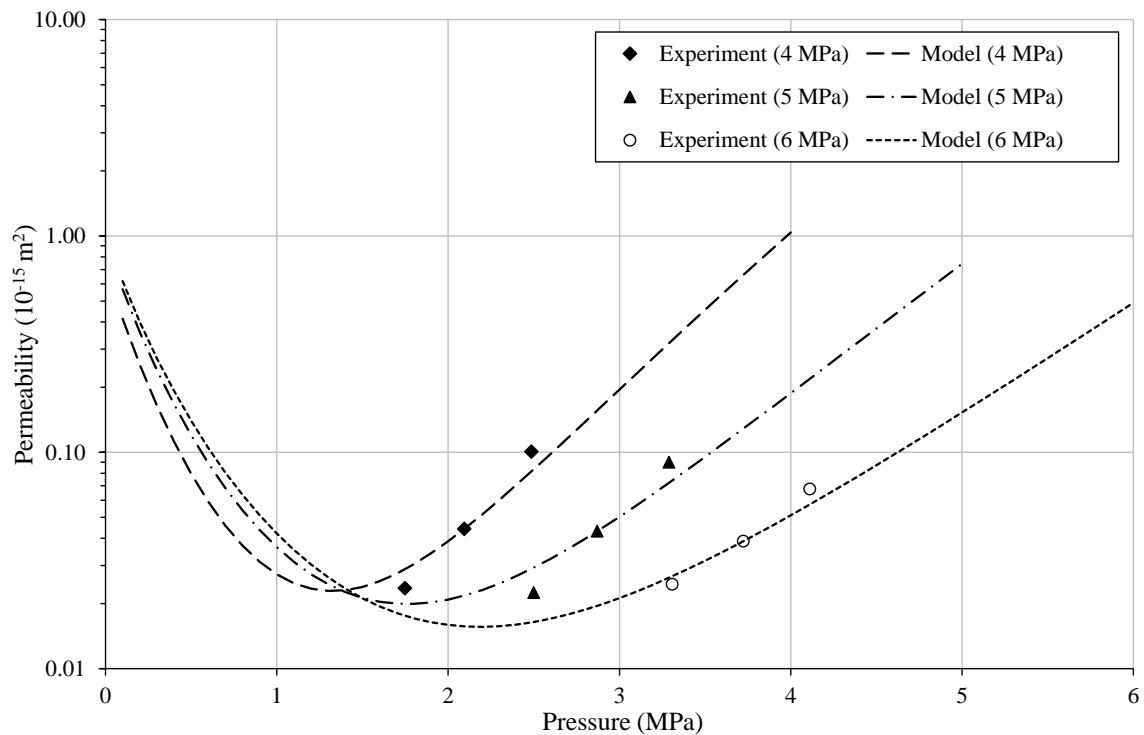
Figure 6.8 Variation of the coal permeability to methane with pressure observed in the experimental work and predicted by equation (6.11) at each confining pressure.

Figure 6.9 Variation of the coal permeability to carbon dioxide with pressure observed in the experimental work and predicted by equation (6.11) at each confining pressure.

This uncertainty may be significant since the pore gas pressure distribution across the core would have been influenced not only by the gas compressibility, but also the variations in permeability across the sample. Based on these points, and considering that the comparisons with the experimental data are limited to the flow of pure gas, it can be concluded that the multicomponent deformation model has only been partially validated.

Whilst the overall trends of the predicted permeability curves are similar to those observed in other studies (e.g. Palmer and Mansoori, 1998; Pekot and Reeves, 2002; Ma et al., 2011), further tests indicate that the model performance requires further evaluation in relation to:

   i. A possible over-prediction of the sorption strain as the pressure is reduced, giving a greater permeability rebound at low pressure compared to other models.

   ii. The prediction of a negative permeability under certain conditions involving a low sorption strain (i.e. close to zero) or a high sorption strain (e.g. where adsorbed N_2 or CH_4 is displaced by CO_2).

The above mentioned behaviour becomes more apparent as the initial fracture porosity is reduced below 0.01, which may be attributed to the greater sensitivity of the permeability to small changes in the fracture aperture. These limits of the deformation model should be appreciated for its application in the developed numerical model.

Importantly, the deformation model has been partially validated for the flow of pure gas. Furthermore, the predicted trends for a multicomponent system are reasonable, i.e. the displacement of adsorbed CH_4 by N_2 increases the permeability by coal shrinkage, whereas displacement by CO_2 reduces the permeability by coal swelling. This species dependent behaviour is discussed in greater detail below. It can be concluded that the developed deformation model may be applied in the simulation of multicomponent gas transport in coal, provided an appropriate lower bound (i.e. threshold) is placed on the permeability. Nonetheless, it is clear that future development and testing of the deformation model is required.

Changes in the permeability due to fracture compressibility, matrix block compressibility and sorption induced matrix block swelling are included in the deformation model. The first two mechanisms are physico-mechanical processes and depend only on the bulk pore gas pressure at a constant confining pressure. Sorption induced swelling is a chemo-mechanical and species dependent process, since coal has a greater preference to adsorb CO_2 ahead of CH_4, and CH_4 ahead of N_2, as shown in Figure 6.3. The sorption induced swelling effect, which may cause a loss in the permeability, is likewise greatest for CO_2 and lowest for N_2. This effect is shown in Figure 6.7 and Figure 6.9, where CO_2 permeability is on average 7.04 times lower than N_2 permeability across the full range of effective stress conditions considered in the deformation model.

As expected, the permeability to CH_4 falls between the other two gases and is on average 3.67 times lower than N_2 permeability. In fact, the reported CH_4 permeabilities are slightly smaller than might be expected because the CH_4 tests were conducted after the CO_2 tests. Although the coal core was vacuumed after the CO_2 tests, it is possible that the coal did not recover its original permeability before the start of the CH_4 tests. This would explain why the experimental CH_4 permeabilities increased at a faster rate than predicted by the deformation model in Figure 6.8, since the permeability recovery would have been on-

going during the CH$_4$ testing.

In a given coal, the relative importance of fracture compressibility, matrix block compressibility and sorption strain in determining permeability depends on the pore gas and confining pressures, i.e. the effective stress, and the gas species. By considering the effect of each mechanism in isolation, it is possible to analyse the behaviour in greater detail. Figure 6.10, Figure 6.11 and Figure 6.12 show how the permeability ratio, K_R, varies due to each mechanism at 6 MPa confining pressure for N$_2$, CH$_4$ and CO$_2$, respectively. The permeability ratio is defined by:

$$K_R = \frac{K_F}{K_{F0}} \tag{6.12}$$

where K_{F0} is the permeability obtained in the experimental work for the step 2 injection pressure and K_F is the permeability predicted by the deformation model.

From the curves in Figure 6.10, Figure 6.11 and Figure 6.12, it can be seen that the effects
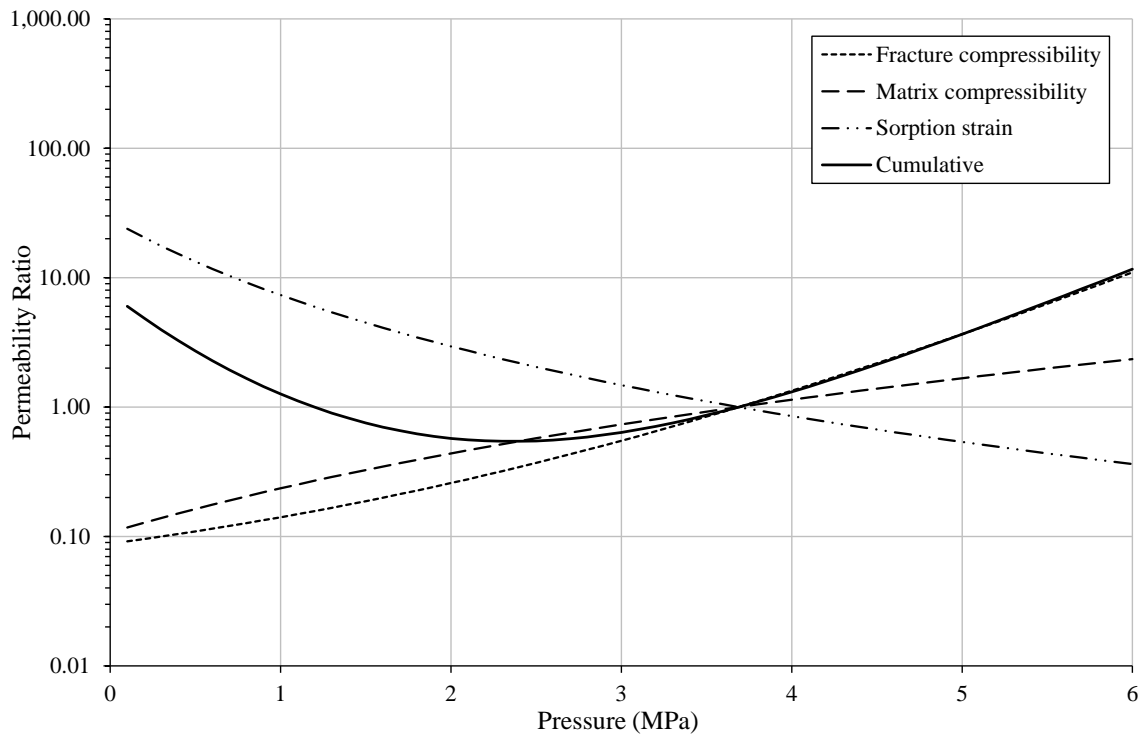
Figure 6.10 Effect of each deformation mechanism on coal permeability to nitrogen at 6 MPa confining pressure.
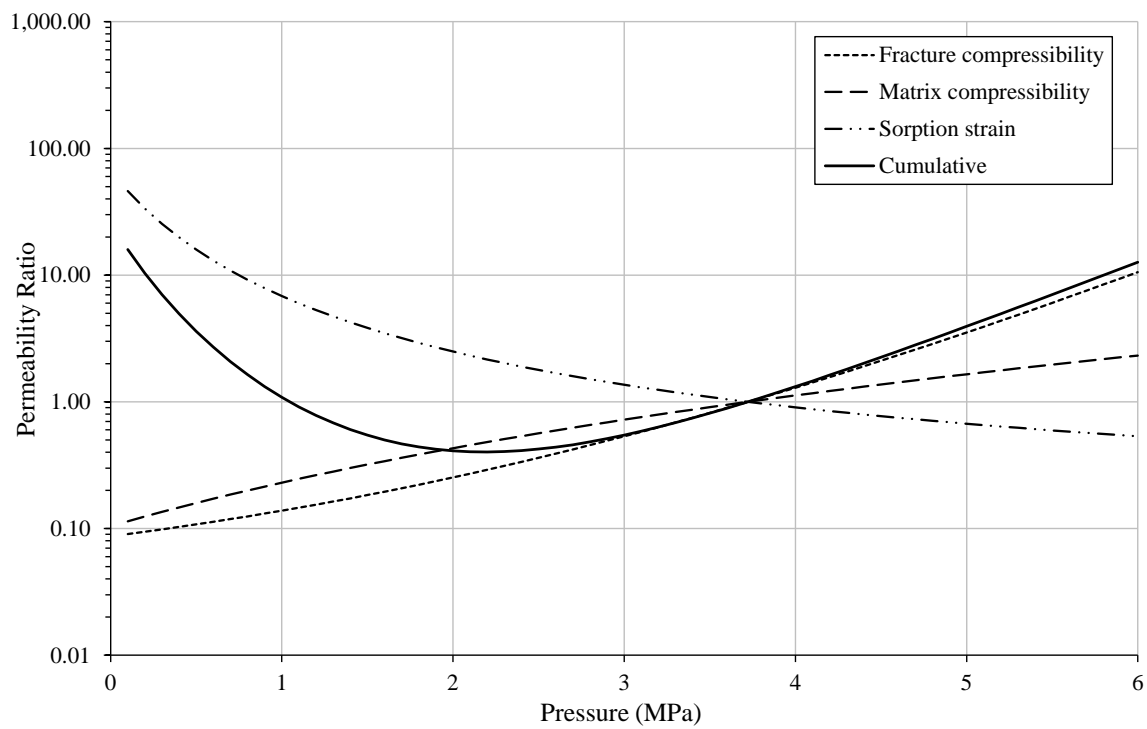
Figure 6.11 Effect of each deformation mechanism on coal permeability to methane at 6 MPa confining pressure.
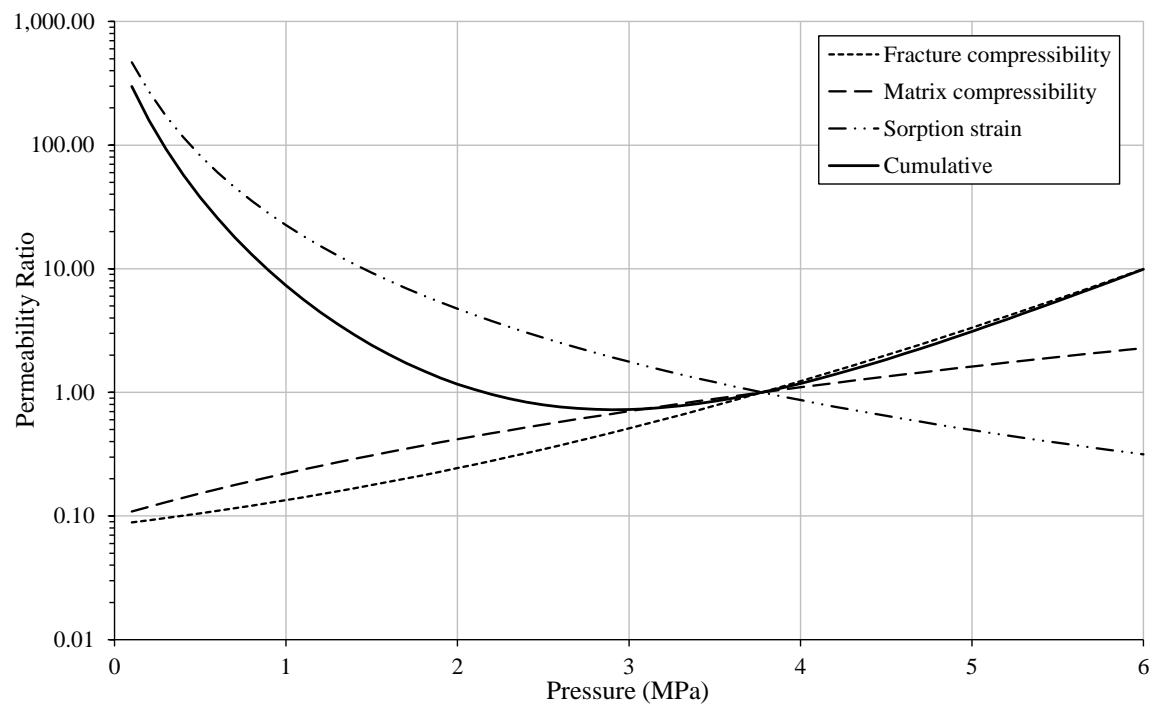
Figure 6.12 Effect of each deformation mechanism on coal permeability to carbon dioxide at 6 MPa confining pressure.

of fracture and matrix compressibility are the same for each gas. This is because these mechanisms depend on the bulk pore gas pressure and not gas composition. As expected, the species dependent changes in permeability are due to the swelling/shrinking of the coal via gas adsorption/desorption.

As the pore gas pressure is reduced from the initial value of around 3.8 MPa, the effective stress is increased and the applied confining pressure compresses the fractures, thereby reducing permeability. Since the matrix blocks are assumed to be compressed by the hydrostatic load of the pore gas pressure in the fractures, the lowered pore pressure also allows a small mechanical expansion of the matrix blocks. This causes an additional, albeit smaller, loss in permeability. These processes are reflected in the fracture and matrix compressibility curves, which fall below 1.0 as the pressure is lowered. In contrast, a reduction in pore gas pressure also causes desorption induced matrix shrinking, which increases the permeability. This is reflected in the sorption strain curves, which increase above 1.0 as the pressure is lowered. The opposite occurs as the pore pressure is increased from the initial value. The effective stress is then reduced and the higher pore pressure dilates the fractures and compresses the matrix blocks, thereby increasing the fracture permeability, whilst adsorption induced matrix swelling reduces the permeability.

From the above observations, the changes in coal permeability are governed by the balance of the contrasting effects of the physico-mechanical compressibility terms and the chemo-mechanical sorption strain term. In the case of N_2, the sorption strain is less influential and so the overall behaviour is more dependent on the compressibility terms. However, sorption strain affects the overall trend of the CO_2 permeability curve much more, especially at low pore gas pressures or high confining pressures where fracture compressibility is at a minimum.

In this section, the performance of the deformation model described in section 3.6 has been evaluated via comparisons with experimental data for gas flow in coal at three different confining pressures. There was generally a good agreement between the predicted permeabilities and those observed in the experimental work. However, it is recognised that the experimental data covered a relatively narrow range of effective stress and was limited to the flow of pure gas. In addition, the permeability rebound due to desorption induced

coal matrix shrinkage may be over-predicted compared to existing models, and the prediction of negative permeabilities under certain conditions has been noted. These limitations should be recognised when applying the deformation model, for example by defining an appropriate lower bound (threshold) permeability. It can be concluded that further development and testing is necessary to build upon the partial validation provided in this section.

An analysis of the deformation mechanisms considered showed that fracture compressibility has a more significant role in permeability changes compared to matrix block compressibility. The sorption strains were found to counteract these compression terms, an effect that was found to be greatest in the case of CO_2.

6.5   Simulation of Gas Injection and Methane Displacement in Coal

In sections 6.2 and 6.4, the aspects of the formulation related to gas adsorption kinetics and permeability changes in coal were examined and the related material parameters were established. The main objective now is to build on this work by exploring the validity of the dual porosity, dual permeability multicomponent reactive gas transport model as a whole. This involves comparing the results of the experiments performed by Hadi Mosleh (2014) for gas injection and CH_4 displacement with numerical simulation results. Recalling from section 6.2, two injection scenarios have been considered. Test A considered the injection of pure N_2 and Test B considered the injection of pure CO_2. For each scenario, the gas breakthrough curves observed in the experimental work are compared with those predicted by the numerical model. This includes an in-depth discussion on the processes and behaviour involved.

6.5.1   Model Domain and Analysis Details

As reported in appendix A, the gas injection and displacement experiments were conducted using coal cores of 0.12 m length and 0.07 m diameter. Gas was injected into the bottom face of the core and abstracted from the top face. Since the injection and abstraction pressures were applied uniformly over these surfaces, the system was treated as a two-dimensional problem in which the flow of gas between the injection and abstraction

boundaries was effectively one-dimensional.

The domain was discretised into 100 equally sized 4-noded quadrilateral elements. A variable time step was used, which allowed the size of the time step to vary depending on the state of convergence. Under this scheme, if the convergence criterion was met within a specified number of iterations, the time step was increased by a factor. Conversely, if the convergence criterion was not met within a specified maximum number of iterations, the time step was decreased by a factor. The initial and maximum time steps adopted were 1 second and 10 seconds, respectively. This ensured a good resolution in the temporal output of the model for the 90 minute simulation period considered.

6.5.2   Material Parameters

As far as possible, the physical and chemical parameters of the coal-gas system were based on the work presented in sections 6.3 and 6.4. Otherwise, the values were chosen based on a combination of literature review and history matching of the experimental data. A summary of the additional material parameters required in the simulations is provided in Table 6.6.

The adsorption isotherm parameters for N_2 and CO_2 were the same as those provided in Table 6.1. Since only CH_4 desorption occurred in the simulations, it was not appropriate to use the adsorption isotherm parameters for CH_4. This is because of the hysteresis in the adsorption/desorption behaviour reported by Hadi Mosleh (2014). The desorption isotherm parameters were therefore applied for CH_4 in the simulations, which are reported in Table 6.6. For completeness, the adsorption isotherm parameters for N_2 and CO_2 have been repeated. The adsorption kinetics parameters reported in Table 6.3 were used in the simulations, i.e. it was assumed that the CH_4 desorption kinetics are the same as the adsorption kinetics.

As explained in section 6.4.2, the CH_4 permeability presented in Figure 6.8 was generally lower than expected. It was concluded that this lower permeability may have resulted from the CH_4 experiment being conducted after the CO_2 experiment. The coal may not have recovered its original permeability after CO_2 permeation, despite being subjected to a

vacuum for 24 hours between experiments. Furthermore, these results relate to a different coal core to the one used in Tests A and B. As a result, Hadi Mosleh (2014) completed additional CH_4 permeability testing on this coal core. The test was conducted at the required confining pressure of 6 MPa, and the results are presented in Figure 6.13. The permeability curve predicted by the deformation model in equation (6.11) has also been included. The best match with the experimental results was achieved with an initial fracture compressibility of 3.77×10^{-7} Pa^{-1}, which is slightly higher than that reported for the previous core in Table 6.5.

Table 6.6 Additional material parameters required for the simulation of Tests A and B conducted by Hadi Mosleh (2014). Remaining parameters for the adsorption/desorption and deformation behaviour can be found in Table 6.1, Table 6.3 and Table 6.5.

Material parameter	Relationship / value		
Matrix block dimension, l (m)	0.010		
Initial total porosity, n_{T0} (-)	0.025		
Volumetric weighting factor, w_f (-)	0.005		
	Fracture	Matrix	
Initial local porosity, $n_{\alpha 0}^L$ (-)	0.500	—	
Initial porosity, $n_{\alpha 0}$ (-)	0.0025	0.0225	
Initial local permeability, $K_{\alpha 0}^L$ (m^2)	4.50×10^{-16}	4.50×10^{-24}	
Initial permeability, $K_{\alpha 0}$ (m^2)	2.25×10^{-18}	4.48×10^{-24}	
	N$_2$	CH$_4$	CO$_2$
Diffusion coefficient (free), D_g^i (m^2 s^{-1})	2.04×10^{-5}	2.23×10^{-5}	1.10×10^{-5}
Langmuir capacity, n_L^i (mol kg^{-1})	0.68	1.04	1.26
Langmuir pressure, P_L^i (Pa)	1.86×10^6	0.45×10^6	0.20×10^6
Langmuir constant, b_L^i (Pa^{-1})	5.38×10^{-7}	2.22×10^{-6}	5.00×10^{-6}

At the start of Tests A and B, the CH_4 gas pressure in the core was uniform at 5 MPa. From Figure 6.13, the predicted CH_4 permeability at 5 MPa is 4.50×10^{-16}, which was used as the initial local permeability in the fracture pore region, K_{F0}^L, as reported in Table 6.6.
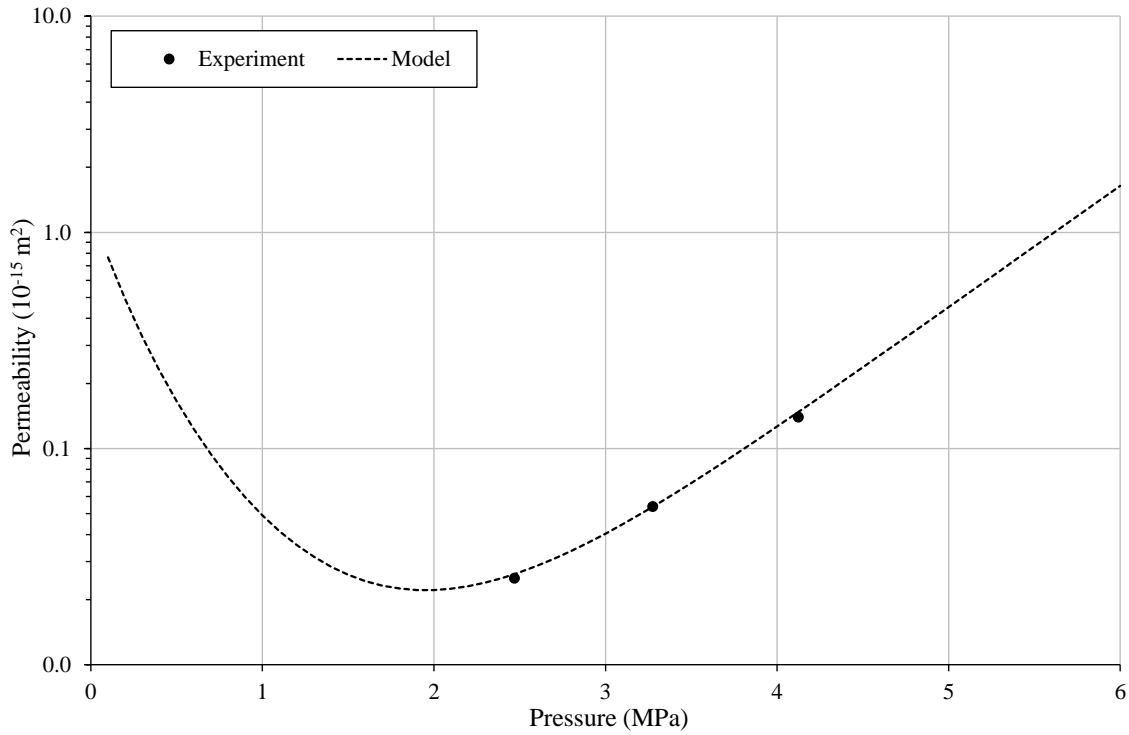
Figure 6.13 Variation of coal permeability to methane with pressure observed for the coal core used in Tests A and B, and predicted by equation (6.11) at 6 MPa confining pressure.

The initial local permeability in the matrix pore region, K_{M0}^L, was set to eight orders of magnitude less than the fracture value, based on the recommendation of Seidle (2011). Recalling from chapter 3, the initial permeabilities, $K_{\alpha 0}$, were obtained using the following relationships:

$$K_{F0} = w_f K_{F0}^L \tag{6.13}$$

$$K_{M0} = \left(1 - w_f\right) K_{M0}^L \tag{6.14}$$

As reported in section 6.4, the deformation model developed in this work has been noted to predict negative permeabilities under certain conditions. In order to apply the model in the numerical simulations presented in this section, a lower bound (threshold) permeability of $K_F^L = 4.5 \times 10^{-18}$ m^2 was employed, i.e. 100 times lower than the initial value given in Table 6.6. This is viewed as a reasonable threshold since the lowest coal permeability measured by Hadi Mosleh (2014) was $K_F^L = 6.4 \times 10^{-18}$ m^2, i.e. 70.4 times lower than the initial value. Similarly, a matrix permeability threshold of $K_M^L = 4.5 \times 10^{-26}$ m^2 was

employed.

In the absence of supporting data, the volumetric weighting factor, w_f, was varied as a fitting parameter. The reported value of 0.005 was found to provide an optimal fit with the experimental data for the N_2 and CO_2 injection scenarios. This implies that the fracture domain, including the volume occupied by open fractures, infilling minerals and the altered rock zone (ref. Figure 3.1), would have occupied somewhere in the region of 0.5% of the total volume of the coal core.

The range of total porosities presented in Table A.1 in appendix A was explored and it was found that the lower limit of 0.025 provided the best fit to the experimental data. This falls in the range of 0.025 to 0.18 suggested by Anderson et al. (1956) and is slightly lower than the range of 0.041 to 0.232 suggested by Gan et al. (1972), although it is noted that these studies were conducted on different coals (American coals varying in rank from lignite to anthracite).

Recalling from chapter 3, the initial porosity in the fracture continuum, i.e. the bulk scale parameter n_{F0}, is related to the local porosity in the fractured zone, $n_{\alpha 0}^L$, by the following expression:

$$n_{F0} = w_f n_{F0}^L \qquad (6.15)$$

As shown in Table 6.6, n_{F0}^L was set to 0.50. Substituting this value into equation (6.15) gave n_{F0} as 0.0025. This is the same value that was used in section 6.4, and is similar to the values suggested by Gash et al. (1992) and Harpalani and Chen (1995).

The porosity in the matrix continuum reported in Table 6.6 was calculated using equation (3.9), which is recalled as:

$$n_{M0} = n_{T0} - n_{F0} \qquad (6.16)$$

Substituting for n_{T0} and n_{F0} in equation (6.16) from Table 6.6 gave n_{M0} as 0.0225.

Despite coal being a physically and chemically heterogeneous rock (Lee, 1996), the fracture spacing is typically more uniform and can range between a fraction of a centimetre

to several centimetres in different coals (King et al., 1986). This made choosing a value for the matrix block dimension, l, difficult in the absence of a detailed analysis of the particular coal sample. As a result, this was varied as a fitting parameter. The final value of 0.010 m is in the range suggested by King et al. (1986) and is similar to the values used in the modelling studies conducted by Shi et al. (2008) and Wu et al. (2010).

Finally, the self-diffusion coefficient of each gas reported in Table 6.6 was calculated using the Chapman-Enskog equation (Chapman and Cowling, 1970):

$$D_g^i = \frac{1.86 \times 10^{-7} T^{3/2} \left(2/M_g^i\right)^{1/2}}{u_{gAtm} \sigma_i^2 \Omega_i} \tag{6.17}$$

where M_g^i is the molecular mass and u_{gAtm} is the gas pressure equal to 1 atm. The parameters σ_i and Ω_i are the collision diameter and collision integral, respectively, and describe the nature of collisions between molecules. The collision integral, Ω_i, varies with the temperature and the energy of interaction of the colliding molecules. The values of σ_i and Ω_i were calculated using an approach outlined by Cussler (1997). The resulting values for N_2, CH_4 and CO_2 at the experimental temperature of 298 K are provided in Table 6.7.

Table 6.7 Values of the collision diameter, σ_i, and collision integral, Ω_i, for N_2, CH_4 and CO_2 at a temperature of 298 K.

Gas parameter	Value		
	N_2	CH_4	CO_2
Collision diameter, σ_i (Å)	3.798	3.758	3.941
Collision integral, Ω_i (-)	0.870	1.075	1.198

In contrast to the general formulation for flow in fractured rock developed in chapter 3, the effect of pressure on D_g^i was not considered in these simulations. Furthermore, Knudsen diffusion was not considered and the constrictivity factors, δ_{iM}, related to configurational diffusion were set to 1.0 for all three gas species. Finally, the sink/source term for mass exchange was reduced to a pure diffusion form. In other words, the effect of advection was

not included so that the mass exchange process was assumed to be dominated by diffusion in the matrix blocks.

6.5.3 Simulation Conditions

A schematic of the initial and boundary conditions used in the simulations of Tests A and B is provided in Figure 6.14, where the left- and right-hand boundaries are the injection and abstraction faces of the coal core, respectively. As discussed in appendix A, the initial gas contained in the coal core was pure CH_4 at 5 MPa. At the start of the experiment, the injection boundary was exposed to either N_2 or CO_2 at 5 MPa at the same time as the abstraction boundary was set to atmospheric pressure. In Figure 6.14, these gas pressures were converted to the equivalent concentrations using the real gas law, given by:

$$c_g = \frac{u_g}{ZRT} = \frac{5.0 \times 10^6}{Z(8.314 \times 298)} = \frac{2017.99}{Z} \tag{6.18}$$

where c_g is the gas concentration equivalent to a gas pressure, u_g, of 5 MPa at a temperature, T, of 298 K, R is the universal gas constant and Z is the compressibility factor obtained using the Peng and Robinson (1976) equation of state.

The initial amount of adsorbed CH_4 was assumed to be at equilibrium with the free gas phase, and was calculated via the Langmuir isotherm using the parameters given in Table 6.1.

As indicated in Figure 6.14, the injection and abstraction boundary conditions were applied in the fracture continuum, but not in the matrix continuum. This was necessary because the sorption strain in the deformation model was calculated at equilibrium with the free gas concentrations in the matrix continuum, and not using the actual adsorbed amounts calculated in the adsorption kinetics module. This meant that applying the fixed concentration boundary conditions in the matrix continuum would have caused instantaneous sorption strains at the boundary. For example, at the injection boundary for CO_2 injection, the permeability would have been immediately reduced as a result of the large adsorption induced strain. Since gas adsorption in coal is known to be a kinetic

reaction, as shown in section 6.2, this behaviour would not have been realistic. As a result, the boundary conditions were applied in the fracture continuum but not in the matrix continuum.

Injection boundary conditions	Initial conditions	Abstraction boundary conditions
	Free gas:	
Test A (N_2 injection):	$c_{g\alpha}^{N_2} = c_{g\alpha}^{CO_2} = 0.0 \ mol \ m^{-3}$	$RT \sum_{j=1}^{n_g} c_{gF}^{j} = 0.1 \times 10^{6} Pa$
$c_{gF}^{N_2} = 2046.93 \ mol \ m^{-3}$	$c_{g\alpha}^{CH_4} = 2243.60 \ mol \ m^{-3}$	
	Adsorbed gas:	$\sum_{j=1}^{n_g} \dfrac{\partial c_{gF}^{j}}{\partial t} = 0.0$
Test B (CO_2 injection):	$s_{gM}^{N_2} = s_{gM}^{CO_2} = 0.0 \ mol \ kg^{-1}$	
$c_{gF}^{CO_2} = 3060.49 \ mol \ m^{-3}$	$s_{gM}^{CH_4} = 0.977 \ mol \ kg^{-1}$	

Figure 6.14 Schematic of the initial and boundary conditions used in the simulations of Tests A and B.

6.5.4 Simulation Results

Figure 6.15 presents the produced gas composition obtained in the numerical simulation of Test A (N_2 injection). Taken as when the composition of the produced gas reached 10% N_2, the breakthrough occurred at just over 2 minutes and the composition of the produced gas increased rapidly to 84.3% N_2 at 5 minutes. A more gradual increase in the fraction of N_2 in the produced gas was observed in the longer term, reaching 99.8% at the end of the simulation period. As shown by the good agreement with the experimental results in Figure 6.15, a similar breakthrough trend was observed in the laboratory.

The produced gas composition obtained in the numerical simulation of Test B (CO_2 injection) is provided in Figure 6.16. Although the trend is similar to that observed in the experiment, the agreement is not as good as that observed for Test A. The breakthrough of CO_2 occurred at 10 minutes in the simulation, compared to 15 minutes in the experiment. Furthermore, the fraction of CO_2 in the produced gas was generally over-predicted. At the end of the simulation period, the produced gas composition had reached 89.8% CO_2,
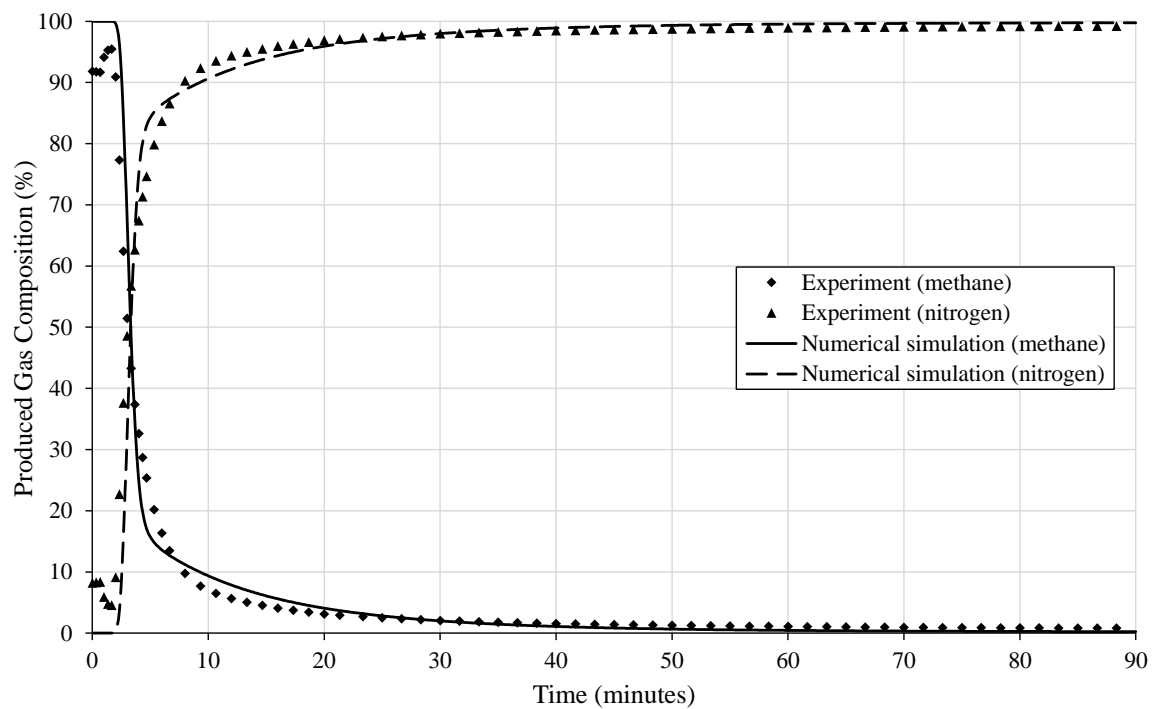
Figure 6.15 Produced gas compositions for Test A (N_2 injection) observed in the experimental work and predicted by the numerical model.
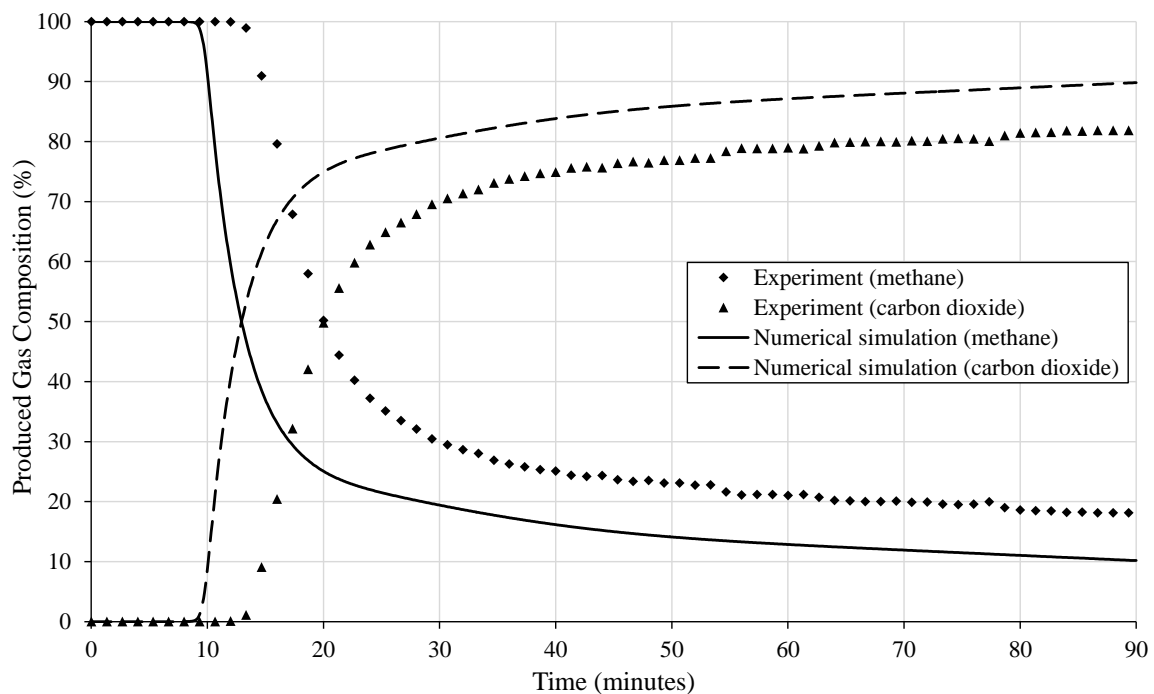
Figure 6.16 Produced gas compositions for Test B (CO_2 injection) observed in the experimental work and predicted by the numerical model.

compared to 82.2% in the experiment. A discussion on the differences between the experimental and simulation results for Test B is provided in section 6.5.4.2. This follows a more general discussion of the simulation results given in section 6.5.4.1.

6.5.4.1   Discussion of the Simulation Results

It can be seen in Figure 6.15 and Figure 6.16 that the breakthrough of N_2 and CO_2 can be divided into two fairly distinct stages, namely, a sharp primary breakthrough stage and a gradual secondary breakthrough stage. The primary breakthrough stage is mainly due to the displacement of the free CH_4 in the fractures by the injected gas. The secondary breakthrough stage is due to the displacement of the free and adsorbed CH_4 stored in the matrix blocks.

The primary breakthrough in the simulation of Test B occurred 5 times later and was more dispersed than in the simulation of Test A. This is mainly due to the progressive reduction in the fracture permeability associated with the CO_2 adsorption induced swelling of the coal matrix, which was discussed in detail in section 6.4. In the secondary breakthrough stage, the produced gas in Test B comprised a greater mole fraction of CH_4 than in Test A. From sections 6.3 and 6.4, the major species dependent coal-gas interactions that may be responsible for this difference are:

 i. Coal has a higher preference to adsorb CO_2 than N_2 and CH_4, and CO_2 adsorption occurs much more rapidly.

 ii. Permeability loss in coal due to adsorption induced swelling is larger for CO_2 adsorption than for N_2 and CH_4 adsorption.

Since N_2 has a lower preference to adsorb in coal than CH_4, as shown in Figure 6.3, it has a lower tendency to displace the adsorbed CH_4 compared to CO_2. This implies that the adsorbed CH_4 was more gradually displaced in Test A. The contribution of CH_4 desorption to the produced gas would then have been less apparent than in Test B. This behaviour may be indicated by the presence of 0.2% CH_4 in the produced gas at the end of the N_2 simulation, compared to 10.2% at the end of the CO_2 simulation.

However, the gas adsorption kinetics examined in section 6.3.2 effectively limited the role

of the preferential CH_4 desorption discussed above. Since it was assumed that the CH_4 adsorption and desorption kinetics are the same, CH_4 desorption is a relatively slow process that occurs over a longer time scale than that considered in the simulations. In fact, the half-life of CH_4 desorption in the coal is around 180 minutes, compared to the 90 minute simulation time. As a result, a large portion of the initial adsorbed CH_4 remained in the adsorbed phase at the end of both simulations, i.e. 79.7% in Test A and 83.1% in Test B. It can be concluded that the preferential CH_4 desorption was not a major factor in the different gas breakthrough curves in Test A and Test B.

This is supported by comparisons with the results of the verification tests presented in section 5.4, which were obtained for similar injection scenarios in a 100 m long "single porosity" coal with adsorption/desorption kinetics. At the larger scale, the injection of N_2 produced a highly dispersed breakthrough due to the slow rate of CH_4 desorption. In contrast, the breakthrough of CO_2 was much sharper. This is because the rate of CH_4 desorption was effectively enhanced by the preferential CO_2 adsorption. The breakthrough profiles in Figure 6.15 and Figure 6.16 do not follow the trends observed at the larger scale. This can be attributed to the limited role of preferential CH_4 desorption in Tests A and B discussed above.

In relation to the species dependent permeability response of coal, the significant CO_2 adsorption strains in Test B effectively choked the flow due to a significant loss in the fracture permeability. This is in accordance with the analysis of coal permeability to N_2, CH_4 and CO_2 presented in section 6.2. The lower fracture flow rate restricted both the injection of CO_2 and its arrival at the abstraction boundary, thereby limiting the amount of CO_2 in the produced gas. In contrast, the higher fracture flow rate maintained in Test A meant that more N_2 was arriving at the abstraction boundary, thereby increasing its contribution to the produced gas relative to CH_4. This is supported by the experimental observations of Hadi Mosleh (2014). After 90 minutes, a total of 1.60 mol of N_2 had been injected, of which 1.41 mol (88%) had been produced. For CO_2, only 0.13 mol had been injected, with just 0.07 mol (54%) of this being produced.

It may be concluded that the different time and size of the primary breakthrough of CO_2 compared to N_2 was mainly due to the significant CO_2 adsorption induced permeability

loss. The short time scale involved in the flow in the 0.12 m long coal core, combined with the relatively slow CH_4 desorption kinetics, effectively limited the role of preferential CH_4 desorption in the gas breakthrough behaviour.

As mentioned previously, the breakthrough of CO_2 in the simulation of Test B occurred earlier than in the experiment and the fraction of CO_2 in the produced gas was generally over-predicted. Based on the above conclusion, the evolution in coal permeability is a principal factor that controls the gas breakthrough trend at the laboratory scale considered. The next section therefore examines the role of the permeability in the different experimental and simulated breakthrough profiles in Figure 6.16.

6.5.4.2   Differences in the Experimental and Simulated Results in Test B

Following the conclusion reached in the previous section, additional simulations of Test B were performed with a reduced initial permeability. It was found that an initial local fracture permeability of 3.0×10^{-16} m^2 provided a much improved agreement with the experimental data, as shown in Figure 6.17. This is one third lower than the original permeability used in the simulation presented in Figure 6.16.

For the reduced initial permeability, it can be seen that the breakthrough of CO_2 occurred at 14 minutes, compared to 15 minutes in the experiment. Whilst the breakthrough profile is qualitatively similar to the simulation results at the original permeability, there is a closer quantitative agreement with the experimental results. The remainder of this section discusses the experimental and computational factors which may be responsible for the improved agreement at the lower initial permeability.

One possibility is that the permeability of the coal core used in the laboratory was reduced between the start of Tests A and B. This is because the permeability of coal is known to depend on the stress history, as reported in a number of experimental studies (e.g. Somerton et al., 1975; Durucan and Edwards, 1986; Meng and Li, 2013). Somerton et al. (1975) found that coal can exhibit varying levels of permeability hysteresis as a result of cyclic loading. After exposing different coal samples to triaxial and hydrostatic load cycles ranging between 0.7 and 13.8 MPa, losses in permeability of up to one order of magnitude were observed. Although the confining pressure remained at 6 MPa after the CH_4

permeability testing, a number of pore pressure cycles were involved in the experimental procedure for Tests A and B, as follows:

    i. Permeability test (CH_4).

    ii. Downstream valve closed and core saturated with CH_4 to a uniform 5 MPa.

    iii. Test A (N_2 injection and CH_4 displacement).

    iv. Vacuum applied at downstream valve for 24 hours, with CH_4 injection at upstream valve to accelerate the purge of N_2.

    v. Downstream valve closed and core saturated with CH_4 to a uniform 5 MPa.

    vi. Test B (CO_2 injection and CH_4 displacement).

Based on the observations of Somerton et al. (1975), it is possible that the effective stress cycles caused a reduction in permeability between the two experiments.
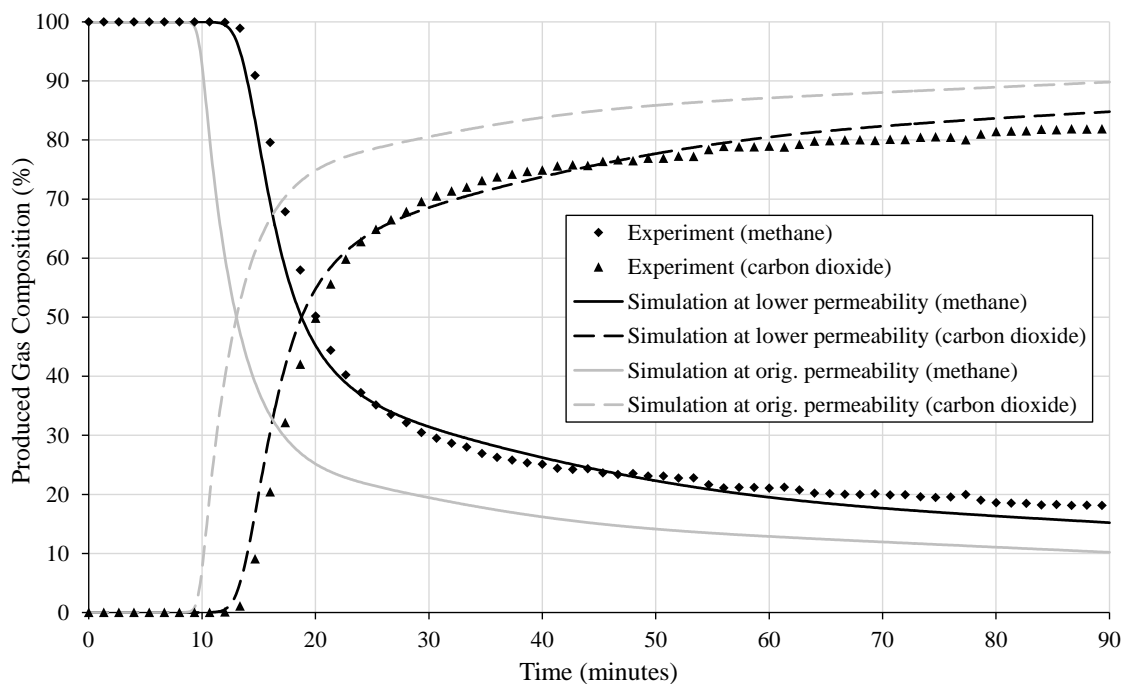
Figure 6.17 Produced gas compositions for Test B (CO_2 injection) observed in the experimental work and predicted by the numerical model for a reduced initial local fracture permeability of 3.0×10^{-16} m^2. Simulation results from Figure 6.16 are included for comparison.

As expected, the breakthrough of CO_2 occurred later than N_2, even before implementing the reduced initial permeability. A major factor that governed the delayed breakthrough

was the progressive reduction in fracture permeability due to the CO_2 adsorption induced swelling of the coal matrix, which was discussed in detail in section 6.4. A lower initial permeability may therefore have been required in the simulation of Test B to compensate for the predicted rate of sorption swelling being too slow. The permeability threshold discussed in section 6.4 and defined as $K_F^L = 4.5 \times 10^{-18}$ m^2 in section 6.5.2 is not believed to have had a role in the early breakthrough of CO_2. This is because this permeability is almost 30% less than the lowest permeability measured in the laboratory by Hadi Mosleh (2014) for the steady state flow of CO_2.

The sorption strain was calculated at equilibrium with the free gas concentrations in the matrix continuum. As discussed in section 6.5.3, this meant that no injection boundary condition could be prescribed in the matrix continuum to avoid unrealistic instantaneous adsorption strains. Considering these factors, there are two likely explanations for an insufficient rate of CO_2 adsorption strain development in the simulation of Test B, namely:

i. An insufficient rate of CO_2 exchange into the matrix continuum delayed the development of the equilibrium adsorption strain.

ii. The equilibrium sorption strain approach is not appropriate, i.e. the sorption strain should be calculated using the kinetic adsorbed amounts.

As mentioned in section 6.5.2, only diffusive mass exchange was considered, i.e. the role of advection was ignored. As a result, the mass exchange coefficient was reduced to a function of the matrix block dimension, l, and the matrix effective diffusion coefficients, D_{geM}^i. Since the effect of pressure on D_{geM}^i was not considered, changes in the matrix diffusivity were governed by the evolution in matrix porosity predicted by the deformation model. The parameter l was treated as a constant at 0.01 m. Smaller values increased the rate of inter-porosity mass exchange, thereby increasing the rate of CO_2 adsorption strain development in the simulation of Test B. However, the elevated mass exchange rate also reduced the size of the primary breakthrough stage in the simulation of Test A compared to the experimental results. The value of 0.01 m provided the best balance of these contrasting effects prior to the adoption of a reduced initial permeability in the simulation of Test B.

The mass exchange model adopted in this work assumed that a quasi-steady state gas pressure distribution prevailed in the matrix blocks at all times, allowing the mass exchange to be modelled as a first-order rate process. Gerke and van Genuchten (1993a; 1993b) state that this simplification is strictly only valid at large times after the pressure front has reached the centre of the matrix blocks. Despite this, they regard it as a practical approach considering the high level of uncertainty generally involved in the modelling of flow processes in dual porosity media.

A number of authors (e.g. Chang et al., 1993; Bouribaux et al., 1999) have reported on a transient period that follows the development of a concentration, i.e. pressure, difference between the fracture and matrix continua. This implies that the assumption of quasi-steady state mass exchange may lose validity in the region of the breakthrough front. Bouribaux et al. (1999) reported an initial mass exchange coefficient 8 times higher than the steady state value. In their model, the time taken to reach the steady state mass exchange rate depended on the matrix block permeability, porosity and size, as well as certain properties of the pore fluid being exchanged.

An increase in the mass exchange rate for even a short time in the region of the primary breakthrough front would have had a significant impact on the rate of CO_2 adsorption strain development. This is because CO_2 has a low Langmuir adsorption pressure, $P_L^{CO_2}$, of 0.2 MPa in the coal. As a result, the adsorption strain was sensitive to small changes in the matrix CO_2 concentration at early mass exchange times, i.e. in the region of the breakthrough front. The implementation of a transient mass exchange coefficient would therefore have increased the rate of adsorption strain development in the simulation of Test B, thereby potentially improving the agreement with the experimental results without the need to prescribe a lower initial permeability. Assuming that the elevated mass exchange rate would have tended towards the steady-state value in a relatively short time, the impact on the size of the primary breakthrough in the simulation of Test A would have been less than that caused by simply reducing the matrix block dimension, l.

In contrast to the simulation of Test B, the quasi-steady state approach to mass exchange gave a good agreement with the experimental data in the simulation of Test A. This is logical since the flow of N_2 is not significantly affected by the adsorption strain, as

discussed in section 6.4. The flow of N_2 is therefore much less sensitive to small changes in the rate of mass exchange compared to CO_2.

Point ii. above implies that the adsorption strain may have developed faster if it was calculated using the actual adsorbed amounts from the kinetics module, rather than the equilibrium values which were used. This is because the fixed concentration CO_2 injection boundary condition could then have been applied in the matrix continuum without causing unrealistic instantaneous adsorption strains. The rate of adsorption strain would then have been directly related to the rate of CO_2 adsorption, which from section 6.2 is known to occur significantly faster than N_2 or CH_4. In fact, the half-life of CO_2 adsorption, i.e. the time taken to reach 50% of the adsorption capacity, is around 17 minutes. This is similar to the time taken for the breakthrough of CO_2 in the experiment, i.e. 15 minutes. It is therefore possible that the adsorption strain would have developed faster if the deformation model was coupled with the adsorption/desorption kinetics module, with the injection boundary condition applied in both continua.

Implementing this change would require a good understanding of the relationship between the adsorbed amount and sorption strain at non-equilibrium conditions. A linear relationship is generally assumed (Chikatamarla et al., 2009), which indicates that the sorption strain kinetics would follow the same trend as the sorption kinetics. However, Pekot and Reeves (2002) reported that CO_2 may cause a higher sorption strain per unit adsorbed amount compared to CH_4. In other words, if the same amount of CO_2 and CH_4 are adsorbed in coal, the swelling effect may be greater for CO_2. Pekot and Reeves (2002) referred to this as the "differential swelling" effect, and included it in their permeability model using an empirical differential swelling term to factor the equilibrium sorption strain for different gases.

In order to extend the concept of Pekot and Reeves (2002) for non-equilibrium conditions, sufficient sorption strain kinetics data would be required. Although Majewska et al. (2009) and Czerw (2011) present some such data, the development and implementation of a relationship is beyond the scope of the present work. In fact, the practicality of this approach compared to the equilibrium approach is somewhat limited by the comparative lack of data for different types of coal. Furthermore, the numerical formulation adopted in

this work is not ideally suited to the use of the non-equilibrium adsorbed amounts in the deformation module. This is because of the time splitting approach which has been adopted to couple the transport and reaction components in the model.

6.6   Conclusions

In this chapter, the developed numerical model has been applied to simulate two scenarios for gas injection and methane displacement in coal, namely, pure nitrogen injection and pure carbon dioxide injection. The main objective was to explore the validity of the developed dual porosity, dual permeability model in relation to the processes and behaviour involved in gas flow and interactions in coal. This has been achieved by comparing the simulation results with those observed in the experimental study conducted by Hadi Mosleh (2014). Prior to the gas injection and displacement simulations, the theoretical models describing the adsorption kinetics and deformation were examined in detail. This was an important stage since the parameters and enhanced understanding of these processes were applied in the gas injection and displacement simulations.

In relation to the adsorption kinetics of nitrogen, methane and carbon dioxide in powdered coal, a combination of two weighted first-order rate models provided a closer agreement to the experimental results compared to a single first-order rate model. In general, the first rate in the combined model was around one order of magnitude greater than the second rate. This implies that gas adsorption in coal may be described by two distinct stages, i.e. a rapid first stage followed by a more gradual second stage. The adsorption kinetics of carbon dioxide were governed by the more rapid first stage of adsorption. In contrast, the more gradual second stage governed the adsorption kinetics of nitrogen and methane.

The differences in the adsorption kinetics may have been due to the adsorption of carbon dioxide in multiple layers in the mesopores, with nitrogen and methane being restricted to single layer adsorption. In addition, carbon dioxide has a greater adsorption energy and smaller kinetic diameter, thereby promoting access to the micropore adsorption sites compared to nitrogen and methane. This effect would be enhanced if the pore network in the coal grains was highly constricted by ultra-micropores.

The permeability trends predicted by the deformation model developed in section 3.6 were found to agree well with the experimental permeability measurements for the steady state flow of pure nitrogen, pure methane and pure carbon dioxide. Coal permeability to nitrogen was found to be on average 7.04 times greater compared to carbon dioxide, and 3.67 times greater compared to methane for the range of effective stress considered. The species dependent permeability was attributed to the different sorption strains associated with the adsorption of each gas.

Some limitations of the deformation model have been identified. Firstly, since the experimental results covered a relatively narrow range of effective stress and only considered the flow of pure gas, the multicomponent deformation model can only be considered as partially validated. In addition, the permeability rebound caused by desorption induced coal matrix shrinkage may be over-predicted and negative permeabilities have been noted under certain conditions. The latter necessitated the use of a lower bound (threshold) permeability in the numerical simulations. Aside from these limitations, the predicted trends for a multicomponent system are reasonable, i.e. the displacement of adsorbed methane by nitrogen increases the permeability by coal shrinkage, whereas displacement by carbon dioxide reduces the permeability by coal swelling. Nonetheless, it is clear that future development and testing of the deformation model is required.

In the simulations of the gas injection and displacement experiments, the breakthrough for the injection of carbon dioxide in Test B occurred 5 times later than for the injection of nitrogen in Test A. In addition, a greater mole fraction of methane was maintained in the produced gas after carbon dioxide breakthrough than after nitrogen breakthrough. The main cause of the different behaviour was found to be the carbon dioxide adsorption induced loss in the fracture permeability. The short time scale involved in the flow in the 0.12 m long coal core, combined with the relatively slow rate of methane desorption, effectively limited the role of preferential methane desorption by carbon dioxide.

There was a good agreement between the experimental and simulation results for Test A. Although the breakthrough trend in the simulation of Test B was similar to that observed in the experiment, the agreement was not as good as in the simulation of Test A. The

breakthrough of carbon dioxide occurred too early and its mole fraction in the produced gas was generally over-predicted. A further simulation of Test B performed with a one-third lower initial permeability produced an improved quantitative agreement with the experimental results.

Considering that coal permeability is sensitive to effective stress cycles, it is possible that the initial permeability of the core in Test B was lower than in Test A. Alternatively, the improved agreement at the lower initial permeability indicates that the permeability loss due to the carbon dioxide adsorption induced coal swelling did not develop at the required rate. It is believed that the applied permeability threshold did not contribute to the early breakthrough. This is because the chosen threshold was almost 30% less than the lowest coal permeability measured in the laboratory for the steady state flow of carbon dioxide.

A possible explanation for the rate of coal swelling being too low is that the inter-porosity mass exchange is transient at early breakthrough times, i.e. in the region of the primary breakthrough front. The quasi-steady state approach adopted may therefore have resulted in the under-prediction of the amount of gas exchange into the matrix continuum, giving a lower carbon dioxide adsorption strain rate. An alternative explanation is related to the equilibrium approach used to calculate the sorption strains. A consequence of this approach was that the boundary conditions were not applied in the matrix continuum to avoid unrealistic sorption strains. The carbon dioxide adsorption strain rate may have been higher if the sorption strains were calculated using the actual adsorbed amounts calculated in the kinetics module, allowing the injection boundary condition to be applied in the matrix continuum. This is because the adsorption strain rate would then have been directly related to the rate of carbon dioxide adsorption, which is significantly higher than that of nitrogen and methane.

The importance of each of the factors given above is difficult to establish without further investigation. It is recommended that future work focuses on the components in the formulation that govern the rate of sorption strain development, namely, the rate of inter-porosity mass exchange and the approach used to calculate the sorption strain. In particular, this should involve an analysis on the mechanisms that may govern transiency in the mass exchange.

Overall, the different stages in the breakthrough of nitrogen and carbon dioxide observed in the experiments were predicted in the numerical simulations. Therefore, whilst acknowledging the suggested improvements to the formulation discussed above, it may be concluded that the developed model is capable of simulating the major processes and behaviour involved in gas flow in coal. The applications of the general dual porosity, dual permeability model considered in this work are related to carbon dioxide sequestration in coal and enhanced methane recovery. Following the validation exercises and detailed analysis of the processes involved given in this chapter, it is appropriate that some of the more practical aspects of these applications are explored in greater detail in the next chapter. This will involve looking at how the gas injection and methane recovery are influenced by the sample size and the injected gas pressure and composition at the laboratory scale.

6.7   References

Anderson, R.B., Hall, W.K., Lecky, J.A. and Stein, K.C. (1956). Sorption studies on American coals. *The Journal of Physical Chemistry*, **60**(11), 1548-1558.

Bouribaux, B., Granet, S., Landereau, P., Noetinger, B., Sarda, S. and Sabathier, J.C. (1999). Scaling up matrix-fracture transfers in dual-porosity models: theory and application. *In Proceedings of the SPE Annual Technical Conference and Exhibition*, 3-6 October, Houston, Texas, USA.

Busch, A., Gensterblum, Y., Kroos, B.M. and Littke, R. (2004). Methane and carbon dioxide adsorption-diffusion experiments on coal: upscaling and numerical modeling. *International Journal of Coal Geology*, **60**, 151-168.

Chang, M-M. (1993). *Deriving the shape factor of a fractured rock matrix*. Technical Report NIPER-696 (DE93000170), National Institute for Petroleum and Energy Research, Bartlesville, Oklahoma, USA.

Chapman, S. and Cowling, T.G. (1970). *The mathematical theory of non-uniform gases: an account of the kinetic theory of viscosity, thermal conduction and diffusion in gases*, Cambridge University Press, Cambridge, UK.

Chikatamarla, L., Bustin, R.M. and Cui, X. (2009). CO_2 sequestration into coalbeds: Insights from laboratory experiments and numerical modeling. In: Grobe et al., eds. *Carbon dioxide sequestration in geological media: State of the Science*, AAPG Studies in Geology 59, Tulsa, Oklahoma.

Clarkson, C.R. and Bustin, R.M. (1999). The effect of pore structure and gas pressure upon the transport properties of coal: A laboratory and modeling study. 2. Adsorption rate modeling. *Fuel*, **78**, 1345-1362.

Connell, L.D. (2009). Coupled flow and geomechanical processes during gas production from coal seams. *International Journal of Coal Geology*, **79**, 18-28.

Cui, X., Bustin, R.M. and Dipple, G. (2004). Selective transport of CO_2, CH_4 and N_2 in coals: insights from modeling of experimental gas adsorption data. *Fuel*, **83**, 293-303.

Cussler, E.L. (1997). *Diffusion: mass transfer in fluid systems*. 2nd Edition. Cambridge University Press, Cambridge.

Czerw, K. (2011). Methane and carbon dioxide sorption/desorption on bituminous coal – Experiments on cuboid sample cut from the primal coal lump. *International Journal of Coal Geology*, **85**, 72-77.

Durucan, S. and Edwards, J.S. (1986). The effects of stress and fracturing on permeability of coal. *Mining Science and Technology*, **3**, 205-216.

Gan, H., Nandi, S.P. and Walker Jr, P.L. (1972). Nature of the porosity in American coals. *Fuel*, **51**(4), 272-277.

Gash, B.W., Volz, R.F., Potter, G. and Corgan, J.M. (1992). The effects of cleat orientation and confining pressure on cleat porosity, permeability and relative permeability in coal. *In Proceedings of the 1992 SCA Conference*, Oklahoma City, 15–16 June.

Gerke, H.H. and van Genuchten, M.T. (1993a). A dual-porosity model for simulating the preferential movement of water and solutes in structured porous media. *Water Resources Research*. **29**(2), 305-319.

Gerke, H.H. and van Genuchten, M.T. (1993b). Evaluation of a first-order water transfer term for variably saturated dual-porosity flow models. *Water Resources Reseach*, **29**(4), 1225-1238.

Hadi Mosleh, M. (2014). *An experimental investigation of flow and reaction processes during gas storage and displacement in coal*. Ph.D. Thesis, Cardiff University, Wales, UK.

Harpalani, S. and Chen, G. (1995). Estimation of changes in fracture porosity of coal with gas emission. *Fuel*, **74**(10), 1491-1498.

King, G.R., Ertekin, T. and Schwerer, F.C. (1986). Numerical simulation of the transient behaviour of coal-seam degasification wells. *Society of Petroleum Engineers Formation Evaluation*, **1**(2), 165-183.

Lee, S. (1996). *Alternative Fuels*. Taylor and Francis, Washington, D.C., USA.

Levine, J.R. (1996). Model study of the influence of matrix shrinkage on absolute permeability of coal bed reservoirs. In: Gayer, R. and Harris, I., eds. *Coalbed Methane and Coal Geology*, Geological Society Special Publication No. 109, London, 197-212.

Liu, H-H. and Rutqvist, J. (2010). A new coal-permeability model: Internal swelling stress and fracture-matrix interaction. *Transport in Porous Media*, **82**, 157-171.

Ma, Q., Harpalani, S. and Liu, S. (2011). A simplified permeability model for coalbed methane reservoirs based on matchstick strain and constant volume theory. *International Journal of Coal Geology*, **85**, 43-48.

Mastalerz, M., Gluskoter, H. and Rupp, J. (2004). Carbon dioxide and methane sorption in high volatile bituminous coals from Indiana, USA. *International Journal of Coal Geology*, **60**, 43-55.

Meng, Z. and Li, G. (2013). Experimental research on the permeability of high-rank coal under a varying stress and its influencing factors. *Engineering Geology*, **162**, 108-117.

Milewska-Duda, J., Duda, J., Nodzeñski, A. and Lakatos, J. (2000). Absorption and adsorption of methane and carbon dioxide in hard coal and active carbon. *Langmuir*, **16**, 5458-5466.

Palmer, I. and Mansoori, J. (1998). How permeability depends on stress and pore pressure in coalbeds: A new model. *Society of Petroleum Engineers Reservoir Evaluation and Engineering*, **1**(6), 539-544.

Pekot, L.J. and Reeves, S.R. (2002). *Modeling coal matrix shrinkage and differential swelling with CO_2 injection for enhanced coalbed methane recovery and carbon sequestration applications*. US DOE Topical Report, Contract No. DE-FC26-00NT40924.

Peng, D-Y. and Robinson, D.B. (1976). A new two-constant equation of state. *Industrial and Engineering Chemistry Fundamentals*, **15**(1), 59-64.

Robertson, E.P. and Christiansen, R.L. (2006). A permeability model for coal and other fractured, sorptive-elastic media. *Society of Petroleum Engineers Journal*, **13**(3), 314-324.

Ruthven, D.M. (1984). *Principles of adsorption and adsorption processes*. Wiley, New York.

Seidle, J. (2011). *Fundamentals of coalbed methane reservoir engineering*. PennWell Corporation, Tulsa, Oklahoma, USA.

Shi, J.Q., and Durucan, S. (2003). A bidisperse pore diffusion model for methane displacement desorption in coal by CO_2 injection. *Fuel*, **82**, 1219-1229.

Shi, J.Q., Mazumder, S., Wolf, K-H. and Durucan, S. (2008). Competitive methane desorption by supercritical CO_2 injection in coal. *Transport in Porous Media*, **75**, 35-54.

Somerton, W.H., Söylemezoğlu, I.M. and Dudley, R.C. (1975). Effect of stress on permeability of coal. *International Journal of Rock Mechanics and Mining Sciences & Geomechanics Abstracts*, **12**, 129-145.

Wu, Y., Liu, J., Elsworth, D., Chen, Z., Connell, L. and Pan, Z. (2010). Dual poroelastic response of a coal seam to CO_2 injection. *International Journal of Greenhouse Gas Control*, **4**, 668-678.

Yang, R.T. (1987). *Gas separation by adsorption processes*. Butterworth, London.

Young, G.B.C., Paul, G.W., McElhiney, J.E. and McBane, R.A. (1992). A parametric analysis of Fruitland coal methane reservoir productivity. *In Proceedings of the SPE Annual Technical Conference and Exhibition*, Society of Petroleum Engineers, Richardson, Texas, USA.

Zhou, F., Hussain, F. and Cinar, Y. (2013). Injecting pure N_2 and CO_2 to coal for enhanced coalbed methane: experimental observations and numerical simulation. *International Journal of Coal Geology*, **116-117**, 53-62.

7

High Pressure Gas Transport and Displacement in Coal

7.1 Introduction

The main objective in chapter 6 was the validation of the developed model in relation to the physical and chemical interactions involved in gas flow in coal. Laboratory scale simulations were presented for nitrogen and subcritical carbon dioxide storage in coal cores and methane displacement. The simulations presented in this chapter deal with the injection of supercritical carbon dioxide and selected carbon dioxide rich gas mixtures at high pressure. The injection of pure nitrogen at high pressure has also been studied for comparison. The main objective of the discussion provided is to assess the role of the injection pressure and gas composition on flow and coal-gas interactions at the laboratory scale. This is of practical importance in terms of enhancing the knowledge of the major processes involved in gas transport, storage and displacement in coal. The related applications are carbon dioxide sequestration in coal and methane production.

The development of the simulation scenarios is discussed in section 7.2, including the

model domain, time scheme, material parameters and initial and boundary conditions. A larger domain, i.e. 1 m long, was used for the simulations, compared to the 0.12 m long domain considered in the previous chapter. This was decided based on a conclusion in chapter 6 that the short time scale of flow in the 0.12 m long sample had a considerable impact on the observed gas transport and displacement behaviour. In addition to the pure nitrogen injection scenario, four carbon dioxide injection scenarios were simulated. The simulations were developed to investigate the effects of the sample size, injection pressure and composition on gas transport, displacement and interactions in the coal sample considered.

Section 7.3 presents the results of the above simulations. The results are presented in terms of the temporal evolution of the produced gas composition and the gas storage in the system, i.e. the gas in place. A discussion of the results is provided, which focuses on the gas transport and displacement behaviour for the laboratory scale simulation scenarios considered. In particular, the efficiency of the carbon dioxide storage and methane displacement is evaluated.

The overall conclusions of the chapter are presented in section 7.4.

7.2   Simulation Conditions and Material Parameters

This section covers the simulation scenarios developed to investigate the effects of sample size, injection pressure and composition on gas flow and interactions in coal. The validation exercises presented in the previous chapter considered the injection of pure nitrogen (N_2) and pure carbon dioxide (CO_2) at 5 MPa with methane (CH_4) displacement in the coal sample of 0.12 m length and 0.07 m diameter. It was concluded that the small time scale of flow in the 0.12 m long sample may have had a considerable impact on the observed gas transport and displacement behaviour. As a result, the simulations in this chapter consider a larger sample of 1 m length.

As in chapter 6, the system was treated as a two-dimensional problem in which the gas transport between the injection and abstraction boundaries is effectively one-dimensional. This is reasonable when modelling a situation in which the injection and abstraction

pressures are applied uniformly over the respective faces of the core.

The domain was discretised into 200 equally sized 4-noded quadrilateral elements. A variable time step was used for a 10 day simulation period, which allowed the size of the time step to vary depending on the state of convergence. Under this scheme, if the convergence criterion was met within a specified number of iterations, the time step was increased by a factor. Conversely, if the convergence criterion was not met within a specified maximum number of iterations, the time step was decreased by a factor. The initial and maximum time steps were set to 1 second and 60 seconds, respectively.

A summary of the gas injection scenarios considered in the simulations is provided in Table 7.1.

Table 7.1 Summary of the scenarios considered in this chapter for the simulation of N_2 and CO_2 storage in coal with CH_4 displacement.

ID	Pressure [MPa]	Temperature [K]	Composition
Test I	5.0	298	Pure N_2
Test II	5.0	298	Pure CO_2
Test III	8.0	313	Pure CO_2
Test IV	8.0	313	CO_2:N_2 (80%:20%)
Test V	8.0	313	CO_2-rich flue gas mixture

Tests I and II were intended to link this chapter with the validation exercises presented in chapter 6. In particular, these simulations allow an analysis into the effect of sample size on the observed behaviour. The main aim of Tests III to V was to investigate the role of an elevated gas injection pressure and the injected gas composition on the flow and coal-gas interactions. In particular, the phase behaviour of CO_2, and therefore its transport behaviour, can be significantly affected by the presence of impurities (Wang et al., 2011). The CO_2-rich flue gas mixture considered in Test IV was obtained from Wang et al. (2011) for oxyfuel combustion, where a hydrocarbon or carbonaceous fuel is combusted in pure oxygen to produce a flue gas comprised of 80 to 98% CO_2 for capture and storage (Metz et al., 2005). The gas composition reported by Wang et al (2011) was 85% CO_2, 5.8% N_2,

4.7% oxygen (O_2) and 4.47% argon (Ar), in addition to smaller amounts of other impurities not considered in this work.

The injection temperature in Tests I and II was the same as that considered in chapter 6, i.e. 298 K. In Tests III to V, a temperature of 313 K was chosen to represent the approximate temperature at 800 m below the ground level (Han et al., 2011). This is a realistic depth for the geological sequestration of CO_2 (Roddy and González, 2010). In particular, the adopted conditions ensured that the CO_2 injection in Test III was in the supercritical state, i.e. above the critical pressure (7.38 MPa) and critical temperature (304.21 K) (Wang et al., 2005).

A schematic of the initial and boundary conditions used in Tests I and II is provided in Figure 6.14, where the left- and right-hand boundaries are the injection and abstraction faces of the coal core, respectively. The initial and boundary conditions adopted in Tests III to V are detailed in Figure 7.1 and Table 7.2. As in chapter 6, the initial condition of the coal in each simulation was pure CH_4 at 5 MPa. The fixed injection pressures in Table 7.1 were converted to the equivalent gas concentrations, c_g^i, using the real gas law, given by:

$$c_g^i = \frac{X_g^i u_g}{ZRT} \tag{7.1}$$

where X_g^i is the mole fraction, Z is the compressibility factor, R is the universal gas constant and u_g and T are the gas pressures and temperatures for the injection scenarios reported in Table 7.1.

It was assumed that the physical and chemical parameters of the coal-gas system were the same as those used in the simulations presented in section 6.5. Accordingly, Table 6.6 provides the parameters for the adsorption isotherms of N_2 and CO_2 and the desorption isotherm of CH_4. The adsorption kinetics parameters reported in Table 6.3 were also used in the simulations, i.e. it was again assumed that the CH_4 desorption kinetics are the same as the adsorption kinetics.

Table 6.5 in section 6.4 details the mechanical properties of the coal required in the deformation model, with the exception of the confining pressure, u_c, and the initial fracture

compressibility, c_{f0}. In Tests I and II, these parameters were set to the same values used in the simulations presented in section 6.5, i.e. 6 MPa and 3.77×10^{-7} Pa^{-1}, respectively.

Since the injection pressure in Tests III to V was set to 8 MPa, it was necessary to consider a higher confining pressure, as would be required in the laboratory. A confining pressure of 10 MPa was chosen. An approximate value of c_{f0} was obtained by plotting the values of u_c and c_{f0} from Table 6.5 and assuming an exponential decay in c_{f0} with u_c, which provided a good agreement with the values adopted at lower confining pressures (R^2 = 0.9986). As illustrated in Figure 7.2, this gave c_{f0} as 6.53×10^{-8} Pa^{-1} at 10 MPa confining pressure. The remaining properties of the coal were provided in Table 6.6 in section 6.5.

| Injection boundary conditions	Initial conditions	Abstraction boundary conditions
Refer to Table 7.2 for the injection boundary conditions prescribed in Tests III to V.	Free gas: $c_{g\alpha}^{CO_2} = c_{g\alpha}^{N_2} = c_{g\alpha}^{O_2} = c_{g\alpha}^{Ar}$ $= 0.0\ mol\ m^{-3}$ $c_{g\alpha}^{CH_4} = 2097.21\ mol\ m^{-3}$ Adsorbed gas: $s_{gM}^{CO_2} = s_{gM}^{N_2} = s_{gM}^{O_2} = s_{gM}^{Ar}$ $= 0.0\ mol\ kg^{-1}$ $s_{gM}^{CH_4} = 0.977\ mol\ kg^{-1}$	$RT \sum_{j=1}^{n_g} c_{gF}^{j} = 0.1 \times 10^6 Pa$ $RT \sum_{j=1}^{n_g} \dfrac{\partial c_{gF}^{j}}{\partial t} = 0.0$

Figure 7.1 Schematic of the initial and boundary conditions used in Tests III to V.

Table 7.2 Fixed concentration injection boundary conditions prescribed in the fracture continuum in Tests I to IV.

ID	CO$_2$ [mol m^{-3}]	N$_2$ [mol m^{-3}]	O$_2$ [mol m^{-3}]	Ar [mol m^{-3}]
Test III	6503.49 (100 %)	-	-	-
Test IV	3521.83 (80 %)	880.46 (20 %)	-	-
Test V	3968.34 (85 %)	270.78 (5.8 %)	219.43 (4.7 %)	208.69 (4.47 %)

The adsorption of O$_2$ and Ar was not considered and so their only influence was on the free

gas properties and transport behaviour. The Peng and Robinson (1976) equation of state (EoS) was used to calculate the gas compressibility factor and the dense gas viscosity model presented by Chung et al. (1988) was used to calculate the bulk gas viscosity. A summary of the chemical parameters of O_2 and Ar required in the EoS and viscosity models is provided in Table 7.3.
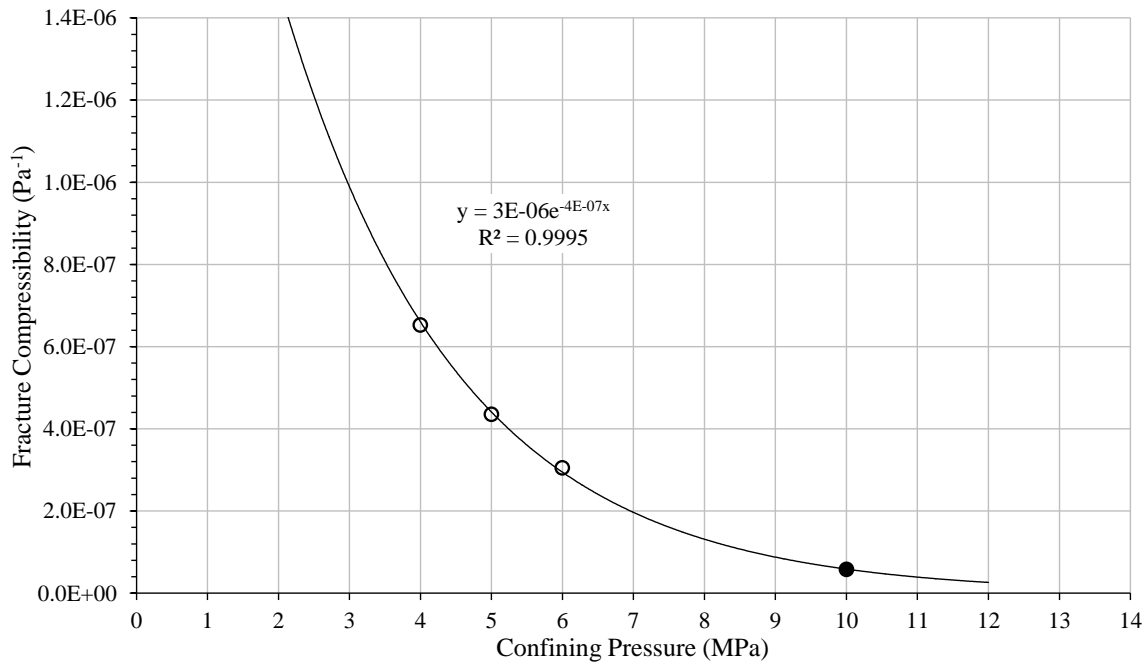
Figure 7.2 Projected variation of initial fracture compressibility with confining pressure, assuming an exponential type relationship. Empty circles are plotted from Table 6.6 and the filled circle is the projected compressibility at 10 MPa confining pressure.

7.3   Simulation Results

The results of the numerical simulations for Tests I to V, described in section 7.2, are presented in sections 7.3.1 to 7.3.5. For the injection scenarios considered, the results are presented in terms of the temporal evolution of the produced gas composition and the gas storage in the system, i.e. the gas in place (GIP).

The GIP was calculated considering the free gas contained in the pore volume and the adsorbed gas contained in the solid phase, giving:

$$G_T^i = G_F^i + G_A^i \qquad (7.2)$$

where G_T^i, G_F^i and G_A^i are the total, free and adsorbed GIP for the ith gas component.

Table 7.3 Selected gas properties required by the equation of state and gas mixture viscosity model for O_2 and Ar (Reid et al., 1977). See Table 5.4 for the equivalent properties of N_2, CH_4 and CO_2.

Gas parameter	Relationship / value	
	O_2	Ar
Critical pressure, u_{gc}^i (Pa)	5.04×10^6	4.87×10^6
Critical temperature, T_c^i (K)	154.60	150.80
Critical volume, V_c^i (m^3 mol^{-1})	7.34×10^{-5}	7.49×10^{-5}
Acentricity factor, ω_i (-)	0.025	0.001
Molecular mass, M_g^i (kg mol^{-1})	0.0320	0.0400

As described in chapter 4, a time splitting technique, i.e. the sequential non-iterative approach (SNIA), was employed to couple the transport module with the inter-porosity mass exchange and adsorption/desorption kinetics modules. Under this scheme, G_T^i was calculated at the end of each time step after the converged transport solution had been modified to account for inter-porosity mass exchange and adsorption/desorption.

In the experimental work described in chapter 6, the injection and abstraction pressures were applied uniformly over the respective surfaces of the coal core using diffusion plates. As mentioned previously, this allowed the coal core to be modelled as a two dimensional system in which the flow effectively occurred in one dimension between the injection and abstraction boundaries. Based on this simplification, the solutions obtained in the two dimensional simulations were used to estimate G_T^i for a coal core with a bulk volume, V_B, given by:

$$V_B = L_x \pi r^2 \qquad (7.3)$$

where L_x is the length of the coal core, i.e. 0.12 m or 1 m depending on the simulation scenario, and r is the radius of the coal core, i.e. 0.035 m.

For the fully dry dual porosity systems considered, G_F^i was calculated in units of moles of gas contained in the bulk volume, V_B, via the following expression:

$$G_F^i = \frac{V_B}{n_{nod}} \sum_{s=1}^{n_{nod}} \left[n_F c_{gF}^i + n_M c_{gM}^i \right]_s \tag{7.4}$$

where n_{nod} is the number of nodes in the mesh and the counter s is used to denote the use of the nodal values of n_F, n_M, c_{gF}^i and c_{gM}^i.

The nodal porosities in equation (7.4) were calculated via the developed deformation model (ref. section 3.6), using the converged free gas concentrations at the end of each time step. It was not appropriate to use a fixed value for the porosity due to the non-uniform deformation associated with the physical and chemical coal-gas interactions.

Using an expression similar to that given in Andrews (2013), G_A^i was calculated in units of moles of gas contained in the bulk volume, V_B, as:

$$G_A^i = \rho_s \frac{V_B}{n_{nod}} \sum_{s=1}^{n_{nod}} \left[s_{gM}^i \right]_s \tag{7.5}$$

where it is recalled that ρ_s is the coal density and s_{gM}^i is the adsorbed amount of the ith gas component in the matrix continuum.

In equations (7.4) and (7.5), the fraction V_B/n_{nod} provides a good approximation of the amount of the bulk volume associated with each node provided the spatial discretisation is uniform (i.e. equally sized elements), as was the case under the simulation conditions described in section 7.2. To increase the practical importance of the values of G_T^i presented, they were converted to the equivalent cubic meters of gas at standard pressure and temperature (SPT), i.e. 0.101 MPa and 293.15 K (Wright et al., 2003), per cubic meter of coal, as:

$$G_T^i \Big|_{SPT} = \frac{G_T^i}{c_{g,SPT}^i V_B} \tag{7.6}$$

where $c_{g,SPT}^i$ is the concentration of the ith gas component at the SPT.

No additional CH_4 was injected into the system, which allowed the percentage of CH_4 production to be calculated as:

$$R^{CH_4} = 100 \frac{G_T^{CH_4}}{G_{T0}^{CH_4}} \tag{7.7}$$

where R^{CH_4} is the percentage of methane produced and $G_{T0}^{CH_4}$ is the total CH_4 contained in the system under the initial conditions.

7.3.1   Test I (Pure N_2 Injected at 5 MPa and 298 K)

The main purpose of the simulation presented in this section is to assess the influence of the coal sample size on the N_2 transport and CH_4 displacement behaviour at the laboratory scale. This is achieved via comparison with the simulation results for N_2 injection with CH_4 displacement in a 0.12 m long sample, as presented in Figure 6.15.

Figure 7.3 presents the evolution of the produced gas composition predicted in the numerical simulation for Test I. The breakthrough of N_2, which is taken as when the produced gas composition exceeded 10% N_2, occurred at 7.4 hours. This is 217.8 times longer than the simulation in Figure 6.15, compared to the 8.3 times increase in the flow distance. It can be concluded that the rate of advance of N_2 across the system was slower at the larger scale, i.e. there is a nonlinear relationship between the sample length and the breakthrough time. The main cause of this was the greater amount of N_2 being exchanged into the matrix continuum over the longer flow distance. This N_2 was effectively immobilised by a combination of the low matrix permeability and adsorption.

As shown in the previous chapter, coal has a lower preference to adsorb N_2 than CH_4. The main cause of the CH_4 desorption was therefore the reduction in its free gas concentration due to N_2 flushing and gas abstraction. In the absence of preferential desorption, the displacement of the adsorbed CH_4 was a gradual process which occurred mainly in the region behind the advancing N_2 breakthrough front. Combined with the increase in N_2 mass exchange and adsorption discussed above, this explains the significant spreading of the breakthrough profile in Figure 7.3 compared to Figure 6.15.
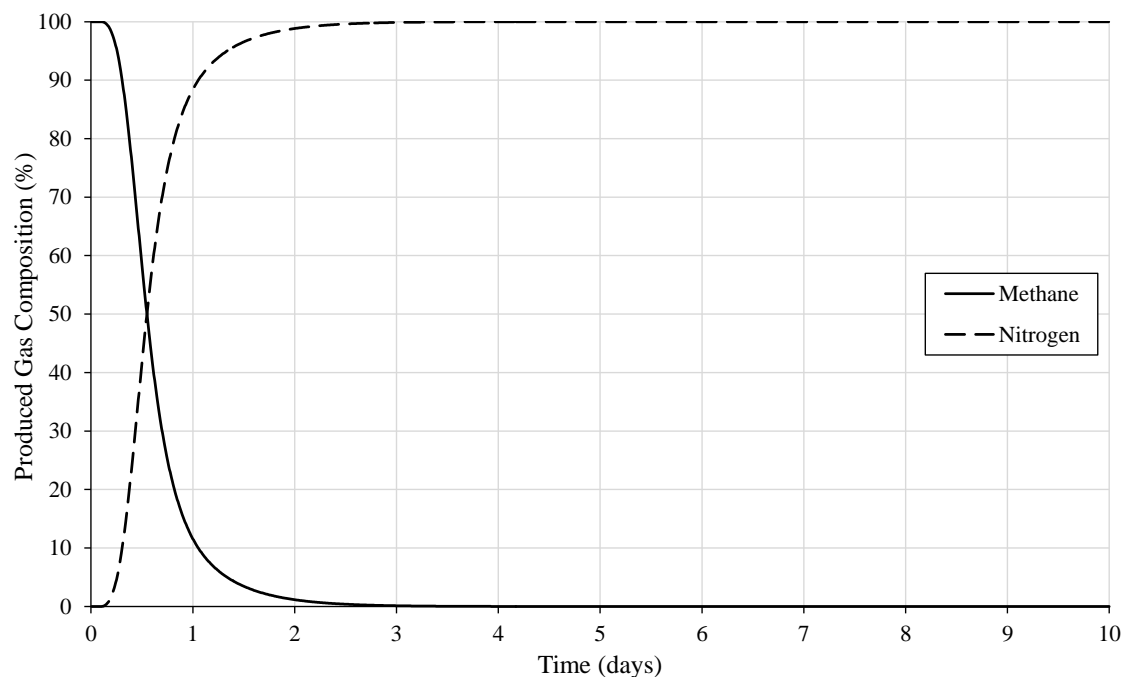
Figure 7.3 Evolution of the produced gas composition predicted by the numerical model for Test I.

The evolution of the GIP in Test I, expressed in cubic meters of gas at SPT per cubic meter of coal (ref. equation (7.6)), is illustrated in Figure 7.4. The vertical dotted line indicates the time of N_2 breakthrough according to Figure 7.3.

It can be seen that the longer time scale considered in Test I meant that all of the CH_4 was displaced within the simulation period. This is in contrast to the displacement in the 0.12 m long sample, where 79.7% of the initial adsorbed CH_4 remained in the adsorbed phase at the end of the simulation period. As discussed in the previous chapter, the half-life for CH_4 desorption was two times longer than the simulation period considered. Hence, the majority of the CH_4 that remained in the system was therefore in the adsorbed phase. This indicates that whilst the produced gas composition in Figure 6.15 reached 99.76% N_2, it was tending very slowly towards the steady state condition of pure N_2. By comparison, the produced gas in Figure 7.3 was pure N_2 after around 4 days. It can be concluded that, relative to the time scale involved in the flow across the sample, the produced gas composition reached the steady state more rapidly at the larger scale. This is because the time taken for N_2 to flow across the sample was longer than the half-life for CH_4 desorption. In other words, a greater proportion of the adsorbed CH_4 was mobilised via

desorption prior to the N_2 breakthrough.
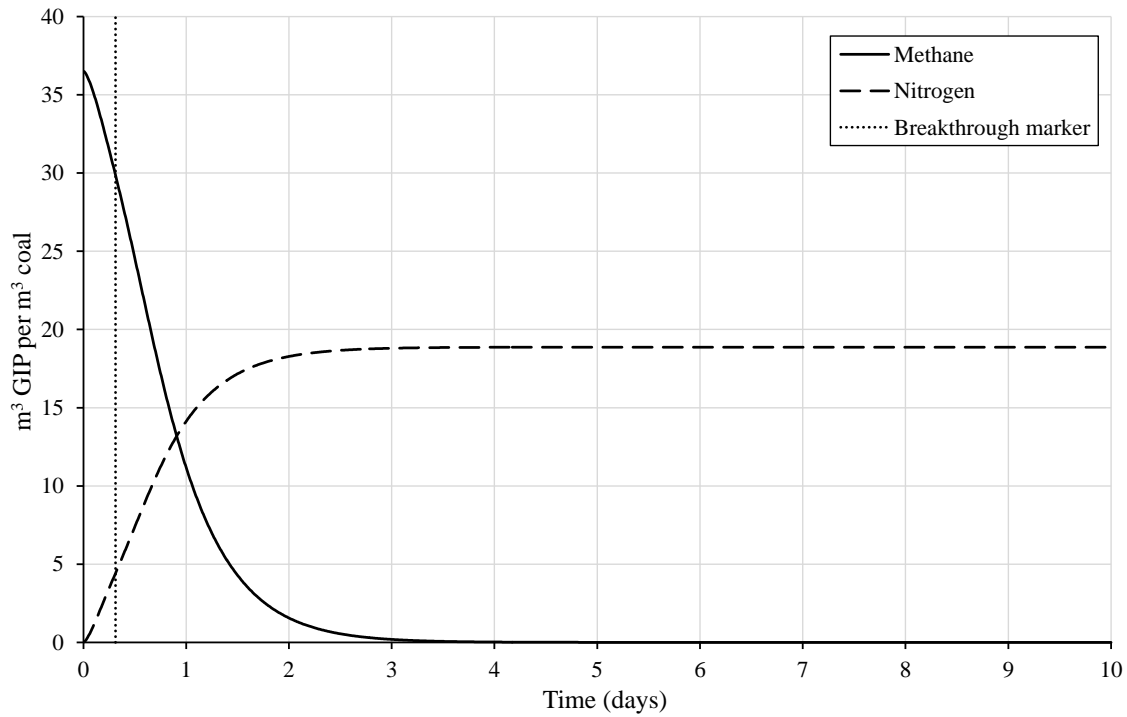
Figure 7.4 Evolution of the gas in place (GIP) per cubic meter of coal predicted by the numerical model for Test I. Breakthrough of N_2 is indicated by the red line.

The N_2 breakthrough occurred when 6.6 m^3 CH_4 per m^3 coal had been produced, which is equivalent to 18.2% of the CH_4 initially contained in the system. This shows that a significant quantity of CH_4 remained in the system when the N_2 reached the abstraction boundary. Therefore, although all of the CH_4 had been produced after 4 days, the produced gas stream for a large part of the displacement was predominantly comprised of N_2. It can be concluded that the displacement of CH_4 by N_2 injection is not efficient under the simulation conditions considered.

Figure 7.4 shows that the coal was saturated with N_2 at 18.9 m^3 gas per m^3 coal, which is around half of the volume of CH_4 initially stored, i.e. 36.5 m^3 gas per m^3 coal. This reflects that the coal adsorbs significantly less N_2 than CH_4.

7.3.2   Test II (Pure CO_2 Injected at 5 MPa and 298 K)

Similar to the N_2 injection scenario considered in Test I, the simulation presented in this section looks at the influence of the coal sample size on the CO_2 storage and CH_4 displacement behaviour at the laboratory scale. This is achieved via comparison with the simulation results for CO_2 storage and CH_4 displacement in a 0.12 m long sample, as presented in Figure 6.16.

Figure 7.5 presents the produced gas composition predicted in the numerical simulation for Test II. It can be seen that the breakthrough of CO_2 (i.e. > 10% CO_2) occurred at 1.15 days of analysis. This is 165.6 times longer than in Figure 6.16, compared to the 8.3 times increase in flow distance. Similar to the observation in Test I, this indicates a nonlinear relationship between the sample length and the breakthrough time. As described in the previous section, this can be attributed to the greater amount of CO_2 which was exchanged into the matrix continuum over the longer flow distance and thereby effectively immobilised by the low matrix permeability and adsorption.
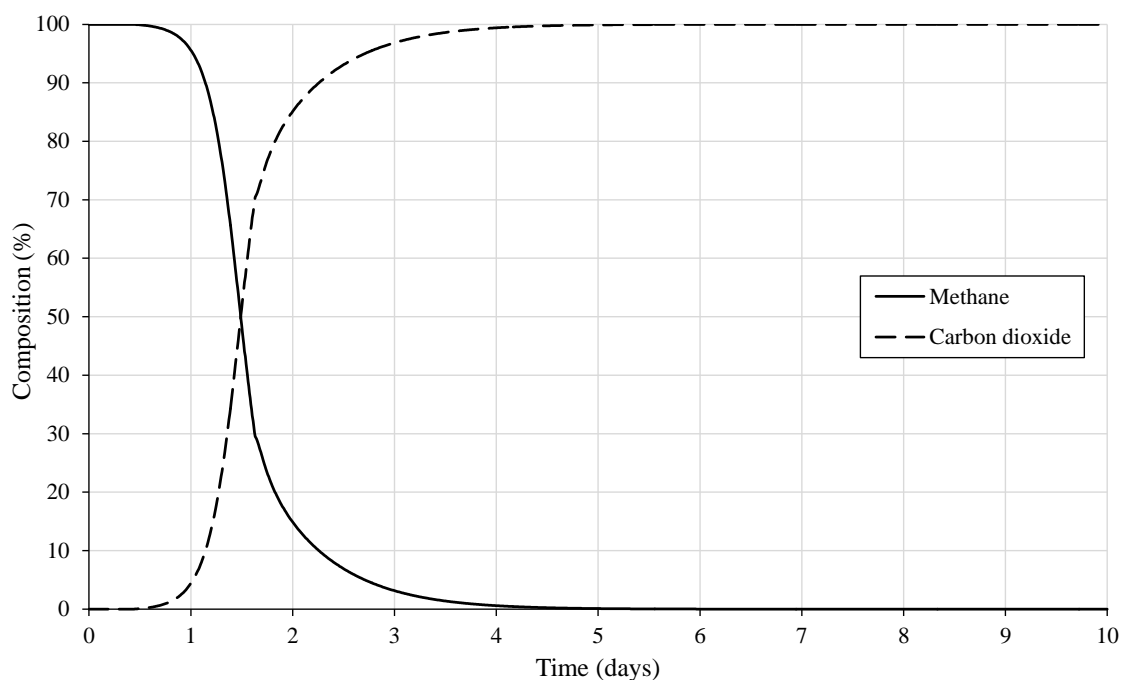
Figure 7.5 Evolution of the produced gas composition predicted by the numerical model for Test II.

The breakthrough in Test II took 3.7 times longer than in Test I. As discussed in the

previous chapter, the major species dependent behaviour involved was the coal-gas interactions, i.e. gas adsorption/desorption and the associated coal swelling. During gas flow across the system, the coal adsorbed a much greater amount of CO_2 than N_2. In addition, the coal swelling response to CO_2 adsorption reduced the permeability and choked the flow. The CO_2 breakthrough therefore occurred later than the N_2 breakthrough.

In contrast to the shorter system considered in the previous chapter, the overall trends of the N_2 and CO_2 breakthrough profiles in Tests I and II are similar. This implies that the increase in flow distance caused a greater spreading of the N_2 breakthrough profile than that of CO_2. This is the expected trend due to the increased role of the strong preferential CH_4 desorption by CO_2 compared to N_2. Further increases in the flow distance would yield an increasingly dispersed N_2 breakthrough profile, whilst the CO_2 breakthrough profile would remain similar to that shown in Figure 7.5.

It can be seen in Figure 7.5 that the CH_4 displacement in Test II was completed after 5.0 days. At this point, the produced gas reached the steady state condition of pure CO_2. The steady state condition was not achieved in Figure 6.16, since 83.1% of the initial adsorbed CH_4 remained in the adsorbed phase at the end of the simulation period. Similar to Test I, it can be concluded that the increase in scale allowed a greater proportion of the adsorbed CH_4 to be mobilised via desorption prior to CO_2 breakthrough. The produced gas composition therefore reached the steady state more rapidly relative to the breakthrough time.

The evolution of the GIP in Test II is illustrated in Figure 7.6. It can be seen that the rate of CH_4 production in Test II was similar to that observed in Test I, with the major difference being the breakthrough time of the injected gas. Despite the similarity, the processes and behaviour responsible for the CH_4 displacement were different.

In Test I, the injected N_2 did not preferentially displace the adsorbed CH_4. As mentioned previously, this meant that the main cause of CH_4 desorption was the reduction in its free gas concentration caused by N_2 flushing and gas abstraction. The adsorption of N_2 is known to cause less coal swelling than CH_4 (ref. section 6.4). As a result, the fracture permeability was gradually increased during the gas displacement process. The injected N_2

therefore flushed the CH_4 in the fracture continuum to the abstraction boundary at a relatively high rate. This increased the rate of CH_4 exchange into the fracture continuum so that a low CH_4 concentration was maintained in the matrix continuum. In turn, this effectively promoted CH_4 desorption and enhanced the rate of production.
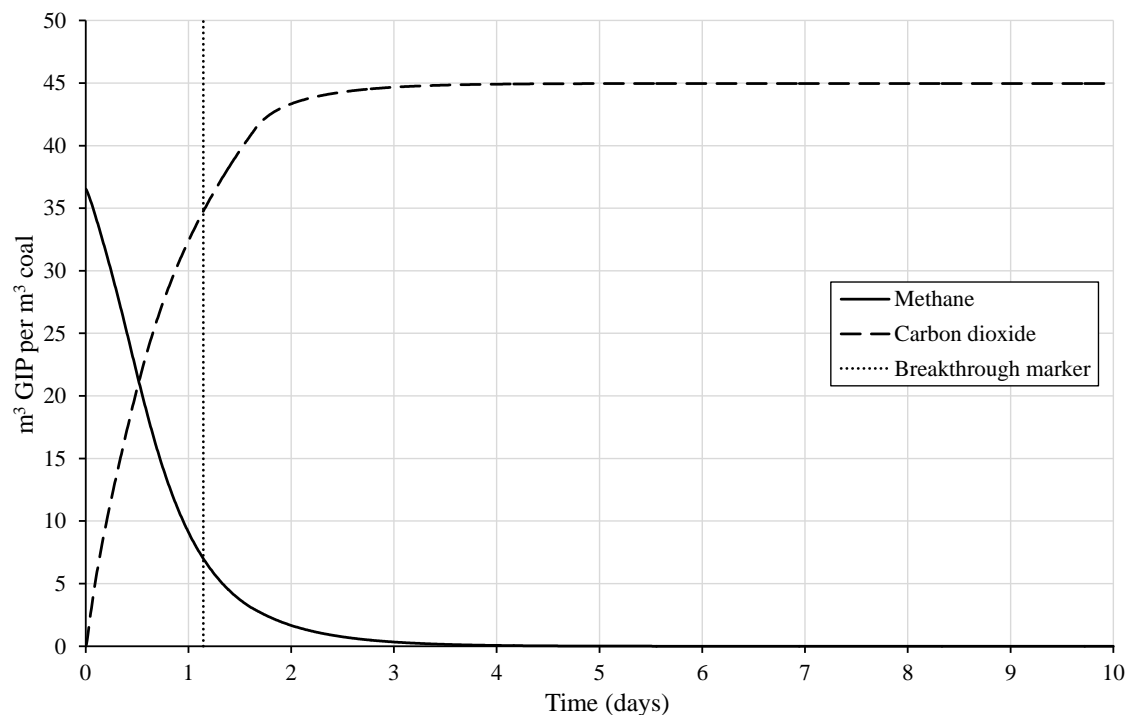
Figure 7.6 Evolution of the gas in place (GIP) per cubic meter of coal predicted by the numerical model for Test II. Breakthrough of CO_2 is indicated by the red line.

The injection of CO_2 in Test II resulted in the preferential desorption of CH_4. However, the concurrent adsorption of CO_2 caused a swelling response. The associated loss in permeability limited the rate of gas flow to the abstraction boundary. The net effect resulted in a similar rate of CH_4 production to that observed in Test I.

As indicated by the vertical red line in Figure 7.6, the breakthrough of CO_2 occurred when 29.6 m^3 CH_4 per m^3 coal had been produced. This corresponds to 81.1% of the CH_4 initially stored in the system. In addition, 34.9 m^3 CO_2 per m^3 coal was injected before breakthrough at the abstraction boundary. This corresponds to 77.6% of the predicted steady state CO_2 capacity of the coal. It can be concluded that the injection of CO_2 was efficient both in terms of CO_2 storage and CH_4 displacement under the laboratory scale

simulation conditions considered. In particular, the CH_4 displacement by CO_2 injection was much more efficient than by N_2 injection.

Following the CO_2 breakthrough, the rate of increase in the stored CO_2 declined sharply. In part, this was caused by the removal of CO_2 in the produced gas stream. However, the main reason for the sudden change in the storage curve was the adsorption kinetics. As discussed in the previous chapter, CO_2 adsorption is a rapid process. This is especially true at early breakthrough times due to its low Langmuir pressure of 0.2 MPa. The amount of CO_2 adsorption therefore increased rapidly at the breakthrough front. As a result, when the CO_2 reached the abstraction boundary, the amount of CO_2 becoming adsorbed was significantly reduced. This was the main cause of the sharp change in the CO_2 storage curve in Figure 7.6. It can be seen that the coal became saturated with CO_2 at 45.0 m^3 gas per m^3 coal, compared to the 36.5 m^3 CH_4 per m^3 coal originally stored in the system. This reflects that the coal adsorbs more CO_2 than CH_4.

7.3.3   Test III (Pure CO_2 Injected at 8 MPa and 313 K)

In the simulations for CO_2 storage with CH_4 displacement presented in sections 6.5 and Test II in this chapter, the CO_2 was injected in the subcritical phase. The simulation presented in this section deals with the injection of supercritical CO_2. A discussion on the impact of the elevated injection pressure and CO_2 phase behaviour on the CO_2 storage and CH_4 displacement behaviour is developed.

The evolution in the produced gas composition predicted in the numerical simulation for Test II is provided in Figure 7.7. Apart from the breakthrough time, it can be seen that the trend is largely the same as that observed in Test II. The breakthrough of CO_2 (i.e. > 10% CO_2) occurred after 9.6 hours, compared to 1.15 days in Test II.

As described in section 7.2, the initial fracture compressibility in Test III was over four times lower than in Test II. This change was made to account for the increase in the confining pressure required at the elevated injection pressure. The lower fracture compressibility limited the dilation effect associated with high pressure gas flow in the fracture continuum. Nonetheless, the earlier breakthrough time in Test III indicates that the

injection of supercritical CO_2 provided more resistance to the loss in permeability caused by the adsorption induced coal swelling. In combination with the increased flux associated with the elevated injection pressure, this explains why the breakthrough of CO_2 occurred earlier than in Test II.
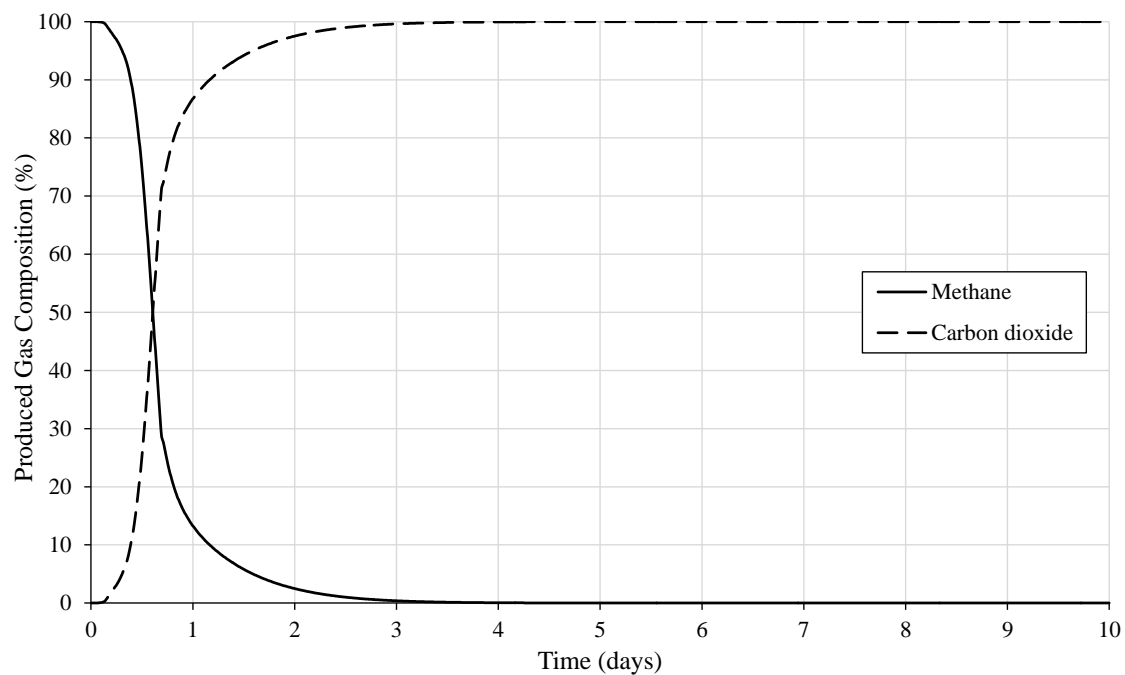

Figure 7.7 Evolution of the produced gas composition predicted by the numerical model for Test III.

As shown in Figure 7.8, the evolution of the GIP in the system followed a similar overall trend to that observed in Test II, only over a shorter time scale. The breakthrough of CO_2 occurred when 20.5 m^3 CH_4 per m^3 coal had been produced. This corresponds to 56.3% of the CH_4 stored in the system under the initial conditions and is 30.1% lower than the amount produced by the breakthrough time in Test II. The main reason for this was the earlier arrival of CO_2 at the abstraction boundary due to the factors discussed above. Likewise, it can be seen that 31.8 m^3 CO_2 per m^3 coal had been stored by the breakthrough time, which is 8.9% less than in Test II. This indicates that the CO_2 storage and CH_4 displacement were more efficient for subcritical CO_2 injection for the adopted laboratory scale simulations conditions.

Under steady state conditions, the system contained 46.7 m^3 CO_2 per m^3 coal. This is only

3.8% higher than for the injection of subcritical CO_2 in Test II. The small increase in the steady state CO_2 storage capacity can be explained with reference to the adsorption isotherm provided in Figure 6.3. At 5 MPa, it can be seen that the equilibrium CO_2 adsorption is 1.22 mol kg^{-1}, which is 96.8% of the saturated capacity. As a result, the injection of supercritical CO_2 did not significantly increase the amount of CO_2 storage in the adsorbed phase. This is important since the low bulk porosity, i.e. 0.025 under the initial conditions, meant that the contribution of the free gas to the total GIP was small. The total steady state storage capacity was therefore governed mainly by the gas storage in the adsorbed phase, which was similar for the injection of subcritical and supercritical CO_2.
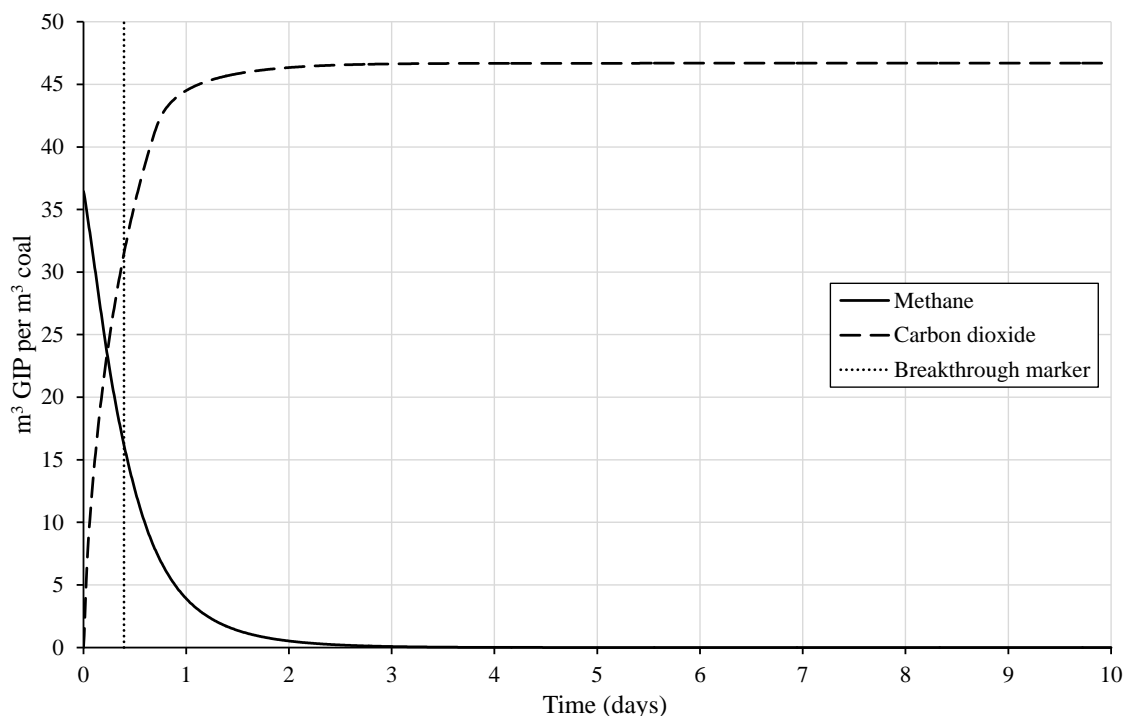

Figure 7.8 Evolution of the gas in place (GIP) per cubic meter of coal predicted by the numerical model for Test III. Breakthrough of the injected gas is indicated by the red line.

7.3.4   Test IV (CO_2:N_2 at 80%:20% Injected at 8 MPa and 313 K)

The simulation presented in this chapter is used to investigate how the CO_2 storage and CH_4 displacement are affected by the composition of the injected gas at the laboratory scale. Accordingly, the injected gas was a binary mixture of CO_2 (80%) and N_2 (20%) at 8

MPa. As discussed in section 7.3.2, a greater permeability was maintained for the injection of pure N_2 in Test I than for the injection of pure CO_2 in Test II. This was attributed to different gas adsorption/desorption and coal swelling behaviour. Based on similar observations, it has been suggested that the injection of a $CO_2:N_2$ mixture may result in a higher permeability being maintained without reducing the efficiency of the CO_2 storage and CH_4 recovery (e.g. Schepers et al., 2010). The applicability of this concept under the adopted simulation conditions is explored via comparisons with the results for the injection of pure supercritical CO_2 in Test III.

Figure 7.9 presents the evolution in the produced gas composition for Test IV. It can be seen that the breakthrough of N_2 occurred before CO_2, reaching a composition of 10% at 10.6 hours compared to 16.6 hours for CO_2.
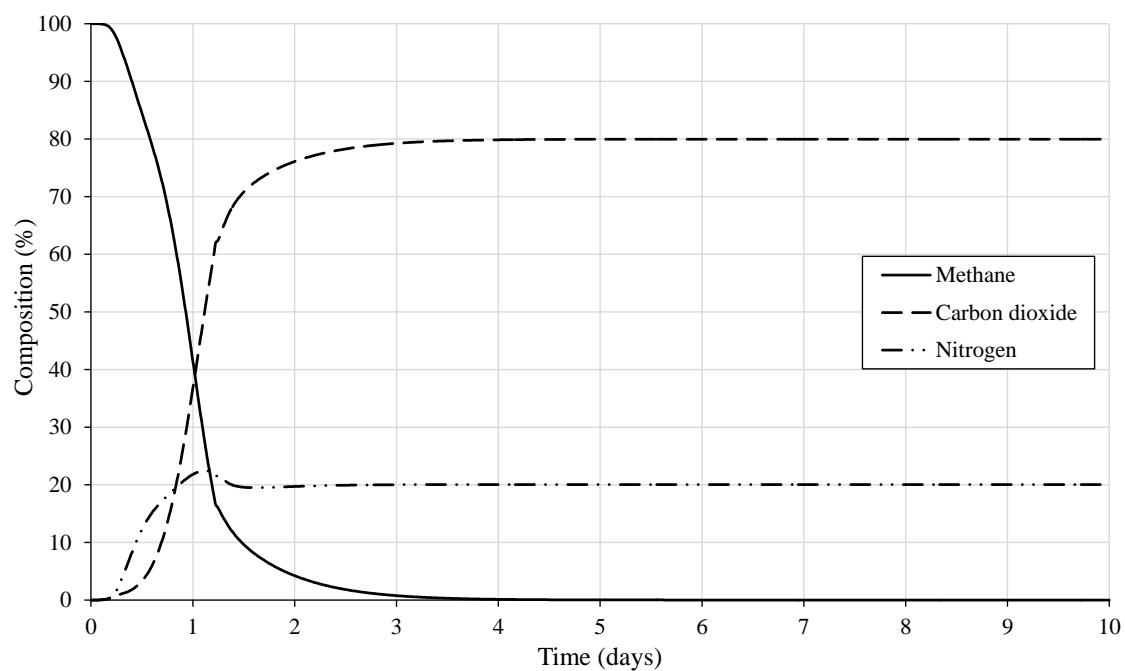

Figure 7.9 Evolution of the produced gas composition predicted by the numerical model for Test IV.

The trend of the CO_2 breakthrough profile is similar to that observed in Tests II and III. After N_2 breakthrough, its composition in the produced gas increased up to slightly above the 20% fraction in the injected gas. A similar trend was observed by Jessen et al. (2008) for the injection $CO_2:N_2$ mixtures into a 25 cm long reconstituted coal core formed from

crushed coal. The elevated breakthrough of N_2 was attributed to the amount of CO_2 becoming adsorbed being greater than the amount of CH_4 becoming desorbed. In other words, the amount of CO_2 immobilisation was higher than the amount of CH_4 mobilisation. As a result, the production of N_2 was briefly elevated relative to the fraction in the injected gas, as shown in Figure 7.9. In the long term, the produced gas composition reached the steady state condition of 80% CO_2 and 20% N_2.

Taken as the time when the produced gas composition became less than 90% CH_4, the breakthrough of the injected gas occurred at 9.6 hours, which is the same as in Test III. Figure 7.10 shows that 18.3 m^3 CH_4 per m^3 coal had been produced at this point. This corresponds to 50.1% of the CH_4 initially stored in the system and is 10.7% lower than at the breakthrough time in Test III. Furthermore, 24.0 m^3 CO_2 per m^3 coal was stored in the system, which is 24.5% less than for the injection of pure supercritical CO_2.
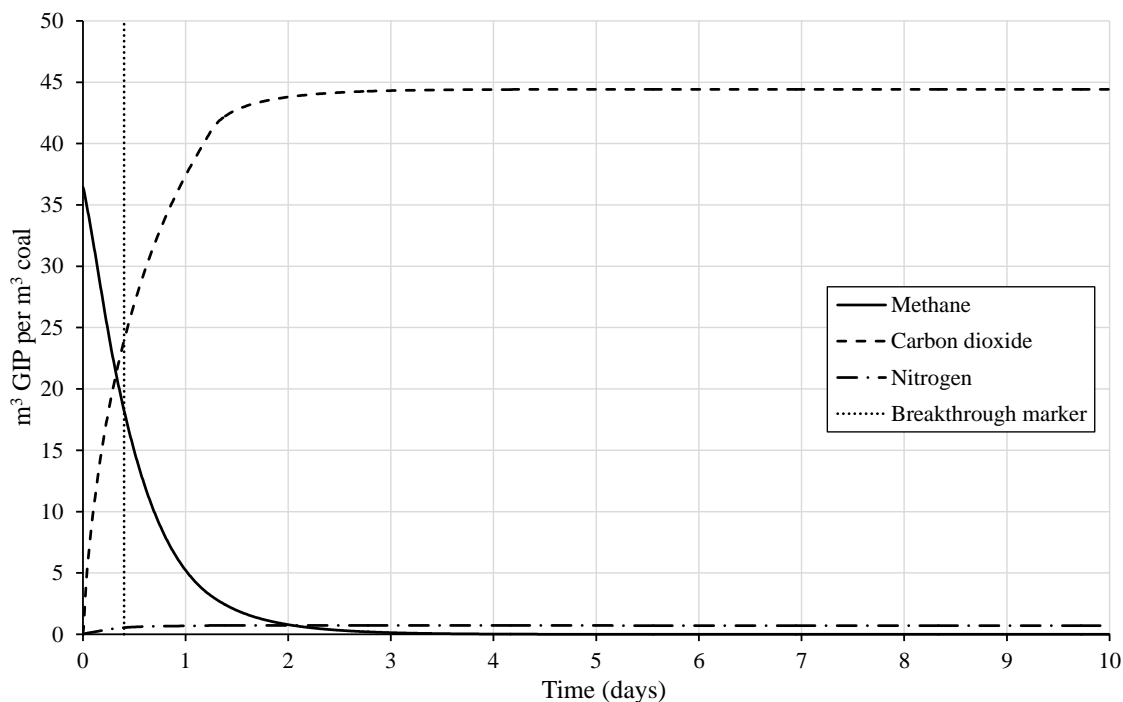
Figure 7.10 Evolution of the gas in place (GIP) per cubic meter of coal predicted by the numerical model for Test IV. Breakthrough of the injected gas is indicated by the red line.

It can be concluded from the above analysis that, under the adopted simulation conditions, the efficiency of the CO_2 storage and CH_4 displacement was lower than for pure CO_2 injection. Furthermore, the presence of N_2 in the injected gas did not reduce the

permeability loss caused by CO_2 adsorption. As discussed in section 7.3.2, much of the CO_2 adsorption occurs at low partial pressures due to the low Langmuir pressure of 0.2 MPa. The inclusion of 20% N_2 in the injected gas therefore had a negligible impact on the associated CO_2 adsorption induced coal swelling. Under different conditions, for example in a coal with a considerably higher CO_2 Langmuir pressure, it is more likely that the injection of a CO_2:N_2 mixture would result in a greater control of the system permeability.

At the steady state, the coal contained 44.4 m^3 CO_2 and just 0.7 m^3 N_2 per m^3 coal. This is because coal has a strong preference to adsorb CO_2 ahead of N_2, which was demonstrated in the previous chapter. As mentioned previously, the low bulk porosity meant that the total steady state storage capacity was controlled mainly by the gas storage in the adsorbed phase. This is illustrated by the fact that only 1.1% of the steady state CO_2 storage in the system was in the free gas phase. By comparison, the low amount of N_2 adsorption meant that 16.6% of the steady state N_2 storage in the system was in the free gas phase.

7.3.5   Test V (CO_2-Rich Flue Gas Mixture Injected at 8 MPa and 313 K)

As shown in Test IV, the composition of the injected gas is an important factor in the CO_2 storage and CH_4 displacement behaviour. The simulation presented in this section is an extension of Test IV in which the injected gas was a CO_2-rich flue gas mixture for oxyfuel combustion.

Figure 7.11 presents the evolution of the produced gas composition with time predicted in the numerical simulation for Test V. The trends of the CH_4 and CO_2 curves are almost identical to those obtained in Test IV. The composition of the produced gas fell below 90% CH_4 after 9.8 hours, compared to 9.6 hours in Test IV. This indicates that the overall behaviour of the system was largely unaffected by the presence of the different impurities compared to Test IV. Likewise, the breakthrough profiles of N_2, O_2 and Ar follow the same trend observed for N_2 in Test IV, as discussed in section 7.3.4.

The temporal evolution of the GIP in the system for Test V is shown in Figure 7.12. The similarity with Figure 7.10 supports the above conclusion that the presence of the different impurities had a negligible effect on the behaviour of the system compared to Test IV.
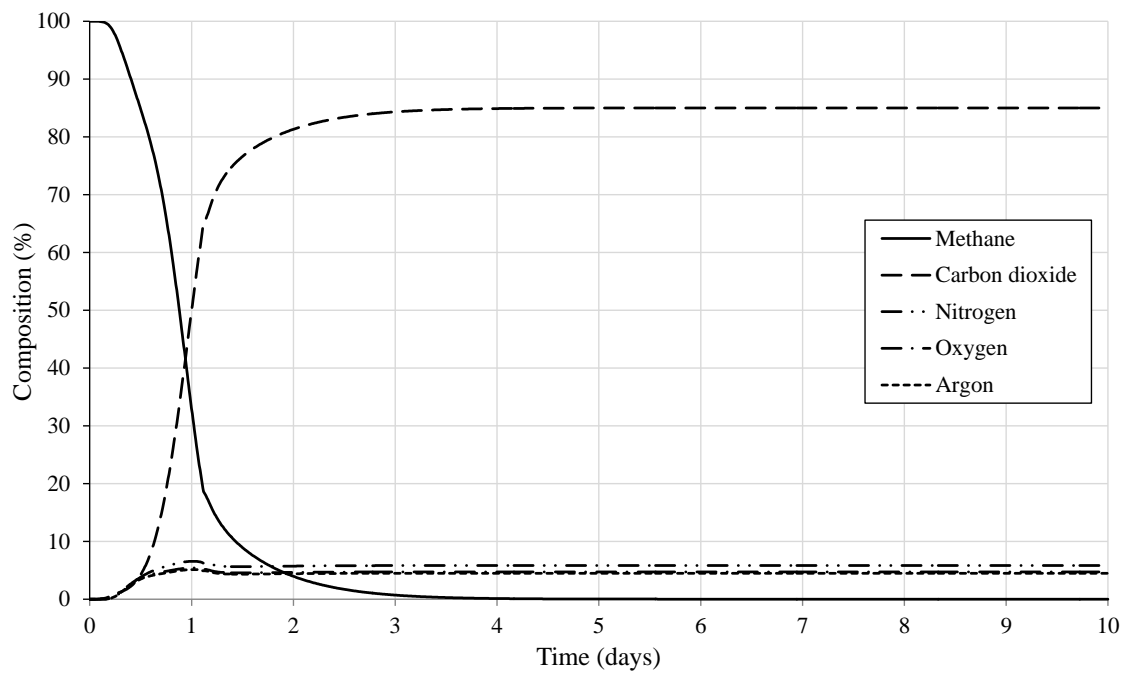
Figure 7.11 Evolution of the produced gas composition predicted by the numerical model for Test V.
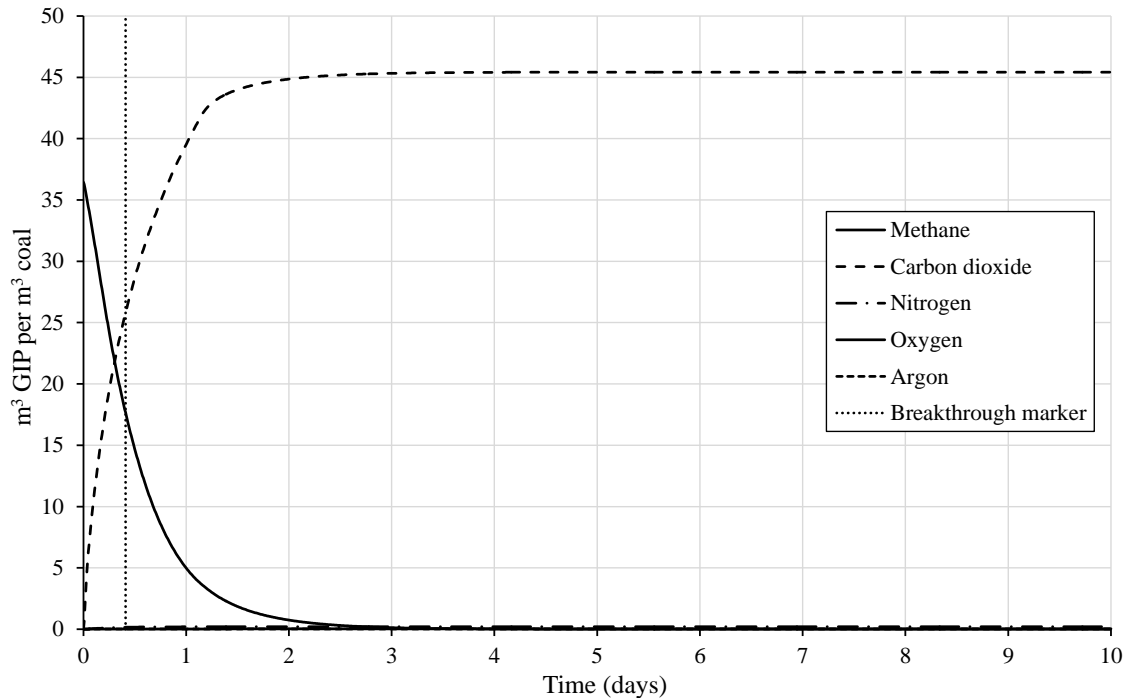
Figure 7.12 Evolution of the gas in place (GIP) per cubic meter of coal predicted by the numerical model for Test V. Breakthrough of the injected gas is indicated by the red line.

7.4   Conclusions

A series of laboratory scale simulations were completed to build upon the simulations presented in the previous chapter for gas storage in a coal core with methane displacement. The main objective was to investigate in greater detail the impact of sample size and gas injection pressure and composition on the observed behaviour. The discussion provided in the previous chapter was largely related to the details of the processes involved in high pressure gas flow and reaction in coal. In contrast, this chapter aimed to focus on the more practical/applied aspects of carbon dioxide storage and enhanced methane displacement in coal. Accordingly, the simulation results were presented in terms of the temporal evolution of the gas in place in addition to the gas breakthrough curves.

The impact of sample size was investigated by simulating pure nitrogen and pure carbon dioxide storage in a 1 m long sample with methane displacement. Compared to the 0.12 m long sample considered in the previous chapter, the rate of advance of the injected gas across the system was reduced at the larger scale, i.e. there was a nonlinear relationship between the sample length and the breakthrough time. The main cause of this was the greater amount of the injected gas being exchanged into the matrix continuum over the longer flow distance. This gas was effectively immobilised by a combination of the low matrix permeability and adsorption.

A significant spreading of the nitrogen breakthrough profile was observed at the larger scale, whereas that of carbon dioxide was less affected. This was attributed to the greater influence of the strong preferential methane desorption by carbon dioxide compared to nitrogen. Relative to the time scale involved in the flow across the system, the steady state condition was achieved more rapidly in the 1 m long sample, which is logical since the increase in scale allowed a greater amount of methane to be mobilised via desorption prior to the breakthrough of the injected gas. The produced gas composition therefore reached the steady state more rapidly relative to the breakthrough time. At breakthrough of the injected gas, 81.1% of the original methane in place had been produced for carbon dioxide injection compared to 18.16% for nitrogen injection. It can be concluded that the methane displacement was more efficient for the injection of subcritical carbon dioxide than nitrogen at 5 MPa.

The injection of supercritical carbon dioxide produced a similar overall behaviour as for subcritical injection, only over a shorter time scale. At breakthrough, 8.9% less carbon dioxide had been injected and 30.1% less methane had been produced compared to the subcritical injection scenario. The main reason for this was the reduced time taken for carbon dioxide to flow across the system, which meant less interaction between the fracture and matrix continua, especially in relation to the kinetically controlled preferential adsorption/desorption.

To investigate the impact of the injected gas composition, the injection of a binary mixture of carbon dioxide (80%) and nitrogen (20%) was simulated. The breakthrough of nitrogen occurred before carbon dioxide due to the much larger amount of carbon dioxide immobilisation via adsorption. At the gas breakthrough time, 24.5% less carbon dioxide had been stored and 10.7% less methane had been produced compared to the injection of pure supercritical carbon dioxide.

It can be concluded that, under the adopted simulation conditions, the efficiency of the carbon dioxide storage and methane displacement was lower than for pure carbon dioxide injection. Further, the presence of nitrogen in the injected gas did little to reduce the sample permeability loss. The reason for this was the dominant coal swelling by carbon dioxide adsorption at low partial pressures, resulting from the low Langmuir pressure of 0.2 MPa. It was noted that under different conditions, for example in a coal with a considerably higher Langmuir pressure, it is more likely that the binary gas injection would result in a greater control of the system permeability, as suggested in the literature.

The major contribution of the adsorbed phase to the total gas in place was clearly illustrated under binary gas injection. This was particularly evident given the low porosity of the coal considered in this work, which meant that the free gas phase made a negligible contribution to the total gas in place. Considering these factors and the preferential adsorption of carbon dioxide, the system contained 44.4 m^3 of carbon dioxide and just 0.7 m^3 of nitrogen per m^3 coal under steady state conditions.

Finally, a simulation was performed for the injection of a carbon dioxide-rich flue gas mixture for oxyfuel combustion. The carbon dioxide storage and methane displacement

was similar to the injection of the binary mixture. This indicates that the overall behaviour of the system was largely unaffected by the presence of the different impurities.

The simulations and discussion presented in this chapter have focused on the practical/applied aspects of carbon dioxide storage and methane displacement in coal. Nonetheless, an important outcome of the chapter, in combination with chapter 6, is the insight into the processes and behaviour responsible for a range of observations related to gas flow in coal at the laboratory scale. The enhanced understanding may be applied in the analysis of alternative sets of experimental data, or in the development of future experimental studies.

This chapter has also demonstrated some of the advanced features of the developed model. Specifically, the model has been applied to study the transport, storage and displacement behaviour of supercritical gas and mixed gas in coal at the laboratory scale. These are regarded as essential capabilities in the study of applications such as carbon dioxide sequestration and enhanced methane production, but also have much broader relevance in other areas of geoenergy research.

7.5   References

Andrews, I.J. (2013). *The Carboniferous Bowland Shale gas study: geology and resource estimation*. British Geological Survey for the Department of Energy and Climate Change, London, UK.

Chung, T-H., Ajlan, M., Lee, L.L. and Starling, K.E. (1988). Generalized multiparameter correlation for nonpolar and polar fluid transport properties. *Industrial and Engineering Chemistry Research*, **27**, 671-679.

Hadi Mosleh, M. (2014). *An experimental investigation of flow and reaction processes during gas storage and displacement in coal*. Ph.D. Thesis, Cardiff University, Wales, UK.

Han, W.S., Kim, K-Y.,Lu, M., McPherson, B.J., Lu, C. and Lee, S-Y. (2011). Injectivity changes and associated temperature disequilibrium: numerical study. *Energy Procedia*, **4**, 4552-4558.

Jessen, K., Tang, G-Q. and Kovscek, A.R. (2008). Laboratory and simulation investigation of enhanced coalbed methane recovery by gas injection. *Transport in Porous Media*, **73**, 141-159.

Metz, B., Davidson, O., de Coninck, H., Loos, M. and Meyer, L. (2005). *IPCC special report on carbon capture and storage*. Cambridge University Press, Cambridge.

Peng, D-Y. and Robinson, D.B. (1976). A new two-constant equation of state. *Industrial and Engineering Chemistry Fundamentals*, **15**(1), 59-64.

Reid, R.C., Prausnitz, J.M. and Sherwood, T.K. (1977). *The properties of gases and liquids*. 3rd Edition. McGraw-Hill, New York.

Roddy, D. and González, G. (2010). Underground coal gasification (UCG) with carbon capture and storage (CCS). In: Hester, R.E. and Harrison, R.M., eds. *Carbon capture: sequestration and storage*, The Royal Society of Chemistry, Cambridge, UK.

Schepers, K.C., Oudinot, A.Y. and Ripepi, N. (2010). Enhanced gas recovery and CO_2 storage in coal bed methane reservoirs: optimized injected gas composition for mature basins of various coal rank. *In Proceedings of the SPE International Conference on CO_2 Capture, Storage and Utilisation*, 10-12 November, New Orleans, USA.

Wang, J., Ryan, D., Anthony, E.J. and Wigston, A. (2011). *Effects of impurities on geological storage of carbon dioxide*. IEAGHG.

Wright, J.D., Johnson, A.N. and Moldover, M.R. (2003). Design and uncertainty analysis for a PVTt gas flow standard. *Journal of Research of the National Institute of Standards and Technology*, **108**(1), 21-47.

8

Conclusions and Suggestions for Further Research

8.1   Introduction

The aim of this chapter is to summarise the work as a whole, synthesise the conclusions and highlight the key contributions and advancements along with opportunities for further work.

The work presented in this thesis aimed in general to examine the processes and behaviour that control high pressure gas transport and displacement in fractured rock. Specifically, the applications considered are for the study of gas interactions with coal under carbon dioxide injection and methane production. Recalling from the introduction given in chapter 1, the main objectives were to:

   i. Develop a theoretical framework for the reactive transport of high pressure gas mixtures in fractured rock under coupled hydraulic, gas/chemical and deformation behaviour, based on a dual porosity approach.

  ii. Advance a coupled thermo-hydro-chemo-mechanical (THCM) model to include

high pressure gas and dual porosity simulation capabilities.

iii. Develop and implement constitutive relationships for dual porosity coal deformation caused by physical and chemical coal-gas interactions, enabling the application of the model to study gas transport in coal.

iv. Apply and validate the developed model to examine the processes and behaviour which control gas transport and displacement in coal, with support from high resolution experimental results.

v. Investigate gas transport and displacement in coal at the laboratory scale under a series of conditions of practical importance for carbon dioxide sequestration and methane production.

These objectives provide the focus of the overall analysis of the work presented in this chapter.

A state of the art review indicated that the suitability of a particular technique for modelling fractured rock depends on the problem scale/conditions, the available input data, the output data required and the available computational resources. On the balance of these factors in most practical cases, the dual (or triple) porosity modelling technique has been the most widely applied in the literature. Moreover, this technique has proven to be highly versatile compared to the alternatives offered by the discrete fracture network (DFN) and equivalent continuum techniques. Therefore, the literature review supported the development of a dual porosity model in this work.

Recent experimental and computational research efforts were reviewed to establish the current understanding of coal-gas interactions and gas transport and displacement in coal. These studies emphasised the importance of the strongly species dependent adsorption/desorption and deformation behaviour under high pressure gas transport. Therefore, it was necessary to incorporate certain theoretical features into the generalised fractured rock formulation to account for the specific behaviour of coal.

An overview of the numerical model developed for multiphase, multicomponent gas/chemical reactive transport in fractured rock, including the model verification and the

pertinent conclusions reached, is presented below in section 8.2. This is followed in section 8.3 by an analysis of how the model application has addressed the objectives for the study of gas interactions with coal under carbon dioxide injection and methane production. Finally, sections 8.4 and 8.5 present the overall conclusions drawn from the work and the suggestions for further research, respectively.

8.2   Theoretical and Numerical Model Development

A theoretical formulation for the coupled flow of water and multicomponent gas/chemicals in a deformable dual porosity medium was developed in chapter 3, including high pressure gas effects and geochemistry. The formulation was implemented in a coupled THCM model, thereby providing advanced capabilities to the model to simulate high pressure gas transport in fractured rock under isothermal conditions. An overview of the key features and outcomes of the theoretical and numerical formulations is given below.

In the dual porosity model, the fracture network and matrix blocks were treated as distinct continua which overlap across the domain and interact via a mass exchange process. Accordingly, the governing equations were presented in terms of two sets of material properties and two sets of primary variables, i.e. one set per continuum. The transport and storage properties were expressed in terms of the local pore scale properties and a volumetric weighting factor. The objective of this was to provide an improved physical interpretation of the pore space, especially regarding the mineral infillings and altered rock zone which may influence the transport properties in the fracture network.

Non-equilibrium mass exchange terms were employed, allowing pressure and concentration differences to develop between the continua. This reflects an important characteristic of flow in fractured rock, whereby the conditions in the fracture network typically evolve over a much shorter temporal scale than in the matrix blocks. It was assumed that a quasi-steady state pressure or concentration profile was maintained in the matrix blocks, whereby the mass exchange rate varies in direct proportion to the difference between the fracture pressure or concentration and the volumetric average of the matrix pressure or concentration. The validity of this approach formed a key part of the discussion in the model application phase of the work, for which the conclusions follow in section 8.4.

It was found that high pressure gas properties are generally well characterised in the literature by constitutive relationships. Importantly, the evolution in these properties can have a considerable impact on gas transport and the inclusion of an appropriate equation of state and dense gas viscosity model was prioritised. Descriptions of the pressure effects on gas diffusivity are less theoretically rigorous. Nonetheless, a suitable empirical estimation method was used. These theoretical features are seen as essential components of the model for the accurate simulation of multicomponent gas transport at high pressure.

The developments described above, in combination with relevant advective, dispersive and diffusive fluxes in the fracture and matrix continua, advanced the model for the simulation of non-reactive flow in fractured rock. As in previous works, there is an option in the future to link the dual porosity model with an external geochemical model, PHREEQC, to include a full spectrum of equilibrium and kinetically controlled geochemistry. For the model applications considered in this work, the literature review indicated the dominant role of gas adsorption/desorption in coal. Therefore, it was decided not to employ the external geochemical model at this stage in preference of developing a bespoke geochemical module for the kinetically controlled gas adsorption/desorption, which was described in the work.

Another important theoretical feature to enable the simulation of coal-gas systems was a description of the coal deformation caused by physical and chemical interactions with multicomponent gas. Therefore, constitutive relationships for coal deformation in a dual porosity system were developed. The resulting analytical expressions described the porosity and permeability evolutions in the fracture and matrix continua. This was achieved by extending an approach presented in the literature where the matrix porosity had been neglected. Since the matrix porosity can be influential in terms of free gas storage and controlling the rate of diffusion, this was regarded as an important extension.

A numerical approximation was adopted to solve the series of governing equations for all primary variables in the dual porosity system. A finite element solution was employed for spatial discretisation based on the Galerkin weighted residual method. Temporal discretisation was achieved via a finite difference scheme based on a mid-interval backward-difference time-stepping algorithm. A time-splitting approach, namely, the

sequential non-iterative approach, was used to couple the transport equations and non-equilibrium sink/source terms for inter-continua mass exchange and geochemical reactions, i.e. adsorption/desorption.

The developed theoretical formulation and the numerical solution provide an advanced computational platform to simulate the coupled physical and chemical processes that control gas transport and displacement in fractured rock. Specific theoretical features have also been included to enable to study of coal-gas systems. An overview of the work conducted and conclusions reached in this regard is provided later in section 8.4.

8.3   Model Verification

Prior to employing the model for predictive purposes, a set of verification tests was performed. The principal aim was to assess the correctness of the implementation of the theoretical and numerical developments in the model, as summarised above. The benchmarks for the verification tests were provided by analytical or alternative numerical solutions presented in the literature.

Two simulations were conducted to examine the advective and diffusive flux of a single non-reactive ideal gas component in the fracture and matrix continua. For the particular conditions of the test, including the assumption of no interactions between the continua, the comparisons with analytical solutions indicated that the transport equations have been correctly included in the dual porosity model. A further test on the non-reactive gas transport was performed to ensure that the gas compressibility is reflected in the steady state concentration profile under a concentration (i.e. pressure) gradient. Verification of this behaviour was achieved considering the benchmark provided by the results of an analytical solution.

The high pressure transport of multicomponent gas with kinetically controlled adsorption/desorption was verified against the results of an alternative numerical model presented in the literature. Two flow scenarios were tested and the capability of the model to predict the species dependent gas transport and displacement behaviour at high pressure was demonstrated. Building upon these verifications, a series of tests were conducted to

examine the coupling between the chemical transport and geochemical modules in greater detail. It was found that the changes in the chemical transport behaviour at different adsorption rates followed those reported in the literature for an alternative numerical model, thereby providing further evidence on the successful implementation of the adopted time-splitting approach. A final series of verification tests was conducted to examine the coupling between the chemical transport and inter-porosity mass exchange models in a dual porosity, dual permeability system. Again, the correct functionality was demonstrated via comparisons with numerical solutions presented in the literature.

The verification tests established a good level of confidence regarding the accurate numerical implementation of the theoretical framework for reactive flow in fractured rock. Subsequently, the model was applied at the laboratory scale and a broad validation of the model was achieved in relation to the gas interactions, transport and displacement in coal. This stage of the work is addressed below.

8.4   Model Application and Validation

An integral part of the work was the validation of the developed theoretical and numerical models using high resolution experimental data on coal-gas interactions. This data was obtained in the experimental study by Hadi Mosleh (2014) for anthracite coal provided by the Unity Mine, South Wales, UK, taken from the "6 ft" seam at a depth of 550 m. The culmination of the model application and validation process was the simulation of experiments for gas injection and displacement in coal cores. The experimental data allowed the model capabilities and the accuracy of the underlying theory to be explored further. An overview of the validation tests undertaken and the main conclusions reached is provided below.

Comparisons with the experimental results for gas injection and displacement in coal aimed to assess the validity of the developed dual porosity, dual permeability model as a whole under the conditions tested. Two injection scenarios were considered for a system initially saturated with methane, namely, pure nitrogen injection and pure carbon dioxide injection. Before these simulations were performed, additional experimental results for the gas adsorption kinetics and permeability in coal were used to explore the capabilities of the

relevant theoretical models. This was seen as an important stage since the parameters and enhanced understanding of these processes were applied in the gas injection and displacement simulations. Further to this, the detailed laboratory characterisation of the coal samples gave a good level of confidence in a number of key material properties used throughout the validation.

The gas adsorption/desorption kinetics were described in chapter 3 using a first-order rate model. This approach was found to provide a reasonably good description of the adsorption kinetics of various gases in powdered coal. However, similar to some works presented in the literature, a combination of two first-order rate models was found to improve the agreement with the experimental results. This implied that gas adsorption in coal may be described by two distinct stages, i.e. a rapid first stage followed by a more gradual second stage. The contribution of each stage to the overall kinetics was found to be species dependent. Cited explanations for this related to the varying distributions of adsorbate molecules in the meso- and micro-pores and the promoted access to micropore adsorption sites for species with greater adsorption energies and smaller kinetic diameters.

In terms of simulating the experiments for gas injection and displacement, an essential outcome from examining the adsorption behaviour was the quantitative description of the strongly species dependent gas adsorption in the coal tested. This is especially true regarding the preference of carbon dioxide to adsorb much more rapidly and in greater amounts than nitrogen and methane.

The deformation model developed for dual porosity coal deformation was compared with experimental permeability measurements for the pure flow of the above mentioned gas species. A good agreement was found between the predicted permeability trends and the experimental data. The model was applied to interpret the experimental results based on the physical and chemical mechanisms of deformation included. Similar to above, a strong species dependent behaviour was attributed to the reversible chemo-mechanical deformation (swelling/shrinking) due to gas adsorption. This reflects that the feedback of coal-gas interactions on gas transport is an essential feature in models applied in the study of related applications, as reported in the literature.

A number of limitations were highlighted in the testing of the deformation model. Firstly,

the model was only partially validated since the experimental results covered a relatively narrow range of effective stress and were limited to the flow of pure gas. In addition, it was noted that the permeability rebound caused by desorption induced coal shrinking may be over-predicted and that negative permeabilities are predicted under certain conditions. These findings imply that further development and testing of the deformation model is required in future work. Nonetheless, the model was partially validated and the predicted trends for a multicomponent system were largely reasonable. Therefore, a confident application of the model in the numerical simulations was achieved by prescribing appropriate lower bound (threshold) permeabilities to prevent negative values.

The in-depth analysis of the species dependent interactions in a coal-gas system, summarised above, was invaluable for the correct interpretation of the results of the gas injection and displacement simulations. It was concluded that the different breakthrough profiles of nitrogen and carbon dioxide were predominantly caused by the coal swelling response to carbon dioxide adsorption. Methane desorption was found to have been of little importance in the gas breakthrough profiles since the simulation period (90 minutes) was much shorter than the half-life for methane desorption (180 minutes). Moreover, this effectively restricted the preferential displacement of adsorbed methane by carbon dioxide under the conditions considered.

The evolution in the produced gas composition in the simulation for nitrogen injection showed a good agreement with the experimental results. By comparison, the agreement was not as good for carbon dioxide injection. Although the breakthrough profile was qualitatively similar to that observed in the experiment, it was found that a one-third lower initial permeability provided an improved quantitative agreement. As summarised below, a number of experimental and computational factors were explored to explain this.

From the literature review, it is known that coal permeability is sensitive to effective stress cycles. Hence, in terms of experimental factors, it was concluded that the permeability of the coal sample may have been reduced between the start of the two experiments. The discussed computational factors focused on the likelihood of the rate of permeability loss by coal swelling being under-predicted. Among the factors examined and considering the literature support, it is believed that the assumption of a quasi-steady state mass exchange

rate may have been invalid at early breakthrough times, i.e. in the region of the breakthrough front. Any initial transiency in this region, whereby the mass exchange rate was temporarily elevated, would have increased the flow of carbon dioxide into the matrix and so increased the rate of adsorption induced coal swelling. However, it is difficult to make definitive conclusions without further investigation and this is recommended for future work.

Whilst acknowledging the above recommendation, it was concluded that the salient features of the gas breakthrough behaviour observed in the laboratory were likewise predicted by the numerical model. Accordingly, it is claimed that the developed model is capable of simulating the major physical and chemical phenomena involved in gas injection and displacement in coal at the laboratory scale. The model validation presented in chapter 6 therefore demonstrated that a satisfactory accuracy has in general been achieved in the underlying theory of the model. This allowed more advanced simulations to be performed to study gas transport and displacement in coal under a wider range of conditions. The conclusions arising from the advanced simulations are given below.

8.5   Study of High Pressure Gas Transport and Displacement in Coal

Chapter 7 presented laboratory scale simulations dealing with a series of gas injection and methane displacement conditions, which principally aimed to study how the behaviour changed for different samples sizes and gas injection pressures and compositions. Further, there was an emphasis on the more applied issues of how the carbon dioxide storage and methane displacement were affected, which was achieved by presenting results in terms of the temporal evolutions of the gas in place and the produced gas composition.

It was found that the changes in the above mentioned conditions, most especially an increase in the sample size, had a considerable influence on the observed behaviour. First and foremost, this was because the interactions between the fracture and matrix continua, including the effects of kinetically controlled preferential adsorption/desorption, became more prominent for the longer time scale of flow across the system. Increases in the injection pressure, such as for the injection of supercritical carbon dioxide, had the opposite effect by reducing the time scale. Hence, under the laboratory scale simulation

conditions considered, the elevated injection pressure reduced the amount of carbon dioxide stored and methane produced at the breakthrough time. The injection of carbon dioxide-rich gas mixtures was found to further reduce the performance in these regards.

The analysis of the results of the advanced simulations provided valuable insights into the processes and behaviour responsible for different gas transport and displacement observations in coal at the laboratory scale. A key overall conclusion is that the particular behaviour observed at the laboratory scale is highly dependent on the time scale of flow across the system relative to the time scales of the coal-gas interactions. The in-depth analysis provided may be applied in the interpretation of alternative sets of experimental data, or in the development of future experimental studies.

Equally important is that the advanced capabilities of the developed model have been successfully demonstrated. Specifically, this relates to the features of the model which allow the simulation of complex systems of high pressure multicomponent gas transport in fractured rock, including nonlinear gas behaviour and geochemistry. The latter are regarded as highly important in the simulation of carbon dioxide sequestration in deep rock formations, which typically occurs under conditions very close to the phase change between gas and supercritical fluid and can induce a number of complex solid-water-chemical interactions.

8.6   Overall Conclusions

In terms of overall conclusions that can be drawn from the research performed, the following observations are presented:

    i. A new theoretical and numerical modelling platform has been developed for studying the reactive transport processes in fractured rock. Within a coupled thermal, hydraulic, chemical and mechanical (THCM) modelling approach, the hydraulic, gas/chemical and deformation behaviour has been successfully considered based on a dual porosity, dual permeability framework. The compositional structure of the model provides a flexible scientific tool for both present applications and future development work.

ii. Appropriate constitutive relationships were included in the model to accurately describe the major transport properties of high pressure gas mixtures in deep rock formations, thereby enabling the study of geoenergy applications such as carbon dioxide sequestration.

iii. Key theoretical features included enhance the model capabilities to study coal-gas systems. Most notably, constitutive relationships were developed for the porosity and permeability evolution in coal under the dual porosity framework, thereby placing important controls on bulk gas transport and the flow interactions between the fractures and matrix blocks. The relationships offer an advanced theoretical description of the feedback of dual porosity physico- and chemo-mechanical deformation on gas transport in coal.

iv. Verifications of the model provided further confidence in: (i) the accuracy of the numerical implementation of the dual porosity governing equations, and (ii) the efficiency of the techniques employed for coupling the transport module with the geochemical reaction and mass exchange modules.

v. A detailed validation using high resolution experimental data demonstrated that the developed model is capable of simulating the salient physical and chemical phenomena related to gas interactions, transport and displacement in coal. This served to establish that the underlying theoretical framework of the model is valid under the conditions of the benchmarks considered.

vi. Analysis of the model application results for carbon dioxide storage and methane displacement provided further insight into the coupled behaviour of the material at the laboratory scale which, in the author's opinion, is lacking in the literature. The analysis indicated that the species dependent chemo-mechanical deformation was the dominant factor in the observed behaviour in smaller samples, and that the preferential displacement of adsorbed methane by carbon dioxide was negligible under the experimental conditions and time scales considered.

vii. A series of advanced laboratory scale simulations for larger systems demonstrated the increased influence of the fracture-matrix interactions and preferential methane

desorption on the overall gas transport, storage and displacement behaviour in coal. In the author's opinion, such an analysis into the effects of sample size offers considerable value in terms of interpreting experimental data, and indicates that due care must be taken in interpreting laboratory scale results towards larger scale applications.

viii. It is claimed that the new dual porosity, dual permeability model has represented a significant enhancement in the capabilities of a coupled THCM model. Specifically, the model may now be applied in the study of a broad new range of applications involving multiphase, multicomponent gas/chemical transport phenomena in fractured rock. Applications to the case of coal-gas systems have featured throughout this thesis, and as such the enhanced capabilities of the model have been showcased in this regard.

8.7   Suggestions for Further Research

Within the scope of the research conducted and in particular the theoretical and numerical models developed, a number of areas have been identified for future research. Drawing on the work throughout the thesis, but especially the main findings presented in this chapter, the suggestions for future research are described below.

Uncertainties surrounding the theory and application of the mass exchange term for coupling the fracture and matrix flows have become more apparent as this work progressed. This culminated in the aforementioned conclusion that the assumption of quasi-steady state mass exchange may be invalid under certain conditions, especially in the region of a breakthrough front. Whilst the literature review evidenced some research into transient mass exchange, a leap in understanding of the underlying processes has generally remained evasive. Hence, further attempts to study and theorise the mass exchange process are recommended, for example via microscale flow modelling.

The constitutive relationships developed in this work to describe dual porosity deformation require additional development and testing, as detailed in chapter 6. Further validation should initially focus on comparisons with experimental data for a wider range of effective

stress, before moving onwards to evaluate the multicomponent capabilities in detail. In conjunction with these tests, additional theoretical developments are required, most notably to handle the prediction of negative permeabilities under certain conditions. In this regard, it is suggested that some geomechanical constraints are missing from the model.

Water transfer and the associated couplings of hydraulic and gas/chemical behaviour were included in the developed dual porosity, dual permeability model. However, these features were not studied in detail in this work, since the scope for model application was for dry coal-gas systems. Some prominent research opportunities exist on the effects of water transfer and even residual moisture on high pressure gas transport, storage and displacement in fractured rock. This is especially true in the case of coal. As an example, additional capabilities to model high pressure gas dissolution and the subsequent geochemistry would provide advanced capabilities for studying the long term fate of sequestered carbon dioxide.

The chemo-mechanical behaviour of coal under interactions with different gases has been a major factor in many discussions throughout the model applications considered. In fact, the coal swelling phenomenon is widely regarded as a significant restraint on the prospects for carbon dioxide sequestration in coal (including enhanced methane displacement). An improved understanding of the swelling mechanism increases the likelihood of identifying an engineering solution to this problem, and certainly theoretical and computational developments have an important role to play in this.

It is further recognised that the developed dual porosity model is an expandable component within a wider thermal, hydraulic, chemical and mechanical model and will be subject to continual advancements to improve and test its capabilities. Considering the scope of this work predominantly included the hydraulic and gas/chemical aspects of behaviour in fractured rock, the extension of the thermal and mechanical components of the model for dual porosity capabilities is suggested for future work.

Finally, it is noted that the above suggestions are by no means exhaustive; rather they represent areas of research which are most closely linked to the work presented in this thesis.

8.8   References

Hadi Mosleh, M. (2014). *An experimental investigation of flow and reaction processes during gas storage and displacement in coal*. Ph.D. Thesis, Cardiff University, Wales, UK.

Appendix A

Overview of the Experimental Programme

A.1   Introduction

This appendix provides a summary of the main analysing units in the experimental facilities and the materials and methods developed by Hadi Mosleh (2014) to conduct the adsorption/desorption and transport testing on coal samples. Discussions on the design, construction and commissioning of the apparatus are beyond the scope of this work. Details can be found in Hadi Mosleh (2014). The focus in this appendix is on providing the information that is most relevant to the development and analysis of the laboratory scale numerical simulations presented in chapter 6.

In general, the experimental programme aimed to measure the parameters and investigate the processes that are important in the study of gas transport and storage in coal. An overview of the apparatus designed to meet this aim is provided hereby dividing it into three units:

    i. Adsorption/desorption measurement unit
   ii. Gas transport and flow measurement unit
  iii. Ancillary units (i.e. gas supply unit and gas analysing unit)

A schematic diagram of the apparatus is provided in Figure A.1, in which the main

measurement units have been identified. A brief description of each of the main features of the apparatus is provided in the following sections.
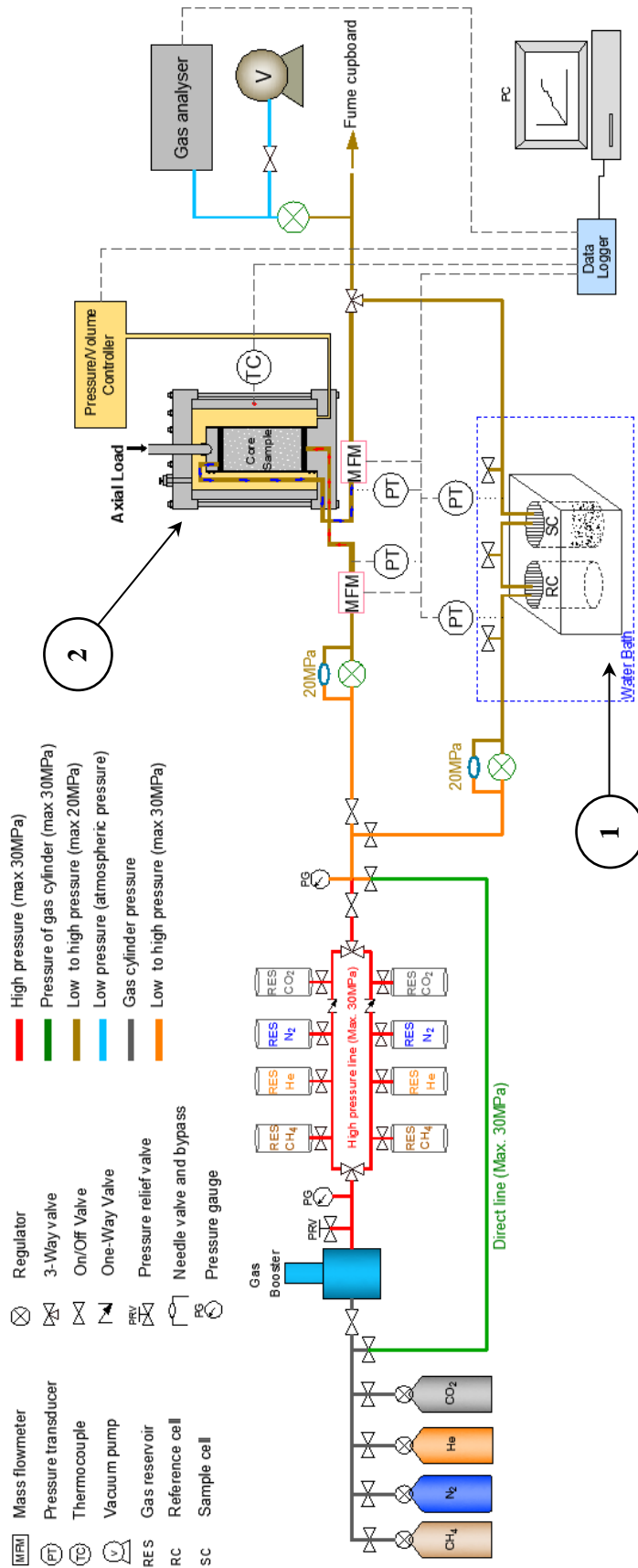
A.2   Adsorption/Desorption Measurement Unit

A manometric unit was designed to investigate the adsorption/desorption behaviour of coal on exposure to high pressure gas (Hadi Mosleh, 2014). The unit consists of a reference cell and a sample cell, each with a volume of 150 cm^3, connected via a needle valve. Two pressure transducers are used measure the pressure in the reference and sample cells separately. A $300 \times 300 \times 300$ mm water tank and a temperature controller are used to maintain the entire unit under isothermal conditions during testing. The system was designed for a maximum gas pressure of 20 MPa and a maximum temperature of 338K. The main features of the adsorption/desorption measurement unit can be seen in Figure A.2.

## A.3   Gas Transport and Flow Measurement Unit

As shown in Figure A.1, a bespoke triaxial cell was used to investigate the flow and deformation behaviour of coal cores up to 0.1 m diameter, with a length twice the diameter (Hadi Mosleh, 2014). A submersible load cell is housed inside the triaxial cell, and local strain transducers can be fitted to samples up to 0.07 m diameter. The core is fitted with a rubber sleeve, to which the confining pressure is applied via the cell fluid (silicone oil 350 polydimethylsiloxane) using a pressure/volume controller. Diffusion plates are used to promote uniform flow across the inlet and outlet surfaces of the core. Axial loads up to 50 kN can be applied using an electro-mechanical digital loading frame and ram. Gases can be injected from the bottom of the cell at pressures up to 20 MPa.

Flow and pressure measurements are made using upstream and downstream flow meters and pressure transducers. Heating elements are wrapped around the pipelines, valves, pressure transducers and triaxial cell to maintain isothermal conditions from ambient temperature up to 338 K. In addition, thermocouples are used to monitor the temperature at the top, middle and bottom of the core. To measure displacement, two axial and one radial

Figure A.1 Schematic diagram of the experimental apparatus (Hadi Mosleh, 2014). The adsorption/desorption and gas transport and flow measurement units are indicated by the numbers 1 and 2, respectively.

local strain transducers are used. Some of the main components of the gas transport and flow measurement measurement unit can be seen in Figure A.3.
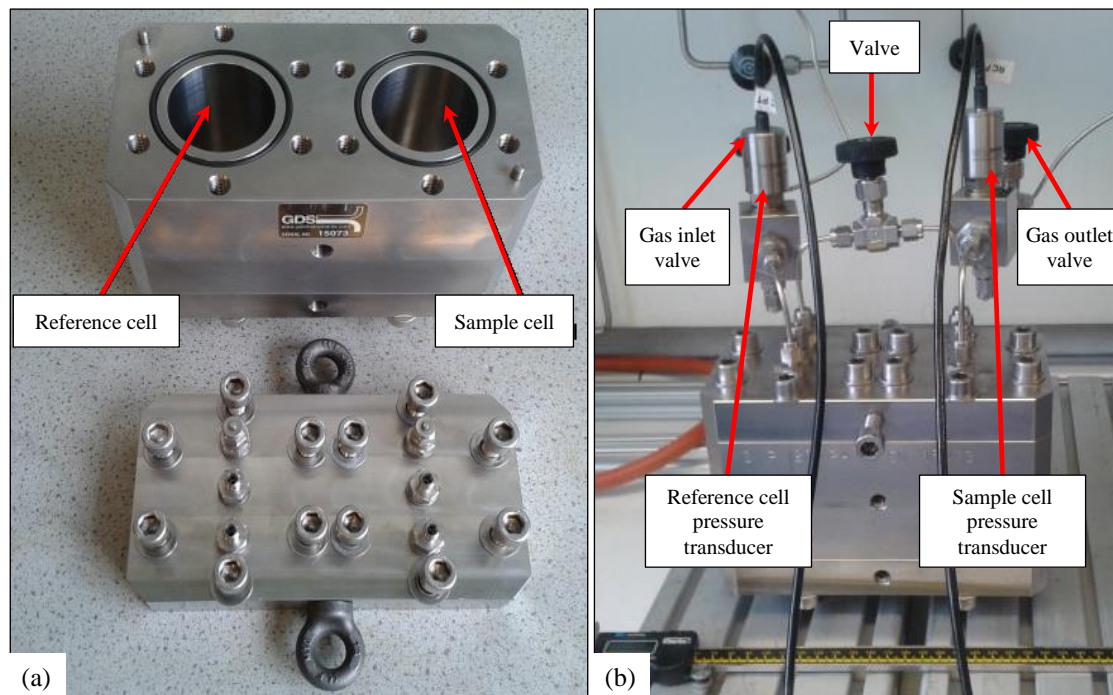

Figure A.2 Adsorption/desorption measurement unit showing (a) disassembled reference and sample cells, and (b) assembled unit with valves and pressure transducers (Hadi Mosleh, 2014).

A.4   Ancillary Units

Gas can be supplied to the measurement units described in the previous sections at pressures up to 20 MPa and temperatures up to 338 K. The gas supply unit comprises carbon dioxide (CO_2), nitrogen (N_2), methane (CH_4) and helium (He) gas cylinders, an air driven gas booster and four high pressure gas reservoirs. These components have been designed to ensure that the gas can be delivered at the required pressure and in the required quantity in a range of test scenarios (Hadi Mosleh, 2014). The supply can be either pure gas or a mixture of gases, as required. A two channel gas analysing unit allows the composition of produced gas to be determined.

Finally, all experimental data is routed through a data logger to a PC for monitoring and analysis.
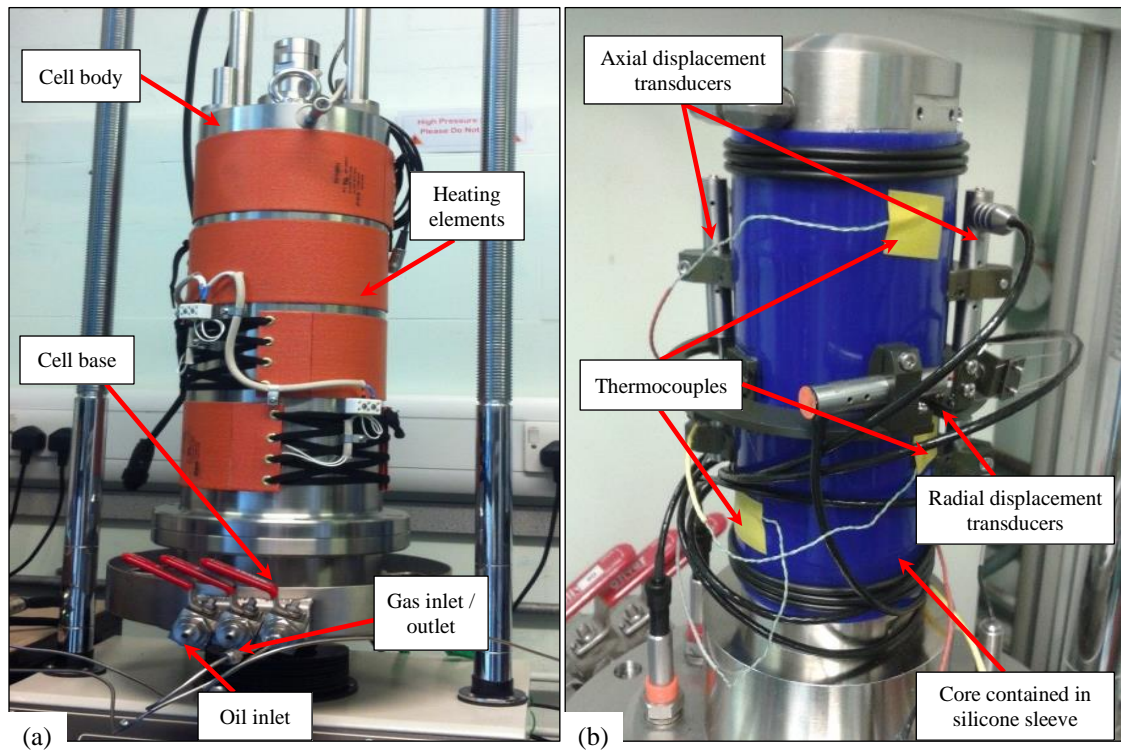
Figure A.3 Transport and flow measurement unit showing (a) high pressure triaxial cell with heating elements attached, and (b) core fitted with silicone sleeve, displacement transducers and thermocouples (Hadi Mosleh, 2014).

A.5   Materials and Methods

This section provides a summary of the characteristics and properties of the coal samples and describes the methods used to conduct the tests. This information is important to ensure that the parameters and conditions prescribed in the numerical simulations reflect the experimental conditions. This allows the validity of the formulation to be explored with more confidence. The remainder of this section comprises a brief description of the coal sampling, characterisation and preparation, in addition to the methods used in the adsorption/desorption and transport and flow measurement tests.

A.5.1   Coal Sampling, Characterisation and Preparation

The coal samples used in the experimental programme were provided by the Unity Mine, South Wales, UK, and were taken from the "6 ft" seam at a depth of 550 m. A combination

of existing information and laboratory measurements, including proximate and ultimate analyses, has been used to characterise the coal. A summary of the results of the characterisation process is provided in Table A.1. Speight (2005) presented typical property ranges for coals of different ranks. Based on these ranges and the results in Table A.1, the coal samples used in the laboratory have been characterised as a high rank coal with properties matching those of anthracite coal (Hadi Mosleh, 2014). A range of likely values for the total porosity has been identified and reported in Table A.1 via a comparison with porosity ranges reported in the literature for high rank coals, as shown in Figure A.4.

Table A.1 Summary of the coal characterisation results obtained by Hadi Mosleh (2014).

Procedure	Coal property	Value
Proximate analysis	Moisture content, % wt	1.19
	Ash content, % wt	4.85
	Volatile matter, % wt	9.56
	Fixed carbon, % wt	84.39
Ultimate analysis	Carbon, % wt	86.42
	Sulphur, % wt	0.79
	Oxygen + Hydrogen + Nitrogen, % wt	12.79
Mass / volume analysis	Average dry bulk density, kg m^{-3}	1495.85
Literature review	Total porosity (approx.)	0.025 to 0.060

In all of the adsorption/desorption measurement test, the coal was powdered and a 50 g sample sieved to ensure a grain size fraction in the region of 0.5 to 1 mm. Furthermore, all adsorption/desorption tests were conducted on air-dry coal to reduce the effect of moisture.

The core samples used in the transport and flow measurement unit were taken from a large coal sample using a coring machine with a 0.07 m diameter diamond coring bit. The cores were then cut to the required length of around 0.12 m using a diamond saw. To reduce the risk of a breach in the silicone sleeve during hydrostatic loading, the cores were made smooth using fine sand paper and wrapped in thick PTFE tape. Details of the sample

preparation can be found in Hadi Mosleh (2014).
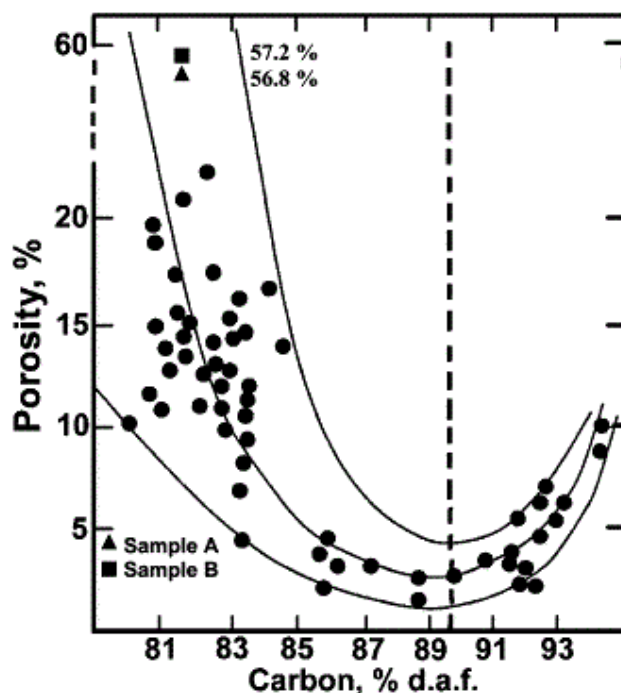
Figure A.4 Relationship between coal rank and porosity (Rodrigues and Lemos de Sousa, 2002).

A.5.2 Adsorption/Desorption Measurement Method

Before the start of each test a vacuum pump was used to evacuate the pipes, valves, reference cell and sample cell to prevent contamination of the injected gas. In order to calculate the excess adsorbed amount, the void volume with and without the sample was required. This information was obtained using the helium pycnometry method. Helium was chosen since it behaves as an ideal gas and is inert so that it remains in the free phase, allowing the void volume of the unit to be determined accurately.

After placing the sample in the sample cell, the unit was subjected to a vacuum of ~100 kPa for 24 hours to evacuate residual gas and moisture. The adsorption behaviour of the sample was then evaluated by increasing the injection pressure in a stepwise manner (values of 0.5, 1.0, 2.0, 3.0, 4.2, 5.5 and 7.0 MPa were used). Before the start of each step, the needle valve between the reference and sample cell was closed and the reference cell pressurised to the injection pressure using the experimental gas. The needle valve was then

opened and adsorption measurements were taken by logging the equilibration of system pressure. Temperature was maintained at 298 K during the adsorption/desorption tests, following an analysis of the conditions at the sampling location by Hadi Mosleh (2014).

A.5.3 Transport and Flow Measurement Method

Again, the first step in each test was to evacuate the coal core of gas by keeping it under vacuum for 24 hours. The core was then saturated with the experimental gas. Permeability tests were conducted by opening the downstream valve to atmospheric pressure and maintaining a constant injection pressure using the experimental gas. Once steady state flow had been achieved, pressure and flow were logged and Darcy's Law was applied to calculate the permeability. A wide range of scenarios were considered using He, N_2, CH_4 and CO_2 as the experimental gas, at injection pressures up to 5.5 MPa and confining pressures between 1 MPa and 6 MPa.

The gas displacement tests involved saturating the core with CH_4 at 5 MPa with the downstream valve closed. Depending on the test, N_2 or CO_2 were injected at a constant upstream pressure of 5 MPa at the same time as the downstream valve was opened to atmospheric pressure. The flow rate and composition of the produced gas were logged continuously. A confining pressure of 6 MPa was used in these tests.

More details of the test procedures can be found in Hadi Mosleh (2014).

A.6 References

Hadi Mosleh, M. (2014). *An experimental investigation of flow and reaction processes during gas storage and displacement in coal*. Ph.D. Thesis, Cardiff University, Wales, UK.

Rodrigues, C.F. and Lemos de Sousa, L. (2002). The measurement of coal porosity with different gases. *International Journal of Coal Geology*, **48**, 245-251.

Speight, J.G. (2005). *Handbook of coal analysis*. John Wiley and Sons, Hoboken, New Jersey.